Technische Universität München
TUM School of Computation, Information and Technology

Modeling Nonplanar Frictional Surface Contacts for Robust Robot Grasping

Jingyi Xu, M.Sc.

Vollständiger Abdruck der von der TUM School of Computation, Information and Technology der Technischen Universität München zur Erlangung des akademischen Grades einer

Doktorin der Ingenieurwissenschaften (Dr.-Ing.)

genehmigten Dissertation.

Vorsitz:		Prof. Dr.-Ing. Sami Haddadin
Prüfer*innen der Dissertation:	1.	Prof. Dr.-Ing. Eckehard Steinbach
	2.	Prof. Dr. Ken Goldberg

Die Dissertation wurde am 21.02.2022 bei der Technischen Universität München eingereicht und durch die TUM School of Computation, Information and Technology am 28.11.2022 angenommen.

Abstract

Deformable gripper jaws are widely applied in robot grasping applications to better resist external disturbances. Grasping with such jaws results in nonplanar surface contacts if the jaws deform to the nonplanar local geometry of an object. The frictional force and torque that can be transmitted through a nonplanar surface contact are both three-dimensional, resulting in a six-dimensional frictional wrench (6DFW). Applying traditional point and planar frictional contact models to such contacts leads to over-conservative results as the models do not consider the nonplanar surface geometry and only compute a three-dimensional subset of the 6DFW. A grasp planner with such overly conservative frictional contact models either fails to find any grasps to manipulate the object or requires an unnecessary large grasp force, which may break fragile objects.

To address this issue, this thesis proposes nonplanar frictional surface contact models, which estimate the force and torque that a deformable gripper jaw can exert on the object via a nonplanar surface contact. Specifically, this thesis presents the derivation of the 6DFW by combining concepts of differential geometry and the Coulomb friction law and further proposes two 6D limit surface (6DLS) models to approximate the frictional force and torque limit. In addition to experiments with six parametric surfaces and 2,932 meshed contacts in simulation, the proposed models are further evaluated in terms of their grasp prediction success rate with more than 3,000 physical grasps of 3D-printed objects collected on three robot setups. In these experiments, the nonplanar frictional surface contact models increase precision and recall by up to 4% and 25% over the traditional frictional contact models, respectively.

The thesis further presents a grasp planner for deformable gripper jaws based on the proposed models. The planner finds the most robust grasp using a depth image of previously unseen objects and achieves 92% grasp success, a 10% increase over the traditional frictional contact models. The presented grasp planner is also able to find robust grasps for flat objects, whereas the traditional ones failed to find successful grasps in this case.

Kurzfassung

Verformbare Greifbacken werden häufig bei Robotergreifanwendungen eingesetzt, um äußeren Störungen besser zu widerstehen. Das Greifen mit solchen Backen führt zu nichtplanaren Oberflächenkontakten, wenn sich die Greifbacken an die nichtplanare lokale Geometrie eines Objektes anpassen. Die Reibungskraft und das Drehmoment, die durch einen nichtplanen Oberflächenkontakt übertragen werden können, sind beide dreidimensional, was zu einer sechsdimensionalen Kraftschraube (engl. six-dimensional frictional wrench, 6DFW) führt. Die Anwendung herkömmlicher Punkt- und Planarreibungsflächenkontaktmodelle auf solche Kontakte führt zu zu konservativen Ergebnissen, da die Modelle die nichtplanare Oberflächengeometrie nicht berücksichtigen und nur eine dreidimensionale Teilmenge der 6DFW berechnen. Ein Greifplaner mit solchen übermäßig konservativen Kontaktmodellen findet entweder keine Greifpunkte zum Manipulieren des Objektes, oder erfordert eine unnötig große Greifkraft, die zerbrechliche Gegenstände zerstören kann.

Um dieses Problem zu adressieren, stellt diese Dissertation nichtplanare Reibungsflächenkontaktmodelle (engl. nonplanar frictional surface contact models) vor, die die Kraft und das Drehmoment abschätzen, die eine verformbare Greifbacke bei einem nichtplanaren Reibungsflächenkontakt auf das Objekt ausüben kann. Diese Dissertation präsentiert insbesondere die Ableitung des 6DFW durch die Kombination von Konzepten der Differentialgeometrie und der Coulombschen Reibung und präsentiert außerdem zwei 6D-Grenzflächenmodelle (engl. six-dimensional limit surface, 6DLS), um die Reibungskraft- und Drehmomentgrenze zu approximieren. Zusätzlich zu Simulationsexperimenten mit sechs parametrischen Oberflächen und 2,932 diskreten Kontakten, werden die vorgeschlagenen Modelle hinsichtlich ihrer Erfolgsrate bei der Grifferfolgsvorhersage für mehr als 3,000 physische Greifvorgänge von 3D-gedruckten Objekten, die auf drei Roboteraufbauten gesammelt wurden, evaluiert. In diesen Experimenten erhöhen die nichtplanaren Reibungsflächenkontaktmodelle die Präzision (engl. precision) und Vollständigkeit (engl. recall) um bis zu 4% beziehungsweise 25% gegenüber den herkömmlichen Reibungsflächenkontaktmodelle.

Diese Arbeit präsentiert außerdem einen Greifplaner für verformbare Greifbacken basierend auf den vorgeschlagenen Modellen. Der Planer findet den robustesten Griff ihm unbekannter Objekte für ein gegebenes Tiefenbild und erzielt eine Erfolgsrate von 92%, 10% mehr als die traditionellen Reibungsflächenkontaktmodelle. Der vorgestellte Greifplaner ist darüber hinaus in der Lage, robuste Griffe für flache Gegenstände zu finden, während die herkömmlichen Planer in diesem Fall keine geeigneten Griffe finden.

Acknowledgements

The work presented in this dissertation was carried out as a member of the academic staff at the Chair of Media Technology (LMT) at the Technical University of Munich and as a visiting researcher at the Autolab at UC Berkeley. Many people have supported me, personally as well as professionally, during the past years.

First of all, I would like to express my deep gratitude to my supervisor Prof. Eckehard Steinbach for his kind generosity and trust. It was an honor to be in his team. Despite his busy schedule, he always has been accessible for discussions. He provided excellent feedback and guided me in the right direction, while giving me space to develop my own ideas. I really appreciate that he supported me to pursue my passion in contact modeling for grasping. I remember hours of discussion for the journal revision and I am deeply thankful for his excellent feedback for both content and writing. I am also sincerely grateful for his support for my visit in the US. His endless support shaped my entire PhD.

I would like to extend my heartfelt thanks to Prof. Ken Goldberg for welcoming me as a member of the Autolab family. Despite his busy schedule, he always took time for discussions and provided me excellent feedback, ranging from the Cantilever effect for grasp analysis to the color map selection for presentations. His positive energy, enthusiasm about robotics, and perseverance really inspired me. I was honored to be in his team.

My sincere appreciation is also devoted to my former and current colleagues at LMT. The group has been a source of friendships and great advises for research and life. They helped me professionally through their continued support. In the meanwhile, they also created a special and enjoyable environment on a personal level. I am particularly grateful to Dr. Nicolas Alt, Dr. Xiao Xu, and Dr. Clemens Schuwerk for a kick-start of my research with their expertise and experiences. I also highly value my colleagues and students at LMT. Particular thanks go to Dr. Tamay Aykut, Mojtaba Karimi, Dr. Matti Strese, Dr. Dominik van Opdenbosch, Dr. Dmytro Bobkov, Alexandra Zayets, Dr. Rahul Chaudhari, Prof. Chenglin Li, Furkan Kaynar, Yuankai Wu, Martin Piccolrovazzi for interesting discussions and helping me for my research, as well as providing an enjoyable atmosphere. I am also grateful to all my students, especially Yeting Dong, Tapan Sharma, Chongze Yu, Ge Sun, Zhongyao Zhang, Liang Ding who contributed to our publications. My appreciation also goes to the professional administrative support provided by Dr. Martin Maier, Marta Giunta, Simon Krapf, and Etienne Mayer.

I also want to thank my colleagues and friends at the Autolab for welcoming, inspiring, and supporting me. I would like to express my sincere thanks to Michael Danielczuk, Dr. Jeff

Ichnowski, Dr. Jeff Mahler, Dr. Daniel Seita, William Wong, Harry Zhang, and Priya Sundaresan for the collaboration and their constructive feedback for research, writing papers, and presentations. I enjoyed working with them as much as our Friday social event at the lab.

I would like to extend my sincere thanks to researchers that I met at conferences. Special thanks to Prof. Alberto Rodriguez, Prof. Su Hao, Prof. Daolin Ma, Dr. Hao Ding, Prof. Miao Li for the fruitful discussions and constructive feedback.

Last but not least, I would like to express my deepest gratitude to my family and friends, in particular to my beloved parents Hang Xu and Manjing Li, my grandparents Jushi Chen, Afeng Lin, Mingqu Li, Chaofa Xu, my aunt and uncle Li Li and Chong Tao, and my cousin Yuning Tao, who always encouraged me and believed in me. Specifically, I want to thank my father for his guidance for my career and for saying it is ok to fail as long as I tried my best; my mother for her spiritual and emotional guidance; my grandfather for pushing me to pursue my PhD since I was in kindergarten; my grandmother for taking me to many classes growing up and for calming me down before my deadlines by telling me to only concentrate on one thing at a time. I would like to extend my gratitude to my friends Dr. Xinyi Guo and Huizhu An for their great suggestions in writing and presentation, as well as for all the interesting discussions and emotional support. I also would like to thank my boyfriend Stefan Lochbrunner and his family. Specifically, I want to thank dear Stefan for all his support, ranging from helping me with all the hardware setups to calming me down when I am anxious. Without their endless support and valuable advice I would not be where I am today.

Contents

Notation

Abbreviations

Abbreviation	Description	Definition
3D	Three-dimensional	page 2
6D	Six-dimensional	page 2
3DLS	Three-dimensional Limit Surface	page 23
6DLS	Six-dimensional Limit Surface	page 74
6DFC	Six-dimensional Friction Cone	page 83
6DFW	Six-dimensional Frictional Wrench	page 2
COR	Center of Rotation	page 15
CNN	Convolutional Neural Network	page 7
DoF	Degrees of freedom	page 17
FEM	Finite Element Method	page 9
ISA	Instantaneous Screw Axis	page 16
LMIs	Linear Matrix Inequalities	page 30
LS	Limit Surface	page 23
GWS	Grasp Wrench Space	page 46
OWS	Object Wrench Space	page 56
SDP	Semidefinite Programming	page 42
TWS	Task Wrench Space	page 55

Scalars and vectors

x	scalar
$\lvert x \rvert$	absolute value of scalar x
$x(\cdot)$	scalar function
$\boldsymbol{x}$	vector
$\lVert \boldsymbol{x} \rVert$	Euclidean norm of vector $\boldsymbol{x}$
$x \cdot y$ or $x \cdot \boldsymbol{y}$	Dot product of scalars x and y or scalar x and vector $\boldsymbol{y}$
$\boldsymbol{x} \oslash \boldsymbol{y}$	Hadamard division of vectors $\boldsymbol{x}$ and $\boldsymbol{y}$
$\boldsymbol{x} \circ \boldsymbol{y}$	Hadamard product of vectors $\boldsymbol{x}$ and $\boldsymbol{y}$
$\boldsymbol{X}$	matrix
$\mathcal{X}$	set
$\mathrm{Conv}(\mathcal{X})$	convex hull of set $\mathcal{X}$
$\mathcal{X} \oplus \mathcal{Y}$	Minkowski sum of sets $\mathcal{X}$ and $\mathcal{Y}$

Subscripts and superscripts

$\hat{\boldsymbol{x}}$	normalized $\boldsymbol{x}$
$\boldsymbol{x}_i$	the ith sample of $\boldsymbol{x}$

Symbols

$f_\perp$	normal force magnitude
l	instantaneous screw axis (ISA)
p	pressure distribution
$\hat{p}$	unit pressure distribution
ε	fitting error of a limit surface model
μ	friction coefficient
$\boldsymbol{c}$	contact wrench
$\boldsymbol{f}$	frictional force
$\boldsymbol{f}_\perp$	normal force
$\boldsymbol{\tau}$	frictional torque
$\boldsymbol{\tau}_\perp$	torque impressed by the normal pressure
$\hat{\boldsymbol{s}}^{\mathrm{LS}}$	point on a limit surface model
$\boldsymbol{v}$	linear velocity
$\boldsymbol{w}$	frictional wrench
$\hat{\boldsymbol{w}}$	normalized friction wrench
$\boldsymbol{w}_\perp$	normal wrench
$\boldsymbol{w}_{\mathrm{ext}}$	external wrench disturbance
$\boldsymbol{\omega}$	angular velocity
$\boldsymbol{\xi}$	twist
$\hat{\boldsymbol{\xi}}$	unit twist
$\mathcal{C}$	set of contact wrench constraints
C	local contact frame
F	sum magnitude of the local normal forces
$\mathcal{F}$	set of frictional wrench constraints
O	object frame
$\mathcal{S}$	contact surface
$\mathbb{N}_0$	set of positive integers and zero
$\boldsymbol{A}$	limit surface model
$\boldsymbol{A}_e$	ellipsoidal limit surface model
$\boldsymbol{A}_q$	quartic limit surface model
$\boldsymbol{B}$	wrench basis

Chapter 1

Introduction

Robot grasping has become an indispensable instrument in industrial and service robots with wide-ranging applications, such as bin picking and decluttering. A robot that executes a successful grasp establishes robust contacts between the gripper jaws and the object so that it can manipulate the object for the desired task at hand. A key research area in grasping is grasp planning, which addresses the problem of finding the most robust grasp to manipulate an object. A grasp is robust if it provides sufficient force and torque to the object to counter external disturbances during the manipulation so that the object remains static relative to the gripper jaws. The force and torque of a grasp are commonly estimated using a *frictional contact model*, if the physical properties of the objects and the gripper jaws are known. Existing frictional contact models [13]–[18] can be applied to grasping with rigid jaws as the models estimate the frictional force and torque at a point or a planar area contact.

Since recent years, deformable gripper jaws have been widely deployed in grasping applications due to their enhanced resistance to external disturbances. Grasps with deformable jaws, such as plastic jaws with a fin ray structure [20], grippers covered with compliant materials [21]–[23], or soft tactile sensors [19], [24]–[26], result in nonplanar surface contacts if the local geometry of the object is nonplanar. Figure 1.1 shows representative nonplanar surface contacts from four pairs of deformable jaws. A nonplanar surface contact results in

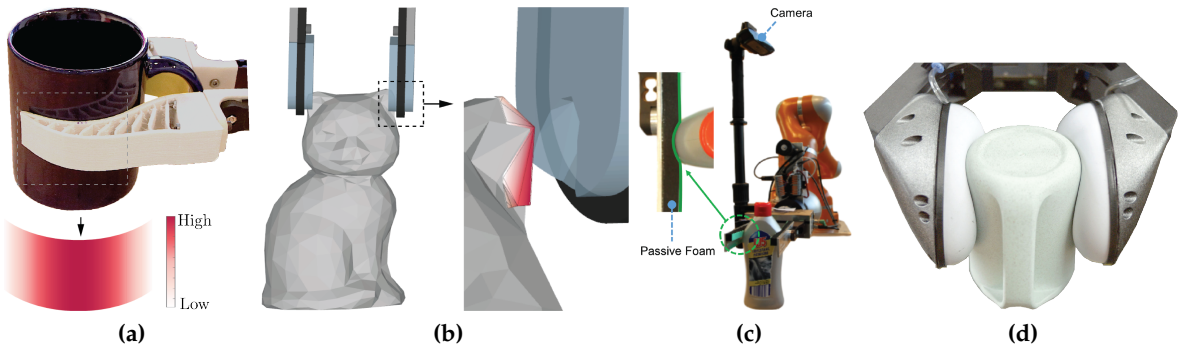

Figure 1.1: Nonplanar surface contacts created by (a) plastic fin ray jaws (figure recreated from [1] ©2021 IEEE); (b) jaws covered with compliant materials (figure recreated from [3] ©2020 IEEE); (c) Visevi ViseTac tactile sensor (figure recreated from [4] ©2017 IEEE); (d) Soft-bubble gripper (figure recreated from [19] ©2020 IEEE). Redder colors in (a) and (b) indicate higher pressure.

a six-dimensional (6D) frictional wrench (frictional force and torque) as the frictional force and torque are in three dimensions, respectively. State-of-the-art grasp planners [27]–[31] apply existing frictional contact models by assuming a point or planar contact surface. Such models neglect the nonplanar surface geometry and only consider a three-dimensional (3D) subset of the *6D frictional wrench (6DFW)*, which may result in an overly conservative friction estimation. Danielczuk *et al.* [5] modeled the frictional wrench for curved surface contacts by discretizing the contact surface to planar elements and fitting a planar area contact model for each element, which is less efficient for surfaces that consist of a large number of triangles, such as curved or complex surface geometry.

To address this issue, this thesis models the 6D frictional wrenches that a deformable gripper jaw can exert on the grasped object via a nonplanar surface contact. The 6D frictional wrenches are derived based on the differential geometry and Coulomb friction law. The latter states that the frictional wrench depends on the relative motion, or its tendency, between two bodies in contact. Specifically, with an external disturbance acting on an object during a successful grasp, there is no relative motion between the object and the gripper jaws. The impact of the external disturbance can be interpreted as the tendency of a relative motion. Once the disturbance overcomes the maximum static friction, slip occurs and kinematic friction arises. In this thesis, the tendency of a motion is modeled the same way as an instantaneous body motion, since grasp planning algorithms estimate the maximum static friction, which occurs if the object is about to slip. In summary, given an instantaneous motion of the grasped object, this thesis first derives the relative motion between the object and a gripper jaw, followed by the 6D frictional wrench that the jaw can exert on the object based on this relative motion. However, for many robot grasping applications, the instantaneous object motion or the relative motion between the object and the jaws caused by external disturbances during the manipulation is unknown at the time of grasp planning. To address this issue, this thesis proposes the *6D limit surface (6DLS)*, generalized from the *3D limit surface (3DLS)* proposed by Goyal *et al.* [13], to describe all possible 6D frictional wrenches that can be transmitted through a nonplanar surface contact. To improve computational efficiency, this thesis further presents an ellipsoid and a quartic model as two low-dimensional representations to approximate a 6D limit surface. By using a 6DLS model, the algorithms presented in this thesis can efficiently plan grasps or infer the grasp success without any prior knowledge about the object motion or the relative motion between the object and the jaws. While the 6DLS considers the frictional wrench limit at a given grasp force, there are many scenarios where the exact grasp force is unknown, such as grasping with a robot gripper without force sensors or solving grasp force optimization problems. Therefore, this thesis extends the 6DLS models and further proposes the *6D friction cone (6DFC)*, which approximates the wrench limit, including the normal wrench and the frictional wrench, by considering grasp forces between 0N and the force limit of the gripper. The 6DLS and the 6DFC models are referred to as the *nonplanar frictional surface contact models*. This thesis evaluates the proposed models by predicting the success of over 3,000 physical grasps collected on three robot setups.

Similar to the existing models, the proposed nonplanar frictional surface contact models

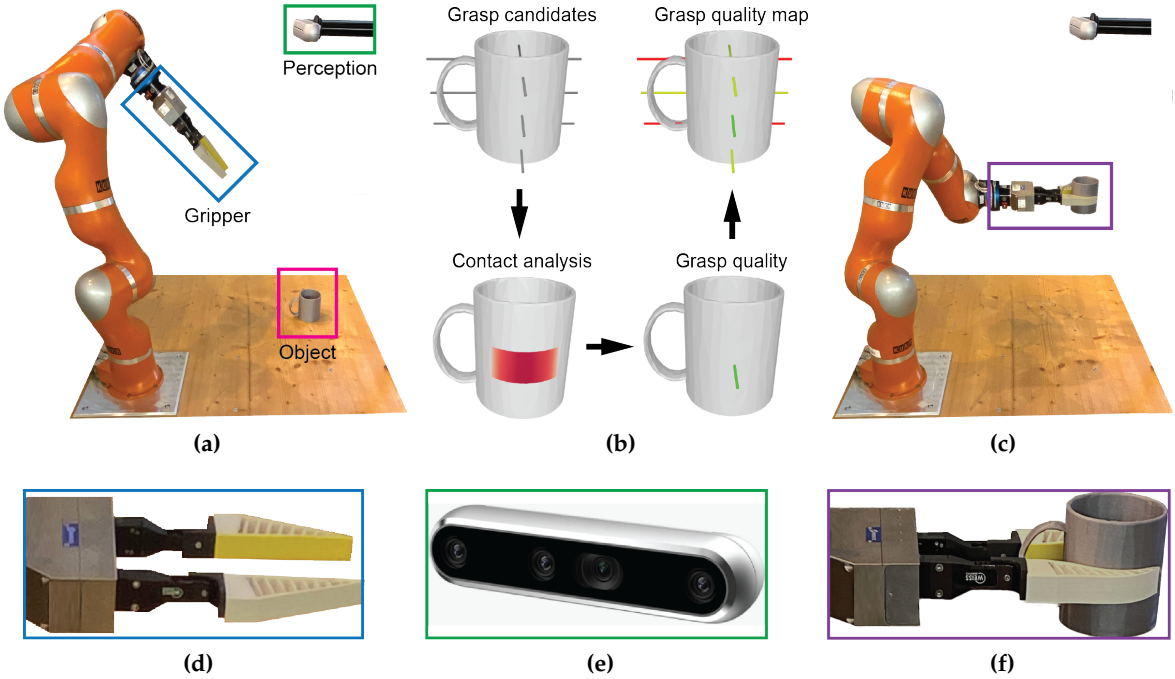

Figure 1.2: Common pipeline of an analytical grasp planner. (a) Initial state of the setup with the KUKA robot and the SCHUNK gripper. (b) Algorithm to find the grasp quality map, or the grasp candidates ranked by the grasp quality. (c) Execution of the highest-quality collision-free grasp from the grasp quality map. (d) Enlarged view of the gripper from the initial state. (e) Enlarged view of the perception system (RGBD camera) from the initial state (figure adapted from [32] ©2022 Intel). (f) Enlarged view of the executed grasp.

can also be used as a key component of an analytical grasp planner, which finds the optimal grasps to manipulate known objects. Figure 1.2 shows a common pipeline of an analytical grasp planner. Specifically, Figure 1.2(a) illustrates the initial state, which consists of three major components: a perception system to obtain object information, a gripper, and an object to be grasped. If the object and the gripper geometries are available (for instance, 3D printed objects, objects scanned by a depth camera, tactile sensor, etc), Figure 1.2(b) depicts the algorithm to find ranked grasp candidates in simulation. The algorithm first samples grasp candidates, shown as cylinders representing the grasp axis between the two jaws of a parallel-jaw gripper. For a candidate, each contact of a grasp is analyzed to compute the grasp quality. The contact analysis includes the estimation of the contact surface, pressure distribution, and the frictional wrench limit. The grasp candidates associated with the qualities, or the grasp quality map, are stored for the object. The colors, red, yellow, and green, of the cylinders indicate low, medium, and high quality of the grasp, respectively. At runtime, the 6D pose of the object is estimated from the perception system to retrieve the reachable ranked grasps. Finally, the grasp with the highest quality and which can be performed without collision is executed, as shown in Figure 1.2(c).

While analytical grasp planners are widely deployed since the physics underlying the frictional contact models are universal [33], it is less realistic to assume that a visual perception system can provide accurate estimations of object properties [31], [33], [34]. Therefore,

this thesis also presents a hybrid grasp planner, which combines the proposed nonplanar surface contact models and modern deep-learning techniques, to plan grasps for previously unseen rigid objects with deformable jaws. A grasp dataset is created with the proposed frictional contact models in a simulation setup with a depth sensor and the SCHUNK gripper equipped with compliant parallel jaws. Given the grasp dataset, the synthetic depth images are rendered for each grasp and used to train a *convolutional neural network (CNN)*. At runtime, the grasp planner finds the most robust grasp for a given depth image by first sampling grasp candidates in the image, followed by feeding each of them into the CNN for grasp quality prediction. Finally, the grasp planner returns the highest quality grasp among all candidates.

In addition to rigid objects, this thesis also applies the proposed 6DLS model to the grasping of known deformable objects. Deformable jaws are commonly preferred to grasp deformable fragile objects as less grasp force is required to establish robust contacts; therefore, such jaws reduce the risk of irreversible damages due to less object deformation. Grasping deformable hollow objects, such as plastic bottles and cups, is challenging, as the grasp should resist disturbances while minimally deforming the object so as not to damage it or dislodge liquids. To plan grasps for known deformable hollow objects, this thesis proposes *minimal work* as a novel grasp quality metric. Specifically, the proposed metric analyzes the wrenches using the 6DLS models, while considering object deformation caused by the grasp. A grasp planner that uses the minimal work metric is able to find a robust grasp while minimally deforming the object.

In summary, this thesis makes the following contributions:

1. **Nonplanar frictional surface contact models:** Contact models that estimate the wrench limit that a deformable jaw can apply on the object via a nonplanar surface contact.

    a) **6DFW:** Derivation of the 6D frictional wrench for nonplanar surfaces by combining concepts of differential geometry and the Coulomb friction law.

    b) **6DLS:** A concept of the 6D limit surface, generalized from 3DLS [13], to represent the 6D frictional wrench limit for a nonplanar surface contact.

    c) **6DLS models:** Two geometric models to approximate a 6DLS and efficient algorithms to compute the models.

    d) **6DFC:** A model to approximate the wrench limit for unknown grasp forces.

2. **Robust robot grasping with deformable gripper jaws:** Grasp analysis and grasp planning using nonplanar frictional surface contact models.

    a) **Grasp success prediction:** Two algorithms, by either building a grasp wrench space or solving a quadratic program, to predict multicontact grasp success for known rigid objects.

    b) **Grasp planning:** A grasp planner for compliant gripper jaws. Specifically, the proposed planner detects the most robust grasp for previously unseen rigid objects given a depth image.

c) **Minimal work metric:** A grasp quality metric that evaluates a grasp for known deformable hollow objects, such as plastic cups and bottles.

1.1 Thesis Organization

This thesis follows the subsequent structure.

- Chapter 2 covers relevant background and state-of-the-art for robot grasping, including common perception systems, gripper design to increase grasp robustness, frictional contact models and their applications in grasp analysis, grasp quality metrics, and grasp planning algorithms.
- Chapter 3 presents the nonplanar frictional surface contact models and their evaluations in simulation.
- Chapter 4 introduces three applications of the proposed nonplanar frictional surface contact models, including physical grasp success prediction for known rigid objects, grasp planning for unknown rigid objects, and grasp planning for known deformable hollow objects.
- Chapter 5 concludes the thesis. The chapter summarizes the results and further discusses the limitations of the proposed models, as well as future research directions in grasp planning.

Parts of the work presented in this thesis have been published in [1], [3], [4], [6].

Chapter 2

Background and Related Work

The chapter presents the most relevant background and related work for robot grasping. In particular, this chapter first provides the state-of-the-art of perception system (Section 2.1) and gripper design (Section 2.2), which are two key modules to improve the grasp success. To better understand the third module, grasp planning, the chapter first introduces the frictional contact models (Section 2.3), which is the main focus of the thesis, followed by the method to combine the wrench limit of each contact into a grasp (Section 2.4) to compute the grasp quality (Section 2.5), or the goodness of a grasp. Finally, three types of grasp planners are introduced (Section 2.6): analytical planners using the computed grasp qualities, empirical planners using modern learning techniques, and hybrid planners, which combine the advantages of the analytical and empirical planners.

2.1 Perception

A perception system (also referred to as sensing system) provides object information, such as pose and material properties, for a grasp planner. Two commonly used perception modalities for robot grasping are visual (Section 2.1.1) and tactile sensing (Section 2.1.2).

2.1.1 Visual Sensing

Vision-based grasping algorithms plan grasps directly from visual data by using learning techniques without physics reasoning (see Bohg *et al.* [34] for review). Common visual sensors are depth, monocular, and RGBD cameras.

2.1.1.1 Depth Image-based Grasping

Depth camera is perhaps the most commonly used sensing module for grasp planning as the object pose and other information, such as partial geometry, can be computed or estimated from the sensor data. Due to the success of *Convolutional Neural Networks (CNNs)* in image processing, many works [35], [36] predicted optimal grasp points by training a CNN with depth images. Johns *et al.* [37] trained a CNN on a synthetic dataset collected with physical and depth image simulations to detect grasps. To segment cluttered objects for robot

grasping, Danielczuk *et al.* [38] proposed a variation of Mask R-CNN [39] and trained it on synthetic depth images and object masks using simulated heaps of 3D CAD models.

2.1.1.2 Monocular Image-based Grasping

To avoid the complexity of 3D data, other work detects grasps directly from monocular RGB images [34]. Saxena *et al.* [40] proposed a grasp point model trained on labeled synthetic monocular images. Given two RGB images of an object as input, the model outputs a few good grasp points in each image. The set of points are then triangulated for a 3D location of the grasp attempt. Redmon *et al.* [41] proposed an algorithm that classifies images into 16 categories using a CNN and find the optimal grasp associated with the class given an object image. As human-labeled data are expensive to collect and can be biased, Pinto *et al.* [42] proposed a robot self-supervising method to collect the grasp dataset. Specifically, the robot collected over 700 hours of grasp attempts by trial and error, leading to a dataset of 50,000 data points to train a CNN. Levine *et al.* [43] further scaled up the dataset and proposed a learning-based method to hand-eye coordination for robot grasping using a CNN trained on 800,000 grasp attempts collected with up to 14 robot manipulators over two months.

2.1.1.3 RGBD Image-based Grasping

While the aforementioned methods performed well in specific scenarios, detecting 6D grasp configurations from monocular images alone is an underconstrained problem [34]. Therefore, many previous works proposed algorithms that learn from both monocular and depth images. Given RGB and depth images, Rao *et al.* [44] segmented objects in a cluttered scene and identified graspable segments. To avoid handcrafted features, Lenz *et al.* [45] proposed a deep-learning-based algorithm to detect grasps from an RGBD image of the grasped object. Danielczuk *et al.* [46] trained a neural network with a synthetic dataset of RGBD heap images to search and grasp a specific object in a heap of objects.

2.1.2 Tactile Sensing

In addition to visual sensing, tactile sensing provides the sense of touch (see Luo *et al.* [47] and Li *et al.* [48] for review). Specifically, a tactile sensor provides a diverse set of signals containing contact details for robots to better interact with the unstructured environments. There are two types of tactile sensors that are commonly used for robot grasping: force sensors and image-based tactile sensors.

A force sensor provides the contact force between the gripper jaw and the object, such as the normal force [49], [50] or the 3D force measurement [51], including the normal and tangential force, such as the frictional force.

An image-based tactile sensors consist of an array of sensor elements [25], [26], [52]–[56] and provides *tactile images*, or *contact profiles*, which describe the contact area and the pressure distribution of a contact. Such tactile sensors can be used either alone [57], [7] or assist vision [58], [59] for robot grasping. The image-based tactile sensors have wide applications,

such as grasp adjustment [57], slip detection [60], object property estimation [61], by using analytical [62] and data-driven methods [63], [64].

2.2 Gripper Design

As the second key component to improve the grasp success, gripper designs are studied to facilitate grasping, including adhesive fingertips [65], [66], compliant fingertips [23], [67], underactuated grippers [68]–[72], and soft hands [73]–[75].

Among the advanced gripper designs, compliant fingertips on the rigid grippers increase grasp robustness and are easier to control compared to underactuated or soft hands. Furthermore, compared to grippers with three to five jaws, a parallel-jaw gripper has significantly less number of grasp candidates; therefore, grasping with a parallel-jaw gripper reduces the search space of grasp candidates. Consequently, a large body of research uses parallel-jaw grippers with compliant fingertips in grasp planning.

2.3 Frictional Contact Modeling

Next, the foundation of the third key component, grasp planning algorithms, is introduced. An analytical grasp planner requires a *frictional contact model*, which provides a realistic estimation of the possible forces and torques that a gripper jaw can exert on the object. Estimating the *frictional wrench*, a vector that is composed of the frictional force and torque, is essential, as a grasp largely relies on the frictional wrench to successfully lift up and rotate an object. An accurate estimation is especially important for grasping fragile objects, since the object may be damaged if squeezed too hard or the manipulation may fail if the grasp force is too small. As a frictional wrench depends on the contact profile and the relative motion between the object and the jaw, this section first introduces methods to estimate the contact profile (Section 2.3.1), followed by formulating the object motion (Section 2.3.2) and the frictional wrench that resists this motion (Section 2.3.3), and finally, the frictional contact models describing the frictional wrench limit (Section 2.3.4 – Section 2.3.5).

2.3.1 Contact Profile Estimation

As an input of the majority of the frictional contact models, a *contact profile* can be captured by an image-based tactile sensor (Section 2.1.2), or estimated by the *Finite Element Method (FEM)* or a *contact model*. Note that a contact model, also referred to as a contact theory, outputs an estimated contact profile, while a frictional contact model outputs the estimated frictional wrench limit. While the FEM can accurately estimate the contact profiles between deformable jaws and grasped objects [27], [8], [76], it is computationally demanding and is potentially infeasible for real-time grasp planning. As a compromise between computational effort and accuracy, soft contact models require significantly less computational effort, including kinetostatic analysis for jaws with the fin ray structure [20], modeling hemispherical soft fingertips [77]–[80], and modeling planar compliant jaw pads [30], [5]. This section

introduces a subset of these efficient models that estimate both contact area and pressure distribution.

2.3.1.1 Hertz Theory of Linear Elastic Contact

Before presenting the theory, consider the concept of *nonconforming contact*, which happens if the geometries of two solids do not fit each other, such as two ellipsoids are in touch or the nonplanar surface of a cylinder contacts a plane. Consider the scenario where two nonconforming solids are brought into contact. The initial contact area is a point or a line. As a normal force is applied as load, the solids deform and the contact area increases. A contact theory aims to predict the shape of the contact area and how it grows in size with an increasing normal force, as well as the pressure distribution at the contact. Heinrich Hertz [81], [82] proposed the first contact theory for nonconforming solids in 1882. Note that the Hertz theory is restricted to frictionless surfaces and linear elastic solids [83, Ch. 4]. This section summarizes the Hertz theory based on [81], [82], [83, Ch. 4].

Contact Surface Approximation This part first presents the contact surface formulation, which helps to better understand the theory. Consider two nonconforming bodies, $\mathcal{B}_1$ and $\mathcal{B}_2$, are just in contact with $\mathcal{B}_1$ below $\mathcal{B}_2$. A rectilinear coordinate system is defined so that the origin is located at the initial contact point. The xy-plane is the tangent plane to the two surfaces and the z-axis is pointing downwards into the lower solid $\mathcal{B}_1$. Before selecting the x- and y-axes, consider the temporary x'- and y'-axes, which are two arbitrary axes in the xy-plane and are perpendicular to each other. With the temporary axes, the surface of $\mathcal{B}_1$ in the region close to the initial contact point can be approximated with

$$z_1 = A_1 x'^2 + B_1 y'^2 + C_1 x' y' \tag{2.1}$$

where the higher order terms in x and y are neglected. Next, one defines the x_1 and y_1 axes for z_1, which are also in the xy-plane and perpendicular to each other. The orientation of x_1 and y_1-axes are chosen so that the term $x_1 y_1$ vanishes. Therefore, the equation above can be written as

$$z_1 = \frac{1}{2R_{x,1}} x_1^2 + \frac{1}{2R_{y,1}} y_1^2 \tag{2.2}$$

where $R_{x,1}$ and $R_{y,1}$ are the *principal radii of curvature* of the surface at the origin. To better understand $R_{x,1}$ and $R_{y,1}$, three special geometries of $\mathcal{B}_1$ are considered:

1. A sphere with radius R, $R_{x,1} = R_{y,1} = R$;
2. A cylindrical lens, or a cylinder, with radius R, $R_{x,1} = R, R_{y,1} = \infty$;
3. A plane, $R_{x_1} = R_{y,1} = \infty$.

Similarly, the second surface can be expressed as

$$\begin{aligned} z_2 &= A_2 x'^2 + B_2 y'^2 + C_2 x' y' \\ &= -\left(\frac{1}{2R_{x,2}} x_2^2 + \frac{1}{2R_{y,2}} y_2^2 \right). \end{aligned} \tag{2.3}$$

Note that the principal axes of the two surfaces, for instance x_1 and x_2, can be inclined to each other by an angle α in the range of $0°$ to $90°$.

Next, the *separation* h between the two surfaces is defined as

$$h = z_1 - z_2 = (A_1 - A_2)x'^2 + (B_1 - B_2)y'^2 + (C_1 - C_2)x'y'. \tag{2.4}$$

Finally, one selects the x- and y-axes for the contact, whose orientation are chosen so that the xy term vanishes. Therefore, the separation h can be reformulated as

$$h = \frac{1}{2R_x}x^2 + \frac{1}{2R_y}y^2 \tag{2.5}$$

where R_x and R_y are the *principal relative radii of curvature*. The computation of R_x and R_y can be found in [83, pp. 84–90] and [84].

Assumptions By approximating the contact surfaces this way, Hertz hypothesized that the contact area between two solids is an ellipse with a and b being the semi-axes, which is also validated in his observations presented in [82]. To apply the Hertz theory, the following conditions have to be satisfied

1. The surfaces are continuous and nonconforming.
2. The strains, or the local deformations, are small and within the elastic limit.
3. The contact area is small compared to the dimensions of each body.
4. The contact area is small compared to the relative radii of curvature of the surfaces.
5. The surfaces are frictionless.

Circular Contact Profile If the conditions are satisfied, the Hertz theory provides an accurate estimation of the contact area and the pressure distribution for a given normal force F as load. First, consider a simplified case where two spheres with radii R_1 and R_2 are in contact, which means $R_{x,1} = R_{y,1} = R_1$ and $R_{x,2} = R_{y,2} = R_2$. The relative radii of curvature $R = R_x = R_y$ can be computed from

$$\frac{1}{R} = \frac{1}{R_1} + \frac{1}{R_2}. \tag{2.6}$$

The contact area between two spheres is a circle with radius a. Denoting r as the radius, which is the distance between a point within the contact circle to the origin of the coordinate system, the pressure distribution $p(r)$ is computed with

$$p(r) = p_0 \left[1 - \left(\frac{r}{a}\right)^2\right]^{\frac{1}{2}} \tag{2.7}$$

where p_0 is the maximal pressure value. Before computing a and p_0 from the normal force F, the *effective elastic modulus* E needs to be defined first. Denoting E_1 and E_2 as the elastic

moduli for the two spheres respectively, and let ν_1, ν_2 be the Poisson's ratios, the effective elastic modulus E can be computed with

$$\frac{1}{E} = \frac{1-\nu_1^2}{E_1} + \frac{1-\nu_2^2}{E_2}. \tag{2.8}$$

Finally, the radius of the contact circle is computed with

$$a = \left(\frac{3RF}{4E}\right)^{\frac{1}{3}}. \tag{2.9}$$

Since R and E are constant, the relation between the radius and the normal force F is

$$a \propto F^{\frac{1}{3}}. \tag{2.10}$$

Next, since the normal force F is computed with

$$F = \int_0^a p\,(r)\, 2\pi r \,\mathrm{d}r = \frac{2}{3} p_0 \pi a^2 \tag{2.11}$$

p_0 can be expressed with

$$p_0 = \frac{3F}{2\pi a^2} = \left(\frac{6E^2F}{\pi^3 R^2}\right)^{\frac{1}{3}}. \tag{2.12}$$

In summary, Equation (2.7) describes the pressure distribution of the circular contact area, while Equation (2.9) and Equation (2.12) compute the radius of the circle a and the maximal pressure value p_0, respectively.

Elliptical Contact Profile For the general cases in Hertz contact theory, the contact area is an ellipse with a and b being the semi-axes with a pressure distribution described by

$$p(r) = p_0 \left[1 - \left(\frac{x}{a}\right)^2 - \left(\frac{y}{b}\right)^2\right]^{\frac{1}{2}}. \tag{2.13}$$

Detailed steps to compute p_0, a, and b can be found in [83, pp.95–96].

Experiments After proposing the contact theory in [81], Hertz further evaluated it in [82] with two experiments. The first experiment aimed to evaluate the relation between the normal force and the radius of the contact circle expressed in Equation (2.9). The contacts are created from a spherical glass lens with radius $R = 28$ mm and a glass plate made with the same material. By applying different loads between 0.2–3.5 kg to the glass lens, Hertz measured with a microscope the diameter of the resulting contact area, which is between 1.56–4.02 mm. The main observation is that the ratio $a/\sqrt[3]{F}$ remains a constant, which validates the theory expressed in Equation (2.10).

During the second experiment, Hertz evaluated the elliptical contact area between two identical cylindrical glass lenses. The two lenses are inclined with the angle α between $10°$–$90°$ and the same normal force is applied in each trial. Hertz observed that the measured radii did not match the theoretical values well when the angle α is relatively small. One

reason is that it is difficult to put the two lenses in the desired position, so that their common tangent plane is exactly horizontal. Hertz also evaluated the contacts between a spherical steel lens and various plates of different metals. However, the experiments were unsatisfactory. In addition to the difficulty of detecting the initial contact point, the deformation exceeded the elastic limit and resulted in a plastic deformation during many trials.

2.3.1.2 Power-law Pressure Distribution and its Extensions

While the Hertz contact theory predicts the contact profile for objects with linear elastic materials, Xydas *et al.* [80] extended the theory for objects with nonlinear elastic materials. Specifically, Xydas *et al.* proposed a general power-law model to describe the pressure distribution between an hemispherical soft jaw and a rigid surface. By assuming a planar circular contact area with radius a, the contact pressure distribution is formulated as

$$p(r) = p_0 \left[1 - \left(\frac{r}{a}\right)^k\right]^{\frac{1}{k}} \tag{2.14}$$

where $k = 2$ represents the Hertzian pressure distribution and $k = \infty$ describes a uniform distribution.

Xydas *et al.* further used the power-law pressure model with different exponents to compute the *limit surface (LS)*, which is the boundary of the set of all possible frictional forces and torques that can be transmitted via a contact. Details about the limit surface and its geometric approximations are later introduced in Section 2.3.4 – Section 2.3.5. Fakhari *et al.* [85] considered the asymmetric pressure distributions caused by the tangential force disturbances, which leads to a smaller LS and potentially a less robust grasp.

2.3.1.3 Pressure Estimation based on Contact Area

Other works computed the contact area based on the local geometry of the grasped object and the gripper jaw, and estimated the pressure based on the area. Ciocarlie *et al.* [28] computed the local geometry of two contact bodies based on the elastic contact theory [83] for real-time grasp score computation. Under the assumption of an elliptical contact area, Ciocarlie *et al.* used the Hertzian theory and the Winkler elastic foundation to compute the pressure distribution. Tsuji *et al.* [29] generalized the contact area approximation from ellipses to 2D quadric surfaces. Harada *et al.* [30] analyzed the contacts between rigid objects and a parallel-jaw gripper with a deformable pad attached to each jaw. Harada *et al.* estimated the contact region by clustering the object model and obtained the contact area by projecting the contact region onto the plane that contains the undeformed jaw pad.

While the aforementioned algorithms assumed a planar contact area, Danielczuk *et al.* [5] proposed the Robust Efficient Area Contact Hypothesis (REACH) model to approximate the nonplanar contact surface between soft jaw pads and rigid objects. Given an object's geometry modeled as a triangular mesh, the contact area is computed as the constructive solid geometry intersection of the extruded polygon of the jaw with the object. The intersection provides an estimation of the deformation of the soft pad around the object at each point on the contact. The pressure distribution linearly scales with the gripper pad deformation. The

REACH model thus provides the contact area, consisting of a triangular mesh, and the pressure distribution over each triangle of the contact area mesh. The combination of the limit surface of each triangle defines the frictional constraints of the contact. The REACH model is applied in three physical experiments of this thesis (Section 4.1.4, Section 4.2, Section 4.3) to estimate the contact profiles for compliant gripper jaws.

2.3.2 Instantaneous Body Motion

In addition to a contact model, an instantaneous body motion is the second component required to compute a frictional wrench, as friction resists the relative motion, or its tendency, between the grasped object and the gripper jaws. The next part introduces the tendency of the relative motion in more detail. Consider a representative contact adapted from [86, ch. 12], where a block is resting on a table as illustrated below. To cancel the gravitational force,

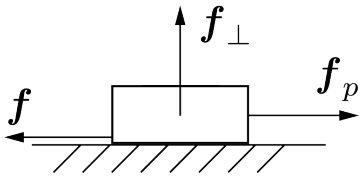

the table pushes the block upward with a normal force $\boldsymbol{f}_\perp$. The block is pulled with a slowly increasing force $\boldsymbol{f}_p$, which is opposite to the frictional force $\boldsymbol{f}$ exerted by the table. At first, $\boldsymbol{f}_p$ is too small to move the block, but results in a tendency of motion of the block. In this case, the static frictional force $\boldsymbol{f}$ is equal and opposite to $\boldsymbol{f}_p$. Once $\boldsymbol{f}_p$ overcomes the maximum static frictional force, slip occurs and kinematic friction arises. Next, the frictional force is expressed mathematically for the Coulomb friction law. If the sliding velocity $\boldsymbol{v}$ of the block is zero, $\boldsymbol{f}$ could act in any direction with the magnitude

$$\|\boldsymbol{f}\| \leq \mu \|\boldsymbol{f}_\perp\| \text{ with } \|\boldsymbol{v}\| = 0. \tag{2.15}$$

If the block slides with a velocity $\boldsymbol{v}$, $\boldsymbol{f}$ is opposite to $\boldsymbol{v}$ and is computed with

$$\boldsymbol{f} = -\mu \|\boldsymbol{f}_\perp\| \frac{\boldsymbol{v}}{\|\boldsymbol{v}\|} \text{ with } \|\boldsymbol{v}\| \neq 0 \tag{2.16}$$

where $\mu > 0$ is the friction coefficient.

If the velocity is zero, but the acceleration $\boldsymbol{a}$ is not zero, which occurs when the block is about to slip, $\boldsymbol{f}$ is

$$\boldsymbol{f} = -\mu \|\boldsymbol{f}_\perp\| \frac{\boldsymbol{a}}{\|\boldsymbol{a}\|} \text{ with } \|\boldsymbol{v}\| = 0, \|\boldsymbol{a}\| \neq 0. \tag{2.17}$$

The static frictional force reaches the maximum in this case and is opposite to $\boldsymbol{a}$.

To apply this representative contact to grasping, the table can be substituted with a gripper jaw and $\boldsymbol{f}_p$ can be considered as an external disturbance during the manipulation, which may cause a relative motion between the object and the jaw if $\boldsymbol{f}_p$ is sufficiently large. By estimating the maximum static friction using Equation (2.17), one can infer if the expected external disturbance can be counterbalanced by the frictional force and torque at each contact of the grasp, so that there is no relative motion between the object and the gripper jaws,

which is considered as a successful grasp. By comparing Equations (2.16) and (2.17), one can observe that if the direction of $\boldsymbol{v}$ and $\boldsymbol{a}$ is the same unit vector, then the resulting frictional forces have the same magnitude and direction, regardless if the block is about to slip or is sliding. Therefore, for grasping applications, one can compute the frictional force and torque based on the sliding velocity, instead of the acceleration, to avoid the potential complexity of a second-order dynamic system involving forces and accelerations. Similarly, this thesis also computes the frictional wrench at a nonplanar surface contact based on the object velocity, or object motion, instead of the object acceleration. The following section describes instantaneous object motion in two and three dimensions.

2.3.2.1 Instantaneous Motion in Two Dimensions

In two dimensions, the instantaneous motion of a body can be described as a rotation around a point, defined as the *center of rotation (COR)*. A translation can be considered as a rotation around a COR that is infinitely far away. The concept of COR is used to compute the frictional wrench for planar surface contacts in Section 2.3.3.3.

Given a COR, the linear velocity $\boldsymbol{v}$ at a point is perpendicular to the vector from the COR to this point. Figure 2.1(a) illustrates the linear velocities $\boldsymbol{v}_a, \boldsymbol{v}_b, \boldsymbol{v}_c$ at three points a, b, c given a representative COR, respectively. As the COR is further away along the x-axis in Figure 2.1(b) than in Figure 2.1(a), the linear velocities $\boldsymbol{v}_a, \boldsymbol{v}_b, \boldsymbol{v}_c$ are closer to parallel to the y-axis. If the COR is infinitely far away along the x-axis, $\boldsymbol{v}_a, \boldsymbol{v}_b, \boldsymbol{v}_c$ are parallel to the y-axis, resulting in a pure translation along the negative y-axis.

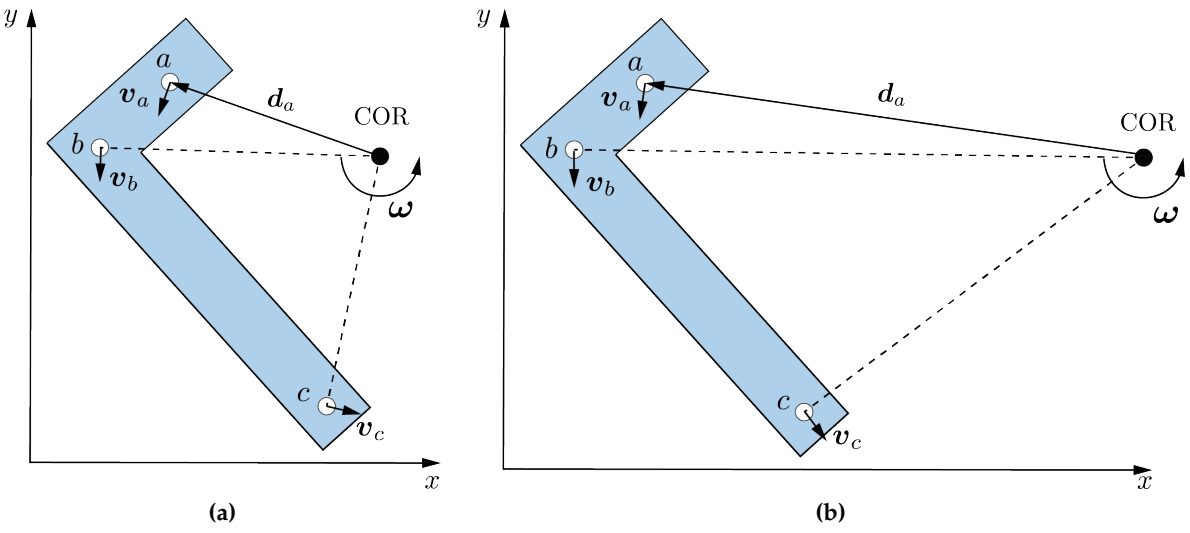

Figure 2.1: Two representative center of rotations (CORs) of a rigid body and the corresponding linear velocities $\boldsymbol{v}_a, \boldsymbol{v}_b, \boldsymbol{v}_c$ at the points a, b, c, respectively.

Next, the linear velocity at a point on the object for a given COR is formulated mathematically. Let $\boldsymbol{\omega} = [0, 0, \omega_z]^T$ be the counter-clockwise angular velocity of the object that rotates around the COR, let $\boldsymbol{d}$ be the vector from the COR to the point of interest. Figure 2.1 depicts the angular velocity for the representative COR and $\boldsymbol{d}_a$ for the point a. The linear velocity at

the point is computed with

$$\boldsymbol{v} = \begin{bmatrix} v_x \\ v_y \end{bmatrix} = \boldsymbol{\omega} \times \boldsymbol{d} = \begin{bmatrix} -\omega_z \cdot d_y \\ \omega_z \cdot d_x \end{bmatrix} \tag{2.18}$$

The Coulomb friction law states that the frictional force and torque depend on the direction of the linear velocity, not on its magnitude. Therefore, the definition of a *unit linear velocity* $\hat{\boldsymbol{v}}$ becomes handy. $\hat{\boldsymbol{v}}$ is the direction vector of the linear velocity and is computed with

$$\hat{\boldsymbol{v}} = \frac{1}{\|\boldsymbol{d}\|} \begin{bmatrix} -d_y \\ d_x \end{bmatrix}. \tag{2.19}$$

The translational and rotational motion of a rigid body are often combined into a single motion, defined as the *body twist* $\boldsymbol{\xi}$, or generalized velocity. For an instantaneous motion in the 2D space, $\boldsymbol{\xi}$ at a point is in three dimensions. In summary, $\boldsymbol{\xi}$ is

$$\boldsymbol{\xi} = \begin{bmatrix} v_x \\ v_y \\ \omega_z \end{bmatrix}. \tag{2.20}$$

2.3.2.2 Instantaneous Motion in Three Dimensions

The instantaneous motion in 3D is used to derive the frictional wrench that resists the motion at a nonplanar surface contact (Section 3.2). The 3D generalization of the concept of COR is the *instantaneous screw axis (ISA)*. An instantaneous motion in three dimensions can be described as the combination of a translation along an axis and a rotation about the same axis. This axis is defined as the instantaneous screw axis. Specifically, the linear velocity $\boldsymbol{v} \in \mathbb{R}^3$ at a point can be considered as the sum of a velocity parallel to the ISA and a velocity perpendicular to the ISA, denoted as $\boldsymbol{v}_\parallel$ and $\boldsymbol{v}_\perp$, respectively.

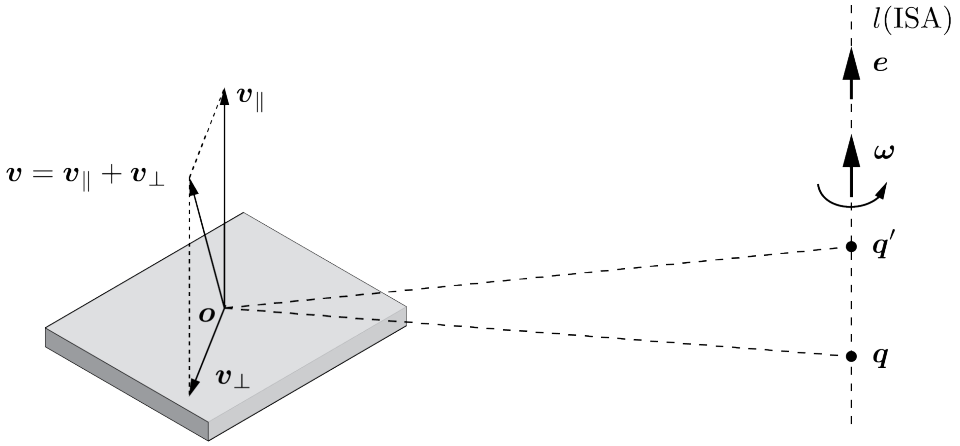

Figure 2.2: Instantaneous body motion in three dimensions.

Before computing the linear velocity, this part first formulates the instantaneous screw axis. Figure 2.2 illustrates a representative ISA. The instantaneous screw axis is represented as a line l with direction $\boldsymbol{e} \in \mathbb{R}^3$ that goes through a point $\boldsymbol{q} \in \mathbb{R}^3$. Note that a line is completely defined by $\boldsymbol{e}$ and $\boldsymbol{q}$, where $\|\boldsymbol{e}\| = 1$ and $\boldsymbol{q}$ is an arbitrary point. The *Plücker coordinates* [87], [88, pp. 60–68] of l are defined as $(\boldsymbol{e}, \boldsymbol{m})$, where $\boldsymbol{m}$ is the *moment vector* and is defined as

$$\boldsymbol{m} = \boldsymbol{q} \times \boldsymbol{e} \text{ with } \|\boldsymbol{e}\| = 1. \tag{2.21}$$

Using the Plücker coordinates to describe a line is beneficial since $\boldsymbol{m}$ remains the same, regardless of which point $\boldsymbol{q}$ on the line is chosen to compute $\boldsymbol{m}$. For instance, the point $\boldsymbol{q}$ and $\boldsymbol{q}'$ in Figure 2.2 have the same moment $\boldsymbol{m}$. Note that a line in the space has four degrees of freedom (DoF), since a translation along the line or a rotation about itself leads to the same line. In addition to the constraint $\|\boldsymbol{e}\| = 1$, the Plücker coordinates $(\boldsymbol{e}, \boldsymbol{m})$ reflect the four DoF of l by satisfying

$$\boldsymbol{e}^T \boldsymbol{m} = \boldsymbol{e}^T (\boldsymbol{q} \times \boldsymbol{e}) = 0. \tag{2.22}$$

Given the Plücker coordinates $(\boldsymbol{e}, \boldsymbol{m})$ of an ISA, the following part presents the computation of the angular and linear velocity at a point. The angular velocity $\boldsymbol{\omega} \in \mathbb{R}^3$ rotating about the ISA is the same at any point on the object and can be written as

$$\boldsymbol{\omega} = \|\boldsymbol{\omega}\| \boldsymbol{e}. \tag{2.23}$$

As the linear velocity at a point depends on the coordinate of this point, the origin $\boldsymbol{o}$ of the object is selected as a representative point to derive the linear velocity, which is a component of the twist. The linear velocity $\boldsymbol{v}$ at $\boldsymbol{o}$ consists of $\boldsymbol{v}_\perp$ and $\boldsymbol{v}_\parallel$, where $\boldsymbol{v}_\perp$ is the velocity perpendicular to the ISA and is computed with

$$\boldsymbol{v}_\perp = \boldsymbol{\omega} \times (-\boldsymbol{q}) = \boldsymbol{q} \times \boldsymbol{\omega} = \|\boldsymbol{\omega}\| \boldsymbol{m}. \tag{2.24}$$

The velocity $\boldsymbol{v}_\parallel$ parallel to l can be expressed as

$$\boldsymbol{v}_\parallel = \|\boldsymbol{v}_\parallel\| \boldsymbol{e}. \tag{2.25}$$

Another common way to express $\boldsymbol{v}_\parallel$ is by defining the *scalar pitch* h, which is the ratio of translational to rotational motion. Mathematically, h is defined as $h = \boldsymbol{v}^T \boldsymbol{\omega} / \|\boldsymbol{\omega}\|^2$. Therefore, $\boldsymbol{v}_\perp$ can also be expressed with

$$\boldsymbol{v}_\parallel = h \boldsymbol{\omega}. \tag{2.26}$$

Finally, the linear velocity $\boldsymbol{v}$ at $\boldsymbol{o}$ is computed with

$$\boldsymbol{v} = \boldsymbol{v}_\parallel + \boldsymbol{v}_\perp = h \boldsymbol{\omega} + \|\boldsymbol{\omega}\| \boldsymbol{m}. \tag{2.27}$$

The twist $\boldsymbol{\xi}$ at the origin $\boldsymbol{o}$ is defined as

$$\boldsymbol{\xi} = \begin{bmatrix} \boldsymbol{v} \\ \boldsymbol{\omega} \end{bmatrix} = \begin{bmatrix} h\boldsymbol{\omega} + \|\boldsymbol{\omega}\| \boldsymbol{m} \\ \boldsymbol{e} \end{bmatrix} = \|\boldsymbol{\omega}\| \begin{bmatrix} h\boldsymbol{e} + \boldsymbol{m} \\ \boldsymbol{e} \end{bmatrix}. \tag{2.28}$$

There are two important special cases. If $\|\boldsymbol{\omega}\| \neq 0$ and $h = 0$, a twist is a pure rotation about l. If $\|\boldsymbol{\omega}\| = 0$ and $h = \infty$, a twist is a pure translation along l; mathematically, $\boldsymbol{\xi}$ is expressed as $\boldsymbol{\xi} = \|\boldsymbol{v}\| \left[\boldsymbol{e}^T, \mathbf{0}^T\right]^T$ in this case.

Since the magnitude of $\boldsymbol{\omega}$ or $\boldsymbol{v}$ does not affect the frictional wrench for the Coulomb friction law, the definition of a unit twist becomes handy. First, the *magnitude of twist* $M \geq 0$ is defined as

$$M = \begin{cases} \|\boldsymbol{\omega}\|, & \text{if } \boldsymbol{\omega} \neq 0 \\ \|\boldsymbol{v}\|, & \text{if } \boldsymbol{\omega} = 0. \end{cases} \tag{2.29}$$

Next, consider the definition of the *unit twist* $\hat{\boldsymbol{\xi}} \in \mathbb{R}^6$, which is a twist whose magnitude is one. Specifically, the unit twist for motions that include a rotation can be obtained by substituting $\|\boldsymbol{\omega}\| = 1$ in Equation (2.28), while $\hat{\boldsymbol{\xi}}$ for pure translations is obtained by substituting $\|\boldsymbol{\omega}\| = 0$ and $\|\boldsymbol{v}\| = 1$. In summary, the unit twist $\hat{\boldsymbol{\xi}}$ is defined as

$$\hat{\boldsymbol{\xi}} = \begin{cases} \begin{bmatrix} h\boldsymbol{e} + \boldsymbol{m} \\ \boldsymbol{e} \end{bmatrix} & \text{if } \|\boldsymbol{\omega}\| = 1 \\ \begin{bmatrix} \boldsymbol{e} \\ \mathbf{0} \end{bmatrix} & \text{if } \|\boldsymbol{\omega}\| = 0. \end{cases} \tag{2.30}$$

Note that the triplet $(\boldsymbol{e}, \boldsymbol{m}, h)$ or the vector $\boldsymbol{e}$ alone completely define $\hat{\boldsymbol{\xi}}$. Therefore, one can parametrize $\hat{\boldsymbol{\xi}}$ with $(\boldsymbol{e}, \boldsymbol{m}, h)$ or $\boldsymbol{e}$ to compute relative motion and the frictional constraints of a contact.

2.3.3 Frictional Wrench Computation

Given an instantaneous object motion (Section 2.3.2), this section presents the frictional force and torque that a gripper jaw can exert on the object via the contact to resist this motion. Since a rigid and a deformable gripper jaw transmit different frictional forces and torques, there are three commonly used contact types, the *hard point contact*, the *soft point contact*, and the *planar area contact*. For each contact type, the computation pipeline takes the object motion and the contact profile as inputs, then outputs the corresponding maximum static frictional force and torque that can be transmitted through the contact.

The friction computation requires the following assumptions

- The contact profile, including the contact area and the pressure distribution, is known. The contact area can be a point, multiple discrete points, a line segment, or a planar area.
- The friction coefficient μ is known and is a constant over the contact area.
- Coulomb friction model applies. Specifically, the frictional force is antiparallel to the relative velocity and does not depend on the magnitude of the velocity. The magnitude of the maximal static frictional force is proportional to the normal force.

Rather than dealing with a pair of vectors, the force $\boldsymbol{f}$ and torque $\boldsymbol{\tau}$ are commonly combined into a single vector, defined as the *wrench* $\boldsymbol{w}$

$$\boldsymbol{w} = \begin{bmatrix} \boldsymbol{f} \\ \boldsymbol{\tau} \end{bmatrix}. \tag{2.31}$$

The frictional wrench computation for each contact type is reviewed in the following.

2.3.3.1 Hard Point Contact

The hard point contact is commonly used in the scenarios, where two nonconforming rigid bodies are in contact and the contact area is negligible. Figure 2.3 depicts the front view of a representative hard point contact caused by a spherical rigid jaw pressing onto a rigid cube. For a hard point contact, the gripper jaw transmits a two-dimensional frictional force at the contact point to the object.

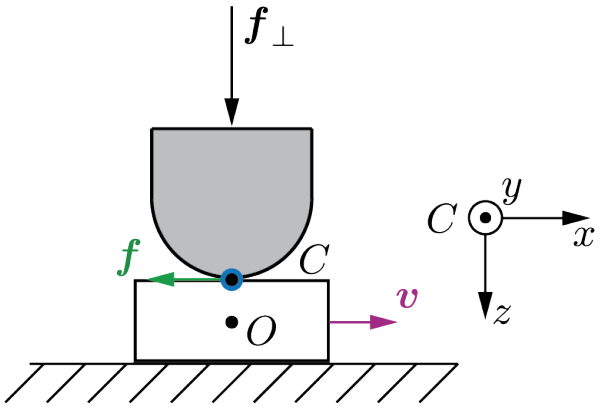

Figure 2.3: The front view of a representative hard point contact.

Given the relative velocity between the object and the jaw, the frictional force at the contact point is computed next. Let $\boldsymbol{v}$ be the sliding velocity of the object, which is the velocity of the cube depicted as a pink arrow in Figure 2.3. By assuming the jaw is static after the contact before the manipulation, the relative velocity $\boldsymbol{v}_r$, which is the velocity of the cube relative to the jaw, is $\boldsymbol{v}_r = \boldsymbol{v}$. Let O denote the object frame located at the object center of mass and let C be the contact frame at the contact point, depicted as the blue dot in Figure 2.3. The z-axis of the contact frame C is in the direction of the inward surface normal at the contact point, same as the direction of the normal force that the jaw exerts on the object. Let $\boldsymbol{f}_\perp = [0, 0, f_\perp]^T, f_\perp \geq 0$ be the normal force acting on the cube and let $\boldsymbol{f} = [f_x, f_y]^T$ be the maximum static frictional force in the frame C. The frictional force $\boldsymbol{f}$ acting on the cube is antiparallel to $\boldsymbol{v}$ and is computed with

$$\boldsymbol{f} = \begin{bmatrix} f_x \\ f_y \end{bmatrix} = -\mu f_\perp \frac{\boldsymbol{v}}{\|\boldsymbol{v}\|}. \tag{2.32}$$

Note that the magnitude of $\boldsymbol{f}$ is a constant with a fixed normal force $f_\perp$

$$\|\boldsymbol{f}\| = \mu f_\perp. \tag{2.33}$$

The frictional wrench $\boldsymbol{w}$ for a hard point contact in the local contact frame C is $\boldsymbol{w} = [f_x, f_y]^T$ as there is no frictional torque if the contact area is negligible.

2.3.3.2 Soft Point Contact

Although the hard point contact is widely used to estimate the frictional force, it does not consider the frictional torque even if the contact area is not negligible, for instance, if a deformable gripper jaw presses onto a rigid cube, as shown in Figure 2.4, where the dashed line depicts the undeformed shape of the jaw and the grey area illustrates the deformed jaw.

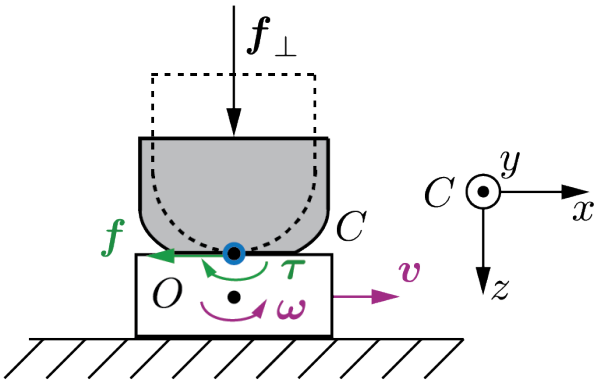

Figure 2.4: The front view of a representative soft point contact.

To address the issue with the overly conservative frictional torque estimation, Murray *et al.* [15] proposed the soft point contact type. This contact type decouples the angular and linear velocity of the grasped object to compute the frictional force and torque individually. Figure 2.4 illustrates the decoupled twist and frictional wrench as the pink and green arrows, respectively. Let $\gamma \in \mathbb{R}^+$ be the torsional friction coefficient and let $\boldsymbol{\omega}$ be the angular velocity of the object. For instance, the representative angular velocity shown in Figure 2.4 can be expressed with $\boldsymbol{\omega} = [0, 0, -\omega_z]^T$ with $\omega_z > 0$, which is an angular velocity about the negative z-axis in contact frame C. The maximum static frictional force $\boldsymbol{f}$ and the frictional torque $\boldsymbol{\tau}$, or the torsional friction, in the contact frame C are computed with

$$\begin{aligned} \boldsymbol{f} &= \begin{bmatrix} f_x \\ f_y \\ 0 \end{bmatrix} = -\mu f_\perp \frac{\boldsymbol{v}}{\|\boldsymbol{v}\|} \\ \boldsymbol{\tau} &= \begin{bmatrix} 0 \\ 0 \\ \tau_z \end{bmatrix} = -\gamma f_\perp \frac{\boldsymbol{\omega}}{\|\boldsymbol{\omega}\|}. \end{aligned} \tag{2.34}$$

The magnitudes of $\boldsymbol{f}$ and $\boldsymbol{\tau}$ are also constant with a fixed normal force $f_\perp$

$$\begin{aligned} \|\boldsymbol{f}\| &= \sqrt{f_x^2 + f_y^2} = \mu f_\perp \\ \|\boldsymbol{\tau}\| &= |\tau_z| = \gamma f_\perp. \end{aligned} \tag{2.35}$$

While a soft point contact provides a potentially unrealistic frictional wrench estimation due to the decoupling of angular and linear velocity, it is a practical model due to its efficiency; therefore, it is commonly applied in grasp planning [89], [90]. In summary, a soft point contact transmits a 3D frictional wrench $\boldsymbol{w} = [f_x, f_y, \tau_z]^T$ in the contact frame C.

2.3.3.3 Planar Area Contact

Compared to the soft point contact type, the frictional wrench for a planar area contact, also called a planar surface contact, is a more realistic estimation but requires higher computational effort. In contrast to the hard and soft point contacts, the frictional wrench for a planar surface contact is computed by summing up the local frictional wrench contribution at each point across the contact. Specifically, given a 2D instantaneous object motion (Section 2.3.2), the wrench computation pipeline first determines the relative motion of each point on the contact area, then computes the local frictional wrench at each point, finally integrates or sums up the local frictional contributions.

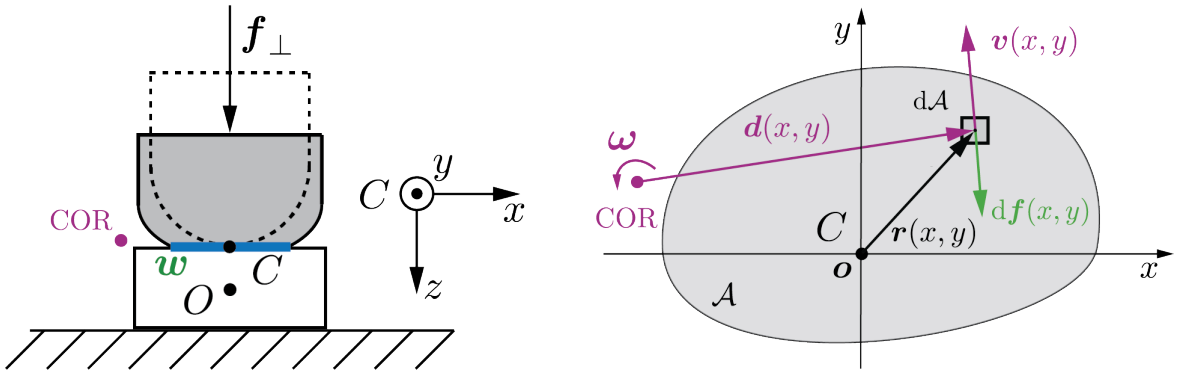

Figure 2.5: Left: the front view of a representative planar area contact. Right: the local frictional force at a point on the contact area for the given COR.

Figure 2.5 (left) shows the front view of an area contact when a jaw deforms onto a rigid cube. The blue line depicts the contact area. Figure 2.5 (right) illustrates the contact area $\mathcal{A}$ between the two bodies. As the contact area can be of arbitrary shape, it is not illustrated as a circle to avoid potential confusion.

First, consider the local contact frame C, which lies in the 2D plane that contains the contact area. The frictional wrench and the relative motion are computed in C. Directly computing the frictional wrench in the object frame O leads to a 6D frictional wrench instead of 3D, thus potentially becomes less efficient. Next, consider a rectilinear coordinate system in C fixed in the plane with the x- and y-axes being arbitrarily chosen. The origin of C is located at the pressure center $\boldsymbol{o} = [o_x, o_y]^T$ of the contact, as the frictional torque is computed with respect to $\boldsymbol{o}$ [13]. This origin selection simplifies the process of transforming the frictional

wrench applied at C into an equivalent wrench applied at O for multicontact grasp analysis. To compute the pressure center, let $\mathcal{A}$ be the contact area and let p be the pressure distribution of $\mathcal{A}$, where $p(x, y) \geq 0$ is the pressure value at the point $(x, y) \in \mathcal{A}$. The pressure center $\boldsymbol{o}$ is computed with

$$o_x = \frac{\int_{\mathcal{A}} x \cdot p(x, y)\, \mathrm{d}\mathcal{A}}{\int_{\mathcal{A}} p(x, y)\, \mathrm{d}\mathcal{A}}, \quad o_y = \frac{\int_{\mathcal{A}} y \cdot p(x, y)\, \mathrm{d}\mathcal{A}}{\int_{\mathcal{A}} p(x, y)\, \mathrm{d}\mathcal{A}}. \tag{2.36}$$

Given an instantaneous object motion described as a rotation around the center of rotation (COR) in the xy-plane, the next part computes the linear velocity of a point, or an infinitesimally small area, and its local frictional contribution. Denoting $\mathrm{d}\mathcal{A}$ as an infinitesimally small area at (x, y) on $\mathcal{A}$, the linear velocity $\boldsymbol{v}(x, y)$ of $\mathrm{d}\mathcal{A}$ is perpendicular to the vector from the COR to (x, y), denoted as $\boldsymbol{d}(x, y)$, since $\mathrm{d}\mathcal{A}$ rotates around the COR. The local frictional force $\mathrm{d}\boldsymbol{f}(x, y)$ is opposite to $\boldsymbol{v}(x, y)$ and is computed as

$$\mathrm{d}\boldsymbol{f}(x, y) = -\mu \cdot p(x, y) \cdot \frac{\boldsymbol{v}(x, y)}{\|\boldsymbol{v}(x, y)\|}\, \mathrm{d}\mathcal{A}. \tag{2.37}$$

Let $\mathrm{d}\tau_z(x, y)$ be the local frictional torque of $\mathrm{d}\mathcal{A}$ about the z-axis pointing outward. With $\boldsymbol{r}(x, y)$ being the torque arm, $\mathrm{d}\tau_z(x, y)$ is computed with respect to the pressure center $\boldsymbol{o}$ by

$$\mathrm{d}\tau_z(x, y) = \boldsymbol{r}(x, y) \times \mathrm{d}\boldsymbol{f}(x, y), \quad \text{where } \boldsymbol{r}(x, y) = \begin{bmatrix} x \\ y \end{bmatrix} - \boldsymbol{o}. \tag{2.38}$$

By integrating the local frictional force and torque, the frictional wrench $\boldsymbol{w} = [f_x, f_y, \tau_z]^T$ of the contact area $\mathcal{A}$ is computed as

$$\begin{aligned} \boldsymbol{f} &= \begin{bmatrix} f_x \\ f_y \end{bmatrix} = \int_{\mathcal{A}} \mathrm{d}\boldsymbol{f}(x, y)\, \mathrm{d}\mathcal{A} = -\mu \int_{\mathcal{A}} p(x, y) \cdot \frac{\boldsymbol{v}(x, y)}{\|\boldsymbol{v}(x, y)\|}\, \mathrm{d}\mathcal{A} \\ \tau_z &= \int_{\mathcal{A}} \mathrm{d}\tau_z(x, y)\, \mathrm{d}\mathcal{A} = -\mu \int_{\mathcal{A}} p(x, y) \cdot \left[\left(\begin{bmatrix} x \\ y \end{bmatrix} - \boldsymbol{o} \right) \times \frac{\boldsymbol{v}(x, y)}{\|\boldsymbol{v}(x, y)\|} \right] \mathrm{d}\mathcal{A}. \end{aligned} \tag{2.39}$$

To better understand the frictional wrench limit of a planar area contact, the following part discusses the extremes of the frictional force and torque at the contact. Figure 2.6 illustrates the local frictional force direction vectors with two representative CORs. As illustrated on the left of Figure 2.6, the frictional force f_x along the x-axis reaches the maximum if the COR is infinitely far away along the negative y-axis as the local frictional force at each point is parallel to the x-axis. This COR location results in a zero frictional torque with respect to $\boldsymbol{o}$. As shown on the right of Figure 2.6, the magnitude of τ_z reaches the maximum if the COR locates at $\boldsymbol{o}$, since the torque arm of each small area is perpendicular to the local frictional force. This COR location results in a zero frictional force only if the pressure distribution is circular symmetric.

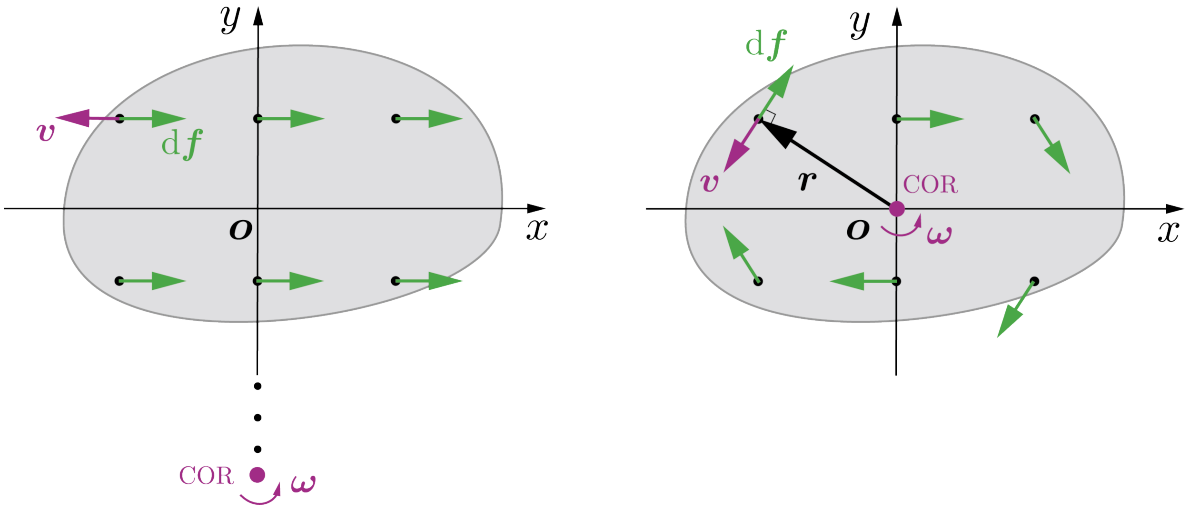

Figure 2.6: Direction vectors of the local frictional forces correspond to two locations of the center of rotation (COR), which result in the maximum frictional force along the x-axis (left) and the maximum frictional torque about the negative z-axis (right), respectively.

2.3.4 Limit Surface

So far, the frictional wrench is derived for a given relative motion between two bodies in contact. However, for many robot applications, such as grasp planning, the relative motion between the grasped object and the gripper jaws caused by external disturbances during the manipulation is unknown at the time of planning. Therefore, this section presents the frictional wrench limit that a gripper jaw can act on the object by considering all possible object motions. Goyal *et al.* [13] proposed a so-called *limit surface (LS)* to describe the frictional wrench limit, which is widely used to plan grasps [27], [28], [91]. The LS is also referred to as the *three-dimensional limit surface (3DLS)* in this thesis, as it describes the frictional wrenches in 3D. In addition to describing all possible frictional wrenches, the limit surface also provides an estimation of the relative motion between two bodies in contact. Thus, the LS is also applied in pushing manipulation [16], [88], [92]–[95].

The limit surface in the wrench space can be obtained by sampling the relative motion space and computing the frictional wrench for each motion. The inverse problem of finding the relative motion associated with a given frictional wrench is addressed in [13] with the assumption of *maximal work inequality*. Although the inverse problem is not needed in grasping applications, the LS properties regarding this part are also reviewed in the following. As a foundation of the limit surface, the limit curve at a point and the maximum work inequality are introduced first.

2.3.4.1 Limit Curve and Maximum Work Inequality

At a point of a frictional contact in the xy-plane with a fixed normal force, the frictional forces in the (f_x, f_y)-space form a closed curve, defined as the *limit curve (LC)*. The frictional forces on the LC correspond to all possible directions of the relative linear velocity at the point.

The assumption of maximal work inequality [96], or principle of maximal dissipation,

states that the frictional forces are adjusted to cause maximum dissipation with a given sliding velocity. Specifically, let $\boldsymbol{f} = [f_x, f_y]^T$ be the frictional force, let $\boldsymbol{f}^* \in \mathbb{R}^2$ be an arbitrary frictional force within the LC, and let $\boldsymbol{v}$ be the relative linear velocity, the maximum work inequality can be stated as

$$(\boldsymbol{f} - \boldsymbol{f}^*)^T \boldsymbol{v} \geq 0 \tag{2.40}$$

which implies that the LC must be convex and the direction of $\boldsymbol{v}$ is given by the normal to the LC at $\boldsymbol{f}$, where the limit curve is smooth [96]. The LC is a circle for the Coulomb friction law, or isotropic friction.

2.3.4.2 Load Motion Inequality

The limit curve specifies the frictional force limit at a point and the unique relation between $\boldsymbol{f}$ and $\boldsymbol{v}$. However, the LC does not include the frictional torque or the relative angular velocity for a planar area contact. Thus, Goyal *et al.* [13] generalized the limit curve to 3D, called the limit surface, to describe the 3D frictional wrench limit and to fully characterize the relation between the 3D frictional wrench and the relative motion.

Goyal *et al.* [13] considered the scenario, where a rigid object slides on a planar surface. Figure 2.7 illustrates a representative contact, where the object motion is a pure translation. In contrast to grasping applications, which require the frictional wrench limit acting on the object (green arrow in Figure 2.7), the limit surface for planar pushing applications provides the relation between the frictional wrench that the object acts on the supporting surface (orange arrow) and the object motion relative to the surface (pink arrow). In other words, with the Coulomb friction law, the frictional force acting on the surface has the same direction as the object relative velocity. Note that if the limit surface is only used to describe the frictional wrench limit without considering the wrench motion relation and the Coulomb friction law applies, the LS is identical for the frictional wrenches acting on the object and acting on the supporting surface since the LS is symmetric. Details about the symmetry are discussed in Section 2.3.4.4.

Recall that a twist $\boldsymbol{\xi} = [v_x, v_y, \omega_z]^T$ describes the instantaneous object motion (Section 2.3.2.1). As the supporting surface is static and planar, the relative object motion is equivalent to the object twist, which is also referred to as the complete velocity in [13] with its direction $\boldsymbol{\xi}/\|\boldsymbol{\xi}\|$ being the motion vector. The frictional wrench $\boldsymbol{w}$ and the twist $\boldsymbol{\xi}$ are with respect to the same reference point $\boldsymbol{o}$, typically the contact pressure center or center of mass of the object.

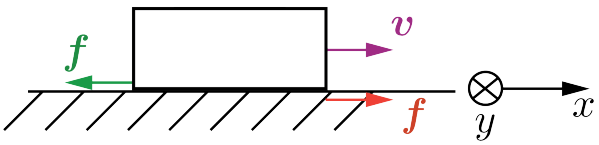

Figure 2.7: The front view of a representative sliding contact in the xy-plane.

Let $\boldsymbol{w} = [f_x, f_y, \tau_z]^T$ be the frictional wrench that the object acts on the surface, let $\boldsymbol{w}^* \in \mathbb{R}^3$ be an arbitrary frictional wrench, and let $\boldsymbol{\xi} = [v_x, v_y, \omega_z]^T$ be the object twist with respect

to the reference point $\boldsymbol{o}$. By applying the principle of virtual work and the maximum work inequality described with Equation (2.40), one obtains the following *load motion inequality*

$$(\boldsymbol{w} - \boldsymbol{w}^*)^T \boldsymbol{\xi} \geq 0. \tag{2.41}$$

The load motion inequality has the same structure as Equation (2.40) and provides important properties of the limit surface. The definition and properties of the limit surface are reviewed in the following.

2.3.4.3 Limit Surface Definition

The limit surface is defined as the boundary of the set of all possible frictional wrenches that can be applied through one contact or a set of contacts. The LS is a closed, convex surface in the three-dimensional wrench (load) space. Figure 2.8 depicts a representative limit surface. Let $f(\boldsymbol{x}) = 1$ with $\boldsymbol{x} \in \mathbb{R}^3$ define the limit surface, an arbitrary frictional wrench $\boldsymbol{w}^*$ that can be transmitted through the contact or the set of contacts is constrained by

$$f(\boldsymbol{w}^*) \leq 1. \tag{2.42}$$

Equation (2.42) provides the frictional wrench constraints, or the frictional wrench limit, of a contact. Specifically, if the required frictional wrench to counter an external disturbance is inside of the LS, no relative motion occurs. The LS definition is often used to plan grasps or to predict grasp success [27], [5], [91].

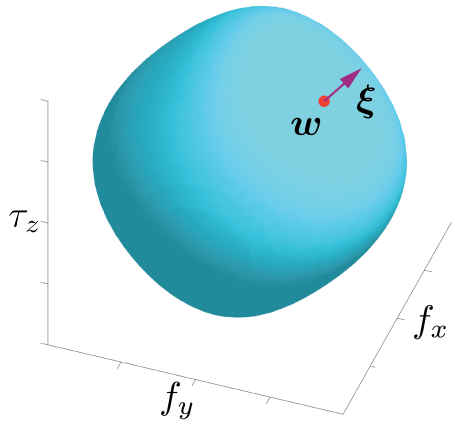

Figure 2.8: A representative limit surface in the wrench space.

2.3.4.4 Limit Surface Properties

From the load motion inequality in Equation (2.41), one obtains the following properties of the limit surface. Note that the properties reviewed here are for the Coulomb friction law, or isotropic friction, which means that the frictional force is parallel to the relative linear velocity and its magnitude is a constant with a fixed normal force.

1. The limit surface is closed, convex and symmetric about the origin in the wrench space.

2. If a relative motion occurs, the frictional wrench $\boldsymbol{w}$ lies on the limit surface and the associated twist $\boldsymbol{\xi}$ is normal to the LS at $\boldsymbol{w}$ if the normal is well-defined.

As the first property, the LS is symmetric about the origin ($[0, 0, 0]^T$) in the wrench space. Specifically, if the frictional wrench $\boldsymbol{w}$ associated with the twist $\boldsymbol{\xi}$ is on the LS, then $-\boldsymbol{w}$ associated with $-\boldsymbol{\xi}$ is also on the LS, since the reversal of a twist leads to the reversal of the frictional force direction at each point on the contact.

The second property describes the relation between the frictional wrench and the associated twist at the reference point $\boldsymbol{o}$. This property is widely applied in planar pushing [88], [92], [95], where the object twist $\boldsymbol{\xi}$ relative to the supporting surface is predicted for a given frictional wrench $\boldsymbol{w}$ acting on the surface, as illustrated in Figure 2.8. If $\boldsymbol{w}$ lies at a vertex or on a flat region of the limit surface, the relation between the twist and the frictional wrench is not unique. Such non-unique load motion relations happen if the contact area consists of discrete points or is a line segment, which is discussed next.

2.3.4.5 Vertices and Facets on a Limit Surface

For isotropic friction, vertices or facets (flat regions) on the limit surface occur if the contact is a line segment or consists of discrete points. On a vertex of the LS, multiple twist directions are associated with a frictional wrench; whereas on a facet, a range of frictional wrenches are associated with the same twist direction. If the contact pressure distribution is continuous and the contact area is not a line segment, the limit surface is smooth and the load motion relation is well-defined.

Vertices on the LS occur if the contact area is a line segment or all discrete points of the contact are colinear. The sets of CORs lying on this line but outside of the contact region lead to the same total frictional wrench of the contact. This is due to the fact that each of the CORs in these sets results in the same direction of relative velocity at each point on the contact. Consider an example illustrated in Figure 2.9(a). The blue line segment, which is colinear to the x-axis, is the contact area. Two representative CORs (purple dots) are on the x-axis but outside of the contact region. The two CORs lead to the same local frictional forces, whose direction vectors are illustrated in green, and therefore, the same total frictional wrench of the contact. Figure 2.9(b) illustrates the total frictional wrench as an orange vertex on the LS. The twists corresponding to the two CORs are shown as purple arrows.

Facets on the LS occur if the contact consists of discrete non-colinear points. The underlying reason is that if the COR coincides with one of the points, the twist of this point is indeterminate. Therefore, the frictional force at this point can have any direction. By adding each of the possible frictional contributions at this point to the contributions at the rest of the points on the contact, one obtains the set of possible frictional wrenches of the contact that corresponds to the same COR. Therefore, the number of facets on the LS is same as the number of contact points. For a larger number of points, the contribution of each point to the total frictional wrench becomes smaller; therefore, the associated facet shrinks. The facets vanish if the contact pressure distribution is continuous. Figure 2.10(a) depicts a representative three-point contact resulting from three screws mounted on a triangular pad, where the

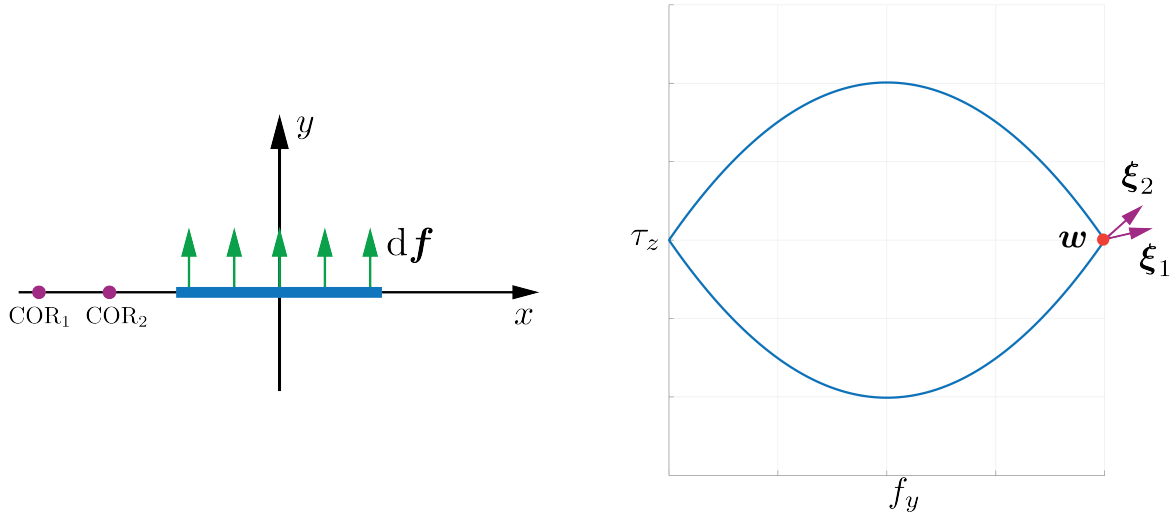

(a) (b)

Figure 2.9: (a) A line segment contact. (b) The corresponding limit surface with vertices.

contact points a, b, c are marked in blue. Figure 2.10(b) shows the limit surface of the contact. Each facet on the LS is caused by locating the COR at a, b, and c, respectively. The normal of each facet is the direction vector of the twist ξ that corresponds to one of the three CORs.

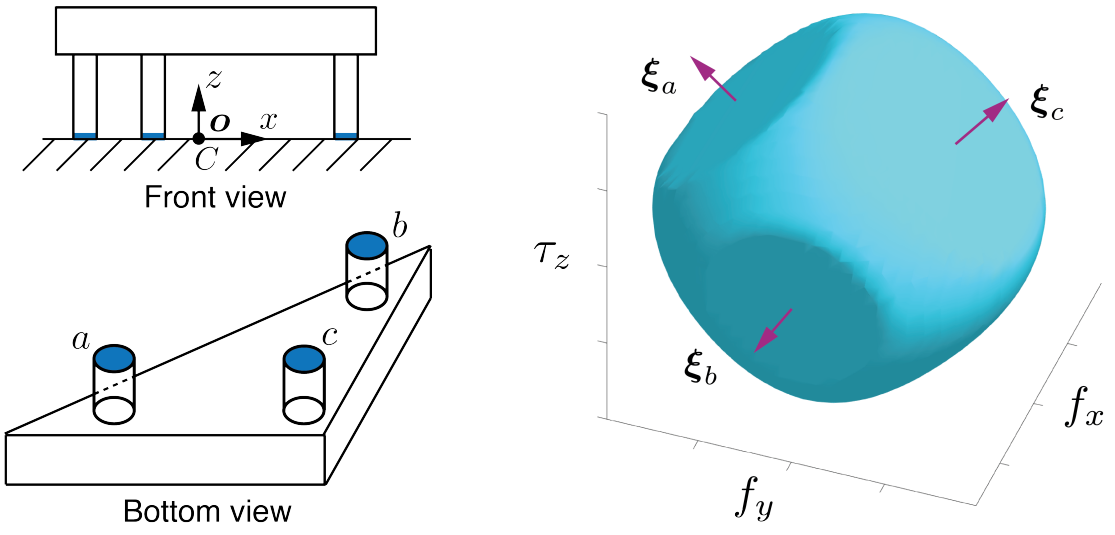

(a) (b)

Figure 2.10: (a) Front and bottom view of a triangular pad with three screws, which results in a three-point contact between the object and the ground. (b) The corresponding limit surface with three facets in the wrench space.

2.3.4.6 Constructing a Limit Surface

Given the contact profile, Goyal *et al.* [13] proposed three ways to construct the limit surface. The most common way is to compute the frictional wrenches for each of the possible relative motions. This process requires a dense sampling in the motion space and is potentially time-consuming. For a contact that consists of discrete contact points with a known limit surface for each individual point, the LS of the contact is the outer envelope of the convolution of each limit surface, followed by adding the facets to the LS.

The existing methods are either of low efficiency or not suitable for general planar area contacts. Therefore, many works approximate the limit surface with different geometric models for efficiency. Most commonly used LS models are reviewed in the following section.

2.3.5 Frictional Contact Models

Given a contact profile, a *frictional contact model* outputs the possible wrenches that a gripper jaw can act on the object via the contact. The possible wrenches, or the *contact wrenches*, are the sum of the possible frictional wrenches and the wrench impressed by the normal force. This thesis defines the *contact wrench model* and the *limit surface model* as the geometric model that represents or approximates the contact wrench limit and the frictional wrench limit, respectively. The contact wrench model and the limit surface model for each of the three contact types described in Section 2.3.3 are introduced in the following. Figure 2.11 provides a summary of these models.

2.3.5.1 Hard Point Contact Model

As introduced in Section 2.3.3.1, a hard point contact transmits 2D frictional forces in the local contact frame C, whose z-axis is in the direction of the inward surface normal at the contact point of the object. The magnitude of the frictional force $\|\boldsymbol{f}\|$ is upper bounded by $\mu f_\perp$, where $\boldsymbol{f}_\perp = [0, 0, f_\perp]^T$ with $f_\perp \geq 0$ is the normal force. In other words, any frictional force $\boldsymbol{f}$ at a hard point contact for the given $\boldsymbol{f}_\perp$ is constrained by the limit circle. Mathematically, the set of frictional wrench constraints $\mathcal{F}_{\text{HP}}$ for a hard point contact is

$$\mathcal{F}_{\text{HP}} = \left\{ \boldsymbol{f} = [f_x, f_y]^T \;\middle|\; \sqrt{f_x^2 + f_y^2} \leq \mu f_\perp \right\}. \tag{2.43}$$

The contact force, or the sum of the normal and frictional force, lies in a cone aligned with the contact normal, commonly known as the *friction cone* as illustrated in Figure 2.12(a). The contact wrench is equivalent to the contact force for a hard point contact, as the contact force is a vector that goes through the origin of C, hence does not generate torque with respect to the origin. The friction cone for the hard point contact model $\mathcal{C}_{\text{HP}}$, which constraints the contact wrench $\boldsymbol{c} = [f_x, f_y, f_\perp]^T$, is represented as

$$\mathcal{C}_{\text{HP}} = \left\{ \boldsymbol{c} = [f_x, f_y, f_\perp]^T \;\middle|\; \sqrt{f_x^2 + f_y^2} \leq \mu f_\perp, \;\; f_\perp \geq 0 \right\}. \tag{2.44}$$

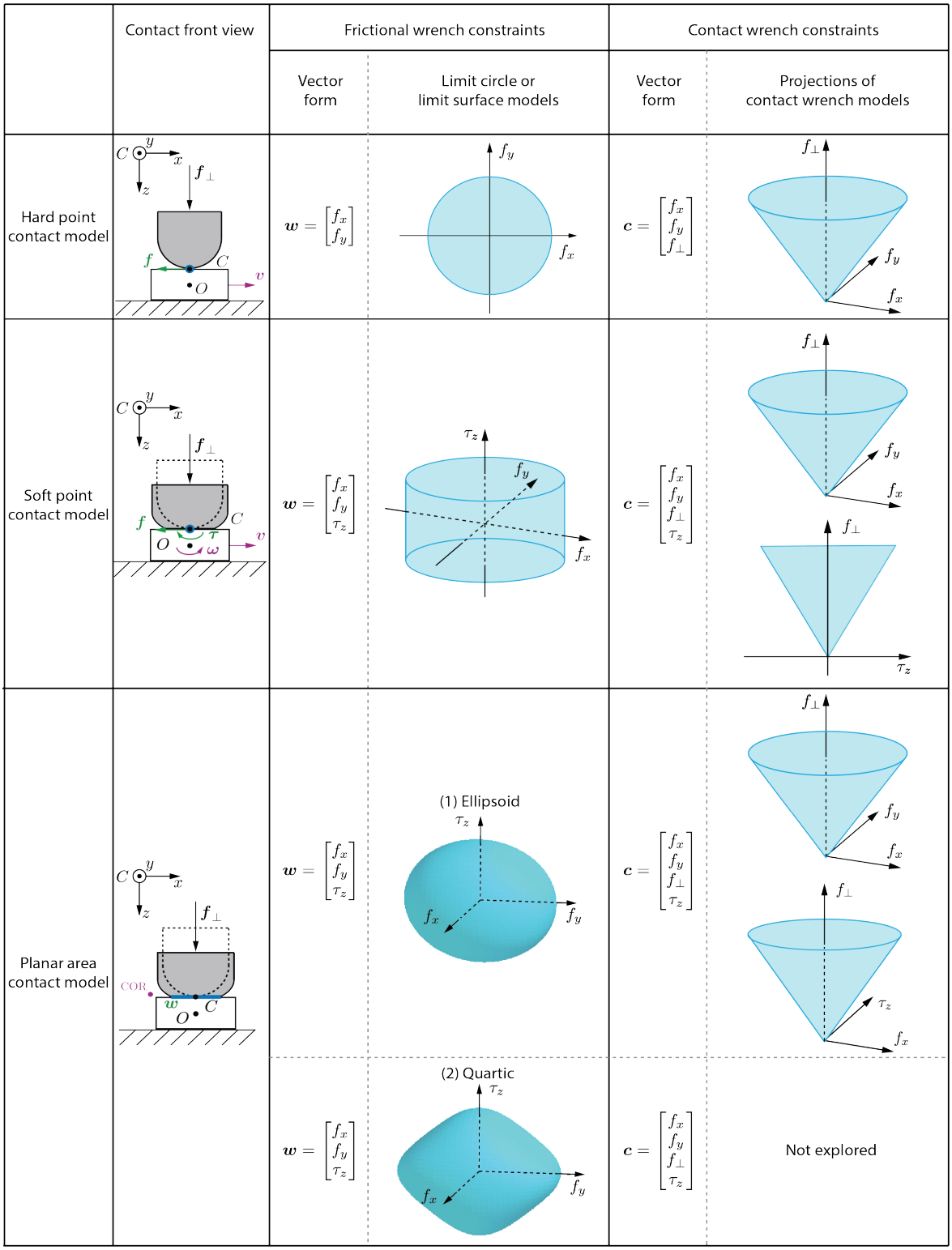

Figure 2.11: The limit surface and contact wrench models for three common contact types.

Note that in some literature, the surface of the friction cone is defined as the limit surface of a point contact, whereas the cone is defined as the contact wrench model of a hard point contact in this thesis.

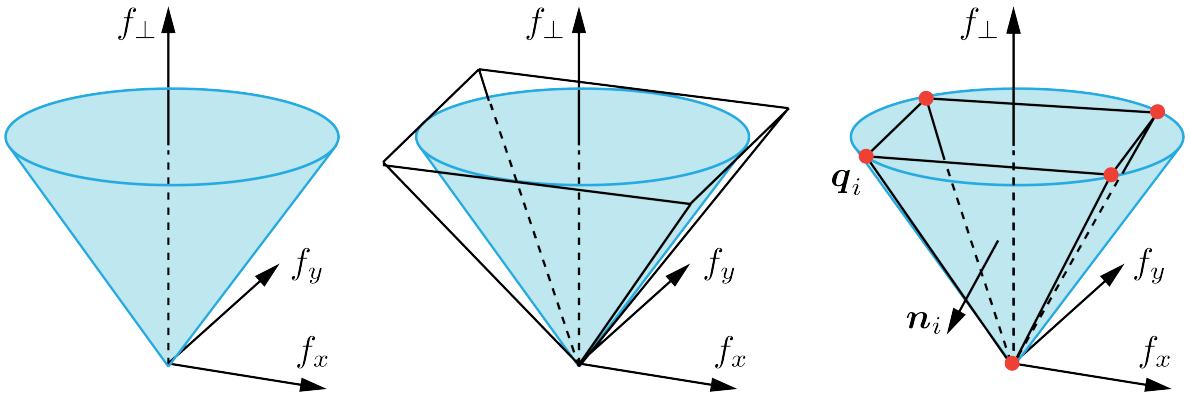

(a) Friction cone. **(b)** Outer cone approximation **(c)** Inner cone approximation

Figure 2.12: Friction cone and its approximations.

Contact Wrench Constraints as Linear Matrix Inequalities To apply the hard point contact model to grasping, Buss *et al.* [97] discovered that the contact wrench constraints can be transformed into positive (semi)definite constraints on certain symmetric matrices. Based on this observation, Buss *et al.* [97] formulated the frictional constraints as *linear matrix inequalities (LMIs)* to optimize grasp force. Han *et al.* [98] addressed three fundamental problems in grasp analysis by solving convex optimization problems involving LMIs, which can be efficiently solved in polynomial time. This part introduces the method to cast the contact wrench constraints from the hard point model to a linear matrix inequality (LMI). The LMI-based convex optimization problems for grasp analysis are introduced later in Section 2.5.

Recall that the contact wrench constraints for the hard point model are

$$\sqrt{f_x^2 + f_y^2} \leq \mu f_\perp, \quad f_\perp \geq 0.$$

The constraints are equivalent to enforcing positive semidefiniteness of the following matrix $\boldsymbol{P}_{\text{HP}}$

$$\boldsymbol{P}_{\text{HP}} = \begin{bmatrix} \mu f_\perp & 0 & f_x \\ 0 & \mu f_\perp & f_y \\ f_x & f_y & \mu f_\perp \end{bmatrix} \succeq 0 \tag{2.45}$$

since the eigenvalues of $\boldsymbol{P}_{\text{HP}}$ are

$$\begin{aligned} \lambda_1 &= \mu f_\perp \\ \lambda_2 &= \mu f_\perp - \sqrt{f_x^2 + f_y^2} \\ \lambda_3 &= \mu f_\perp + \sqrt{f_x^2 + f_y^2}. \end{aligned} \tag{2.46}$$

The positive semidefiniteness of $\boldsymbol{P}_{\text{HP}}$ is equivalent to $\lambda_1, \lambda_2 \geq 0$, as $\lambda_1 \geq 0$ implies $\lambda_3 \geq 0$.

Friction Cone Approximations A second-order friction cone leads to quadratic contact wrench constraints. To increase efficiency, a friction cone is commonly linearized to approximate the contact wrench limit with linear constraints. Figure 2.12(b) and (c) illustrate the

linearized outer and inner friction cone approximations as two N-sided polyhedral cones, where N is the number of edges of the cone. The linear contact wrench constraints for the outer and inner cone approximations are computed next.

Consider a N-sided polyhedral cone with evenly distributed edges as an **outer cone approximation**. Mathematically, the outer cone approximation is represented as

$$\mathcal{C}_{\text{HP}}^{\text{outer}} = \left\{ \boldsymbol{c} = [f_x, f_y, f_\perp]^T \middle| \cos\left(\frac{2\pi \cdot i}{N}\right) f_x + \sin\left(\frac{2\pi \cdot i}{N}\right) f_y \leq \mu f_\perp, \right. \\ \left. f_\perp \geq 0, \ \ \forall i \in \{1, \ldots, N\} \right\}. \tag{2.47}$$

There are in total $N + 1$ contact wrench constraints for an N-sided outer polyhedral cone.

A common **inner cone approximation** is the convex hull of the forces along the extrema of the friction cone, which is the smallest convex set that contains the forces. The forces along the extrema are illustrated as orange dots in Figure 2.12(c). Consider a convex hull with M facets. Let $\boldsymbol{n}_{i\in\{1,\ldots,M\}}^{\text{Hull}} \in \mathbb{R}^3$ be the outward normal of the ith facet and let $\boldsymbol{q}_i \in \mathbb{R}^3$ be a point on the facet. The inner cone contact wrench constraints are represented as

$$\mathcal{C}_{\text{HP}}^{\text{inner}} = \left\{ \boldsymbol{c} = [f_x, f_y, f_\perp]^T \middle| \ \boldsymbol{c}^T \boldsymbol{n}_i^{\text{Hull}} \leq \boldsymbol{q}_i^T \boldsymbol{n}_i^{\text{Hull}}, \ \ \forall i \in \{1, \ldots, M\} \right\}. \tag{2.48}$$

There are M contact wrench constraints for a convex hull with M facets. Although an inner cone approximation provides conservative constraints, which are preferred in grasping applications due to less false positive predictions, building a convex hull is potentially time consuming since its time complexity is $O(N\log N)$ with N being the input size of the points.

Other work [99] approximated the friction cone with multiple ellipsoids for fast grasp planning [100].

2.3.5.2 Soft Point Contact Model

Recall that a soft point contact transmits 3D frictional wrenches in the local contact frame C (Section 2.3.3.2). The frictional forces and torques are decoupled, which means that their magnitudes are individually upper bounded. Given a normal force with magnitude $f_\perp \geq 0$, the set of frictional wrench constraints $\mathcal{F}_{\text{SP}}$ for a soft point contact model is

$$\mathcal{F}_{\text{SP}} = \left\{ \boldsymbol{w} = [f_x, f_y, \tau_z]^T \middle| \ \sqrt{f_x^2 + f_y^2} \leq \mu f_\perp, \ \ |\tau_z| \leq \gamma f_\perp \right\}. \tag{2.49}$$

The set of constraints above indicates that the limit surface model is an elliptic cylinder in the (f_x, f_y, τ_z)-space, as illustrated in Figure 2.13(a).

From $\mathcal{F}_{\text{SP}}$, one can derive the contact wrench constraints. The contact wrench $\boldsymbol{c} = [f_x, f_y, f_\perp, \tau_z]^T$ of a soft point contact is in four dimensions, since the torque caused by the normal force is zero with respect to the origin of the contact frame C. The contact force is constrained by the friction cone, same as for a hard point contact. The torque component of

$\boldsymbol{c}$ equals the frictional torque, which is constrained by $\gamma f_\perp$. In summary, the set of contact wrench constraints $\mathcal{C}_{SP}$ is

$$\mathcal{C}_{\text{SP}} = \left\{ \boldsymbol{c} = [f_x, f_y, f_\perp, \tau_z]^T \;\middle|\; \sqrt{f_x^2 + f_y^2} \leq \mu f_\perp, \;\; |\tau_z| \leq \gamma f_\perp, \;\; f_\perp \geq 0 \right\}. \tag{2.50}$$

Figure 2.13(b) and (c) illustrate a 3D and a 2D projection of the 4D contact wrench model for a soft point contact, respectively.

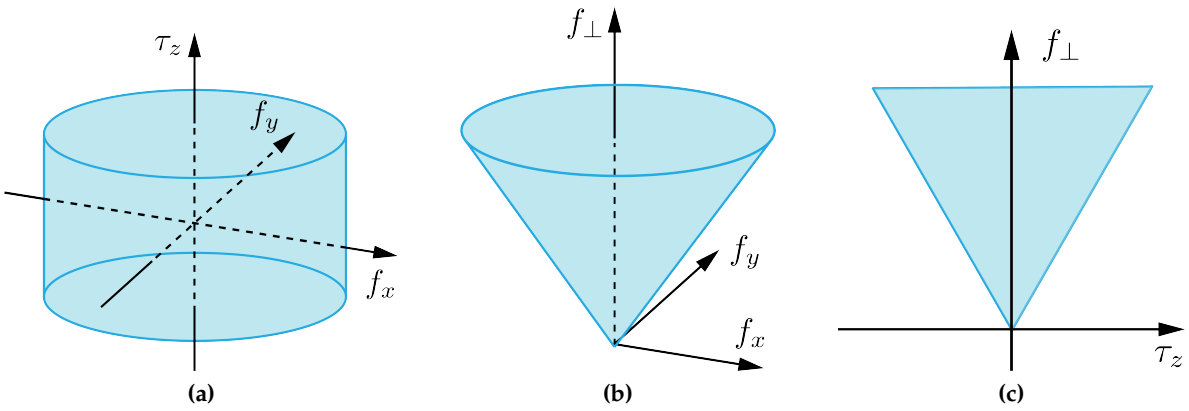

Figure 2.13: Soft point contact limit surface and contact wrench models. (a) Elliptic cylinder as the limit surface model. (b): Friction cone, which is a 3D projection of the contact wrench model in the $(f_x, f_y, f_\perp)$-space. (c): Triangle, which is a 2D projection of the contact wrench model.

Approximation of Contact Wrench Constraints The contact wrench constraints can be approximated with an outer or inner polyhedral cone for the 3D contact forces, same as for the hard point contact model (Section 2.3.5.1), and linear constraints for the frictional torque with Equation (2.49).

2.3.5.3 Ellipsoidal Planar Area Contact Model

There are two commonly used models to approximate the limit surface for a planar area contact: an ellipsoid and a convex fourth-order polynomial, or a convex quartic.

The ellipsoidal model is a data-driven approach proposed by Lee *et al.* [101] and is discovered by plotting the 3D frictional wrenches in the (f_x, f_y, τ_z)-space. As the ellipsoid has an analytic form, one can easily determine if a relative motion will occur by checking whether the required frictional wrench to counterbalance the external disturbance is contained within the ellipsoid.

This part presents the methods to construct an ellipsoid. Given the contact area $\mathcal{A}$ and the pressure distribution p of a contact, Lee *et al.* [101] proposed a method to construct the ellipsoid by computing the ellipsoid end points with the corresponding locations of the center of rotation. The two end points $[f_{x,\max}, 0, 0]^T$ and $[0, f_{y,\max}, 0]^T$ correspond to pure translations along the x- and y-axis, respectively. Note that $f_{x,\max} = f_{y,\max} = \mu \int_A p \, \mathrm{d}\mathcal{A}$. The third end point $(f_x, f_y, \tau_{z,max})$ is computed with Equation (2.39) by locating the COR at the pressure

center, which is also the origin of the contact frame C. With this COR location, the frictional torque τ_z is maximized, while the frictional forces f_x and f_y are only zero if the pressure distribution is circular symmetric, such as Kao's pressure distribution (Section 2.3.1.2). In other words, for a circular symmetric contact pressure distribution, the ellipsoid LS model is axis-aligned, which means that the radii of the ellipsoid are aligned with the f_x, f_y, τ_z-axes, respectively. For a non-circular symmetric pressure distribution, one can find the tilted, or non-axis-aligned ellipsoid, by defining a new coordinate frame (f'_x, f'_y, τ'_z) that aligns with the major axes of the ellipsoid [101].

The ellipsoidal limit surface function is derived next. Let $f_1(\boldsymbol{x}) = 1$ of the variable $\boldsymbol{x} \in \mathbb{R}^3$ be the limit surface function of an arbitrary zero-centered ellipsoid with

$$f_1(\boldsymbol{x}) = \boldsymbol{x}^T \boldsymbol{A}_e \boldsymbol{x} = 1 \tag{2.51}$$

where $\boldsymbol{A}_e \in \mathbb{R}^{3\times3}$ is a positive definite matrix. As $\boldsymbol{A}_e$ uniquely defines an ellipsoid, $\boldsymbol{A}_e$ also denotes the ellipsoid LS model in this theses. The eigenvectors of $\boldsymbol{A}_e$ define the principal axes of the ellipsoid, while the eigenvalues of $\boldsymbol{A}_e$ are the reciprocals of the squares of the radii.

As a special case of $\boldsymbol{A}_e$, an axis-aligned ellipsoid largely simplifies the computational effort. Therefore, many works [27], [5] assume a circular symmetric pressure distribution to apply such ellipsoids for grasp analysis. Hence, this thesis also derives the frictional and contact wrench constraints for such cases. As a special case of f_1, the axis-aligned ellipsoid function $f_{1,a}(\boldsymbol{x})$ is defined as

$$\begin{aligned} f_{1,a}(\boldsymbol{w}) &= \left(\frac{f_x}{f_{\max}}\right)^2 + \left(\frac{f_y}{f_{\max}}\right)^2 + \left(\frac{\tau_z}{\tau_{z,\max}}\right)^2 = 1, \\ \text{where } f_\perp &= \int_A p \,\mathrm{d}\mathcal{A}, \quad f_{\max} = \mu f_\perp. \end{aligned} \tag{2.52}$$

or in matrix form

$$f_{1,a}(\boldsymbol{w}) = [f_x, f_y, \tau_z] \begin{bmatrix} \frac{1}{f_{\max}^2} & 0 & 0 \\ 0 & \frac{1}{f_{\max}^2} & 0 \\ 0 & 0 & \frac{1}{\tau_{z,\max}^2} \end{bmatrix} \begin{bmatrix} f_x \\ f_y \\ \tau_z \end{bmatrix} = 1. \tag{2.53}$$

Similar to $f_{\max}$, $\tau_{\max}$ also linearly scales with $f_\perp$ if the shape of the pressure distribution remains unchanged. Therefore, one can express $\tau_{\max}$ with $\tau_{\max} = \mu_t f_\perp$, where $\mu_t > 0$ depends on the contact profile and μ. In summary, given $f_\perp$, the set of frictional wrench constraints $\mathcal{F}_{\text{EA}}$ for the axis-aligned ellipsoidal planar area contact model is

$$\mathcal{F}_{\text{EA}} = \left\{ \boldsymbol{w} = [f_x, f_y, \tau_z]^T \;\middle|\; \frac{f_x^2 + f_y^2}{\mu^2} + \frac{\tau_z^2}{\mu_t^2} \leq f_\perp^2 \right\}. \tag{2.54}$$

Add Facets to an Ellipsoid Recall that a limit surface has facets if the contact area is discrete points (Section 2.3.4.5). Therefore, for a contact that consists of N discrete points, one

needs to add N facets to the limit surface model. Each facet can be obtained by intersecting the ellipsoid with one plane in the wrench space. To define a plane, one needs the plane normal, which is also the normal of the facet, and a point that goes through the plane. Let (x_i, y_i) be the coordinate of the ith contact point in the contact frame C with $i \in \{1 \dots N\}$. The ith facet in the wrench space, or the (f_x, f_y, τ_z)-space, occurs when the COR locates at (x_i, y_i). The COR location (x_i, y_i) corresponds to the twist $\boldsymbol{\xi} = [y_i, -x_i, 1]^T$, which is parallel to the normal of the ith facet. The next step is to find a point that goes through the plane. Recall that the frictional force at (x_i, y_i) is not uniquely defined if the COR locates at (x_i, y_i). Therefore, one can use zero force at this point and sum up the local frictional wrenches at the remaining N-1 contact points. This frictional wrench is a point on the plane. This point and the plane normal uniquely define the plane.

Consider the following example to better understand the method to add facets to an ellipsoid. Figure 2.14(a) illustrates a representative four point contact with a uniform pressure distribution. Since the pressure distribution is circular symmetric, the limit surface shown in Figure 2.14(b) is an axis-aligned ellipsoid with three end points marked as orange dots. The ellipsoid with four facets are shown in Figure 2.14(c). To create a facet, one first locates the COR at a contact point, say a. Then, one can compute the corresponding twist $\boldsymbol{\xi}_a$ using Equation (2.18) and (2.20). The direction vector of $\boldsymbol{\xi}_a$ is the plane normal $\boldsymbol{n}_a$ in the wrench space. Figure 2.14(c) illustrates $\boldsymbol{n}_a$ as a purple arrow, which is parallel to $\boldsymbol{\xi}_a$. By using zero local force at a, the point $\boldsymbol{q}_a$ on the plane can be computed by summing up the local frictional wrench at b, c, d. As the plane is uniquely defined with the normal $\boldsymbol{n}_a$ and the point $\boldsymbol{q}_a$, the facet is created by intersecting the ellipsoid with the plane.

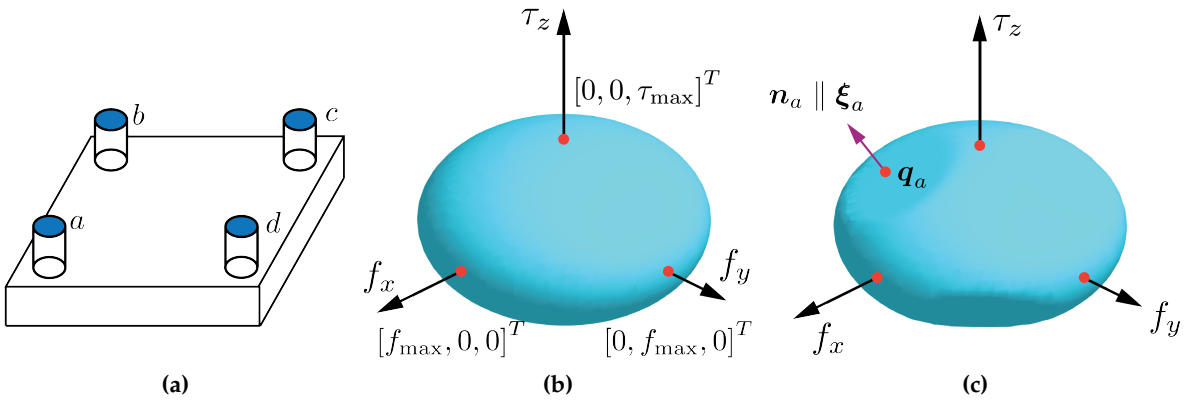

Figure 2.14: A representative four-point contact (a) and its ellipsoidal limit surface model without facets (b) and with facets (c).

Linearized Ellipsoid Approximation without Sampling As an ellipsoid provides quadratic constraints for the frictional wrench, it is a common technique to linearize the ellipsoid and compute linear constraints for efficiency. Howe *et al.* [102] proposed a practical ellipsoid approximation, which is a conservative approximation without decoupling the frictional force and torque. Denoting $f_t = \sqrt{f_x^2 + f_y^2}$ as the tangential frictional force, the linearly approxi-

mated contact wrench constraints are

$$\frac{1}{\mu} f_t + \frac{1}{\mu_t} |\tau_z| \leq f_\perp \text{ with } f_\perp \geq 0. \tag{2.55}$$

As shown in Figure 2.15, the linearized ellipsoid approximation is more conservative than decoupling the frictional force and torque constraints used in a soft point contact model.

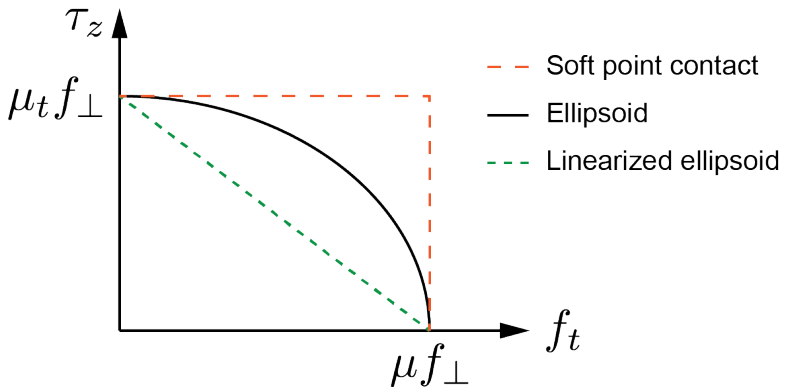

Figure 2.15: Frictional force and torque with a soft point contact, an ellipsoid, and a linearized ellipsoid approximation.

Buss *et al.* [97] also introduced the linear matrix inequalities for the linear ellipsoid model. The contact wrench constraints in Equation (2.50) are equivalent to enforcing the following matrix $\boldsymbol{P}_{\text{LE}}$ to be positive semidefinite

$$\boldsymbol{P}_{\text{LE}} = \begin{bmatrix} f_\perp & 0 & 0 & 0 & & & \\ 0 & \alpha & 0 & f_x & & & \\ 0 & 0 & \alpha & f_y & & \mathbf{0}_{4\times 3} & \\ 0 & f_x & f_y & \alpha & & & \\ & & & & \beta & 0 & f_x \\ & \mathbf{0}_{3\times 4} & & & 0 & \beta & f_y \\ & & & & f_x & f_y & \beta \end{bmatrix} \succeq 0 \tag{2.56}$$

where

$$\alpha = \mu \left(f_\perp + \frac{1}{\mu_t} \tau_z \right), \quad \beta = \mu \left(f_\perp - \frac{1}{\mu_t} \tau_z \right). \tag{2.57}$$

The eigenvalues of $\boldsymbol{P}_{\text{LE}}$ are

$$\begin{aligned}
\lambda_1 &= f_\perp \\
\lambda_2 &= \alpha \\
\lambda_3 &= \beta \\
\lambda_4 &= \alpha - \sqrt{f_x^2 + f_y^2} \\
\lambda_5 &= \alpha + \sqrt{f_x^2 + f_y^2} \\
\lambda_6 &= \beta - \sqrt{f_x^2 + f_y^2} \\
\lambda_7 &= \beta + \sqrt{f_x^2 + f_y^2}.
\end{aligned}$$

Similar to the LMIs for hard point contacts, $\lambda_1 \geq 0$ ensures a nonnegative normal force, while $\lambda_4 \geq 0$ and $\lambda_6 \geq 0$ correspond to the contact wrench constraints in (2.55).

Sampling-based Linearized Ellipsoidal Limit Surface Model While the aforementioned linearized ellipsoid model is practical, there is still a large difference between the linearized and original ellipsoid as illustrated in Figure 2.15. Therefore, an ellipsoid can also be sampled for linear constraints so that the accuracy of the approximation can be adjusted based on the number of samples.

Before moving on to computing the linear frictional constraints for a 3D ellipsoid, the next part first introduces the linear constraints for a 2D ellipse. Figure 2.16 illustrates an outer and an inner approximation of an ellipse with four sampled points $\boldsymbol{s}_{i\in\{1,\dots,4\}}$ marked as purple dots. For the outer approximation, the point $\boldsymbol{s}_i \in \mathbb{R}^2$ constrains an arbitrary 2D frictional wrench to be on one side of the line, which is defined with $\boldsymbol{s}_i$ and the ellipse normal $\boldsymbol{n}_i$ at $\boldsymbol{s}_i$. The ellipse normal $\boldsymbol{n}_i$ is computed with $\boldsymbol{n}_i = \boldsymbol{A}_e\boldsymbol{s}_i$, where $\boldsymbol{A}_e \in \mathbb{R}^{2\times 2}$ is the ellipse matrix. Therefore, the outer linear approximation of the representative discrete ellipse is a rectangle, illustrated with black lines in Figure 2.16(a). In other words, an arbitrary frictional wrench is constrained to be inside the rectangle. For an inner approximation, one first builds the convex hull of the discrete points and constrains the frictional wrenches to be on one side of each edge of the hull. Therefore, one obtains a parallelogram as the inner approximation of the representative ellipse, as shown in Figure 2.16(a). Note that the computation of an outer approximation requires both the sampled points $\boldsymbol{s}_{i\in\{1,\dots,4\}}$ and the ellipse matrix $\boldsymbol{A}_e$, whereas an inner approximation only needs the sampled points.

The outer and inner approximations of a 3D ellipsoid can be computed in a similar manner. Note that the equations that express the approximations are the same for an axis-aligned ellipsoid and for an arbitrary zero-centered ellipsoid.

Figure 2.17(a) shows an ellipsoid sampled with N discrete points $\{\boldsymbol{s}_1, \dots, \boldsymbol{s}_N\}$ with $\boldsymbol{s}_i \in \mathbb{R}^3, i \in \{1, \dots, N\}$. Given the points and the ellipsoid matrix $\boldsymbol{A}_e \in \mathbb{R}^{3\times 3}$, the set of frictional wrench constraints $\mathcal{F}_{\text{EA}}^{\text{outer}}$ for the outer approximation is

$$\mathcal{F}_{\text{EA}}^{\text{outer}} = \left\{ \boldsymbol{w} = [f_x, f_y, \tau_z]^T \;\middle|\; \boldsymbol{w}^T\boldsymbol{n}_i \leq (\boldsymbol{s}_i)^T\boldsymbol{n}_i, \;\; \boldsymbol{n}_i = \frac{\boldsymbol{A}_e\boldsymbol{s}_i}{\|\boldsymbol{A}_e\boldsymbol{s}_i\|}, \;\; \forall i \in \{1, \dots, N\} \right\}. \quad (2.58)$$

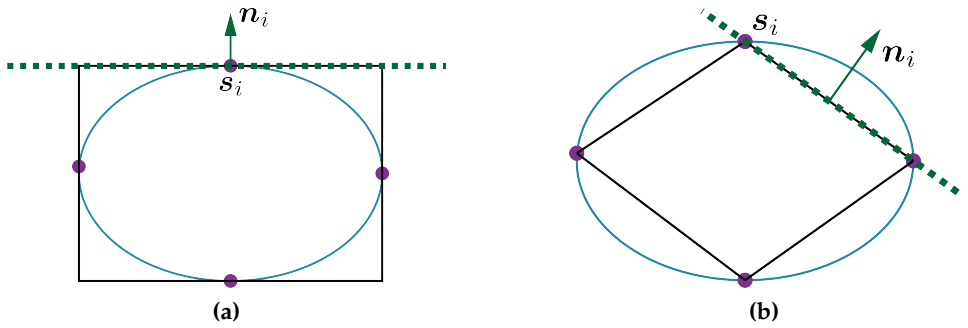

Figure 2.16: An outer approximation (a) and an inner approximation (b) of a 2D ellipse.

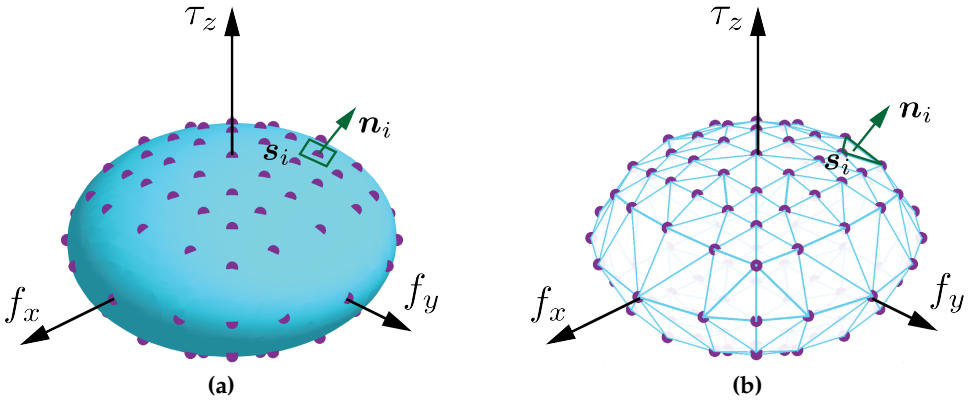

Figure 2.17: (a) A 3D ellipsoid (blue) sampled with discrete points (purple). The ith point $\boldsymbol{s}_i$ in the green square and the ellipsoid normal $\boldsymbol{n}_i$ at $\boldsymbol{s}_i$ define the ith linear frictional wrench constraint for the outer approximation. (b) Inner approximation of the ellipsoid.

One important property of the limit surface is that the LS linearly scales with the magnitude of the normal force $f_\perp$. Therefore, the equation above is rewritten in terms of $f_\perp$ to better reveal this property. First, consider a unit ellipsoid, which is an arbitrary zero-centered 3D ellipsoid corresponds to a unit normal force where $f_\perp = 1$. Let $\hat{\boldsymbol{A}}_e$ be the unit ellipsoid matrix and let $\hat{\boldsymbol{s}}_i$ be the ith point on the unit ellipsoid. As the eigenvectors $\{\boldsymbol{v}_1, \boldsymbol{v}_2, \boldsymbol{v}_3\}$ of the ellipsoid matrix define the principal axes of the ellipsoid and the eigenvalues $\{\lambda_1, \lambda_2, \lambda_3\}$ are the reciprocals of the squares of the radii, $\hat{\boldsymbol{A}}_e$ and $\boldsymbol{A}_e$ can be written as

$$\begin{aligned}
\hat{\boldsymbol{A}}_e &= [\boldsymbol{v}_1 \quad \boldsymbol{v}_2 \quad \boldsymbol{v}_3] \begin{bmatrix} \lambda_1 & 0 & 0 \\ 0 & \lambda_2 & 0 \\ 0 & 0 & \lambda_3 \end{bmatrix} [\boldsymbol{v}_1 \quad \boldsymbol{v}_2 \quad \boldsymbol{v}_3]^{-1} \\
\boldsymbol{A}_e &= [\boldsymbol{v}_1 \quad \boldsymbol{v}_2 \quad \boldsymbol{v}_3] \begin{bmatrix} \frac{\lambda_1}{f_\perp^2} & 0 & 0 \\ 0 & \frac{\lambda_2}{f_\perp^2} & 0 \\ 0 & 0 & \frac{\lambda_3}{f_\perp^2} \end{bmatrix} [\boldsymbol{v}_1 \quad \boldsymbol{v}_2 \quad \boldsymbol{v}_3]^{-1}
\end{aligned} \tag{2.59}$$

Therefore, one obtains

$$\boldsymbol{A}_e = \frac{1}{f_\perp^2}\hat{\boldsymbol{A}}_e \tag{2.60}$$

Finally, $\mathcal{F}_{\text{HP}}^{\text{outer}}$ can be reformulated as

$$\begin{aligned}\mathcal{F}_{\text{EA}}^{\text{outer}} = \Bigg\{ \boldsymbol{w} = [f_x, f_y, \tau_z]^T \;\Bigg|\; & \boldsymbol{w}^T \boldsymbol{n}_i \leq f_\perp \cdot (\hat{\boldsymbol{s}}_i)^T \boldsymbol{n}_i, \;\; \boldsymbol{s}_i = f_\perp \cdot \hat{\boldsymbol{s}}_i, \\ & \boldsymbol{n}_i = \frac{\hat{\boldsymbol{A}}_e \hat{\boldsymbol{s}}_i}{\|\hat{\boldsymbol{A}}_e \hat{\boldsymbol{s}}_i\|} = \frac{\boldsymbol{A}_e \boldsymbol{s}_i}{\|\boldsymbol{A}_e \boldsymbol{s}_i\|}, \;\; \forall i \in \{1, \dots, N\} \Bigg\}.\end{aligned} \tag{2.61}$$

Figure 2.17(b) shows the inner approximation of the ellipsoid, which is the M-facet convex hull of the N points. Let $\boldsymbol{n}_i^{\text{Hull}}$ be the normal of the ith facet and let $\boldsymbol{s}_i$ be a point on the facet, the set of frictional wrench constraints $\mathcal{F}_{\text{EA}}^{\text{inner}}$ for the inner approximation is

$$\mathcal{F}_{\text{EA}}^{\text{inner}} = \left\{ \boldsymbol{w} = [f_x, f_y, \tau_z]^T \;\middle|\; \boldsymbol{w}^T \boldsymbol{n}_i^{\text{Hull}} \leq (\boldsymbol{s}_i)^T \boldsymbol{n}_i^{\text{Hull}}, \;\; \forall i \in \{1, \dots, M\} \right\}. \tag{2.62}$$

While the outer ellipsoid approximation is more efficient as it does not compute the convex hull, the inner approximation provides more conservative constraints, which are preferred in grasp analysis. Danielczuk *et al.* [5] used the former to predict grasp robustness and Ciocarlie *et al.* [27] applied the latter to efficiently plan grasps.

Contact Wrench Model Next, the contact wrench limit is derived based on the frictional wrench limit described with Equation (2.54) for an axis-aligned ellipsoid. The contact wrench $\boldsymbol{c}$ is in four dimensions as the torque caused by the normal force is zero with respect to the origin in the contact frame C. The contact wrench lies in a 4D cone since the frictional wrench linearly scales with the magnitude of normal force $f_\perp$. Mathematically, the set of contact wrench constraints $\mathcal{C}_{\text{EA}}$ is

$$\mathcal{C}_{\text{EA}} = \left\{ \boldsymbol{c} = [f_x, f_y, f_\perp, \tau_z]^T \;\middle|\; \frac{f_x^2 + f_y^2}{\mu^2} + \frac{\tau_z^2}{\mu_t^2} \leq f_\perp^2, \;\; f_\perp \geq 0 \right\}. \tag{2.63}$$

Figure 2.18 illustrates two 3D projections of the contact wrench model, or the 4D cone that limits the contact wrench for an ellipsoidal area contact model. Note that the 2D projection of the 4D cone in the (f_x, τ_z) or the (f_y, τ_z) space is an ellipse, which is only axis-aligned if the contact pressure distribution is circular symmetric.

Contact Wrench Constraints as LMIs The set of contact wrench constraints $\mathcal{C}_{\text{EA}}$ can also be expressed as LMIs. The symmetric matrix $\boldsymbol{P}_{\text{EA}} \succeq 0$ that describes the contact wrench constraints in Equation (2.63) is

$$\boldsymbol{P}_{\text{EA}} = \begin{bmatrix} f_\perp & 0 & 0 & \frac{1}{\sqrt{\mu}} f_x \\ 0 & f_\perp & 0 & \frac{1}{\sqrt{\mu}} f_y \\ 0 & 0 & f_\perp & \frac{1}{\sqrt{\mu_t}} \tau_z \\ \frac{1}{\sqrt{\mu}} f_x & \frac{1}{\sqrt{\mu}} f_y & \frac{1}{\sqrt{\mu_t}} \tau_z & f_\perp \end{bmatrix} \succeq 0. \tag{2.64}$$

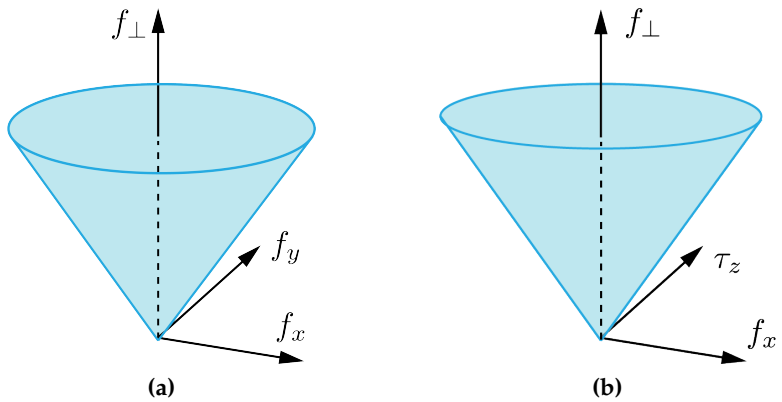

Figure 2.18: Two 3D projections of the 4D cone, or the contact wrench model, for an axis-aligned ellipsoidal planar area contact model.

The eigenvalues of $\boldsymbol{P}_{\text{EA}}$ are

$$\begin{aligned} \lambda_{1,2} &= f_\perp \\ \lambda_3 &= f_\perp - \sqrt{\frac{1}{\mu}\left(f_x^2 + f_y^2\right) + \frac{1}{\mu_t}\tau_z^2} \\ \lambda_4 &= f_\perp + \sqrt{\frac{1}{\mu}\left(f_x^2 + f_y^2\right) + \frac{1}{\mu_t}\tau_z^2}. \end{aligned} \tag{2.65}$$

Again, $\lambda_{1,2,3} \geq 0$ corresponds to the contact wrench constraints for the ellipsoidal LS model and λ_4 is always nonnegative.

Limitations Although an ellipsoid is a practical model, Howe *et al.* [16] also discovered a characteristic flattening of the limit surface for some contact profiles, which potentially makes the ellipsoid less accurate for such cases.

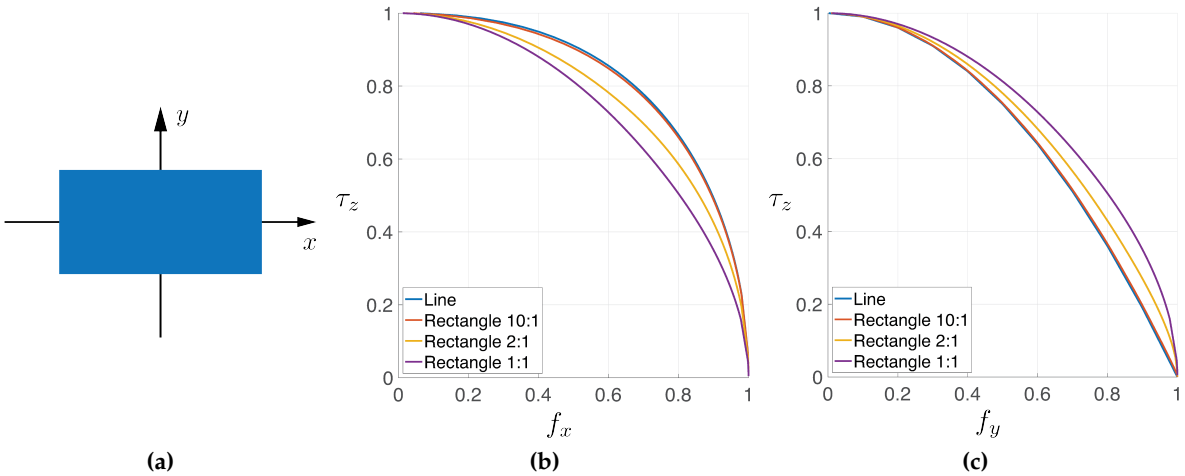

Figure 2.19: (a) A 2:1 rectangular contact area. (b) and (c) show the LS cross-sections in the (f_x, τ_z)-space and in the (f_y, τ_z)-space for four contacts, respectively

Consider a rectangular contact area with a uniform pressure distribution. The side lengths of the rectangle are of ratio N:1 with x-axis being the major axis. Such rectangle is called a $N:1$ rectangle in this thesis and Figure 2.19(a) shows a 2:1 rectangle. Figure 2.19(b) and (c) illustrate the 2D cross-sections of the limit surface for four contacts, which are a 1:1 rectangle, a 2:1 rectangle, a 10:1 rectangle, and a line, which corresponds to a 1:0 rectangle. The contacts are created by varying the side length on the y-axis and fixing the major axis. With the rectangle being more narrow, the limit surface in the (f_x, τ_z)-space becomes more convex, whereas the LS in the (f_y, τ_z)-space is more flat. Note that the LS for the 10:1 rectangle and the LS for the line are almost identical. In summary, as a contact area is narrow in one direction, say in the y direction, there is a corresponding LS flattening in the space of the frictional force in this direction and the frictional torque, which is the (f_y, τ_z)-space [16]. As a result, the ellipsoid LS model may not well capture such flattening and becomes overconfident.

2.3.5.4 Quartic Area Contact Model

To better capture the facets or flattening on the LS, Zhou *et al.* [92] proposed a strictly convex homogeneous quartic polynomial to approximate a limit surface for planar pushing applications. Specifically, a homogeneous quartic is defined by a polynomial, whose nonzero terms have the degree of four. Zhou *et al.* [92] used the quartic LS model to address the problem of estimating the direction of the object twist given a frictional wrench and the inverse problem of finding the frictional wrench given a measured twist. The next part discusses the properties of a quartic LS about frictional wrenches and twists, although the latter is not applied in this thesis.

Based on the LS properties described in Section 2.3.4, a geometric model to approximate a limit surface should be convex, symmetric, and differentiable. In addition to these properties, Zhou *et al.* [92] pointed out that the LS model should also be scale invariant and invertible. Scale invariant is important since a limit surface linearly scales with the normal force, the frictional coefficient, etc. Changing, for instance, the normal force should only result in a scaled LS model without changing its geometric shape. The invertibility is essential to the inverse problem about finding the friction wrench for a given twist. Specifically, let $\boldsymbol{w} \in \mathbb{R}^3$ be the frictional wrench acting on the supporting table and let $\boldsymbol{\xi} \in \mathbb{R}^3$ be the twist of the object being pushed. The inverse problem is to find a $\boldsymbol{w}$, such that $\nabla f(\boldsymbol{w})/\|\nabla f(\boldsymbol{w})\| = \hat{\boldsymbol{\xi}}$ for a given unit twist $\hat{\boldsymbol{\xi}}$, where $\nabla f(\cdot)$ denotes the gradient of the function $f(\cdot)$. Zhou *et al.* [92] discovered and proofed that a strictly convex homogeneous quartic fulfills the requirements.

To mathematically describe a quartic, let $f_2(\boldsymbol{x})$ be a quartic of the variable $\boldsymbol{x} \in \mathbb{R}^3$ and let the nonnegative integer d_1, d_2, d_3 be the degree of the variable x_1, x_2, x_3, respectively. The homogeneous quartic polynomial has the form $f_2(\boldsymbol{x}) = \sum_{i=1}^{N} a_i x_1^{d_1} x_2^{d_2} x_3^{d_3} = a_1 x_1^4 + a_2 x_1^3 x_2 + \ldots + a_N x_3^4$, where a_i are the coefficients of the terms and $d_1 + d_2 + d_3 = 4$. Here, $N = \binom{4+3-1}{3-1} = 15$. As the coefficients uniquely define $f_2(\boldsymbol{x})$, $\boldsymbol{A}_q = [a_1, \ldots, a_N]^T$ is denoted as the quartic model in this thesis. Although $\boldsymbol{A}_q$ is a vector, the variable is capital for consistency, since $\boldsymbol{A}$ denotes a limit surface model and $\boldsymbol{A}_e$ denotes the ellipsoidal LS model. The quartic limit surface model is the surface of the form $f_2(\boldsymbol{x}) = 1$.

To describe the strict convexity of $f_2(\boldsymbol{x})$, let $\boldsymbol{z} \in \mathbb{R}^3$ denote a nonzero auxiliary variable and let $\nabla^2 f_2(\boldsymbol{x})$ be the hessian matrix. A necessary and sufficient condition for $f_2(\boldsymbol{x})$ to be strictly convex is

$$\boldsymbol{z}^T \nabla^2 f_2(\boldsymbol{x}) \boldsymbol{z} > 0. \tag{2.66}$$

Enforcing convexity of a homogeneous quartic with more than one term is NP-hard. Zhou *et al.* [92] used a relaxation technique that enforces the convexity of $f_2(\boldsymbol{x})$ only on a region by using the concept of sum-of-squares (SOS) [103]. Specifically, let $\boldsymbol{y} \in \mathbb{R}^{36}$ be another nonzero auxilary variale, where $\boldsymbol{y}(\boldsymbol{x}, \boldsymbol{z}) = \left[x_1 \boldsymbol{z}^T, x_2 \boldsymbol{z}^T, x_3 \boldsymbol{z}^T\right]^T \in \mathbb{R}^9$, the quartic $f_2(\boldsymbol{x})$ is defined as *SOS convex*, if there exists a positive definite matrix $\boldsymbol{M} \in \mathbb{R}^{9\times 9}$, so that the following equation holds

$$\boldsymbol{z}^T \nabla^2 f_2(\boldsymbol{x}) \boldsymbol{z} = \boldsymbol{y}(\boldsymbol{x}, \boldsymbol{z})^T \boldsymbol{M} \boldsymbol{y}(\boldsymbol{x}, \boldsymbol{z}) > 0 \text{ with } \boldsymbol{M} \succ 0 \tag{2.67}$$

where the operator $\succ 0$ means the left-hand side is positive definite. The equation above can also be written as sparse linear constraints

$$\boldsymbol{V}_1 \boldsymbol{A}_q = \boldsymbol{V}_2 \text{vec}(\boldsymbol{M}) \text{ with } \boldsymbol{M} \succ 0 \tag{2.68}$$

where each row represents a linear constraint. The matrices $\boldsymbol{V}_1 \in \mathbb{N}_0^{36\times 15}$ and $\boldsymbol{V}_2 \in \mathbb{N}_0^{36\times 81}$ with $\mathbb{N}_0 = \{\mathbb{N} \cup \{0\}\}$ are constant sparse matrices and vec$(\cdot)$ denotes the vectorization operation. $\boldsymbol{V}_1$ and $\boldsymbol{V}_2$ are essentially the coefficient of each identical term on the left and right side of Equation (2.67), respectively.

The next part presents the $\boldsymbol{V}_1$ and $\boldsymbol{V}_2$ computation by expanding the left- and right-hand side of Equation (2.67). By expanding and sorting the polynomial on the left-hand side of Equation (2.67), one obtains

$$\boldsymbol{z}^T \nabla^2 f_2(\boldsymbol{x}) \boldsymbol{z} = 12a_1 x_1^2 z_1^2 + 6a_2 x_1 x_2 z_1^2 + 6a_3 x_1 x_3 z_1^2 + 6a_2 x_1^2 z_1 z_2 + \dots$$

which is a polynomial of 36 terms. By expanding the right-hand side and sorting the terms in the same order, one has

$$\boldsymbol{y}(\boldsymbol{x}, \boldsymbol{z})^T \boldsymbol{M} \boldsymbol{y}(\boldsymbol{x}, \boldsymbol{z}) = \boldsymbol{M}_{1,1} x_1^2 z_1^2 + 2\boldsymbol{M}_{2,1} x_1 x_2 z_1^2 + 2\boldsymbol{M}_{3,1} x_1 x_3 z_1^2 + 2\boldsymbol{M}_{4,1} x_1^2 z_1 z_2 + \dots$$

By equaling each term in the two polynomials above, one obtains 36 linear constraints

$$\begin{aligned} 12a_1 &= \boldsymbol{M}_{1,1} \\ 6a_1 &= 2\boldsymbol{M}_{2,1} \\ 6a_3 &= 2\boldsymbol{M}_{3,1} \\ 6a_2 &= 2\boldsymbol{M}_{4,1} \\ &\vdots \end{aligned}$$

With the vectorization of $\boldsymbol{M}$ being vec$(\boldsymbol{M}) = [\boldsymbol{M}_{1,1}, \boldsymbol{M}_{2,1}, \boldsymbol{M}_{3,1}, \dots, \boldsymbol{M}_{9,9}]^T \in \mathbb{R}^{81}$, the 36 linear constraints above can be formulated in matrix form shown in Equation (2.68) with $\boldsymbol{V}_1$

and $\boldsymbol{V}_2$ being

$$\boldsymbol{V}_1 = \begin{bmatrix} 12 & 0 & 0 & 0 & \cdots \\ 0 & 6 & 0 & 0 & \\ 0 & 0 & 6 & 0 & \\ 0 & 6 & 0 & 0 & \\ \vdots & & & & \ddots \end{bmatrix}, \boldsymbol{V}_2 = \left[\begin{array}{ccccc|c} 1 & 0 & 0 & 0 & \cdots & \\ 0 & 2 & 0 & 0 & & \\ 0 & 0 & 2 & 0 & & \mathbf{0}_{36\times 36} \\ 0 & 0 & 0 & 2 & & \\ \vdots & & & & \ddots & \end{array}\right]$$

The right part of $\boldsymbol{V}_2$ is a 36×36 zero matrix as $\boldsymbol{M}$ is symmetric. Specifically, the elements in the upper triangle of $\boldsymbol{M}$ are identical as the ones in the lower triangle. Therefore, these constraints are combined and represented with the $81 - 36 = 45$ elements in the lower triangle.

Zhou *et al.* [92] used semidefinite programming (SDP) to find a quartic LS model fit to K frictional wrench and twist pairs. The next part presents the data normalization as well as the objective function and the constraints of the SDP.

The wrenches and twists are normalized for numerical stability. Denoting $\rho \in \mathbb{R}^+$ as the radius of gyration and let $(\boldsymbol{w}_i, \boldsymbol{\xi}_i)$ with $i \in \{1, \ldots, K\}$ be the ith frictional wrench and twist pair. The normalized frictional wrench and twist pair $(\hat{\boldsymbol{w}}_i, \hat{\boldsymbol{\xi}}_i)$ is computed with

$$\hat{\boldsymbol{w}}_i = \begin{bmatrix} f_{x_i} \\ f_{y_i} \\ \tau_{z_i}/\rho \end{bmatrix}, \quad \hat{\boldsymbol{\xi}}_i = \frac{1}{\sqrt{(v_{x_i}^2 + v_{y_i}^2 + \omega_{z_i}^2 \cdot \rho^2)}} \begin{bmatrix} v_{x_i} \\ v_{y_i} \\ \omega_{z_i} \cdot \rho \end{bmatrix} \tag{2.69}$$

The normalization step allows unified units of the components in $\hat{\boldsymbol{w}}$ and $\hat{\boldsymbol{\xi}}$, respectively. The norm of the normalized twist is one, since the limit surface model estimates the direction of the twist. Note that the normalized wrench and twist samples still obey the maximum work inequality. The normalization technique for quartic 6D limit surface model proposed by this thesis differs from Equation (2.69).

For an ideal limit surface model, the frictional wrenches should be on the surface and the corresponding surface normals should be parallel to the measured twists. Hence, the nonnegative wrench error ε_{w_i} of the ith normalized wrench $\hat{\boldsymbol{w}}_i$ is defined as the distance from $\hat{\boldsymbol{w}}_i$ to the LS, since the distance is zero for an ideal LS model. Denoting $\nabla f_2(\hat{\boldsymbol{w}}_i)$ as the normal of f_2 at $\hat{\boldsymbol{w}}_i$, the nonnegative twist error ε_{t_i} of the ith measured normalized twist $\hat{\boldsymbol{\xi}}_i$ is computed as the projection residual of $\nabla f_2(\hat{\boldsymbol{w}}_i)$ to $\hat{\boldsymbol{\xi}}_i$. The sum wrench error ε_w and twist error ε_t are computed with

$$\begin{aligned} \varepsilon_w &= \sum_{i=1}^{K} \| f_2(\hat{\boldsymbol{w}}_i) - 1 \|, \\ \varepsilon_t &= \sum_{i=1}^{K} \| \nabla f_2(\hat{\boldsymbol{w}}_i) - (\nabla f_2(\hat{\boldsymbol{w}}_i)^T \hat{\boldsymbol{\xi}}_i) \cdot \hat{\boldsymbol{\xi}}_i \| \\ &= \sum_{i=1}^{K} \| \left(\boldsymbol{I}_{3\times 3} - \hat{\boldsymbol{\xi}}_i \hat{\boldsymbol{\xi}}_i^T \right) \nabla f_2(\hat{\boldsymbol{w}}_i) \|. \end{aligned} \tag{2.70}$$

ε_w and ε_t can be weighted based on, for instance, the sensory noise with the positive parameters η_w and η_t, respectively. Finally, the SDP to find the quartic limit surface model fit to K normalized wrench and twist pairs is

$$\begin{aligned} \underset{\boldsymbol{A}_q, \boldsymbol{M}}{\text{minimize}} \quad & \|\boldsymbol{A}_q\| + \eta_w \cdot \varepsilon_w + \eta_t \cdot \varepsilon_t \\ \text{subject to} \quad & \boldsymbol{V}_1 \boldsymbol{A}_q = \boldsymbol{V}_2 \text{vec}(\boldsymbol{M}) \\ & \boldsymbol{M} \succ 0. \end{aligned} \tag{2.71}$$

where the term $\|\boldsymbol{A}_q\|$ regularizes the parameters.

As $\boldsymbol{A}_q$ uniquely defines $f_2(\boldsymbol{x})$, the set of frictional wrench constraints $\mathcal{F}_{\text{QA}}$ for the quartic area contact model is

$$\mathcal{F}_{\text{QA}} = \left\{ \boldsymbol{w} = [f_x, f_y, \tau_z]^T \;\middle|\; f_2(\boldsymbol{w}) \leq 1 \right\}. \tag{2.72}$$

Contact Wrench Model As the frictional wrench linearly scales with the magnitude of the normal force, the set $\mathcal{C}_{\text{QA}}$ of contact wrench constraints is

$$\mathcal{C}_{\text{QA}} = \left\{ \boldsymbol{c} = [f_x, f_y, f_\perp, \tau_z]^T \;\middle|\; f_{2,u}(\boldsymbol{w}) \leq f_\perp^4, \;\; f_\perp \geq 0 \right\} \tag{2.73}$$

where $f_{2,u}(\cdot)$ is the quartic computed with a unit normal force $f_\perp = 1$.

The quartic LS model is applied in planar pushing applications such as trajectory planning [18], [92], [104]. To the author's knowledge, the quartic is not applied in grasp planning; therefore, the geometric shape of its contact wrench model and the linearization technique are not explored.

2.4 From Contacts to Grasping

Based on the contact wrench constraints for each contact of a grasp, this section introduces the method to combine these constraints to obtain the total wrench that a grasp can exert on the object.

2.4.1 The Wrench Basis

Recall that the contact wrenches of a contact are computed with respect to the origin of the contact frame C. To determine the effect of the total contact wrenches of a grasp, the first step is to transform the contact wrench constraints from C of each contact to a common reference frame O, or the object frame, typically located at the object center of mass (COM). Although a contact wrench in C is 3D or 4D depending on the contact type, the equivalent contact wrench in O is in six dimensions for a 3D object. Therefore, one commonly uses the *wrench basis* $\boldsymbol{B}$ to express a contact wrench in C in six dimensions, which allows the computation of the equivalent 6D contact wrench in O.

For a hard point contact model with the set of contact wrench constraints $\mathcal{C}_{\text{HP}}$, or the contact wrench model, the 6D contact wrench $\boldsymbol{c}_{\text{6D}}$ in C is

$$\boldsymbol{c}_{\text{6D}} = \boldsymbol{B}_{\text{H}} \boldsymbol{c}, \;\; \boldsymbol{c} \in \mathcal{C}_{\text{HP}} \tag{2.74}$$

where $\boldsymbol{B}_{\mathrm{H}} \in \mathbb{R}^{6\times 3}$ is the wrench basis

$$\boldsymbol{B}_{\mathrm{H}} = \begin{bmatrix} 1 & 0 & 0 \\ 0 & 1 & 0 \\ 0 & 0 & 1 \\ 0 & 0 & 0 \\ 0 & 0 & 0 \\ 0 & 0 & 0 \end{bmatrix}. \tag{2.75}$$

Since a soft contact model, including the soft point, ellipsoidal area, and quartic area contact models, transmits 4D contact wrenches, the 6D contact wrench for a soft contact in C is

$$\boldsymbol{c}_{\mathrm{6D}} = \boldsymbol{B}_{\mathrm{S}}\,\boldsymbol{c}, \quad \boldsymbol{c} \in \mathcal{C}_{\mathrm{SP}} \cup \mathcal{C}_{\mathrm{EA}} \cup \mathcal{C}_{\mathrm{QA}} \tag{2.76}$$

where the wrench basis $\boldsymbol{B}_{\mathrm{S}}$ is

$$\boldsymbol{B}_{\mathrm{S}} = \begin{bmatrix} 1 & 0 & 0 & 0 \\ 0 & 1 & 0 & 0 \\ 0 & 0 & 1 & 0 \\ 0 & 0 & 0 & 0 \\ 0 & 0 & 0 & 0 \\ 0 & 0 & 0 & 1 \end{bmatrix}. \tag{2.77}$$

2.4.2 The Grasp Map

Given the contact wrench of each of the gripper jaws, the total wrench acting on the object in the object frame O can be computed with a *grasp map*. Consider the nth contact, where $n \in \{1, \ldots, N\}$ with N being the number of contacts. For instance, $N = 2$ for a parallel jaw gripper if both jaws are in contact with the object. Let C_n denote the nth contact frame. Let $\boldsymbol{c}^{C_n}$ be the contact wrench exerted by the nth contact and computed in C_n. The goal of this part is to compute the equivalent contact wrench in the object frame O, denoted as $\boldsymbol{c}_n^O$. Let $\boldsymbol{t}_n \in \mathbb{R}^3$ and $\boldsymbol{R}_n \in \mathbb{R}^{3\times 3}$ be the translation and rotation of C_n relative to O, respectively, and let $\hat{\boldsymbol{t}}_n \in \mathbb{R}^{3\times 3}$ be the cross product matrix of $\boldsymbol{t}_n$. $\boldsymbol{c}_n^O$ is

$$\boldsymbol{c}_n^O = \begin{bmatrix} \boldsymbol{R}_n & \boldsymbol{0} \\ \hat{\boldsymbol{t}}_n \boldsymbol{R}_n & \boldsymbol{R}_n \end{bmatrix} \boldsymbol{B}_n \boldsymbol{c}^{C_n}, \quad \boldsymbol{c}^{C_n} \in \mathcal{C}_n \tag{2.78}$$

where $\boldsymbol{B}_n$ is the wrench basis and $\mathcal{C}_n$ is the contact wrench model. If the same contact model is selected for each jaw, the wrench basis for each contact is identical $\boldsymbol{B}_1 = \ldots = \boldsymbol{B}_N = \boldsymbol{B}$.

To simplify Equation (2.78), one can define the *contact map* $\boldsymbol{G}_n$ to be the linear map between the contact wrench with respect to C_n and with respect to O. $\boldsymbol{G}_n$ is defined as

$$\boldsymbol{G}_n := \begin{bmatrix} \boldsymbol{R}_n & \boldsymbol{0} \\ \hat{\boldsymbol{t}}_n \boldsymbol{R}_n & \boldsymbol{R}_n \end{bmatrix} \boldsymbol{B}_n. \tag{2.79}$$

With N jaws contacting an object, the total contact wrench $\boldsymbol{c}^O$ on the object , or also referred to as the grasp wrench, is computed by summing up the contact wrench of each jaw with respect to O. Mathematically, $\boldsymbol{c}^O$ is

$$\boldsymbol{c}^O = \boldsymbol{G}_1 \boldsymbol{c}^{C_1} +, \ldots, + \boldsymbol{G}_N \boldsymbol{c}^{C_N} = [\boldsymbol{G}_1 \ldots \boldsymbol{G}_N] \begin{bmatrix} \boldsymbol{c}^{C_1} \\ \vdots \\ \boldsymbol{c}^{C_N} \end{bmatrix}. \tag{2.80}$$

Finally, the grasp map $\boldsymbol{G}$ is defined as

$$\boldsymbol{G} := [\boldsymbol{G}_1 \ldots \boldsymbol{G}_N] \tag{2.81}$$

which maps the contact wrenches in the contact frames to $\boldsymbol{c}^O$. In summary, with $\boldsymbol{c}^{C_1}, \ldots, \boldsymbol{c}^{C_N}$ combined into a vector, denoted as $\boldsymbol{c}^C$, the total contact wrench $\boldsymbol{c}^O \in \mathbb{R}^6$ acting on the object is

$$\boldsymbol{c}^O = \boldsymbol{G}\boldsymbol{c}^C, \text{ where } \boldsymbol{c}^C = \begin{bmatrix} \boldsymbol{c}^{C_1} \\ \vdots \\ \boldsymbol{c}^{C_N} \end{bmatrix}, \boldsymbol{c}^{C_n} \in \mathcal{C}^{C_n}, n \in \{1, \ldots, N\}. \tag{2.82}$$

The grasp map $\boldsymbol{G}$ can also be considered as the function that maps the domain of $\boldsymbol{c}^C$ to the domain of $\boldsymbol{c}^O$. Let K be the dimension of $\boldsymbol{c}^C$ and let $\mathcal{K}$ be the domain of $\boldsymbol{c}^C$, which means $\mathcal{K} \subseteq \mathbb{R}^K$. For instance, for a grasp with a parallel-jaw gripper with soft point contacts, $\boldsymbol{c}^{C_1}$ and $\boldsymbol{c}^{C_2}$ are in four dimensions, respectively. Then $\mathcal{K} \subseteq \mathbb{R}^8$. To express the function mathematically, let $\mathcal{O}$ denote the domain of $\boldsymbol{c}^O$ with $\mathcal{O} \subseteq \mathbb{R}^6$ regardless which contact model is used as the total wrench that acts on an object is 6D. $\boldsymbol{G}$ is a function that maps $\mathcal{K}$ to $\mathcal{O}$

$$\boldsymbol{G} : \mathcal{K} \to \mathcal{O}. \tag{2.83}$$

The mapping can also be written as

$$\boldsymbol{G}(\mathcal{K}) = \mathcal{O}. \tag{2.84}$$

More details about the grasp map can be found in [15, pp. 219–227], [105].

Geometric Meaning of $\boldsymbol{G}$ The geometric meaning of $\boldsymbol{G}$ is briefly discussed next as many grasp quality metrics are computed directly based on $\boldsymbol{G}$. First, let $\mathcal{U}$ be a unit sphere in $\mathbb{R}^K$ with

$$\mathcal{U} = \left\{ \boldsymbol{c} \in \mathbb{R}^K \;\middle|\; \|\boldsymbol{c}\|^2 \leq 1 \right\}. \tag{2.85}$$

The mapping $\boldsymbol{G}(\mathcal{U})$ essentially maps the unit sphere in $\mathbb{R}^K$ to an ellipsoid in $\mathbb{R}^6$. The singular values of $\boldsymbol{G}$ corresponds to the radii of the ellipsoid. Li *et al.* [105] proposed two quality metrics solidly based on the singular values of $\boldsymbol{G}$, which are introduced later in Section 2.5.2.

2.4.3 The Grasp Wrench Space

Given a specific contact wrench exerted by each of the jaws, the section above introduced the computation of the total contact wrench acting on the object. However, many grasping applications require the space of all possible contact wrenches that a grasp can exert on the object as the specific wrench required to counter the external disturbance is typically unknown at the time of planning. One way to approximate this space is through the *grasp wrench space (GWS)*. Kirkpatrick *et al.* [106] and Ferrari *et al.* [14] proposed two ways to build the GWS, denoted as $\mathcal{W}_{L_\infty}$ and $\mathcal{W}_{L_1}$, respectively, depending on how the normal force magnitudes of the contacts are upper bounded.

First, $\mathcal{W}_{L_\infty}$ is introduced. By assuming that the normal force magnitudes are limited independently and individually, $\mathcal{W}_{L_\infty}$ is the Minkowski sum of the convex hull of each linearized contact wrench model. For instance, for a parallel-jaw gripper with hard point contact models, the convex hull of the linearized friction cone is the smallest convex set that contains this cone. $\mathcal{W}_{L_\infty}$ is built by adding each point of the convex set for the left jaw to each point of the set for the right jaw. Mathematically, for an N-contact grasp with M discrete points of each linearized contact wrench model, $\mathcal{W}_{L_\infty}$ is

$$\mathcal{W}_{L_\infty} = \text{Conv}\left(\left\{\boldsymbol{c}^O_{1,1}, \ldots, \boldsymbol{c}^O_{1,M}\right\}\right) \oplus \ldots \oplus \text{Conv}\left(\left\{\boldsymbol{c}^O_{N,1}, \ldots, \boldsymbol{c}^O_{N,M}\right\}\right) \tag{2.86}$$

where $\text{Conv}(\cdot)$ denotes the convex hull and $\oplus$ is the Minkowski sum operation. Since one can exchange the Minkowski sum with the convex hull operation, the equation above can be rewritten as

$$\mathcal{W}_{L_\infty} = \text{Conv}\left(\oplus_{n=1}^{N}\left\{\boldsymbol{c}^O_{n,1}, \ldots, \boldsymbol{c}^O_{n,M}\right\}\right). \tag{2.87}$$

The Minkowski sum operation outputs M^N 6D wrenches, which are the input of the convex hull operation. Therefore, the time complexity for $\mathcal{W}_{L_\infty}$ is $O\left(M^N \log\left(M^N\right)\right)$.

Another way to build the GWS is by assuming an upper bounded sum magnitude of the normal forces. For instance, for a parallel-jaw gripper whose sum magnitude is limited with 15N, if the normal force magnitude of the left jaw is 12N, the magnitude of the right jaw can be any value between 0N–3N. Intuitively, it is more likely that each jaw has similar normal force magnitude for a parallel jaw gripper in practice; therefore, the normal force of each jaw is up to 7.5N. The intuition behind this assumption is that the sum magnitude is proportional to the current in motors. Rather than limit each individual normal force, one can also limit the current or the power required to actuate the gripper. In this case, the GWS $\mathcal{W}_{L_1}$ is built by taking the union of the linearized contact wrench models, followed by passing the outcome to the convex hull operation. Mathematically, $\mathcal{W}_{L_1}$ is

$$\mathcal{W}_{L_1} = \text{Conv}\left(\cup_{n=1}^{N}\left\{\boldsymbol{c}^O_{n,1}, \ldots, \boldsymbol{c}^O_{n,M}\right\}\right). \tag{2.88}$$

The time complexity for $\mathcal{W}_{L_1}$ is $O\left(MN \log\left(MN\right)\right)$, which is much more efficient than computing $\mathcal{W}_{L_\infty}$ if $M > 2$ and $N \geq 2$. Note that $\mathcal{W}_{L_\infty} \supseteq \mathcal{W}_{L_1}$ for the same set of contact wrenches $\left\{\boldsymbol{c}^O_{n,1}, \ldots, \boldsymbol{c}^O_{n,M}\right\}$.

The next part presents a representative grasp and the corresponding $\mathcal{W}_{L_\infty}$ and $\mathcal{W}_{L_1}$. Figure 2.20(a) illustrates the front view of a grasp between a parallel-jaw gripper and a rigid

cylinder. The normal force magnitudes are $f_{\perp_1} = f_{\perp_2} = f_\perp$ and a hard point contact model is used for each contact. Let f_y^{GWS} and f_z^{GWS} be the total force that the grasp acts on the cylin-

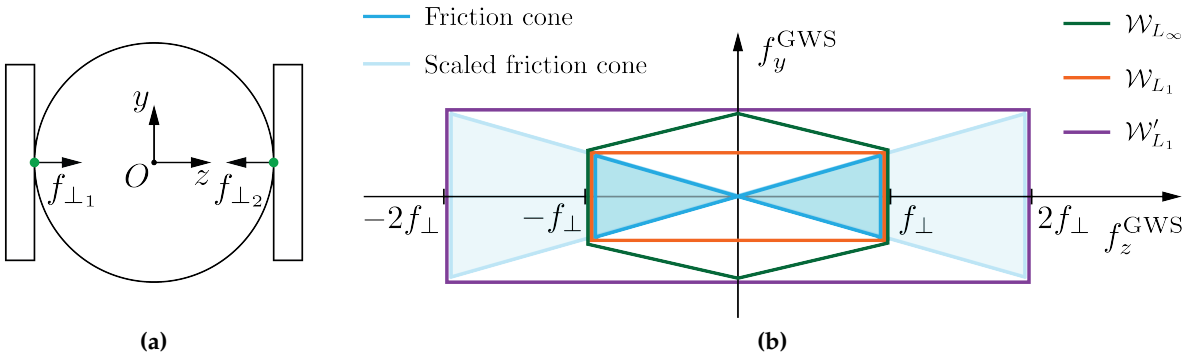

Figure 2.20: (a) The front view of a representative grasp using the hard point contact models. (b) The 2D projection of the grasp wrench spaces in the $(f_y^{\text{GWS}}, f_z^{\text{GWS}})$-space.

der along the y- and z-axis in O, respectively. Figure 2.20(b) shows the 2D projection of each friction cone (blue) in the $(f_y^{\text{GWS}}, f_z^{\text{GWS}})$-space. The outer boundary of $\mathcal{W}_{L_1}$ and $\mathcal{W}_{L_\infty}$ built from the two friction cones are depicted in orange and green, respectively. One observes that $\mathcal{W}_{L_1}$ is smaller than $\mathcal{W}_{L_\infty}$; therefore, $\mathcal{W}_{L_1}$ is potentially over-conservative. However, $\mathcal{W}_{L_1}$ is built under the assumption that the sum magnitude of the normal forces is upper bounded with $f_\perp$. Therefore, $\mathcal{W}_{L_1}$ only includes the wrenches from the normal force magnitudes of, for instance, $f_\perp$ and 0 or $0.5f_\perp$ and $0.5f_\perp$ of the left and the right jaws, respectively, whereas $\mathcal{W}_{L_\infty}$ considers the wrench caused by the magnitudes by up to $f_\perp$ and $f_\perp$ of the left and the right jaws, respectively. To also include the wrench from $f_\perp$ and $f_\perp$ for $\mathcal{W}_{L_1}$, one needs to first linearly scale each friction cone with a factor of two, which is the number of contacts, then compute the union of the scaled friction cone. Figure 2.20 (b) illustrates the scaled friction cones in shallow blue and the outer boundary of $\mathcal{W}'_{L_1}$, which is the union of the scaled friction cones, in purple. $\mathcal{W}'_{L_1}$ can also be computed by scaling $\mathcal{W}_{L_1}$. Specifically, for an N-contact grasp with each contact having the same magnitude of the normal force, $\mathcal{W}'_{L_1}$ can be computed with

$$\mathcal{W}'_{L_1} = \left\{ N \cdot \boldsymbol{c}^{\text{GWS}} \middle| \forall \boldsymbol{c}^{\text{GWS}} \in \mathcal{W}_{L_1}, \;\; f_{\perp_1} = \ldots = f_{\perp_N} \right\}. \tag{2.89}$$

Figure 2.20 (b) shows that $\mathcal{W}_{L_1} \subseteq \mathcal{W}_{L_\infty} \subseteq \mathcal{W}'_{L_1}$. While $\mathcal{W}_{L_1}$ is overly conservative, $\mathcal{W}'_{L_1}$ is too confident, since it also includes the wrench caused by the normal force magnitudes of, for instance, $2f_\perp$ and 0, where $2f_\perp$ exceeds the limit of the normal force magnitude $f_\perp$. Krug *et al.* [107] applied $\mathcal{W}_{L_\infty}$ and $\mathcal{W}_{L_1}$ to predict grasp success. The experiments suggested that assumption of the upper bounded sum magnitude for $\mathcal{W}_{L_1}$ leads to overly conservative results.

In summary, $\mathcal{W}_{L_\infty}$ better describes the space of possible wrenches that a grasp can act on the object with a drawback of high time complexity. Borst *et al.* [108] computed the convex hull incrementally to efficiently compute $\mathcal{W}_{L_\infty}$. Although $\mathcal{W}_{L_1}$ provides a less realistic estimation, it is a practical estimation for certain quality metrics, such as force closure described later in Section 2.5.

2.4.4 Unit Grasp Wrench Space

A *unit grasp wrench space* is the space of wrenches that can be applied by a grasp whose force vector has a magnitude of one. A unit grasp wrench space is commonly used to compute the grasp qualities, which are described later in Section 2.5. A unit GWS also provides computational advantages. Since the grasp wrench space linearly scales with the magnitude of the grasp force, one can precompute the unit GWS $\hat{\mathcal{W}}$ and scale it at runtime with the measured grasp force magnitude, if two conditions are satisfied.

Before introducing the conditions, one needs to define the grasp force. For an N-contact grasp, where $f_{\perp_n}$ with $n \in \{1, \dots, N\}$ is the normal force magnitude of the nth contact. The grasp force is built by piling up the normal force magnitudes

$$\boldsymbol{g} = \begin{bmatrix} f_{\perp_1} \\ \vdots \\ f_{\perp_N} \end{bmatrix}. \tag{2.90}$$

Next, one needs to define the magnitude $\|\boldsymbol{g}\|$ of the grasp force to build a unit GWS. Recall that $\mathcal{W}_{L_\infty}$ is built based on the assumption that the normal forces are independent and individually upper bounded. With this assumption, the grasp force magnitude $\|\boldsymbol{g}\|$ is defined as the L_∞ norm of $\boldsymbol{g}$ with $\|\boldsymbol{g}\| = \|\boldsymbol{g}\|_{L_\infty} = \max(f_{\perp_1}, \dots, f_{\perp_N})$. Consequently, $\hat{\mathcal{W}}_{L_\infty}$ is defined as $\mathcal{W}_{L_\infty}$ with $\|\boldsymbol{g}\|_{L_\infty} = 1$. Similarly, with the assumption that the sum magnitude of the normal forces is upper bounded, the same assumption required for $\mathcal{W}_{L_1}$, $\|\boldsymbol{g}\|$ is defined as the L_1 norm of $\boldsymbol{g}$ with $\|\boldsymbol{g}\| = \|\boldsymbol{g}\|_{L_1} = f_{\perp_1} + \ldots + f_{\perp_N}$. $\hat{\mathcal{W}}_{L_1}$ is defined as $\mathcal{W}_{L_1}$ with $\|\boldsymbol{g}\|_{L_1} = 1$.

Finally, the GWS can be computed from the unit GWS. $\mathcal{W}_{L_\infty}$ and $\mathcal{W}_{L_1}$ can be obtained by scaling $\hat{\mathcal{W}}_{L_\infty}$ and $\hat{\mathcal{W}}_{L_1}$ with the magnitude of the grasp force, respectively, under two conditions. The first condition is that the shape of the contact wrench model remains the same. This indicates that there is no relative motion between the gripper jaws and the grasped object, as well as the contact area and the shape of the pressure distribution remain the same. The second condition is that the ratio between any pair of the normal force magnitudes remains the same. For instance, given $\hat{\mathcal{W}}_{L_\infty}$ for the grasp from a parallel-jaw gripper with the normal force magnitudes 1N and 0.8N. If the measured forces of a physical grasp are, say 10N and 8N, one obtains $\mathcal{W}_{L_\infty}$ by linearly scaling $\hat{\mathcal{W}}_{L_\infty}$ with a factor of ten. However, if the measured forces are 10N and 6N, a scaled $\hat{\mathcal{W}}_{L_\infty}$ will not correctly represent $\mathcal{W}_{L_\infty}$. In summary, if both conditions are satisfied, $\mathcal{W}_{L_\infty}$ for the given $\boldsymbol{g}$ and $\hat{\mathcal{W}}_{L_\infty}$ is computed with

$$\mathcal{W}_{L_\infty} = \left\{ \|\boldsymbol{g}\| \cdot \boldsymbol{c}^{\text{GWS}} \middle| \forall \boldsymbol{c}^{\text{GWS}} \in \hat{\mathcal{W}}_{L_\infty} \right\}. \tag{2.91}$$

One can scale $\hat{\mathcal{W}}_{L_1}$ in a similar manner to obtain $\mathcal{W}_{L_1}$ and $\mathcal{W}'_{L_1}$, if the normal force of each contact has the same magnitude. In other words, for an N-contact grasp, $\mathcal{W}_{L_1}$ and $\mathcal{W}'_{L_1}$ can

be obtained by

$$\begin{aligned}\mathcal{W}_{L_1} &= \left\{ \frac{\|\boldsymbol{g}\|}{N} \cdot \boldsymbol{c}^{\text{GWS}} \middle| \forall \boldsymbol{c}^{\text{GWS}} \in \hat{\mathcal{W}}_{L_1},\ \ f_{\perp_1} = \ldots = f_{\perp_N} \right\} \\ \mathcal{W}'_{L_1} &= \left\{ \|\boldsymbol{g}\| \cdot \boldsymbol{c}^{\text{GWS}} \middle| \forall \boldsymbol{c}^{\text{GWS}} \in \hat{\mathcal{W}}_{L_1},\ \ f_{\perp_1} = \ldots = f_{\perp_N} \right\}.\end{aligned} \tag{2.92}$$

For instance, given the unit grasp wrench space $\hat{\mathcal{W}}_{L_1}$ for a two-contact grasp with the magnitude of the grasp force being $\|\boldsymbol{g}\|_{L_1} = f_{\perp_1} + f_{\perp_2} = 2f_{\perp} = 1$. If the measured normal force of each jaw is 15N, which means $\|\boldsymbol{g}\|_{L_1} = 30$, $\mathcal{W}_{L_1}$ and $\mathcal{W}'_{L_1}$ can be obtained by linearly scaling $\hat{\mathcal{W}}_{L_1}$ with a factor of 15 and 30, respectively.

2.5 Grasp Quality Metrics

The previous section presented the wrench limit that a grasp can act on the object based on the contact wrench models. This wrench limit, among other metrics, can be used to measure the grasp effectiveness [109]. Such a measure is called a *grasp quality metric*, which is an important component of robot grasp planning. A grasp quality metric is either binary, indicating if the grasp has a certain property, or a nonnegative number to quantitatively measure the grasp. There is a substantial literature on quality metrics for robot grasping with notable surveys by Rimon *et al.* [109, pp. 335–362], Roa *et al.* [110], Mishra [111], Rubert *et al.* [112], and Bicchi *et al.* [17]. This section focuses on two types of grasps and the associated metrics:

1. *Immobilizing grasps* can resist object motions in any direction by immobilizing the object with frictionless contacts. The quality metrics are based on the geometry of the grasped object (Section 2.5.1).

2. *Wrench-resistance grasps* can resist wrench disturbances by up to a certain magnitude with frictional contacts. The grasps are commonly measured by the ability of resisting external wrenches with the Coulomb friction law (Section 2.5.2 – Section 2.5.7). As some wrench-based metrics rely on the magnitudes of required grasp forces to counter the disturbance, the algorithms for grasp force optimization are also included in this thesis (Section 2.5.8).

Other common metrics include *dexterity* and *stability* [15], [110]. Dexterity means that the grasp is able to move the object in a way compatible with the desired task [113]. Before introducing the stability, consider the situation where an external disturbance is acting on the grasped object and causes a position error of the object. A grasp is stable if the object moves back to the original position when the disturbance vanishes [114], [115].

2.5.1 Metrics based on Object Geometry

This section introduces the concept of immobilizing grasps and other metrics that are extended from this concept.

Form Closure An *immobilizing grasp* [109], or a *form-closure grasp*, can resist arbitrary object motions by relying only on frictionless contacts [116]. The grasped object, which is impossible to move, is called *form closed* [117, pp. 680–682], [109, pp. 17–18]. Reuleaux [118] showed that at least four frictionless contacts are required to obtain a form-closure grasp for a planar object. Somoff [119] and Lakshminarayana [120] pointed out that seven contact are required for a 3D object. Trinkle [121] proposed a method to quickly check if the grasp has form closure and also provided a metric to measure how far a grasp is from loosing form closure. Rimon *et al.* [109] proposed the *second order immobilization*, which is extended from form closure to also include surface curvature effects. As form closure does not consider friction, it is overly conservative and potentially difficult to be satisfied in robot manipulation.

2.5.1.1 Caging

While a form-closure grasp immobilizes an object, a *caging grasp* allows the object to have a certain amount of mobility [109], [122]. Caging has been an active area with notable surveys and background by Makita *et al.* [123] and Rimon *et al.* [109]. Compared to wrench-based grasp planning, caging does not require accurate finger positions, and therefore, is less sensitive to position errors.

In a multi-finger *cage*, gripper jaws surround the rigid object to be grasped, so that the object may have some amount of mobility but can not move arbitrarily far from its original position [109], [124]. A *cage formulation* refers to the jaw placement around the object. Kuperberg [125] posed the earliest formal definition of the caging problem. Vahedi *et al.* [126] presented the concepts of squeezing and stretching cages for two-finger end-effectors. Specifically, an object is called *squeezing caged* if it remains caged when the fingers close. Rodriguez *et al.* [122] generalized the squeezing and stretching cages to arbitrary number of jaws and showed that cages can be useful waypoints to grasp polygonal objects. Allen *et al.* [124] proposed an algorithm to find all two-finger cage formulations of planar polygonal objects. Wan *et al.* [127] presented an algorithm to efficiently check whether a 2D object can be caged by fingertips or small mobile robots to transport the object. Varava *et al.* [128] applied the caging theory to both rigid and partially deformable 3D object and found caging configurations by using geometric features, such as double forks and necks. Mahler *et al.* [129] proposed an algorithm to synthesize energy-bounded cages for planar objects by finding the grasp and force-direction configuration that maximizes the energy required for the object to escape.

While caging is a promising research direction, many robot grasping applications, such as assembly, require precise object pose control; therefore, a cage grasp is less suitable for such tasks.

2.5.2 Metrics based on the Grasp Map

Staring this section, the quality metrics are based on the wrench resistance with frictional contacts. This part starts with introducing two quality metrics [105] solidly based on the grasp map.

Minimum Singular Value of $\boldsymbol{G}$ Recall that the grasp map $\boldsymbol{G}$ maps the local contact wrenches $\boldsymbol{c}^C \in \mathcal{K} \subseteq \mathbb{R}^K$ to the total contact wrench $\boldsymbol{c}^O \in \mathcal{O} \subseteq \mathbb{R}^6$ acting on the object (Section 2.4.2). If one assumes that the set $\mathcal{K}$ is the entire space $\mathbb{R}^K$, which means that there are no contact wrench constraints, $\boldsymbol{c}^O$ can be computed with

$$\boldsymbol{c}^O = \boldsymbol{G}\boldsymbol{c}^C, \text{ where } \boldsymbol{c}^C = \begin{bmatrix} \boldsymbol{c}^{C_1} \\ \vdots \\ \boldsymbol{c}^{C_N} \end{bmatrix}, \boldsymbol{c}^C \in \mathbb{R}^K, n \in \{1, \dots, N\}. \tag{2.93}$$

Denoting $\mathcal{U}$ as the K-dimensional unit sphere, $\boldsymbol{G}(\mathcal{U})$ maps the sphere to an 6D ellipsoid, whose radii are the singular values of $\boldsymbol{G}$. A full-rank $\boldsymbol{G}$ has six singular values. The smallest singular value corresponds to the weakest direction of the grasp. If a singular value goes to zero, the grasp can not resist the external disturbances in that direction. The minimum singular value (MSV) grasp quality metric q_{MSV} for the given $\boldsymbol{G}$ is denoted as

$$q_{\text{MSV}} = \sigma_{\min}(\boldsymbol{G}) \tag{2.94}$$

where $\sigma_{\min}(\boldsymbol{G})$ represents the minimum singular value of $\boldsymbol{G}$.

To also account for the contact wrench constraints, the quality metric q_{MSV} can be modified into the minimum distance of the set $\boldsymbol{G}(\mathcal{U} \cap \mathcal{K})$ to the origin of $\mathbb{R}^K$. Mathematically, let $\inf\{\mathcal{A}\}$ denote the *infimum*, or the greatest lower bound, of the set $\mathcal{A}$. The equation above can be modified into

$$q_{\text{MSV}} = \inf_{\boldsymbol{c} \in \mathbb{R}^6} \left\{ \|\boldsymbol{c}\| \;\middle|\; \boldsymbol{c} \notin G(\mathcal{U} \cap \mathcal{K}) \right\}. \tag{2.95}$$

If $\mathcal{K}$ is the entire space $\mathbb{R}^K$, the equation above is the same as the smallest singular value of $\boldsymbol{G}$. Note that q_{MSV} is a metric for the worst case analysis and does not represent the quality of the whole grasp. Furthermore, q_{MSV} is not invariant under a different selection of the torque origin.

2.5.2.1 Volume of G

To reflect the quality of the entire grasp, Li *et al.* [105] further proposed the volume of $\boldsymbol{G}$ as a quality metric. Excluding the contact wrench constraints, the metric is the volume of the ellipsoid and is computed with $4\pi/3 \cdot \prod_{i=1}^{6} r_i$, where r_i is the ith radius of the ellipsoid. Mathematically, under the assumption that $\mathcal{K}$ is $\mathbb{R}^K$, the volume-based quality metric can be computed with

$$q_{\text{VOL}} = \prod_{i=1}^{6} r_i = \prod_{i=1}^{6} \sigma_i. \tag{2.96}$$

If one also considers the contact wrench constraints, the metric is modified into

$$q_{\text{VOL}} = \int_{\boldsymbol{G}(\mathcal{U} \cap \mathcal{K})} \mathrm{d}v. \tag{2.97}$$

Although the volume is invariant to the selection of torque origin, it does not reflect the ability of the grasp in resisting disturbances in any direction. Therefore, q_{VOL} is commonly

combined with other metrics. For instance, one can first find all grasp candidates that can resist the expected disturbances during the manipulation, then obtain the optimal grasp candidate with the maximal volume. The following section introduces the methods to examine if a grasp can resist a specific disturbance wrench.

2.5.3 Metrics based on Object Static Equilibrium

Equilibrium analysis is a foundation of wrench-based quality metrics. Assuming that an object is initially at rest, *static equilibrium* means that the static forces and torques acting on the object sum to zero [88, pp. 128–130]. In other words, the object is *in equilibrium* if the total grasp wrench acting on the object can counter the external disturbance $\boldsymbol{w}_{\text{ext}} \in \mathbb{R}^6$

$$\boldsymbol{G}\boldsymbol{c}^C + \boldsymbol{w}_{\text{ext}} = \boldsymbol{0} \text{ with } \boldsymbol{c}^C = \begin{bmatrix} \boldsymbol{c}^{C_1} \\ \vdots \\ \boldsymbol{c}^{C_N} \end{bmatrix}, \text{where} \boldsymbol{c}^{C_n} \in \mathcal{C}^{C_n}, n \in \{1, \dots, N\} \tag{2.98}$$

where $\boldsymbol{0}$ is a 6×1 zero vector. The grasps that balance opposing external wrenches and hold the object in equilibrium are called *equilibrium grasps* [109, pp. 70–73].

Static equilibrium is a common metric to predict binary grasp success. If the total grasp wrench can counter the expected disturbance during the manipulation, the grasp is considered as a success; a failure otherwise. While Hauser *et al.* [130] proposed an efficient algorithm to evaluate static equilibrium with adhesive contacts and anisotropic friction, the majority of research in robot grasping analyzed the equilibrium problem by assuming isotropic (Coulomb) friction, which is also the focus of this thesis. The following part presents two commonly used methods to solve the equilibrium problem with isotropic friction: using a grasp wrench space and solving a quadratic program.

2.5.3.1 GWS-based Method

Given the grasp wrench space $\mathcal{W}$ and the external disturbance $\boldsymbol{w}_{\text{ext}}$, the grasp is predicted as a success if the opposite wrench $-\boldsymbol{w}_{\text{ext}}$ is inside of $\mathcal{W}$. Mathematically, given $\mathcal{W}$ with N_{G} facets, denoting $\hat{\boldsymbol{n}}_i \in \mathbb{R}^6$ as the outward normal of the ith facet with $i \in \{1, \dots, N_{\text{G}}\}$, denoting $\boldsymbol{a}_i \in \mathbb{R}^6$ as a point in the hyperplane of the facet, the prediction y is

$$y = \begin{cases} 1 & \text{if } -\boldsymbol{w}_{\text{ext}}^T \hat{\boldsymbol{n}}_i < \boldsymbol{a}_i^T \hat{\boldsymbol{n}}_i, \forall i \in \{1, \dots, N_{\text{G}}\} \\ 0 & \text{otherwise.} \end{cases} \tag{2.99}$$

2.5.3.2 Solving a Quadratic Program

A grasp wrench space either requires high computational effort or is potentially less realistic in estimating grasp wrench limits. Therefore, grasp analysis is also commonly formulated as a quadratic program (QP). The goal is to find a set of contact wrenches, one contact wrench per jaw, that satisfies static equilibrium and the contact wrench constraints.

For a given external wrench $\boldsymbol{w}_{\text{ext}}$ and the grasp matrix $\boldsymbol{G}$, Mahler *et al.* [131] and Danielczuk *et al.* [5] setup the following quadratic program to estimate the success of a grasp

$$\begin{aligned} \underset{\boldsymbol{c}^C}{\text{minimize}} \quad & \epsilon = \|\boldsymbol{G}\boldsymbol{c}^C + \boldsymbol{w}_{\text{ext}}\|^2 \\ \text{subject to} \quad & \boldsymbol{c}^C = \left[\left(\boldsymbol{c}^{C_1}\right)^T, \ldots, \left(\boldsymbol{c}^{C_N}\right)^T\right]^T \\ & \boldsymbol{c}^{C_n} \in \mathcal{C}^{C_n}, n \in \{1, \ldots, N\}. \end{aligned} \tag{2.100}$$

If the error ϵ is larger than a threshold, it is considered that no solution is found. More variations of the optimization problem are introduced in Section 2.5.8, which also presents algorithms for grasp force optimization, while satisfying static equilibrium and contact wrench constraints.

Based on the static equilibrium, Mahler *et al.* [131] further proposed the *robust wrench resistance metric* for a vertical lifting task in applications, such as bin-picking and pick-and-place. The metric describes the probability of grasp success under perturbations in friction, object pose, gripper pose, and external wrenches, to account for uncertainties in sensing and actuation. First, let $\boldsymbol{x}$ be the state describing the object's properties, such as geometry and material, and let $\boldsymbol{u}$ denote a grasp. Grasp success is described with a binary reward function R, where $R = 1$ if the grasp lifts the object and $R = 0$ otherwise. The robust wrench resistance metric for $\boldsymbol{x}$ and $\boldsymbol{u}$ is a *grasp reliability distribution* $Q(\boldsymbol{x}, \boldsymbol{u})$, where $Q(\boldsymbol{x}, \boldsymbol{u}) = P(R|\boldsymbol{x}, \boldsymbol{u})$ describes the probability of grasp success for $\boldsymbol{x}$ and $\boldsymbol{u}$. In practice, the robust wrench resistance metric q_{robust}, which approximates the distribution $Q(\boldsymbol{x}, \boldsymbol{u})$, is first computed by taking K samples in simulated environments by perturbing object pose, mass, and frictional properties and compute the grasp success using Equation (2.100) for each sample. Then q_{robust} is computed with the mean of grasp successes of K samples

$$Q(\boldsymbol{x}, \boldsymbol{u}) \approx q_{\text{robust}} = \frac{1}{K} \sum_{i=1}^{K} R_i \text{ with } R_i \in \{0, 1\}. \tag{2.101}$$

For instance, given $\boldsymbol{x}$ and $\boldsymbol{u}$, the binary grasp success R_i with $i \in \{1, \ldots, K\}$ is computed in simulation for $K = 10$ times, where each time the grasp pose and object material, such as friction efficient, are slightly different by sampling them within a range. If six out of ten grasps succeeded, $q_{\text{robust}} = 0.6$ for $\boldsymbol{x}$ and $\boldsymbol{u}$. The robust wrench resistance metric is applied in three physical experiments of this thesis (Section 4.1.4, Section 4.2, Section 4.3) to predict grasp success and to plan grasps.

2.5.4 Force Closure

While an equilibrium grasp can resist a specific disturbance wrench, a *force-closure grasp* can counter external disturbances in all directions [105], [15, pp. 223–233]. In other words, assuming the magnitudes of the normal forces are unconstrained, a grasp has *force closure* if given an arbitrary external wrench $\boldsymbol{w}^*_{\text{ext}} \in \mathbb{R}^6$ acting on the object, there exist contact wrenches $\boldsymbol{c}^C \in \mathcal{K}$ such that

$$G\boldsymbol{c}^C = -\boldsymbol{w}^*_{\text{ext}}. \tag{2.102}$$

A formal definition and proof of a force-closure grasp are given in [15, pp. 223–224] and [109, pp. 316–317].

One way to determine if a grasp has force closure is based on the convexity of the contact wrench models. Consider a grasp with the grasp map $\boldsymbol{G}$ associated with the contact wrench domain $\mathcal{K} \subseteq \mathbb{R}^K$, the grasp has force closure if there exists an ϵ-sphere at the origin of $\mathbb{R}^6$ with $\epsilon > 0$ such that

$$\mathcal{O}_\epsilon \subset \boldsymbol{G}\left(\mathcal{K} \cap \mathcal{U}\right). \tag{2.103}$$

This is equivalent of saying that the possible wrenches that the grasp can act on the object has a magnitude of at least ϵ in every direction while satisfying the contact wrench constraints. If such a sphere does not exist, the grasp can not resist the external wrench in at least one direction.

In a similar manner, one can determine the force closure property for a grasp based on its grasp wrench space $\mathcal{W}$. A grasp has force closure if there exists an ϵ-sphere located at the origin of $\mathbb{R}^6$ with $\epsilon > 0$ such that

$$\mathcal{O}_\epsilon \subset \mathcal{W}. \tag{2.104}$$

Since checking the force closure does not require an accurate estimation of the grasp wrench limits, the grasp wrench space $\mathcal{W}_{L_1}$ built by upper bounding the sum magnitude of grasp forces is preferred for its computational efficiency.

From a geometric point of view, Nguyen [132] showed that a two-point-contact grasp in two dimensions, or a planar grasp, with a hard point contact model has force closure if and only if the line connecting the contact points is inside both friction cones. Similarly, a two-point-contact grasp in three dimensions with a soft point contact model has force-closure if and only if the line connecting the contact points is inside of both friction cones. Han *et al.* [98] formulated force closure problem as an optimization problem with linear matrix inequalities without linearizing the contact wrench models, such as friction cones.

Force closure is perhaps the most widely used grasp quality metric. While an object in the 3D space requires seven contacts for form closure, only two contacts with different contact normals and soft point contact models are required for force closure, and three noncolinear contacts with hard point contact models are needed [117]. Therefore, force closure is a more realistic metric and can be easier satisfied in robot manipulation compared to the form closure metric. However, force closure does not quantify the quality of a grasp. Furthermore, due to unconstrained normal force magnitudes, the actual required grasp force to resist a small disturbance can be unrealistically large, or even exceed the upper limit that the end-effector can provide.

2.5.5 Metrics based on the Grasp Wrench Space

The following metrics quantify the grasp quality and are computed from the GWS.

The *ϵ-metric* is one of the most used wrench-based metrics that quantify the grasp quality. It represents the largest disturbance in any direction in the wrench space that the grasp can counter; therefore, it represents the largest lower bound on the magnitude of the external disturbance that the grasp can resist regardless of the direction of the disturbance. Recall

that $\hat{\mathcal{W}}_{L_\infty}$ denotes the unit GWS built by upper bounding the magnitudes of the normal forces individually. Kirkpatrick *et al.* [106] proposed the ϵ-metric, which is the radius of the largest sphere centered at the origin and can be contained in $\hat{\mathcal{W}}_{L_\infty}$. Ferrari *et al.* [14] proposed another variant of the ϵ-metric, where ϵ is the minimal distance from the origin to the nearest facet of $\hat{\mathcal{W}}_{L_1}$, the unit GWS built by upper bounding the sum magnitude of the normal forces. ϵ is also the radius of the largest sphere centered at the origin and just contained in $\hat{\mathcal{W}}_{L_1}$. Zheng [133] proposed an algorithm to efficiently compute the ϵ values of $\mathcal{W}_{L_\infty}$ and $\mathcal{W}_{L_1}$ without calculating the Minkowski sum for $\mathcal{W}_{L_\infty}$.

One potential drawback of the ϵ-metric is that it depends on the reference system to compute the torque. Teichmann [134] proposed the largest ϵ value with respect to all possible choices of the reference system, which is potentially computationally expensive. Miller *et al.* [135] proposed the volume of the grasp wrench space. However, a GWS with high volume can be a non-force-closure grasp. Mirtich *et al.* [136] decoupled forces and torques from the wrenches and first compute a set of grasps that are ideal to resist pure force disturbances, followed by selecting grasps that best counter pure torques from the set. Borst *et al.* [137] discussed the advantages and potential drawbacks of the GWS-based metrics with representative grasps.

2.5.6 Metrics based on Manipulation Tasks

Task-oriented grasp quality metrics are well-suited for specific tasks with prior knowledge such as known external disturbances. A common task representation is a *task wrench space (TWS)*, which describes expected disturbance wrenches during the manipulation and is commonly modeled as a wrench or a set of possible wrenches that will be imposed on an object during a task [137], [138]. If the TWS is modeled as a single disturbance wrench, the grasp quality is commonly measured with the minimal force required for a task [139], [140] or minimal coefficient of friction [141]. Markenscoff *et al.* [139] minimized the sum magnitude of the normal forces required to counter any unit force acting on the object center of mass. Boyd *et al.* [142] efficiently computed the minimal grasp force by formulating a semidefinite program. Kruger *et al.* [143] proposed the *partial closure grasps*, which consider the ability of the grasp to counter the disturbance in certain directions. Specifically, the authors proposed two quality metrics: the maximum magnitude and the sum magnitude of the normal forces that are required to counter a unit wrench disturbance acting on the object for a specific task. Haschke *et al.* [144] presented two representations of a TWS: an external wrench and a *task wrench cone*. The authors used convex optimization to solve for the maximal magnitude of the wrench in the task direction that a grasp with unit contact forces can resist. The frictional constraints are described with the linear matrix inequalities proposed by Buss *et al.* [97]. If the TWS is described with a set of disturbance wrenches, Li *et al.* [105] approximated the TWS with a 6D ellipsoid and proposed the grasp quality as the maximum scale of the TWS such that it remains within the GWS. Lin *et al.* [145] observed that some disturbance wrenches happen more often than others during task execution and selected the grasp whose corresponding GWS covers most frequent disturbances.

In addition to counter the expected wrench disturbances during a task, the grasp planner

proposed by Holladay *et al.* [146] also considers force and motion constraints for tool use applications. Lin *et al.* [147] selected the grasp, which additionally minimizes the required motion effort of the end effector to fulfill a certain task.

Other work considers the object geometry while planning task-directed grasps based on the concept of *object wrench space (OWS)* proposed by Pollard [138]. The OWS is a space that contains any wrench created by a set of disturbance forces acting on the object surface. Note that the OWS is the union of all possible grasp wrench spaces of the grasps on the object. As computing the OWS is nearly infeasible, many works proposed modifications or approximations of the OWS. Strandberg *et al.* [148] proposed a method that is suitable for the scenarios where a single disturbance force is acting on the object. Since the torque caused by the force can be quickly computed, Strandberg *et al.* excluded the torque component of a disturbance wrench and represented the possible disturbances as a closed surface $\mathcal{S}$ in the 3D force space. By sweeping a unit disturbance force, say $\boldsymbol{e}$, over the object surface, one obtains the magnitude of the force $\|\boldsymbol{f}_{\text{ext}}\|$ such that the wrench caused by $\boldsymbol{f}_{\text{ext}} = \|\boldsymbol{f}_{\text{ext}}\|\boldsymbol{e}$ can be just countered by the grasp with unit normal forces. The surface $\mathcal{S}$ can be obtained by repeating the process with the disturbance force in every direction. In the testing phase, a grasp with unit normal forces can resist the external disturbance if the disturbance force is inside of $\mathcal{S}$. If the manipulation task is known, one can remove object vertices that are unlikely to have disturbances during the task for the sweeping step. For instance, when writing with a pencil, the disturbance force is likely coming from the tip of the pen; therefore, the vertices on the upper part of the pen can be removed. While the algorithm considers both object geometry and task information, the computational cost is still expensive due to the sweeping procedure. Borst *et al.* [137] proposed a modified OWS and approximated it with an ellipsoid for efficiency. Specifically, if the disturbances during the task are unknown, the modified OWS is a space that combines the OWS from [138] with the wrench space that is produced by the forces acting on the object center of mass in any direction. The quality metric is the largest scaling factor of the ellipsoid such that it just fit into the GWS. However, the ellipsoid may not well approximate the OWS for asymmetric objects, as pointed out in [149]. Therefore, Jeong *et al.* [149] proposed another modified OWS, which is generated by disturbance forces only in the directions of surface normals. This is equivalent of assuming no friction on the surface, which is realistic for objects consisting of materials with low friction coefficients.

Information about a manipulation task can also be represented as semantic grasp constraints, suggested by Dang *et al.* [150]. For instance, a grasp on the top of a cup is not suitable for a pouring task if it blocks the content. Song *et al.* [151] used *stay-out zones* to describe such semantic constraints. Specifically, Song *et al.* used *Dex-Net as a service* [152] to plan robust task-directed grasps given stay-out zones for a target object with a known mesh and a desired grasp wrench given by the user through an intuitive user interface. The stay-out zones prevent contacts that hinder the task, while the desired wrench counter the expected external disturbance during the task. The disturbance can be the object gravity for a lifting task.

Other work focuses on generalizing example task-specific grasps to new target objects. Pollard [153] proposed an algorithm to generalize a grasp prototype, which is an example

grasp computed offline for the task, to a set of grasps that are suitable for a new target object for the same task. Aleotti *et al.* [154] used human example grasps and collected the wrenches imposed on the object with a haptic glove in virtual reality. The convex hull of these wrenches are called the *functional wrench space (FWS)*. The quality of a candidate grasp for the target object is computed by comparing the GWS of the grasp and the FWS; the quality is high if the GWS and the FWS are close, which means the distance between the two spaces is low.

2.5.7 Metrics for Deformable Objects

So far, the previous parts discussed the quality metrics for rigid objects. However, manipulating deformable objects is an active area, with applications such as food handling [155], fabric manipulation [156], [157], and elastic rod manipulation [158]; a notable survey can be found in [159] by Sanchez *et al.* This section summarizes metrics that are either generalized from metrics for rigid objects or based on the frictional contact models.

Recall that a frictionless grasp that immobilizes a rigid object is called a form-closure grasp. Gopalakrishnan *et al.* [160] generalized this concept to holding deformable objects with frictionless contacts, where a grasp is defined as deform closure when positive work is required to release the object. Wakamatsu *et al.* [161] introduced the bounded force closure metric to grasp deformable objects, which guarantees a force closure grasp under a maximal allowable external force. Delgado *et al.* [162] reduced object deformation for a holding task by computing the maximum allowed force to be exerted on an object. Jia *et al.* [163] proposed a grasping strategy to squeeze deformable planar objects based on work performed by the jaws. When two jaws squeeze and immobilize an object, and a third jaw tries to break the grasp by pushing the object, the strategy selects the translations of the two pushing jaws that minimize the required work to balance the object. Lin *et al.* [76] addressed the problem of lifting a deformable object based on an object mesh model and jaw positions. An FEM formulation computes the object deformation based on the jaw displacements. The object will be lifted if the majority of the contact points are sticking. Similarly, Zaidi *et al.* [164] used FEM simulations to manipulate objects with large deformations, such as objects made of foam or rubber. Alt *et al.* [8] also used the FEM simulations and heuristics to plan grasps for deformable hollow objects, such as plastic cups and bottles.

2.5.8 Grasp Force Optimization

As many quality metrics for the wrench-resistance grasps are computed based on the magnitudes of the grasp forces, this sections introduces the techniques to find the optimal set of grasp forces. Let an object be held by a grasp, represented as the grasp matrix $\boldsymbol{G}$ associated with the contact wrench constraints, against the external wrench disturbance $\boldsymbol{w}_{\text{ext}}$. The *grasp force optimization problem* seeks to find the minimal magnitude of the contact forces to hold the object in equilibrium without violating any contact wrench constraints. There are two common ways to compute the optimal grasp forces depending on the inputs of the problem: using a grasp wrench space or solving a convex optimization problem.

If the grasp wrench space is given, Zheng *et al.* [165] proposed two efficient ray shooting algorithms to compute the minimal required grasp force and the minimum friction coefficient to counter a known external wrench, respectively.

As the grasp wrench space is either less accurate or computationally expensive to build, it is common to formulate a convex optimization problem to compute the optimal forces. Kerr *et al.* [166] used the linear programming (LP) with linearized friction cone constraints to find the optimal grasp that is furthest from violating any constraints. Liu [167] minimized the L_1 norm of the grasp forces by formulating a ray-shooting problem, which is equivalent to an LP problem having inequality constraints only. Cheng *et al.* [168] proposed the compact-dual LP method to efficiently solve for optimal grasp forces. Note that the dual problem of an LP is often used to compute a lower bound of the primal (original) minimization problem; or an upper bound for a maximization problem. If the dual problem has the *strong duality* property, the optimal solutions for the primal and the dual problems are equal. One of the key ideas in [168] is to solve the dual of the primal LP problem to improve efficiency. This is based on the observation that the runtime of an LP largely depends on the number of constraints. Consider a linear program that has n variables and λ constraints; its dual problem has λ variables and n constraints. Since a force optimization problem typically has more constraints than variables to be solved, depending on how well the frictional constraints are approximated, solving the dual problem largely reduces the number of constraints, and therefore, decreases runtime.

As linearized contact wrench constraints are potentially less accurate due to the approximation, Buss *et al.* [97] formulated a semidefinite program (SDP) by casting the constraints into linear matrix inequalities (LMIs) without approximating the frictional constraints. Buss *et al.* [169] further improved the optimization efficiency by using Dikin-type algorithms. In addition to the contact wrench constraints, Han *et al.* [98] and Lippiello *et al.* [170] also considered the joint torque limits of the robot hand while planning grasps. Lobo *et al.* [171] and Han *et al.* [98] formulated the force optimization problem as a second-order cone program (SOCP). Boyd *et al.* [142] proposed a custom interior-point algorithm to solve such an SOCP, which is more efficient than generic SDP and SOCP algorithms. Since the LMI-based convex optimization is a foundation of many work in grasp force optimization, the following section introduces the LMI-based optimization setup based on [97] and [98].

2.5.8.1 LMI-based Semidefinite Programming

As described in Section 2.3.5.1, the contact wrench constraints can be transformed into the positive (semi)definiteness of a certain matrix $\boldsymbol{P}$ described with Equation (2.45), (2.56), and (2.64) for the hard point contact, the linearized ellipsoid, and the axis-aligned ellipsoidal planar area contact model, respectively. The following equations use the hard point contact as a representative model, but are also suitable for the remaining contact models. Recall that

$\boldsymbol{P}_{\text{HP}}$ is defined as

$$\boldsymbol{P}_{\text{HP}} = \begin{bmatrix} \mu f_\perp & 0 & f_x \\ 0 & \mu f_\perp & f_y \\ f_x & f_y & \mu f_\perp \end{bmatrix} \succeq 0. \tag{2.105}$$

Consider an N-contact grasp. For instance, $N = 5$ for a humanoid hand. Let $\boldsymbol{P}_n$ with $n \in \{1, \ldots, N\}$ denote the matrix that describes the contact wrench constraints of the nth jaw. The matrices $\boldsymbol{P}_1, \ldots, \boldsymbol{P}_N$ can be combined into into one matrix $\boldsymbol{P}$ with

$$\boldsymbol{P} = \text{Blockdiag}\left(\boldsymbol{P}_1, \ldots, \boldsymbol{P}_N\right) \succeq 0, \;\; n \in \{1, \ldots, N\}. \tag{2.106}$$

The matrix $\boldsymbol{P}$ is positive semidefinite if and only if each block $\boldsymbol{P}_n$ is positive semidefinite. In other words, the contact wrench constraints of each jaw are ensured by enforcing positive semidefiniteness of $\boldsymbol{P}$.

Note that additional linear constraints for $\boldsymbol{P}$ are required to ensure that $\boldsymbol{P}$ is symmetric and certain elements of $\boldsymbol{P}$ equal specific values. For instance, $\boldsymbol{P}_{1,2} = \boldsymbol{P}_{2,1} = 0$ for the hard point contact model. Han *et al.* [98] expressed $\boldsymbol{P}_i$ as the sum of certain symmetric matrices since $\boldsymbol{P}_n$ is linear and symmetric in the components of the contact wrench $\boldsymbol{c}_n \in \mathbb{R}^{K_n}$. For the hard point contact model, $K_n = 3$ and $\boldsymbol{c}_n = [f_{n,x}, f_{n,y}, f_{n,\perp}]^T = [c_{n,1}, c_{n,2}, c_{n,3}]^T$, where the notations $c_{n,1}, c_{n,2} \ldots$ are used to express $\boldsymbol{c}_n$ in the following.

To formally express $\boldsymbol{P}_n$, let $c_{n,j}$ with $j \in \{1, \ldots, K_n\}$ denote the jth component of the nth contact wrench $\boldsymbol{c}_n$. Let $\boldsymbol{S}_{n,j}$ be the symmetric coefficient matrix associated with $c_{n,j}$. Then the matrix $\boldsymbol{P}_n$ of the nth contact is

$$\boldsymbol{P}_n = \sum_{j=1}^{K_n} c_{n,j} \boldsymbol{S}_{n,j}. \tag{2.107}$$

Before expressing $\boldsymbol{S}_{n,j}$, let $\boldsymbol{E}^a_{b,c} = \left(\boldsymbol{E}^a_{c,b}\right)^T$ be the matrix of dimension $a \times a$ with the element (b, c) being 1, while the remaining elements are zero. For instance, $\boldsymbol{E}^3_{1,2}$ represents

$$\boldsymbol{E}^3_{1,2} = \begin{bmatrix} 0 & 1 & 0 \\ 0 & 0 & 0 \\ 0 & 0 & 0 \end{bmatrix}.$$

The coefficient matrices $\boldsymbol{S}_{n,j}$ can be conveniently expressed as the sum of matrices of the form $\boldsymbol{E}^a_{b,c}$. For instance, the matrices $\boldsymbol{S}_{n,1}, \ldots, \boldsymbol{S}_{n,K_n}$ of the nth hard point contact are

$$\begin{aligned} \boldsymbol{S}_{n,1} &= \boldsymbol{E}^3_{1,3} + \boldsymbol{E}^3_{3,1} \\ \boldsymbol{S}_{n,2} &= \boldsymbol{E}^3_{2,3} + \boldsymbol{E}^3_{3,2} \\ \boldsymbol{S}_{n,3} &= \mu \left(\boldsymbol{E}^3_{1,1} + \boldsymbol{E}^3_{2,2} + \boldsymbol{E}^3_{3,3}\right). \end{aligned}$$

The next step is to write the block diagonal matrix $\boldsymbol{P}$ as a single linear matrix inequality. Recall that the contact wrench vector $\boldsymbol{c}^C \in \mathbb{R}^K$ is defined as $\boldsymbol{c}^C = \left[\boldsymbol{c}_1^T, \ldots, \boldsymbol{c}_N^T\right]^T =$

$[c_1, \ldots, c_K]^T$. If the contact models of a grasp are the same, then $K = N \cdot K_n$. For instance, $K = 15$ for a humanoid robot hand with $N = 5$ and a hard point contact model with $K_n = 3$. The matrix $\boldsymbol{P}$ as a function of $\boldsymbol{c}^C$ can be expressed with the following linear matrix inequality

$$\boldsymbol{P}\left(\boldsymbol{c}^C\right) = \sum_{l=1}^{K} c_l \boldsymbol{S}_l \succeq 0 \tag{2.108}$$

where the double-indexed $c_{n,j}$ is simplified to c_l, which is the lth component of $\boldsymbol{c}^C$. The associated lth symmetric coefficient matrix $\boldsymbol{S}_l = \text{Blockdiag}\left(0, \ldots, 0, \boldsymbol{S}_{n,j}, 0, \ldots, 0\right)$. Equation (2.108) represents the contact wrench constraints of all N contacts. One can also write the torque limit constraints in a similar form, as described in [98].

The next step is to setup the optimization to find the feasible contact wrench vector that satisfies the static equilibrium $\boldsymbol{G}\boldsymbol{c}^C + \boldsymbol{w}_{\text{ext}} = 0$. If minimizing the magnitude of the normal forces is the only objective, the program may push the contact wrench toward the friction limit, which potentially leads to a non-robust grasp due to the uncertainties in contact information, such as the friction coefficient. Such problem can be addressed by adding a penalty term, or a barrier function, to the objective function. This part first defines a vector $\boldsymbol{\sigma} = [\boldsymbol{\sigma}_1, \ldots, \boldsymbol{\sigma}_n, \ldots, \boldsymbol{\sigma}_N] \in \mathbb{R}^K$ to weight the normal force components of the contact wrench $\boldsymbol{c}^C$. For instance, $\boldsymbol{\sigma}_n = [0, 0, \sigma_n]^T$ for the nth hard point contact with the weight $\sigma_n > 0$. Han *et al.* [98] set up the optimization as

$$\begin{aligned} \underset{\boldsymbol{c}^C}{\text{minimize}} \quad & \boldsymbol{\sigma}^T \boldsymbol{c}^C - \log\det\left(\boldsymbol{P}\right) \\ \text{subject to} \quad & \boldsymbol{G}\boldsymbol{c}^C + \boldsymbol{w}_{\text{ext}} = 0 \\ & \boldsymbol{P}\left(\boldsymbol{c}^C\right) = \sum_{l=1}^{K} c_l \boldsymbol{S}_l \succeq 0. \end{aligned} \tag{2.109}$$

The first part of the objective function $\boldsymbol{\sigma}^T \boldsymbol{c}^C$ minimizes the weighted sum of the normal forces. The second part $-\log\det\left(\boldsymbol{P}\right) = \log\det\left(\boldsymbol{P}^{-1}\right)$, where log prevents computing the inverse of $\boldsymbol{P}$, is the barrier term and is toward infinity if the determinant of $\boldsymbol{P}$ tends to zero, which happens if the contact wrench solution is near the friction limit. Buss *et al.* [97] further proposed the smallest eigenvalue of $\boldsymbol{P}$ as a grasp quality metric, since it indicates how far is the grasp from the contact wrench limits. Helmke *et al.* [172] introduced a more compact formulation of the LMIs, where the shape of the matrix $\boldsymbol{P}_{\text{HP}}$ is reduced to 2×2.

2.5.8.2 Second-order Cone Programming (SOCP)

While the LMI-based convex optimization can be efficiently solved with traditional interior-point methods in polynomial time, specifically, $O(N^3)$ with N being the number of contacts, Boyd *et al.* [142] proposed a custom interior-point algorithm that has $O(N)$ time complexity and solves the force optimization problem in only 400 μs with $N = 5$, as opposed to 100 ms required by the LMI-based method. Boyd *et al.* [142] used the hard point contact model but the algorithm is also suitable for other models, such as the ellipsoidal planar area contact model. The following part gives a high level summary of the algorithm presented in [142].

Recall that the set of feasible contact wrenches for the nth hard point contact is

$$\mathcal{C}_n = \left\{ \boldsymbol{c}_n = [c_{n,1}, c_{n,2}, c_{n,3}]^T \;\middle|\; \|[c_{n,1}, c_{n,2}]^T\| = \sqrt{c_{n,1}^2 + c_{n,2}^2} \leq \mu \cdot c_{n,3}, \;\; n \in \{1, \ldots, N\} \right\}.$$

Let $F_{\max}$ be the maximal magnitude of the N contact wrenches with

$$\begin{aligned} F_{\max} = \;& \max\left\{\|\boldsymbol{c}_1\|, \ldots, \|\boldsymbol{c}_N\|\right\} \\ = \;& \max_{n \in \{1,\ldots,N\}} \sqrt{c_{n,1}^2 + c_{n,2}^2 + c_{n,3}^2}. \end{aligned} \tag{2.110}$$

To find the optimal contact wrench vector $\boldsymbol{c}^C = \left[\boldsymbol{c}_1^T, \ldots, \boldsymbol{c}_N^T\right]^T$, Boyd *et al.* [142] set up the optimization as

$$\begin{aligned} \underset{\boldsymbol{c}^C}{\text{minimize}} \quad & F_{\max} \\ \text{subject to} \quad & \boldsymbol{c}_n \in \mathcal{C}_n \\ & \boldsymbol{G}\boldsymbol{c}^C + \boldsymbol{w}_{\text{ext}} = 0. \end{aligned} \tag{2.111}$$

Note that this objective function minimizes the maximal magnitude of the contact wrenches, including the normal and the frictional force components, but the algorithm also works with other objectives such as minimizing the maximal magnitude of the normal forces only.

Equation (2.111) can be expressed in a conic form, or an SOCP, by introduction an additional scalar variable F that limits the magnitude of the contact wrenches

$$\sqrt{c_{n,1}^2 + c_{n,2}^2 + c_{n,3}^2} \leq F. \tag{2.112}$$

Then the SOCP has the form

$$\begin{aligned} \underset{\boldsymbol{c}^C}{\text{minimize}} \quad & F \\ \text{subject to} \quad & \boldsymbol{c}_n \in \mathcal{C}_n \\ & \boldsymbol{G}\boldsymbol{c}^C + \boldsymbol{w}_{\text{ext}} = 0 \\ & \sqrt{c_{n,1}^2 + c_{n,2}^2 + c_{n,3}^2} \leq F. \end{aligned} \tag{2.113}$$

The custom interior-point algorithm starts with defining a barrier subproblem. Let ϕ be a *log barrier* for the cone constraints with

$$\phi\left(\boldsymbol{c}^C, F\right) = \sum_{n=1}^{N} \phi_n\left(\boldsymbol{c}_n, F\right) \tag{2.114}$$

where

$$\begin{aligned} \phi_n\left(\boldsymbol{c}_n, F\right) = & -\log\left(F^2 - c_{n,1}^2 - c_{n,2}^2 - c_{n,3}^2\right) \\ & -\log\left(\mu^2 \cdot c_{n,3}^2 - c_{n,1}^2 - c_{n,2}^2\right) \end{aligned} \tag{2.115}$$

Let $t > 0$ be a parameter, the barrier subproblem, a variation of Equation (2.113), is defined as

$$\begin{aligned} \underset{\boldsymbol{c}^C}{\text{minimize}} \quad & tF + \phi\left(\boldsymbol{c}^C, F\right) \\ \text{subject to} \quad & \boldsymbol{G}\boldsymbol{c}^C + \boldsymbol{w}_{\text{ext}} = 0. \end{aligned} \tag{2.116}$$

The algorithm uses Newton's method to iteratively solve the barrier subproblem above for a fixed value of the parameter t. Once a feasible solution of $\boldsymbol{c}^C$ is obtained at a Newton step, the current maximal magnitude of the contact wrenches F_{max} will be computed from $\boldsymbol{c}^C$. Then F_{dual}, the current lower bound of F_{max}, is also computed by solving a dual problem of Equation (2.111). Finally, the algorithm terminates when the difference between F_{max} and F_{dual} is smaller than a predefined threshold.

2.6 Grasp Planners

The contact models and grasp quality metrics discussed in the previous sections can be applied to grasp planning, which addresses the problem of finding the optimal grasp pose for an object. There are three types of grasp planners: analytical, empirical, and hybrid planners.

Section 2.3 – Section 2.5 serve as a foundation of the analytical grasp planners, which assume known object physical properties, such as geometry and mass. Analytical grasp planners have wide applications since the physics underlying these models are universal [33]. A representative analytical grasp planning algorithm is illustrated in Figure 1.2(b). In the training phase, a common pipeline starts with sampling grasp candidates on a 3D object mesh, then computes the quality of each candidate in simulation. A substantial body of the quality metrics are based on the grasp robustness computed from the frictional contact models. At the test phase, the planner estimates the 6D pose of the object [116], retrieves the ranked grasps from the dataset, and executes the highest-quality grasp that is reachable by the gripper and collision free. While analytical methods are able to efficiently evaluate a large number of grasps on known objects and work well in controlled environments, it is less realistic to assume that a perception system can provide accurate estimations of object properties [31], [33], [34].

On the other hand, empirical approaches do not require specific object information and learn grasp quality functions purely from data, which can be human labeled [45] or collected automatically by the robot by trial and error [42], [43]. While the empirical methods achieve robust performance given sufficiently large number of data, the learned models may not perform well if used in the applications, where the test data are outside of the training data distribution [33]. Therefore, applying the pretrained model to another setting, such as different objects, grippers, or sensors, the training dataset may need to be recollected, which is potentially expensive. Furthermore, it is more difficult to diagnose failures in empirical approaches compared to analytical methods. For instance, Mahler [31] pointed out that if an empirical-based grasp planner fails to manipulate a novel object, the reasons can be wrong labels of the similar examples in the training dataset; a changed setting, such as lightning conditions; or not sufficient training data.

As the third type, a hybrid grasp planner combines the advantages of analytical and empirical methods. State-of-the-art hybrid methods [36], [173]–[175] use analytical approaches to efficiently create a scalable grasp dataset and apply empirical methods to train on the dataset. Therefore, a hybrid grasp planner generalizes well and is robust to uncertainties in perception and actuation. To create a grasp dataset, existing grasp planners either used

simulators [35], [176], [177], such as Flex and Pybullet, or computed the grasp qualities using the traditional frictional contact models and the quality metrics [36], [90], [173]–[175] introduced in Section 2.3.5 and Section 2.5, respectively. However, these methods are not suitable for grasp datasets with deformable gripper jaws, since it is nearly computationally infeasible to simulate deformable contacts for a largescale dataset. Furthermore, traditional frictional contact models assume a point or planar contact area; therefore, they are too conservative for deformable gripper jaws, which create nonplanar surface contacts. To address this issue, building on Dex-Net and Grasp Quality Convolutional Neural Network (GQ-CNN) proposed by Mahler *et al.* [90], this thesis presents a hybrid grasp planner in Section 4.2, which is trained on a grasp dataset using the proposed nonplanar surface contact models, introduced later in Chapter 3. As the foundation of the proposed grasp planner, Dex-Net and GQ-CNN are introduced in the following.

2.6.1 Dex-Net and Grasp Quality Convolutional Neural Network

This section presents three main components of a state-of-the-art hybrid grasp planner, Dex-Net, GQ-CNN, and cross entropy method (CEM)-based grasp sampler. As illustrated in Figure 2.21, the policy to find the best physical grasp works as follows: given a real depth image, grasp candidates are first sampled using the CEM. Next, each grasp candidate associated with a small cropped depth image is feed into GQ-CNN, which outputs the grasp quality. Finally, the policy returns the grasp with the highest quality.

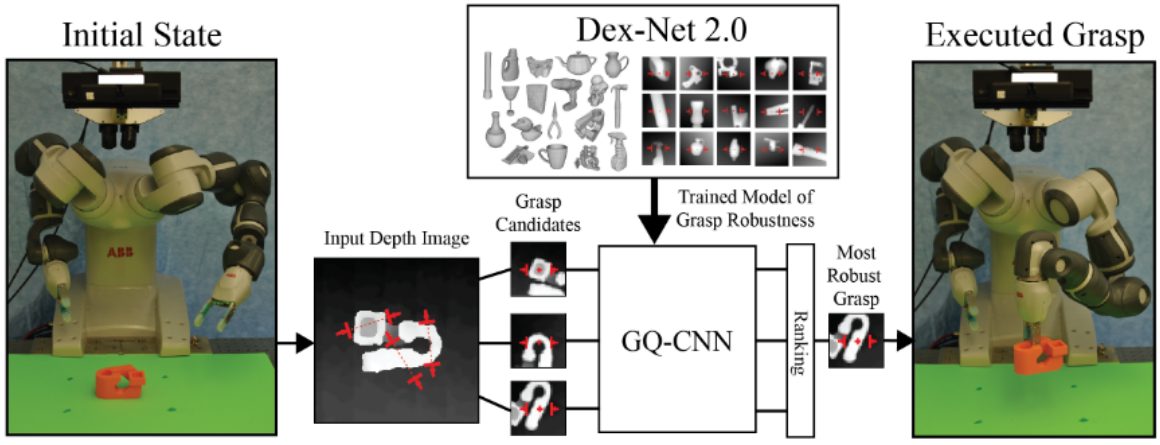

Figure 2.21: Pipeline of the Dex-Net grasp planner (adapted from [90] ©2018 RSS).

GQ-CNN is trained on Dex-Net, which is a dataset of 3D object models associated with analytical grasp metrics computed with the soft point contact model (Section 2.3.5.2). There are four versions of Dex-Net so far, where Dex-Net 2.0 [89] plans grasps for a parallel-jaw gripper, while Dex-Net 4.0 [36] is suitable for an ambidextrous robot mounted with a suction cup and a parallel-jaw gripper. Dex-Net 2.0 uses the ϵ-quality metric (Section 2.5.5), while Dex-Net 4.0 uses the wrench resistance (Section 2.5.3.2) to evaluate a grasp, as the latter is applied in bin-picking scenarios and considers the gravity of the grasped object as the external disturbance. For each grasp, multiple synthetic depth images are rendered by sampling

the pose of a virtual depth camera. Figure 2.22 depicts a grasp in simulation and two associated depth images by sampling the camera pose. Each synthetic depth image is cropped and rotated, so that the grasp is centered at the image center and the grasp axis is aligned with the horizontal axis of the depth image, as shown in Figure 2.22(b). Note that the gripper in Figure 2.22(a) is used to illustrate the grasp and is not visible when rendering the depth images. A dataset of grasp candidates are used to train GQ-CNN, whose architecture is shown in Figure 2.23. Each grasp candidate is represented with a pair of the aligned depth image and the grasp depth to the camera.

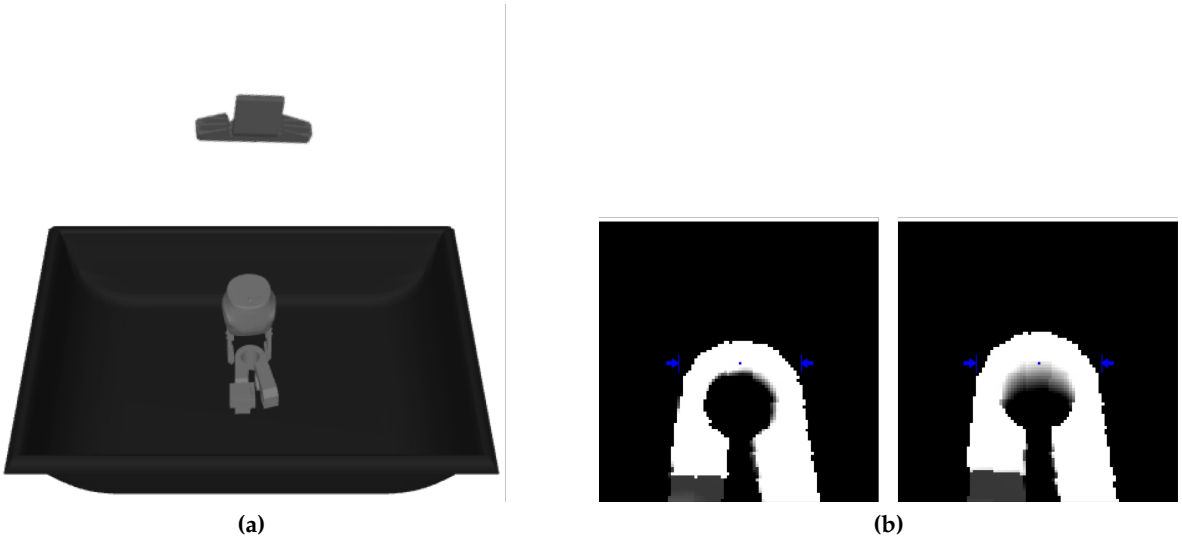

(a) (b)

Figure 2.22: A representative grasp in simulation and the corresponding synthetic depth images generated by sampling virtual camera poses.

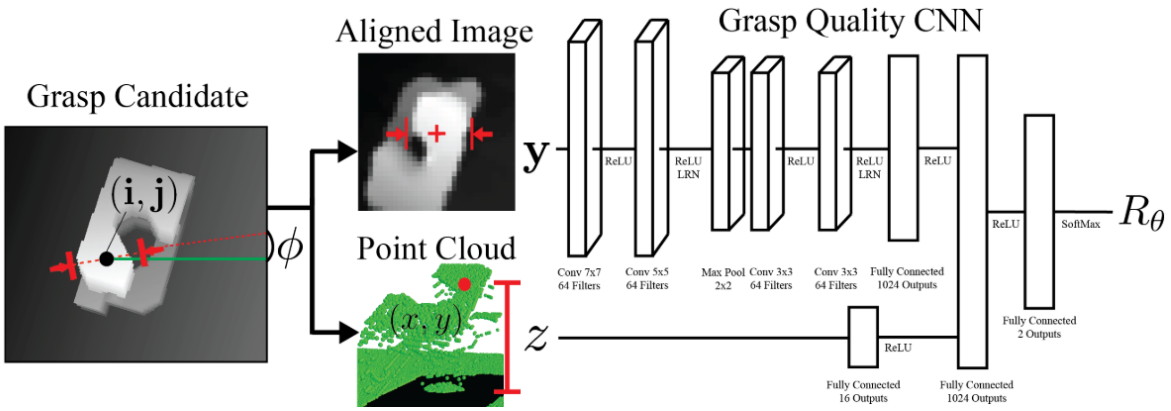

Figure 2.23: The architecture of GQ-CNN (adapted from [90] ©2018 RSS).

At the test phase, a CEM-based sampler is used to sample grasp candidates from the physical depth image. The CEM method models the distribution of good grasp candidates using a Gaussuan Mixutre Model and optimizes the candidates by iteratively resampling grasps and updating the distribution. Specifically, in the first iteration, the CEM method samples antipodal grasps and obtain the quality of each grasp by feeding it to GQ-CNN.

On the next iteration, the region with high quality grasps is sampled more densely and the distribution is updated for the next iteration. Mahler *et al.* [90] proposed the CEM sampler with three iterations, which is a good balance between the quality of grasp candidates and computational efficiency.

2.7 Chapter Summary

This chapter provided the most relevant background and related work for grasp analysis and grasp planning. Specifically, the chapter first introduced recent work in perception system (Section 2.1) and gripper designs (Section 2.2), which are two important components for a grasping system. Next, the foundation of a grasp planner, which is the third key component to improve grasp success, were thoroughly introduced. Specifically, Section 2.3 described the required steps to find the wrench constraints of a contact using the existing frictional contact models. Next, Section 2.4 introduced the method to combine the contact wrench limits of each contact of a grasp, so that one can compute the possible total contact wrenches that a grasp can exert on the object. Section 2.5 provided a detailed review and discussion of grasp quality metrics from different aspects, such as the object geometry, the ability to resist wrench disturbances, and the manipulation tasks. Section 2.6 discussed existing grasp planners and presented Dex-Net [36], [90], a state-of-the-art hybrid grasp planner, which is the foundation of the proposed planner for deformable gripper jaws.

While existing work either assumes a planar contact area or decomposes the surface into planar elements, it is unclear how to model the contact wrench limits that a deformable gripper jaw can exert on the object via the nonplanar surface contact. Inspired from existing work in modeling planar frictional area contacts, the next chapter presents frictional contact models for nonplanar surface contacts and efficient low-dimensional representations to approximate the models.

Chapter 3

Modeling Nonplanar Frictional Surface Contacts

The last chapter presented the traditional frictional contact models and their applications in grasp analysis and grasp planning by assuming either a point or a planar area contact. However, the traditional models are less realistic for nonplanar surface contacts caused by deformable gripper jaws contacting an object with nonplanar local geometry. Figure 3.1 shows two representative nonplanar surface contacts. Such a contact transmits a frictional wrench

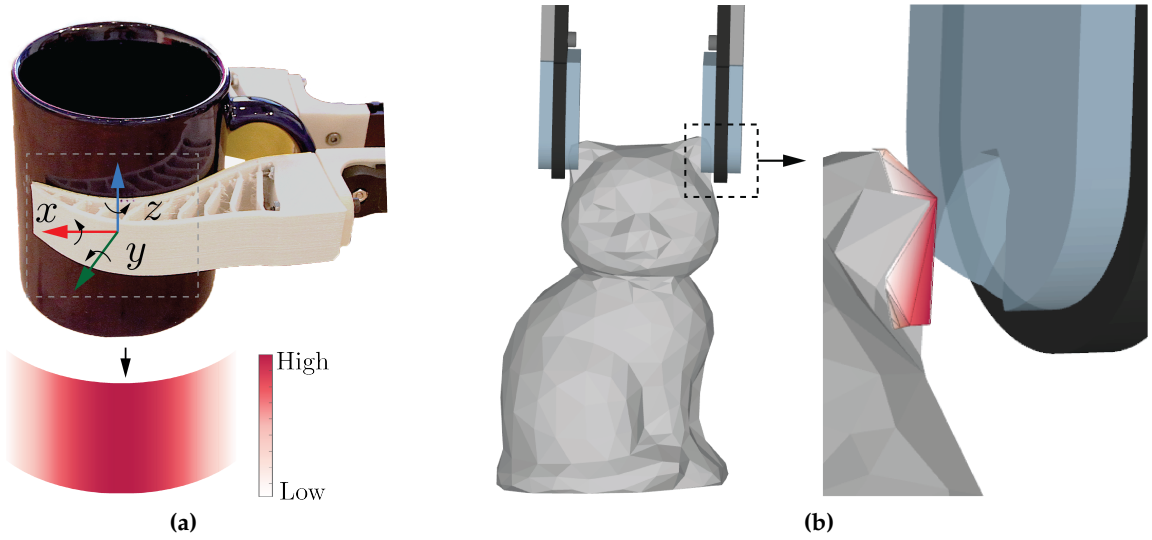

Figure 3.1: (a) A representative nonplanar surface contact is created when (a) a soft parallel-jaw gripper deforms to a rigid cup (adapted from [1] ©2021 IEEE); (b) a compliant gripper jaw surface contacts a nonplanar object's surface (adapted from [3] ©2020 IEEE). The redder colors of the nonplanar contact surface represent higher pressure.

in six dimensions, whereas a planar area contact transmits a 3D frictional wrench, resulting in overly conservative frictional wrench estimations. To address this issue, this chapter proposes frictional contact models that describe the 6D frictional wrenches for a nonplanar surface contact. In particular, Section 3.1 presents the problem to be addressed in this chapter and the assumptions required for the proposed models. Section 3.2 introduces the frictional

wrench computation for a given contact profile and an object motion. As the object motion is typically unknown at the time of planning, Section 3.3 presents the 6D limit surface models to approximate all possible frictional wrenches that can be transmitted through a nonplanar surface contact by sampling the motion space. Section 3.4 introduces the contact wrench model by combining the proposed limit surface models and the normal wrench of a contact. By extending this contact wrench model, Section 3.4 further presents the *6D friction cone* concept to approximate the contact wrench limit with unknown grasp forces. Section 3.5 presents the experiments in simulation to evaluate the proposed 6D limit surface models.

Parts of the work presented in this chapter have been published in [1], [3].

3.1 Problem statement

Given a contact surface and a pressure distribution, this chapter introduces two geometric models to approximate the 6D limit surface (6DLS), which is a surface that bounds the set of all possible 6D frictional wrenches that a deformable gripper jaw can exert on the object via the nonplanar surface contact. Based on the 6DLS model, this chapter further studies the contact wrench model that approximates the contact wrench limit of a nonplanar surface contact.

The following assumptions are required to compute the limit surface and the contact wrench model:

1. Coulomb friction with a known constant friction coefficient;
2. The contact profile, including the contact surface and the pressure distribution, or their estimations are known. A contact profile can be captured by a tactile sensor [24], [26] or estimated by a contact model [80].

3.2 Contact Wrench for a Nonplanar Surface Contact

A 6D contact wrench consists of a normal and a frictional wrench. While the former only depends on the contact profile, the latter also depends on the relative motion between the grasped object and the gripper jaw. As the contact wrench is computed in a local contact frame, the following section first introduces the selection of the local contact frame. This section further presents the computation of the normal wrench and the frictional wrench that resists an object motion in the 3D space. The contact wrench computation is generalized from a planar area contact (Section 2.3.3.3).

3.2.1 Local Contact Frame

To illustrate the object frame O and the local contact frame C, a representative contact is shown in Figure 3.2. Specifically, Figure 3.2(a) shows a representative grasped object (cup) with a nonplanar local geometry. The gray surface is the extracted contact surface between the object and a deformable gripper jaw and its enlarged view is shown in Figure 3.2(b). A common selection of the origin of O is the center of mass (COM) of the cup.

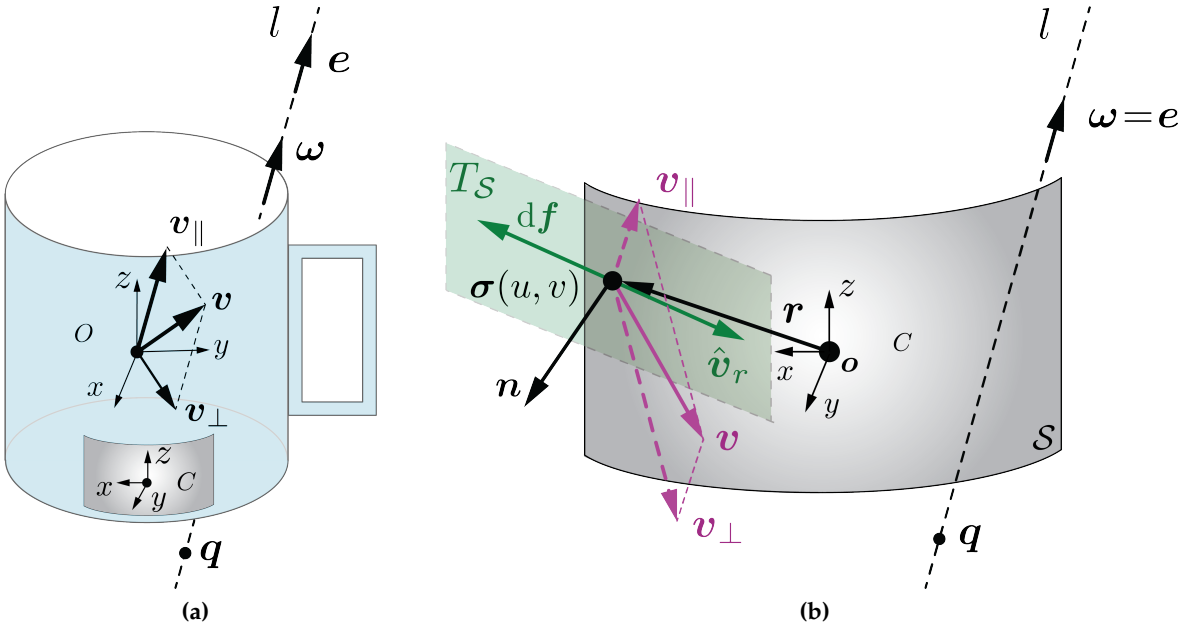

Figure 3.2: (a) Instantaneous motion of a grasped object (cup) described with the instantaneous screw axis l and the pitch h. (b) Enlarged view of the nonplanar contact surface $\mathcal{S}$ and the local frictional force $\mathrm{d}\boldsymbol{f}$ at a representative point on $\mathcal{S}$ given l and h. The figure is adapted from [1] ©2021 IEEE.

Next, the local contact frame C needs to be defined. As the contact wrench is computed with respect to the contact pressure center $\boldsymbol{o}$, let C be a rectilinear coordinate system, whose origin is located at $\boldsymbol{o}$ and axes are arbitrarily chosen. To compute $\boldsymbol{o}$, let p denote the pressure distribution and let $\mathcal{S}$ be the contact surface, whose parametric form is $\boldsymbol{\sigma}(u, v)$ with $(u, v) \in \mathbb{R}^2$ being the parameters. The pressure center $\boldsymbol{o}$ is

$$\boldsymbol{o} = \begin{bmatrix} o_x \\ o_y \\ o_z \end{bmatrix} = \frac{\int_{\mathcal{S}} p(u, v) \cdot \boldsymbol{\sigma}(u, v)\, \mathrm{d}\mathcal{S}}{\int_{\mathcal{S}} p(u, v)\, \mathrm{d}\mathcal{S}} \tag{3.1}$$

where the integral of a 3D vector function is defined as three individual integrals of each component. Note that $\boldsymbol{o}$ may not be on the contact surface.

3.2.2 Normal Wrench

Next, the contact wrench, which consists of a normal wrench and a frictional wrench, can be computed with respect to the pressure center $\boldsymbol{o}$. In this thesis, the *normal wrench* $\boldsymbol{w}_\perp$ is defined as the wrench impressed by the pressure distribution p with respect to $\boldsymbol{o}$. $\boldsymbol{w}_\perp$ is obtained by integrating the local normal force $\mathrm{d}\boldsymbol{f}_\perp$ and torque $\mathrm{d}\boldsymbol{\tau}_\perp$ at each point on the contact surface $\mathcal{S}$

$$\boldsymbol{w}_\perp = \begin{bmatrix} \boldsymbol{f}_\perp \\ \boldsymbol{\tau}_\perp \end{bmatrix} = \begin{bmatrix} -\int_{\mathcal{S}} p(u, v) \cdot \boldsymbol{n}(u, v)\, \mathrm{d}\mathcal{S} \\ -\int_{\mathcal{S}} p(u, v) \cdot [\boldsymbol{r}(u, v) \times \boldsymbol{n}(u, v)]\, \mathrm{d}\mathcal{S} \end{bmatrix} \tag{3.2}$$

where $\boldsymbol{r} = \boldsymbol{\sigma}(u, v) - \boldsymbol{o}$ is the torque arm, $\boldsymbol{n} = \boldsymbol{\sigma}_u \times \boldsymbol{\sigma}_v / \|\boldsymbol{\sigma}_u \times \boldsymbol{\sigma}_v\|$ is the surface normal, and $\mathrm{d}\mathcal{S} = \|\boldsymbol{\sigma}_u \times \boldsymbol{\sigma}_v\| \,\mathrm{d}u \,\mathrm{d}v$ is the area of an infinitesimally small piece of $\mathcal{S}$. $\boldsymbol{f}_\perp$ and $\boldsymbol{\tau}_\perp$ are the normal force and torque impressed by the pressure acting on the object, respectively. The minus sign comes from the fact that the force acting on the object is towards the object, whereas the normal vector $\boldsymbol{n}$ points outward, away from the object. In contrast to the frictional wrench, which depends on the unit twist, $\boldsymbol{w}_\perp$ is uniquely defined by $\mathcal{S}$ and p.

Next, consider the concept *sum magnitude of the local normal forces* F with $F = \int_{\mathcal{S}} p \,\mathrm{d}\mathcal{S}$. Note that $F = \|\boldsymbol{f}_\perp\|$ for a planar area contact, whereas $F > \|\boldsymbol{f}_\perp\|$ for the representative contact surface depicted in Figure 3.2(b) with an axially symmetrical pressure distribution. This is due to the fact that the integral of $\mathrm{d}f_{\perp,x}$ over the left half surface cancels the integral of $\mathrm{d}f_{\perp,x}$ over the right half surface. The sum magnitude F can be used to compute the normalized pressure distribution $\hat{p} = p/F$ so that $\int_{\mathcal{S}} \hat{p} \,\mathrm{d}\mathcal{S} = 1$. $\boldsymbol{w}_\perp$ can be used to construct the grasp wrench space.

3.2.3 Frictional Wrench for a Parametric Nonplanar Surface

While the normal wrench only depends on the contact profile, the frictional wrench also depends on the relative motion between the object and the gripper jaw. Given the object motion described as the unit twist $\hat{\boldsymbol{\xi}}$ (Section 2.3.2.2), the following section provides the computation of the linear velocity of the object at a point on the contact surface and the direction of the relative velocity between the object and the jaw at this point.

Recall that given an instantaneous screw axis (ISA), the linear velocity $\boldsymbol{v} \in \mathbb{R}^3$ at a point can be represented as the sum of a velocity parallel to the ISA and a velocity perpendicular to the ISA, denoted as $\boldsymbol{v}_\parallel$ and $\boldsymbol{v}_\perp$, respectively. Consider the example in Figure 3.2. Given a representative ISA (l) illustrated as a dashed line, Figure 3.2(a) depicts the linear velocity at O of the cup.

The next step is to compute the linear velocity of a point on the contact surface. Figure 3.2(b) shows a representative contact surface. Similar to computing the linear velocity component in Equation (2.30), given the Plücker coordinates $(\boldsymbol{e}, \boldsymbol{m})$ of the ISA and the scalar pitch h, the linear velocity $\boldsymbol{v}$ at a point on the contact surface is

$$\boldsymbol{v}(u, v) = \begin{cases} h\boldsymbol{e} + \boldsymbol{m} - \boldsymbol{\sigma}(u, v) \times \boldsymbol{e} & \text{if } \|\boldsymbol{\omega}\| \neq 0 \\ \boldsymbol{e} & \text{if } \|\boldsymbol{\omega}\| = 0. \end{cases} \tag{3.3}$$

Given l and h, Figure 3.2(b) illustrates the linear velocity $\boldsymbol{v}$, which is the sum of $\boldsymbol{v}_\parallel$ and $\boldsymbol{v}_\perp$, at a representative point on $\mathcal{S}$ as a pink vector.

The direction vector $\hat{\boldsymbol{v}}_r$ of relative velocity at a point depends on the velocity of the gripper jaw and the object in contact, and should be tangential to $\mathcal{S}$ at this point. Since the gripper jaw is static after the grasp and prior to the manipulation, $\hat{\boldsymbol{v}}_r$ can be computed by projecting the linear velocity $\boldsymbol{v}$ of the grasped object at a point onto the tangent plane of $\mathcal{S}$ at that point. Figure 3.2(b) illustrates $\hat{\boldsymbol{v}}_r$ as a green vector, which is parallel to the projection of $\boldsymbol{v}$ in the tangent plane $T_{\mathcal{S}}$, depicted as a green parallelogram. Let $\boldsymbol{\sigma}_u$, $\boldsymbol{\sigma}_v$ be the first-order derivatives of $\boldsymbol{\sigma}(u, v)$ with respect to u and v, respectively. The surface normal of $T_{\mathcal{S}}$ is

$\boldsymbol{n} = \boldsymbol{\sigma}_u \times \boldsymbol{\sigma}_v / \|\boldsymbol{\sigma}_u \times \boldsymbol{\sigma}_v\|$. The direction vector $\hat{\boldsymbol{v}}_r(u,v)$ of relative velocity is

$$\hat{\boldsymbol{v}}_r(u,v) = \frac{\left(\boldsymbol{I} - \boldsymbol{n}(u,v)\,\boldsymbol{n}(u,v)^T\right)\,\boldsymbol{v}(u,v)}{\|\left(\boldsymbol{I} - \boldsymbol{n}(u,v)\,\boldsymbol{n}(u,v)^T\right)\,\boldsymbol{v}(u,v)\|} \tag{3.4}$$

where $\boldsymbol{I}$ is a 3×3 identity matrix.

The local frictional force $\mathrm{d}f$ at a point is antiparallel to $\boldsymbol{v}_r$ and is computed with $\mathrm{d}f = -\mu \cdot p \cdot \boldsymbol{v}_r \,\mathrm{d}\mathcal{S}$, where $\mathrm{d}\mathcal{S} = \|\boldsymbol{\sigma}_u \times \boldsymbol{\sigma}_v\| \,\mathrm{d}u\,\mathrm{d}v$ is the area of an infinitesimally small piece of $\mathcal{S}$. The local frictional torque is $\mathrm{d}\boldsymbol{\tau} = \boldsymbol{r} \times \mathrm{d}\boldsymbol{f}$, where $\boldsymbol{r} = \boldsymbol{\sigma}\,(u,v) - \boldsymbol{o}$ is the torque arm. By integrating $\mathrm{d}f$ and $\mathrm{d}\boldsymbol{\tau}$ over $\mathcal{S}$, the frictional wrench $\boldsymbol{w}$ of the contact surface acting on the object is

$$\boldsymbol{w} = \begin{bmatrix} f \\ \boldsymbol{\tau} \end{bmatrix} = \begin{bmatrix} -\mu \int_{\mathcal{S}} p\,(u,v) \cdot \hat{\boldsymbol{v}}_r(u,v)\,\mathrm{d}\mathcal{S} \\ -\mu \int_{\mathcal{S}} p\,(u,v) \cdot [\boldsymbol{r}\,(u,v) \times \hat{\boldsymbol{v}}_r(u,v)]\,\mathrm{d}\mathcal{S} \end{bmatrix}. \tag{3.5}$$

3.2.4 Frictional Wrench for a Discrete Nonplanar Surface

Computing $\boldsymbol{w}$ for a parametric surface can be inefficient because of the integral operation. Therefore, the following part introduces the frictional wrench computation for a discrete surface with convex polygonal elements. The method is also beneficial for a surface whose parametric form is nontrivial to determine.

Consider a discrete surface consisting of N_s convex polygonal elements. Given a unit twist described with $(\boldsymbol{e}, \boldsymbol{m}, h)$, also given the center $\boldsymbol{c}_i$ and the normal $\boldsymbol{n}_i$ of the ith element with $i \in \{1, \ldots, N_s\}$, one obtains the direction vector $\hat{\boldsymbol{v}}_{r_i}$ of relative velocity at $\boldsymbol{c}_i$ with

$$\begin{aligned} \boldsymbol{v}_i &= \begin{cases} h\boldsymbol{e} + \boldsymbol{m} - \boldsymbol{c}_i \times \boldsymbol{e} & \text{if } \|\boldsymbol{\omega}\| \neq 0 \\ \boldsymbol{e} & \text{if } \|\boldsymbol{\omega}\| = 0 \end{cases} \\ \hat{\boldsymbol{v}}_{r_i} &= \frac{\left(\boldsymbol{I} - \boldsymbol{n}_i \boldsymbol{n}_i^T\right)\,\boldsymbol{v}_i}{\|\left(\boldsymbol{I} - \boldsymbol{n}_i \boldsymbol{n}_i^T\right)\,\boldsymbol{v}_i\|}. \end{aligned} \tag{3.6}$$

Denoting p_i and a_i as the pressure and the area of the ith element, respectively, the pressure center $\boldsymbol{o}$ of the surface is

$$\boldsymbol{o} = \begin{bmatrix} o_x \\ o_y \\ o_z \end{bmatrix} = \frac{\sum_{i=1}^{N_s} \boldsymbol{c}_i \cdot p_i \cdot a_i}{\sum_{i=1}^{N_s} p_i \cdot a_i}. \tag{3.7}$$

The frictional force and torque of the discrete surface are

$$\begin{aligned} \boldsymbol{f} &= -\mu \sum_{i=1}^{N_s} p_i \cdot a_i \cdot \hat{\boldsymbol{v}}_{r_i} \\ \boldsymbol{\tau} &= -\mu \sum_{i=1}^{N_s} p_i \cdot a_i \cdot [(\boldsymbol{c}_i - \boldsymbol{o}) \times \hat{\boldsymbol{v}}_{r_i}]. \end{aligned} \tag{3.8}$$

3.2.5 Example of Contact Wrench Computation for a Parametric Nonplanar Surface

This section shows an example of the contact wrench computation for the representative contact surface shown in Figure 3.2. The units of the parameters are listed as follows:

1. parametric form $\boldsymbol{\sigma}$ of the contact surface: meters (m)
2. pressure distribution p: Newtons (N)/m^2
3. normalized pressure distribution $\hat{p}$: $1/\mathrm{m}^2$
4. friction coefficient μ: unitless
5. pressure center $\boldsymbol{o}$: m
6. frictional force $\boldsymbol{f}$ and normal force $\boldsymbol{f}_\perp$: N
7. torque arm $\boldsymbol{r}$: m
8. frictional torque $\boldsymbol{\tau}$ and normal torque $\boldsymbol{\tau}_\perp$: N·m
9. sum magnitude of local normal forces F: N
10. linear velocity $\boldsymbol{v}$: meters per second (m/s)
11. $\boldsymbol{e}$ of the Plücker coordinates for a unit twist: unitless
12. $\boldsymbol{m}$ of the Plücker coordinates for a unit twist: m
13. scalar pitch h for a unit twist: meters per radians (m/rad)

The units are omitted from now on.

Consider an elliptical cylinder with the parametric form $\boldsymbol{\sigma}^O(u,v) = [0.02\cos u, 0.02\sin u, v]^T, u \in [0.25\pi, 0.75\pi], v \in [-0.05, -0.03]$ in the object frame O. The unit of $\boldsymbol{\sigma}^O(u,v)$ is Given the uniform pressure distribution $p = 10^3$ and the friction coefficient $\mu = 0.3$ as inputs, one first computes the contact wrench with respect to the friction center in the local contact frame C. The frictional wrenches in C do not depend on the jaw position relative to the object COM; therefore, can be precomputed and reused.

As the origin of C is located at the pressure center $\boldsymbol{o}^O$, one needs to determine $\boldsymbol{o}^O$ in the object frame. If the origin of C is not located at $\boldsymbol{o}^O$, one can first compute the equivalent contact wrenches with respect to the origin of C, before transforming the wrenches to O. With $\boldsymbol{\sigma}^O(u,v)$, p, and $\mathrm{d}\mathcal{S} = \|\boldsymbol{\sigma}_u^O \times \boldsymbol{\sigma}_v^O\| \,\mathrm{d}u\,\mathrm{d}v = 0.02\,\mathrm{d}u\,\mathrm{d}v$, $\boldsymbol{o}^O$ is computed using Equation (3.1)

$$\begin{aligned}\boldsymbol{o}^O &= \frac{\int_{-0.05}^{-0.03}\int_{0.25\pi}^{0.75\pi} 10^3 \,[0.02\cos u, 0.02\sin u, v]^T \, 0.02\,\mathrm{d}u\,\mathrm{d}v}{\int_{-0.05}^{-0.03}\int_{0.25\pi}^{0.75\pi} 10^3 \cdot 0.02\,\mathrm{d}u\,\mathrm{d}v} \\ &\approx [0, 0.018, -0.04]^T.\end{aligned}$$

The local contact frame C is obtained by shifting O by $[0, 0.018, -0.04]^T$. The parametric form in C is $\boldsymbol{\sigma}(u,v) = [0.02\cos u, 0.02\sin u, v]^T - [0, 0.018, -0.04]^T$, where the ranges of u and

v remain unchanged. The superscript C is omitted for the variables in the following part as the wrenches are all in the local contact frame C.

3.2.5.1 Normal Wrench

The normal wrench $\boldsymbol{w}_\perp$ in C is computed by substituting $\mathrm{d}\mathcal{S} = \|\boldsymbol{\sigma}_u \times \boldsymbol{\sigma}_v\| \,\mathrm{d}u \,\mathrm{d}v = 0.02 \,\mathrm{d}u \,\mathrm{d}v$, $\boldsymbol{n}(u,v) = \boldsymbol{\sigma}_u \times \boldsymbol{\sigma}_v / \|\boldsymbol{\sigma}_u \times \boldsymbol{\sigma}_v\| = [\cos u, \sin u, 0]^T$, $p = 10^3$, and $\boldsymbol{r}(u,v) = \boldsymbol{\sigma}(u,v) - \boldsymbol{o}$ into Equation (3.2). Finally, one obtains $\boldsymbol{w}_\perp = \left[\boldsymbol{f}_\perp^T, \boldsymbol{\tau}_\perp^T\right]^T \approx [0, -0.5657, 0, 0, 0, 0]^T$. The sum magnitude of local normal forces is $F = \int_{\mathcal{S}} p \,\mathrm{d}\mathcal{S} \approx 0.6283 > \|\boldsymbol{f}_\perp\|$. The normalized pressure distribution is $\hat{p} = p/F \approx 1592$.

3.2.5.2 Frictional Wrench

In addition to the contact profile, the frictional wrench $\boldsymbol{w}$ also depends on μ and the unit twist. Given $\mu = 0.3$ and a unit twist described with $\boldsymbol{e} = [0, -1, 0]^T$, $\boldsymbol{m} = [0, 0, 0]^T$, and $h = 0$, which is a pure rotation around the negative y-axis, $\boldsymbol{w}$ is computed in the following for the same contact profile.

First, the linear velocity of the object is computed by substituting $\boldsymbol{e}, \boldsymbol{m}, \boldsymbol{\sigma}, h$ into Equation (3.3) and one obtains $\boldsymbol{v}(u,v) = [-v - 0.04, 0, 0.02 \cos u]^T$. Next, the direction vector $\hat{\boldsymbol{v}}_r(u,v)$ of the relative velocity is obtained by substituting $\boldsymbol{v}(u,v)$, $\boldsymbol{n}(u,v)$ into Equation (3.4). $\hat{\boldsymbol{v}}_r(u,v)$ is

$$\hat{\boldsymbol{v}}_r(u,v) = \frac{\left[-\sin^2 u(v+0.04), \sin u \cos u(v+0.04), 0.02 \cos u\right]^T}{\sqrt{\sin^2 u(v+0.04)^2 + (0.02 \cos u)^2}}.$$

Finally, the frictional wrench $\boldsymbol{w}$ is computed by substituting μ, p, $\hat{\boldsymbol{v}}_r(u,v)$, $\mathrm{d}\mathcal{S}$, and $\boldsymbol{r}(u,v)$ into Equation (3.5) and one obtains $\boldsymbol{w} \approx [0, 0, 0, 0, 0.0018, 0]^T$. The local frictional force direction vectors for the representative unit twist are shown in Figure 3.3(a).

3.3 Six-dimensional Limit Surface Model

In the previous section, the frictional wrench of a nonplanar surface contact is computed for a given unit twist of the grasped object. The following section defines a 6D limit surface (Section 3.3.1), which models all possible frictional wrenches that can be transmitted through a contact by sampling the space of unit twists (Section 3.3.2). Next, two 6D limit surface models are introduced to approximate a 6D limit surface for computational efficiency. The frictional wrench samples are normalized (Section 3.3.3) and the models are fit to the normalized wrenches. The two 6DLS models are an ellipsoid (Section 3.3.4) and a convex quartic model (Section 3.3.5), generalized from the corresponding 3D models described in Section 2.3.5.3 and Section 2.3.5.4, respectively. Finally, the linearization techniques (Section 3.3.6) for the two models are introduced as a foundation for grasp analysis.

3.3.1 Definition

Recall that a limit surface is the boundary of the set of all possible frictional wrenches that can be applied through one contact or a set of contacts [13] (Section 2.3.4.6). Generalized

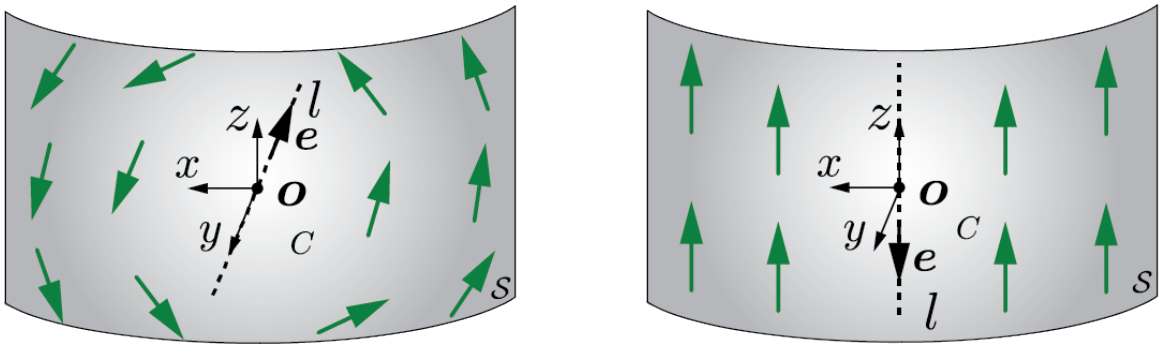

Figure 3.3: Local frictional force direction vectors (green) of a nonplanar surface contact acting on the grasped object, (a) if the object rotates around the negative y-axis, (b) if the object slides along the negative z-axis relative to the gripper. The figures are adapted from [1] ©2021 IEEE.

from 3DLS, let $f(\boldsymbol{x}) = 1$ with $\boldsymbol{x} \in \mathbb{R}^6$ define the *six-dimensional limit surface (6LDS)*, which is a surface that bounds the set of all possible 6D frictional wrenches at a nonplanar surface contact. In other words, an arbitrary frictional wrench $\boldsymbol{w}^*$ that can be transmitted through a contact is constrained to be inside of the 6DLS

$$f(\boldsymbol{w}^*) \leq 1. \tag{3.9}$$

3.3.2 Motion Sampling

One intuitive way to build a 6D limit surface consists of densely sampling the motion space and computing the frictional wrench for each motion, which is potentially a time-consuming operation. To increase efficiency, a finite number of object motions is sampled and the corresponding frictional wrenches are computed using Equation (3.3)–(3.5). Then an ellipsoid or a quartic is fit to the frictional wrenches to approximate the 6D limit surface.

Recall that the triplet $(\boldsymbol{e}, \boldsymbol{m}, h)$ or the direction vector $\boldsymbol{e}$ alone uniquely defines a unit twist. Due to the constraint $\boldsymbol{e}^T\boldsymbol{m} = 0$, one intuitive way is to sample $\boldsymbol{e}$ and two components of $\boldsymbol{m}$, for instance, m_x and m_y, and compute the third component with $m_z = -(e_x m_x + e_y m_y)/e_z$. However, the division leads to numerical instability if $e_z = 0$. Therefore, $(\boldsymbol{e}, \boldsymbol{m}, h)$ is sampled for the motions that include a rotation with $\boldsymbol{m}$ being computed with $\boldsymbol{m} = \boldsymbol{q} \times \boldsymbol{e}$; $\boldsymbol{e}$ is sampled for pure translations.

The specific steps for motion sampling are described as follows. Each component of $(\boldsymbol{e}, \boldsymbol{m}, h)$ is sampled individually. $\boldsymbol{e}$ is uniformly sampled from the unit sphere using the Fibonacci sphere algorithm, $\boldsymbol{q}$ is randomly sampled within a radius r of the pressure center $\boldsymbol{o}$ of the contact, and the pitch h is randomly sampled in the range $[-2, 2]$. The radius r depends on the size of the contact surface. If r is too large or too small, one obtains very unevenly distributed frictional wrenches. To determine r, the smallest rectangular cuboid is first found so that it just contains the nonplanar surface. Denoting l_s as the longest side length of the cuboid, the radius r is experimentally determined to be $0.25l_s$, which results in relatively evenly distributed frictional wrenches. The sampled $\boldsymbol{e}$ is also used to compute the

unit twists that only contain a translation using Equation (2.30). The process leads to a total of K motion samples.

Figure 3.3 shows two representative sampled unit twists and the resulting local frictional force direction vectors, which are used to compute the frictional wrench of the contact. Figure 3.3(a) illustrates a pure rotation around the negative y-axis with $\boldsymbol{e} = [0, -1, 0]^T, \boldsymbol{q} = [0, 0, 0]^T$, $h = 0$, and $\|\boldsymbol{\omega}\| = 1$ in the local contact frame C, where τ_y, the frictional torque component around the y-axis, is maximized for the representative surface. Figure 3.3(b) shows a pure translation along the negative z-axis with $\boldsymbol{e} = [0, 0, -1]^T$ and $\|\boldsymbol{\omega}\| = 0$, where f_z reaches the maximum.

3.3.3 Normalizing Frictional Wrenches

From the K motion samples, one obtains K frictional wrenches using Equation (3.3)–(3.5). Let $\boldsymbol{w}_i$ be the ith frictional wrench with $i \in \{1, \ldots, K\}$. $\boldsymbol{w}_i$ is normalized so that each component of $\boldsymbol{w}_i$ is in the range of $[-1, 1]$ for numerical stability. Let $\boldsymbol{w}_{\max} = [f_{x,\max}, f_{y,\max}, f_{z,\max}, \tau_{x,\max}, \tau_{y,\max}, \tau_{z,\max}]^T$ be the wrench composed of the maximal magnitudes of the K frictional wrenches in the six dimensions. The ith normalized frictional wrench $\hat{\boldsymbol{w}}_i$ is

$$\hat{\boldsymbol{w}}_i = \boldsymbol{w}_i \oslash \boldsymbol{w}_{\max}. \tag{3.10}$$

Note that $\hat{\boldsymbol{w}}$ is dimensionless. A representative set of $\{\hat{\boldsymbol{w}}_1, \ldots, \hat{\boldsymbol{w}}_K\}$ is illustrated in Figure 3.4 as orange dots.

3.3.4 Finding an Ellipsoid

The first proposed model to approximate a 6D limit surface is a 6D ellipsoid. An arbitrarily oriented zero-centered 6D ellipsoid is defined by $f_1(\boldsymbol{x}) = \boldsymbol{x}^T \boldsymbol{A}_e \boldsymbol{x} = 1$, where $\boldsymbol{A}_e \in \mathbb{R}^{6\times 6}$ is a positive definite matrix. Two methods to find $\boldsymbol{A}_e$ are presented here: convex optimization and least square fitting.

3.3.4.1 Convex Optimization

An ellipsoid fit to the normalized frictional wrenches $\{\hat{\boldsymbol{w}}_1, \ldots, \hat{\boldsymbol{w}}_K\}$ can be found by using the optimization problem

$$\begin{aligned} \underset{\boldsymbol{A}_e}{\text{minimize}} \quad & \sum_{i=1}^{K} \left(f_1(\hat{\boldsymbol{w}}_i) - 1\right)^2 \\ \text{subject to} \quad & f_1(\boldsymbol{x}) = \boldsymbol{x}^T \boldsymbol{A}_e \boldsymbol{x} \\ & \boldsymbol{A}_e \succ 0 \end{aligned} \tag{3.11}$$

where $\boldsymbol{A}_e \succ 0$ means that $\boldsymbol{A}_e$ is positive definite. Since $\boldsymbol{A}_e$ uniquely defines an ellipsoid, $\boldsymbol{A}_e$ is denoted as the ellipsoidal LS model.

However, a conventional solver can only constraint $\boldsymbol{A}_e$ to be positive semidefinite. If the frictional wrench samples are linearly dependent in a subspace, for instance, the frictional wrenches are in 3D for a planar area contact, the solver fails to solve the program. Therefore,

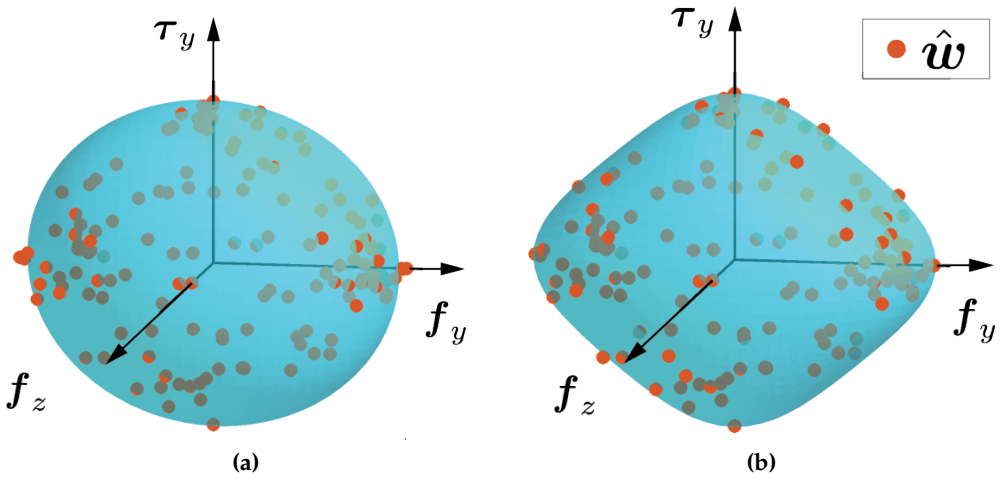

Figure 3.4: A 3D projection of (a) an ellipsoid and (b) a quartic 6DLS model fit to the normalized frictional wrenches illustrated as orange dots. The figures are adapted from [1] ©2021 IEEE.

to ensure the determinant of $\boldsymbol{A}_e$ is positive in practice, a penalty term is added to the objective function. Similar to the penalty term in Equation (2.109), the penalty term is selected as $-\alpha \cdot \log\det(\boldsymbol{A}_e)$ with a coefficient $\alpha > 0$ to adjust the weight of the penalty. In summary, Equation (3.11) is reformulated as a semidefinite program

$$\begin{aligned} \underset{\boldsymbol{A}_e}{\text{minimize}} \quad & \sum_{i=1}^{K} (f_1(\hat{\boldsymbol{w}}_i) - 1)^2 - \alpha \cdot \log\det(\boldsymbol{A}_e) \\ \text{subject to} \quad & f_1(\boldsymbol{x}) = \boldsymbol{x}^T \boldsymbol{A}_e \boldsymbol{x} \\ & \boldsymbol{A}_e \succeq 0 \\ & \alpha > 0. \end{aligned} \tag{3.12}$$

where $\boldsymbol{A}_e \succeq 0$ means that $\boldsymbol{A}_e$ is positive semidefinite. Figure 3.4(a) shows a 3D projection of the 6D ellipsoid fit to the normalized wrenches.

3.3.4.2 Least Square Method

While solving a SDP provides accurate results, the computational effort is demanding. To find a balance between efficiency and accuracy, the least square method is presented to find an ellipsoid. Given K normalized frictional wrenches $\{\hat{\boldsymbol{w}}_1, \ldots, \hat{\boldsymbol{w}}_K\}$, the ellipsoid $\boldsymbol{A}_e^*$ that best fit to the wrenches is

$$\boldsymbol{A}_e^* = \arg\min_{\boldsymbol{A}_e} \sum_{i=1}^{K} \|\hat{\boldsymbol{w}}_i^T \boldsymbol{A}_e \hat{\boldsymbol{w}}_i - 1\|^2 \tag{3.13}$$

Equation (3.13) can be solved using least squares since it is linear in $\boldsymbol{A}_e$. However, this method does not guarantee to result in an ellipsoid if the matrix is not positive definite. Therefore, in practice, the dimensionality of the data is first determined by using principal component analysis. Then, an ellipsoid of the determined dimensionality is fit to the data rotated to the PCA frame. The remaining dimensions with explained variances less than a

small value $\epsilon > 0$ are filtered out. Finally, the ellipsoid is rotated back to the original non-PCA frame. Note that this case subsumes the planar area frictional contact model (Section 2.3.5.3); if the contact surface is planar, the ellipsoidal 6DLS model reduces to a 3D ellipsoid.

3.3.5 Finding a Quartic

While an ellipsoid is a practical LS model for quasi-static [91] and sliding manipulations [16], Zhou *et al.* [18] suggested that a convex homogeneous quartic model better captures the force-motion relation for planar sliding. The quartic (fourth-order polynomial) [18], which describes a limit surface in 3D, is generalized in this thesis to approximate a limit surface in 6D, which requires that the polynomial defining this surface is a function of all six components of $\boldsymbol{x}$.

To formulate the quartic $f_2(\boldsymbol{x})$ with $\boldsymbol{x} \in \mathbb{R}^6$, let the nonnegative integer d_j be the degree of the jth component of $\boldsymbol{x}$ with $\sum_{j=1}^{6} d_j = 4$ for the homogeneous quartic. The quartic surface with up to L terms is defined by $f_2(\boldsymbol{x}) = a_1 x_1^4 + a_2 x_1^3 x_2 + \ldots + a_L x_6^4 = \sum_{\kappa=1}^{L} \left(a_\kappa \prod_{j=1}^{6} x_j^{d_{j,\kappa}} \right) = 1$, where $a_\kappa \in \mathbb{R}$ is the coefficient of the κth term. Here, $L = \binom{4+6-1}{6-1} = 126$. Since the coefficients uniquely define a quartic surface, $\boldsymbol{A}_q = [a_1, \ldots, a_L]^T$ is denoted as the quartic LS model in this thesis. Note that $\boldsymbol{A}_q \in \mathbb{R}^{126}$, whereas $\boldsymbol{A}_e \in \mathbb{R}^{6\times 6}$ for an ellipsoid. $\boldsymbol{A}_q$ is uppercase for consistency as $\boldsymbol{A}$ denotes the LS model.

Zhou *et al.* [18] showed that it is essential to enforce the convexity of the quartic. However, the convexity is NP-hard to determine if $d > 2$ and $L > 1$. Inspired by Magnani *et al.* [103], the proposed method uses a similar relaxation technique that enforces the convexity of $f_2(\boldsymbol{x})$ only on a region by using the concept of *sum-of-squares (SOS)*.

The next part describes the specific steps to find a quartic. Let $\boldsymbol{z} \in \mathbb{R}^6$ be a nonzero auxiliary variable. Let $\boldsymbol{y}(\boldsymbol{x}, \boldsymbol{z})$ be a variable that depends on $\boldsymbol{x}$ and $\boldsymbol{z}$ with

$$\boldsymbol{y}(\boldsymbol{x}, \boldsymbol{z}) = \left[x_1 \boldsymbol{z}^T, x_2 \boldsymbol{z}^T, x_3 \boldsymbol{z}^T, x_4 \boldsymbol{z}^T, x_5 \boldsymbol{z}^T, x_6 \boldsymbol{z}^T \right]^T \in \mathbb{R}^{36}. \tag{3.14}$$

The polynomial $f_2(\boldsymbol{x})$ is defined as *SOS convex*, if there exists a positive definite matrix $\boldsymbol{M} \in \mathbb{R}^{36\times 36}$ such that

$$\boldsymbol{z}^T \nabla^2 f_2(\boldsymbol{x}) \boldsymbol{z} = \boldsymbol{y}(\boldsymbol{x}, \boldsymbol{z})^T \boldsymbol{M} \boldsymbol{y}(\boldsymbol{x}, \boldsymbol{z}). \tag{3.15}$$

Equation (3.15) is reformulated as sparse linear constraints of $\boldsymbol{A}_q$ and the vectorization of $\boldsymbol{M}$ with

$$\boldsymbol{V}_1 \mathrm{vec}(\boldsymbol{M}) = \boldsymbol{V}_2 \boldsymbol{A}_q \tag{3.16}$$

where $\boldsymbol{V}_1 \in \mathbb{N}_0^{441\times 1296}$ and $\boldsymbol{V}_2 \in \mathbb{N}_0^{441\times 126}$ with $\mathbb{N}_0 = \{\mathbb{N} \cup \{0\}\}$ are constant sparse matrices, and $\mathrm{vec}(\cdot)$ denotes the vectorization operation. A quartic surface is fit to $\{\hat{\boldsymbol{w}}_1, \ldots, \hat{\boldsymbol{w}}_K\}$ by

formulating the optimization problem

$$\begin{aligned} \underset{\boldsymbol{A}_q=[a_1,\ldots,a_L]^T,\boldsymbol{M}}{\text{minimize}} \quad & \sum_{i=1}^{K} \left(f_2(\hat{\boldsymbol{w}}_i) - 1\right)^2 \\ \text{subject to} \quad & f_2(\boldsymbol{x}) = \sum_{\kappa=1}^{L} \left(a_\kappa \prod_{j=1}^{6} x_j^{d_{j,\kappa}} \right) \\ & \boldsymbol{V}_1 \text{vec}(\boldsymbol{M}) = \boldsymbol{V}_2 \boldsymbol{A}_q \\ & \boldsymbol{M} \succ 0. \end{aligned} \tag{3.17}$$

Figure 3.4(b) shows a 3D projection of the quartic 6DLS model fit to $\{\hat{\boldsymbol{w}}_1, \ldots, \hat{\boldsymbol{w}}_K\}$. Note that the semidefinite program with a penalty term for the 6D ellipsoid can also be used to find a quartic; however, the method is not explored in this thesis.

To evaluate both models, the mean distance of the wrench samples to the surface is used as the wrench fitting error

$$\varepsilon_{1,2} = \frac{1}{K} \sum_{i=1}^{K} \| f_{1,2}(\hat{\boldsymbol{w}}_i) - 1 \|. \tag{3.18}$$

Note that $\varepsilon_{1,2}$ does not have a unit as the normalized frictional wrenches are unitless.

Algorithm 1 summarizes the process to find a 6DLS model for a nonplanar surface contact. The description after double slash (//) in the algorithm is a comment. As the limit surface models are fit to the normalized frictional wrenches, Algorithm 1 also outputs $\boldsymbol{w}_{\text{max}}$ to denormalize the constraints for multicontact grasp analysis in Section 4.1.2.1.

Algorithm 1 Finding a 6D limit surface model for a nonplanar surface contact.

Require:
- Friction coefficient μ
- Contact surface $\mathcal{S}$ represented with a parametric form or a mesh
- Pressure distribution p

Output: The 6DLS model $\boldsymbol{A}$ and $\boldsymbol{w}_{\text{max}}$

$(\boldsymbol{e}_i, \boldsymbol{q}_i, h_i)$ or $\boldsymbol{e}_i, i \in \{1, \ldots, K\} \leftarrow$ Sampling $(\boldsymbol{e}, \boldsymbol{q}, h)$ or $\boldsymbol{e}$ for possible motions (unit twists)
$\boldsymbol{o} \leftarrow \mathcal{S}, p$ // Equation (3.1)
for $i \leftarrow 1$ to K **do**
  $\boldsymbol{m}_i = \boldsymbol{q}_i \times \boldsymbol{e}_i$
  $\boldsymbol{w}_i \leftarrow \mu, p, \mathcal{S}, \boldsymbol{o}, \boldsymbol{e}_i, \boldsymbol{m}_i, h_i$ // Equation (3.3)–(3.5)
end for
// Normalizing the frictional wrenches
$\boldsymbol{w}_{\text{max}} \leftarrow \{\boldsymbol{w}_1, \ldots, \boldsymbol{w}_K\}$
$\{\hat{\boldsymbol{w}}_1, \ldots, \hat{\boldsymbol{w}}_K\} \leftarrow \boldsymbol{w}_{\text{max}}, \{\boldsymbol{w}_1, \ldots, \boldsymbol{w}_K\}$ // Equation (3.10)
// Fit a 6DLS model to the normalized frictional wrenches
$\boldsymbol{A} \leftarrow \{\hat{\boldsymbol{w}}_1, \ldots, \hat{\boldsymbol{w}}_K\}$ // Equation (3.11) or (3.17) for the ellipsoid or quartic 6DLS model, respectively
return $\boldsymbol{A}$, $\boldsymbol{w}_{\text{max}}$

3.3.6 Linearizing Frictional Constraints

Recall that a 3D limit surface model for a planar area contact is commonly linearized to build a grasp wrench space or to form linear frictional constraints for grasp analysis (Section 2.3.5.3). Similarly, a 6DLS model can also be linearized to approximate frictional constraints for efficiency. Specifically, instead of using Equation (3.9), a frictional wrench is constrained to lie inside the discrete limit surface. The following section presents two types of constraints: inner and outer linear frictional constraints. While the former is used to build a GWS, the latter is used as constraints for a quadratic program. Note that the outer constraints are only for the 6D ellipsoid as the ones for the quartic are not explored in this thesis.

3.3.6.1 Inner Linear Frictional Constraints

There are three steps to find the set of inner linear frictional constraints $\mathcal{F}^{\text{inner}}$. First, a 6DLS model $\boldsymbol{A}$ is discretized by sampling the surface with M vertices $\hat{\boldsymbol{s}}_m^{\text{LS}} \in \mathbb{R}^6, m \in \{1, \dots, M\}$. Then, $\hat{\boldsymbol{s}}_m^{\text{LS}}$ is denormalized as $\boldsymbol{A}$ is fit to normalized frictional wrenches. Finally, $\mathcal{F}^{\text{inner}}$ is the convex hull of the M denormalized vertices. Although one can also use the convex hull of the frictional wrenches $\{\boldsymbol{w}_1, \dots, \boldsymbol{w}_K\}$ from the initial motion sampling, the resulting set of frictional constraints is less accurate and requires higher computational effort. This is because $\{\boldsymbol{w}_1, \dots, \boldsymbol{w}_K\}$ can be unevenly distributed due to the geometry of the contact surface and the convex hull will likely have significantly more facets as the fine surface details are preserved. In contrast, the proposed $\mathcal{F}^{\text{inner}}$ is evenly distributed and further provides a low-dimensional representation of the frictional constraints. Section 4.1.3.4 later presents a comparison of the prediction results and the grasp wrench spaces built with $\{\boldsymbol{w}_1, \dots, \boldsymbol{w}_K\}$ and with the proposed $\mathcal{F}^{\text{inner}}$. Note that the inner constraints only require the denormalized sampled vertices, whereas the outer constraints require both the vertices and the 6DLS model $\boldsymbol{A}$.

The following part introduces the details of the three steps to find $\mathcal{F}^{\text{inner}}$, including surface sampling, denormalization, and the convex hull operation.

While there are multiple techniques to sample an ellipsoid, sampling a quartic surface is nontrivial. The following sampling algorithm is proposed as it is applicable to both surfaces. The idea is to sample M points $\{\boldsymbol{s}_1^{\text{cube}}, \dots, \boldsymbol{s}_M^{\text{cube}}\}$ with $\boldsymbol{s}_m^{\text{cube}} \in \mathbb{R}^6$ on a 6D hypercube, then compute $\hat{\boldsymbol{s}}_m^{\text{LS}}$ from $\boldsymbol{s}_m^{\text{cube}}$ using Newton's method. Specifically, the method first samples M points on the surface of a 6D hypercube, where each side is in $[-1, 1]$. Next, the method defines a ray that starts from $\mathbf{0} \in \mathbb{R}^6$ and goes through $\boldsymbol{s}_m^{\text{cube}}$. The intersection point of the ray and the limit surface model is the mth vertex $\hat{\boldsymbol{s}}_m^{\text{LS}}$ on the model. Figure 3.5 illustrates a representative $\boldsymbol{s}_m^{\text{cube}}$ as the black dot and the ray that goes through $\boldsymbol{s}_m^{\text{cube}}$ as the dashed arrow. The intersection point of the ray and the LS model is $\hat{\boldsymbol{s}}_m^{\text{LS}}$, depicted as the purple dot within the dashed rectangle. To compute $\hat{\boldsymbol{s}}_m^{\text{LS}}$, let the mth ray be parametrized as $\gamma_m \cdot \boldsymbol{s}_m^{\text{cube}}$, where γ_m is a positive scaling factor. Given the LS equation $f(\boldsymbol{x}) = 1$ with $f(\boldsymbol{x})$ being $f_1(\boldsymbol{x})$ for the ellipsoid or $f_2(\boldsymbol{x})$ for the quartic, the intersection point $\hat{\boldsymbol{s}}_m^{\text{LS}}$ can be found by solving the following equation system with Newton's method

$$f(\hat{\boldsymbol{s}}_m^{\text{LS}}) = 1 \text{ and } \hat{\boldsymbol{s}}_m^{\text{LS}} = \gamma_m \cdot \boldsymbol{s}_m^{\text{cube}}, \gamma_m > 0 \tag{3.19}$$

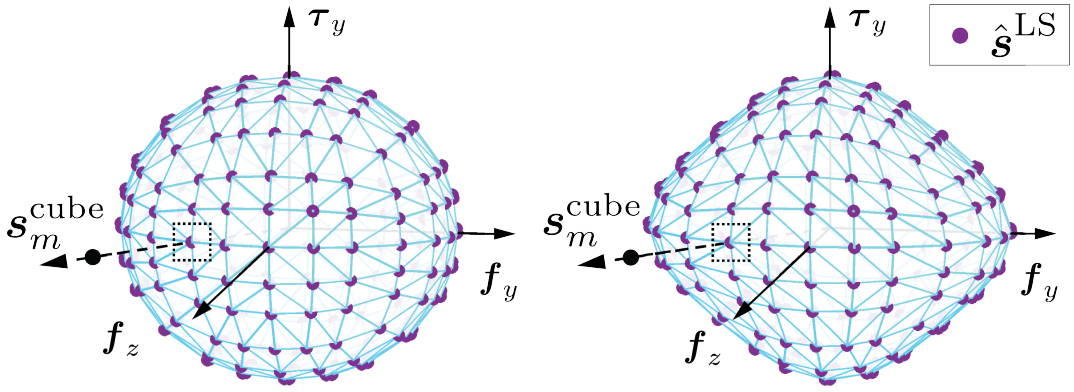

Figure 3.5: The convex hull of the ellipsoidal (left) and the quartic (right) 6DLS models linearized by sampling the surface with vertices, respectively (adapted from [1] ©2021 IEEE).

where $\hat{\boldsymbol{s}}_m^{\text{LS}}$ and γ_m are the variables to be solved in the equation system. The initial guess for the two variables are $\boldsymbol{s}_m^{\text{cube}}$ and 1, respectively, since $\hat{\boldsymbol{s}}_m^{\text{LS}}$ is near $\boldsymbol{s}_m^{\text{cube}}$.

Since both LS models are fit to the set of normalized frictional wrenches (Section 3.3.3), the following part introduces denormalization of the vertices. Given $\{\hat{\boldsymbol{s}}_1^{\text{LS}}, \dots, \hat{\boldsymbol{s}}_M^{\text{LS}}\}$, the set of denormalized frictional wrenches $\mathcal{X}$ is

$$\mathcal{X} = \left\{ \boldsymbol{s}_m^{\text{LS}} \;\middle|\; \boldsymbol{s}_m^{\text{LS}} = \hat{\boldsymbol{s}}_m^{\text{LS}} \circ \boldsymbol{w}_{\max}, m \in \{1, \dots, M\} \right\} \tag{3.20}$$

where $\circ$ is the Hadamard product.

Finally, the set of inner linear frictional constraints $\mathcal{F}^{\text{inner}}$ is the convex hull of $\mathcal{X}$,

$$\mathcal{F}^{\text{inner}} = \text{Conv}\,(\mathcal{X}) \tag{3.21}$$

where $\text{Conv}\,(\cdot)$ denotes the convex hull operation. In other words, an arbitrary frictional wrench $\boldsymbol{w}^*$ is constrained to be inside of the convex hull of $\mathcal{X}$. Note that $\mathcal{F}^{\text{inner}}$ is a conservative approximation of the frictional wrench limit at a nonplanar surface contact. Figure 3.5 illustrates the 3D projection of the convex hull of the linearized ellipsoid and quartic, respectively, where each triangle is a facet of the convex hull. Note that $\mathcal{X}$, instead of $\mathcal{F}^{\text{inner}}$, of each contact of a grasp is used to build a grasp wrench space.

Since the limit surface computation only requires the contact profile, including the contact surface $\mathcal{S}$ and the pressure distribution p, one can precompute the linear frictional constraints $\mathcal{X}$ for the profile and store $\mathcal{X}$ in the dataset $\mathcal{D}$ for efficiency. If the same contact profile is countered, a stored version in $\mathcal{D}$ can be reused. As there are an infinite set of continuous contact profiles, one can discretize the contact surface and the pressure distribution to obtain a finite set. The effect of the discretization is later presented in Section 3.5.1.2. Furthermore, one typically obtains contact profiles with tactile sensors in experiments. As the sensors provide discrete profiles, the possible contact profiles are a finite set and the LS for each profile can be precomputed in extreme cases. However, it is less realistic to assume that the physical contact profile exactly matches a stored version in $\mathcal{D}$. As the tolerable offset of a limit surface depends on the specific application, one can adjust the tolerable offset of a contact profile experimentally. The effect of different offsets in pressure distribution and contact surface is

later discussed in Section 4.1.3.5 for elliptic cylindrical contact surfaces with the power-law pressure model [80].

Also note that $\mathcal{X}$ linearly scales with the sum magnitude of the local normal forces $F = \int_{\mathcal{S}} p \, \mathrm{d}\mathcal{S}$. Therefore, one can precompute $\mathcal{X}$ for the pair $\mathcal{S}$ and the normalized pressure distribution $\hat{p} = p/F$, and scale $\mathcal{X}$ with F or with a force sensor reading for each jaw when constructing the GWS. In summary, defining a *profile pair* $(\mathcal{S}, \hat{p})$ for a contact and compute $\mathcal{X}$ given $(\mathcal{S}, \hat{p})$, the dataset $\mathcal{D}$ can be updated with $\mathcal{D} = \mathcal{D} \cup \mathcal{X}$. When constructing the GWS, the precomputed $\mathcal{X}$ for $(\mathcal{S}, \hat{p})$ is retrieved from $\mathcal{D}$ and denormalized with F or a force sensor reading. If $\mathcal{X} \notin \mathcal{D}$, $\mathcal{X}$ is computed online.

3.3.6.2 Outer Linear Frictional Constraints for Ellipsoid

While the inner linear frictional constraints are more conservative, hence avoid false positive predictions, building a GWS is computationally demanding. Thus, solving a quadratic program (QP) for grasp analysis is preferred for online grasp planning or generating largescale datasets. A QP requires outer linear frictional constraints $\mathcal{F}^{\text{outer}}$, which are introduced in the following. Note that the following outer constraints are only for the ellipsoidal 6DLS model, as the ones for a quartic are not explored in this thesis.

The computation of $\mathcal{F}^{\text{outer}}$ requires three steps. The first step is sampling the surface of $\boldsymbol{A}_e$, same as for the inner constraints. Then, $\hat{\boldsymbol{s}}_m^{\text{LS}}$ is denormalized and the surface normal $\boldsymbol{n}_m^{\text{LS}}$ of the denormalized $\boldsymbol{A}_e$ at $\boldsymbol{s}_m^{\text{LS}}$ is computed. Finally, $\boldsymbol{s}_m^{\text{LS}}$ and $\boldsymbol{n}_m^{\text{LS}}$ are used to defined the mth linear constraint of $\mathcal{F}^{\text{outer}}$.

The specific steps are introduced next. To sample points $\hat{\boldsymbol{s}}_m^{\text{LS}}$ on the ellipsoid, one can use Equation (3.19) or other techniques, such as sampling a 6D sphere, than scale the vertices with the radii of the ellipsoid and rotate them using the eigenvectors of the ellipsoid. Then, one can denormalize $\hat{\boldsymbol{s}}_m^{\text{LS}}$ with $\boldsymbol{s}_m^{\text{LS}} = \hat{\boldsymbol{s}}_m^{\text{LS}} \circ \boldsymbol{w}_{\max}$, which is equivalent to

$$\boldsymbol{s}_m^{\text{LS}} = \boldsymbol{W}_{\max} \hat{\boldsymbol{s}}_m^{\text{LS}}, \quad \text{where } \boldsymbol{W}_{\max} = \begin{bmatrix} f_{x,\max} & & & & & \\ & f_{y,\max} & & & \mathbf{0} & \\ & & f_{z,\max} & & & \\ & & & \tau_{x,\max} & & \\ & \mathbf{0} & & & \tau_{y,\max} & \\ & & & & & \tau_{z,\max} \end{bmatrix}. \tag{3.22}$$

The outward normal $\boldsymbol{n}_m^{\text{LS}}$ of the denormalized ellipsoid at $\boldsymbol{s}_m^{\text{LS}}$ is

$$\boldsymbol{n}_m^{\text{LS}} = \frac{\boldsymbol{W}_{\max}^{-1} \boldsymbol{A}_e \hat{\boldsymbol{s}}_m^{\text{LS}}}{\boldsymbol{W}_{\max}^{-1} \| \boldsymbol{A}_e \hat{\boldsymbol{s}}_m^{\text{LS}} \|}. \tag{3.23}$$

Similar to the set of outer linear constraints for 3D ellipsoid described with Equation (2.58), $\boldsymbol{s}_m^{\text{LS}}$ and its outward normal $\boldsymbol{n}_m^{\text{LS}}$ form a hyperplane. An arbitrary frictional wrench is constrained to the interior of the M hyperplanes. Therefore, the set of outer linear frictional

constraints $\mathcal{F}^{\text{outer}}$ is

$$\mathcal{F}^{\text{outer}} = \left\{ \boldsymbol{w}^* \in \mathbb{R}^6 \;\middle|\; (\boldsymbol{w}^*)^T \boldsymbol{n}_m^{\text{LS}} \leq \left(\boldsymbol{s}_m^{\text{LS}}\right)^T \boldsymbol{n}_m^{\text{LS}}, \;\; \forall m \in \{1, \ldots, M\} \right\}. \tag{3.24}$$

3.4 Six-dimensional Contact Wrench Model

The previous section introduced the 6DLS models, which are the constraints for frictional wrench of a contact. However, a contact can transmit a frictional wrench and a normal wrench, which is the wrench impressed by the normal pressure. This section introduces the contact wrench model, which approximates the 6D contact wrench limit that can be transmitted through a nonplanar surface contact.

A contact wrench $\boldsymbol{c}$ is the sum of a frictional and a normal wrench

$$\boldsymbol{c} = \boldsymbol{w} + \boldsymbol{w}_\perp. \tag{3.25}$$

Given a contact profile, $\boldsymbol{w}_\perp \in \mathbb{R}^6$ can be computed using Equation (3.2) and the frictional wrench $\boldsymbol{w}$ is constrained to be inside of a 6DLS model. Therefore, the contact wrench is constrained to be inside of an ellipsoid or a quartic centered at $\boldsymbol{w}_\perp$. In other words, the contact wrench model is a shifted ellipsoid or quartic, depending on the model. Mathematically, let $f(\boldsymbol{x}) = 1$ be the 6DLS, an arbitrary contact wrench $\boldsymbol{c}^* \in \mathbb{R}^6$ is constrained to be inside of the shifted 6DLS centered at $\boldsymbol{w}_\perp$

$$f\left(\boldsymbol{c}^* - \boldsymbol{w}_\perp\right) \leq 1. \tag{3.26}$$

The set of inner linearized contact wrench constraints $\mathcal{C}^{\text{inner}}$ can be computed with Equation (3.20), (3.21), and (3.25)

$$\mathcal{C}^{\text{inner}} = \text{Conv}\left(\left\{ \boldsymbol{s}_m^{\text{LS}} + \boldsymbol{w}_\perp \;\middle|\; m \in \{1, \ldots, M\} \right\} \right). \tag{3.27}$$

Similarly, the set of outer linearized contact wrench constraints $\mathcal{C}^{\text{outer}}$ using an ellipsoidal 6DLS model $\boldsymbol{A}_e$ can be computed by combining Equation (3.24) and (3.25)

$$\mathcal{C}^{\text{outer}} = \left\{ \boldsymbol{c}^* \in \mathbb{R}^6 \;\middle|\; \left(\boldsymbol{c}^* - \boldsymbol{w}_\perp\right)^T \boldsymbol{n}_m^{\text{LS}} \leq \left(\boldsymbol{s}_m^{\text{LS}}\right)^T \boldsymbol{n}_m^{\text{LS}}, \;\; \forall m \in \{1, \ldots, M\} \right\}. \tag{3.28}$$

$\mathcal{C}^{\text{outer}}$ is also called the *ellipsoidal 6D contact wrench model* in this thesis.

Note that the contact wrench constraints above are computed with a specific contact profile; therefore, the constraints correspond to the *normal force magnitude* computed from the contact profile. The normal force magnitude $f_\perp$ for a nonplanar surface contact is defined as the magnitude of the normal force component along the grasp axis. For instance, for the representative grasp in Figure 3.1(a), one first compute the normal wrench $\boldsymbol{w}_\perp = [f_{\perp_x}, f_{\perp_y}, f_{\perp_z}, \tau_{\perp_x}, \tau_{\perp_y}, \tau_{\perp_z}]^T$ from the contact profile using Equation (3.2). The normal force magnitude $f_\perp$ is $f_{\perp_y}$ in this case, since $f_{\perp_y}$ is the force component along the grasp axis. In practice, if $f_\perp$ is known from a force sensor, one can compute the contact wrench constraints that match the measured force along the grasp axis. Specifically, one can compute the contact wrench constraints for a unit normal force magnitude with $f_\perp = 1$, then scale the constraints by the measured force since a contact wrench linearly scales with $f_\perp$.

3.4.1 Six-dimensional Friction Cone

So far, the contact wrench constraints are computed for a given normal force magnitude $f_\perp$. However, $f_\perp$ is unknown for many scenarios, for instance, when the contact wrench constraints are used to optimize the grasp force (Section 2.5.8) or the physical gripper is not equipped with force sensors, such as the ABB YuMi robot. Therefore, this thesis proposes the *six-dimensional friction cone (6DFC)*, which is a generalization of the traditional friction cone for point contacts (Section 2.3.5.1) and the ellipsoidal 6D contact wrench model. Specifically, the 6DFC constrains the contact wrench of a nonplanar surface contact for any $f_\perp$ between 0N and the upper limit of the grasp force $f_{\perp,\max}$ of the gripper. Figure 3.6 shows the 3D projection of a representative 6D friction cone. Each ellipsoid represents a projection of the ellipsoidal contact wrench model for a given $f_\perp$ and its center corresponds to the normal wrench corresponds to $f_\perp$. Since the contact wrench applied at a contact with $f_\perp$ can be modeled with a 6D ellipsoid that is centered at $\boldsymbol{w}_\perp$, so that varying the value of $f_\perp$ results in a 6D friction cone, whose center lies along the vector $\boldsymbol{w}_\perp$ and has 6D ellipsoids as contours for each value of $f_\perp$. Mathematically, given an ellipsoidal 6DLS model $\boldsymbol{A}_e$ and the normal wrench $\boldsymbol{w}_\perp$ computed with a unit normal force magnitude $f_\perp = 1$, the proposed 6DFC, denoted as $\mathcal{C}_{\text{6DFC}}$, constraints an arbitrary contact wrench $\boldsymbol{c}^* \in \mathbb{R}^6$ by

$$\mathcal{C}_{\text{6DFC}} = \left\{ \boldsymbol{c}^* \in \mathbb{R}^6 \;\middle|\; (\boldsymbol{c}^* - f_\perp \cdot \boldsymbol{w}_\perp)^T \boldsymbol{A}_e \, (\boldsymbol{c}^* - f_\perp \cdot \boldsymbol{w}_\perp) \leq {f_\perp}^2 \text{ with } 0 \leq f_\perp \leq f_{\perp,\max} \right\}. \tag{3.29}$$

By combining Equation (3.28) and Equation (3.29), the set $\mathcal{C}^{\text{outer}}_{\text{6DFC}}$ of outer linear constraints of the 6DFC is

$$\begin{aligned} \mathcal{C}^{\text{outer}}_{\text{6DFC}} = \Bigg\{ \boldsymbol{c}^* \in \mathbb{R}^6 \;\Bigg|\; & (\boldsymbol{c}^* - f_\perp \cdot \boldsymbol{w}_\perp)^T \boldsymbol{n}^{\text{LS}}_m \leq \left(f_\perp \cdot \boldsymbol{s}^{\text{LS}}_m \right)^T \boldsymbol{n}^{\text{LS}}_m \quad \text{with} \\ & \forall m \in \{1, \ldots, M\}, \;\; 0 \leq f_\perp \leq f_{\perp,\max} \Bigg\}. \end{aligned} \tag{3.30}$$

Note that the 6DFC subsumes the ellipsoidal contact wrench model. Also note that a grasp based on the 6DFC can have different normal force magnitude $f_\perp$ of each jaw. For a robot setup with force sensors, the 6DFC can be computed with $f_{\perp,\max}$ being the force sensor reading. For such setups with known grasp forces, one can expect that the 6DFC and the ellipsoidal contact wrench model provide similar grasp planning results.

3.5 Simulation

This section presents the evaluation of the two proposed limit surface models for nonplanar parametric surfaces (Section 3.5.1) and discrete contact surfaces obtained from FEM simulations (Section 3.5.2). For the parametric surfaces, results for three experiments are presented: the maximal frictional wrench computed with different contact models, the surface discretization effect, and the fitting results with the two 6DLS models. For the discrete contact surfaces, the fitting results are further evaluated with more diverse contact profiles. Note

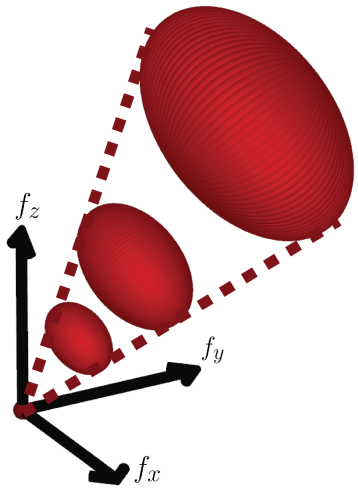

Figure 3.6: 3D projection of a 6D friction cone for a nonplanar surface contact (adapted from [3] ©2020 IEEE).

that the contact wrench models are evaluated in Section 4.1 and Section 4.2 with physical grasps.

3.5.1 Evaluation with Parametric Contact Surfaces

This section starts with the evaluation of six parametric contact surfaces $\mathcal{S}_1, \ldots, \mathcal{S}_6$, as illustrated in Figure 3.7. Table 3.1 summarizes the parametric form of each surface. Although the coordinate system can be arbitrarily chosen, the x, y, z-axes are selected so that the surfaces are symmetric about the yz-plane for easier comparison. The friction coefficient $\mu = 1$ and a normalized uniform pressure distribution $\hat{p}_i$ are selected with $\int_{\mathcal{S}_i} \hat{p}_i \, \mathrm{d}\mathcal{S}_i = 1$ for $\mathcal{S}_i$, where $i \in \{1, \ldots, 6\}$. This selection allows for a more intuitive comparison between the frictional wrenches computed with the proposed nonplanar and the traditional planar area frictional contact model.

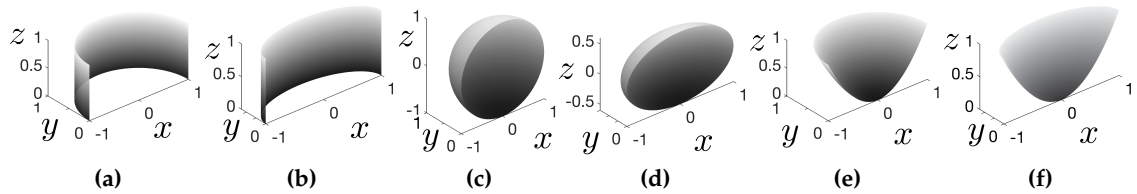

Figure 3.7: Six parametric contact surfaces used to evaluate the 6D frictional wrenches and the proposed 6DLS models (adapted from [1] ©2021 IEEE). (a) $\mathcal{S}_1$: cylinder. (b) $\mathcal{S}_2$: elliptic cylinder. (c) $\mathcal{S}_3$: sphere. (d) $\mathcal{S}_4$: ellipsoid. (e) $\mathcal{S}_5$: paraboloid. (f) $\mathcal{S}_6$: elliptic paraboloid.

3.5.1.1 Maximal Frictional Wrench

For each contact surface, $\boldsymbol{w}_{\max}$ is compared with different contact models, where $\boldsymbol{w}_{\max}$ is the wrench that consists of the maximal magnitudes of the frictional wrenches in the six dimensions with respect to the friction center. Table 3.2 shows $\boldsymbol{w}_{\max}$ for $\mathcal{S}_1$.

Table 3.1: Parametric form of the contact surfaces.

ID	Type	Parametric form
$\mathcal{S}_1$	cylinder	$[\cos u, \sin u, v]^T$ $(u, v) \in [0, \pi] \times [0, 1]$
$\mathcal{S}_2$	elliptic cylinder	$[a \cdot \cos u, b \cdot \sin u, v]^T$ $(u, v) \in [0, \pi] \times [0, 1]$, $a = 1, b = \frac{1}{2}$
$\mathcal{S}_3$	sphere	$[\cos u \cdot \cos v, \cos u \cdot \sin v, \sin u]^T$ $(u, v) \in [-\frac{1}{2}\pi, \frac{1}{2}\pi] \times [0, \pi]$
$\mathcal{S}_4$	ellipsoid	$[a \cdot \cos u \cdot \cos v, b \cdot \cos u \cdot \sin v, c \cdot \sin u]^T$ $(u, v) \in [-\frac{1}{2}\pi, \frac{1}{2}\pi] \times [0, \pi]$, $a = 1, b = \frac{1}{2}, c = \frac{3}{5}$
$\mathcal{S}_5$	paraboloid	$\left[\cos u \cdot v, \sin u \cdot v, v^2\right]^T$ $(u, v) \in [0, \pi] \times [0, 1]$
$\mathcal{S}_6$	elliptic paraboloid	$\left[a \cdot \cos u \cdot v, b \cdot \sin u \cdot v, v^2\right]^T$ $(u, v) \in [0, \pi] \times [0, 1]$, $a = 1, b = \frac{1}{2}$

Table 3.2: Maximal magnitudes of the frictional wrenches in the six dimensions for $\mathcal{S}_1$ computed with three contact models.

Contact model	$f_{x,\max}$	$f_{y,\max}$	$f_{z,\max}$	$\tau_{x,\max}$	$\tau_{y,\max}$	$\tau_{z,\max}$
6D nonplanar	0.64	0.64	1.00	0.34	0.69	0.59
3D nonplanar [4]	0.64	0.00	1.00	0.00	0.69	0.00
Planar	1.00	0.00	1.00	0.00	0.59	0.00

With the nonplanar frictional surface contact model, the magnitude of f_x reaches the maximum if the twist is a pure translation along the (negative) x-axis, which means the instantaneous screw axis l is parallel to the x-axis and $\|\boldsymbol{\omega}\| = 0$. The local frictional force $\mathrm{d}\boldsymbol{f}$ at each point is antiparallel to the projection of the linear velocity, or in this case the (negative) x-axis, onto the surface tangent plane at this point. Similarly, the magnitudes of f_y and f_z are maximized if l is parallel to the y- and z-axes with $\|\boldsymbol{\omega}\| = 0$, respectively. Note that $f_{z,\max} = 1$ as the z-axis is in the tangent plane of each point since there is no curvature along the z-axis for $\mathcal{S}_1$. $f_{x,\max}$ and $f_{y,\max}$ are equal for $\mathcal{S}_1$ as the integrals of the projected x- and y-axis are identical.

$\boldsymbol{w}_{\max}$ for $\mathcal{S}_1$ is also computed with the 3D nonplanar model [4] and the traditional planar area contact model. The former computes only the three largest components f_x, f_z and τ_y for a nonplanar surface and sets the remaining three components to zero, resulting in an overconservative friction estimation compared to the proposed 6D nonplanar surface model. For the latter, the planar area $\mathcal{S}_{\mathrm{pl}}$ is obtained by projecting $\mathcal{S}_1$ onto the xz-plane. The uniform pressure distribution is normalized so that $\int_{\mathcal{S}_{\mathrm{pl}}} \hat{p}_{\mathrm{pl}} \, \mathrm{d}\mathcal{S}_{\mathrm{pl}} = 1$. For $\mathcal{S}_1$, the planar area contact

model results in an overconfident estimation of f_x and an over-conservative estimation of $f_y, \tau_x, \tau_y, \tau_z$. Furthermore, a principle component analysis (PCA) is performed on the sampled normalized frictional wrenches $\{\hat{\boldsymbol{w}}_1, \ldots, \hat{\boldsymbol{w}}_K\}$ for all the studied parametric surfaces. In all cases, one can observe five or even six significant components, which is another indication that a traditional 3D limit surface is not sufficient for nonplanar surface contacts.

3.5.1.2 Surface Discretization Effect

While the friction computation for a parametric surface is less efficient than for a meshed surface due to the integral operation, the frictional wrench for a meshed surface can be less accurate depending on the number of elements. Therefore, these experiments present an analysis of the runtime and $\boldsymbol{w}_{\max}$ for the continuous surfaces $\mathcal{S}_1, \ldots, \mathcal{S}_6$ and their meshes with 25–1,000 triangular elements.

To analyze the error caused by the surface discretization, the value of $\boldsymbol{w}_{\max}$ computed with continuous and discrete surfaces are compared; $\boldsymbol{w}_{\max}$ for the continuous surface is used as the ground truth. To evaluate the error of $\boldsymbol{w}_{\max}$, one defines the *wrench error rate*, which is the difference of $\boldsymbol{w}_{\max}$ divided by the ground truth and averaged over all dimensions of $\boldsymbol{w}_{\max}$. As shown in Figure 3.8, the wrench error rate of all surfaces rapidly decreases with the number of elements since the meshed surfaces are closer to the parametric ones. The error rate is below 4% with 300 triangles, which is acceptable in most applications and is nearly zero with 1,000 elements. $\mathcal{S}_1$ and $\mathcal{S}_2$ have the lowest error since there is no curvature along the z-axis.

The runtime is further measured on an Ubuntu 16.04 machine with an Intel Core i7-8700K CPU (3.7 GHz) with a MATLAB implementation. While the average runtime to integrate a single wrench is 2.62s, the computation for a discrete surface requires 1.3ms and achieves a 2,000-times speedup.

3.5.1.3 6DLS Model Evaluation

The experiments above evaluated the frictional wrench computation for continues and discrete surfaces. Now, the proposed 6DLS models are evaluated by fitting them to different numbers of normalized frictional wrenches computed with the six parametric surfaces using convex optimization. Figure 3.9 shows the mean wrench fitting error and the corresponding runtime. The wrench error is measured as the mean distance of the wrenches to the LS and is computed with 20,000 normalized frictional wrenches with Equation (3.18). While being less efficient, the quartic achieves a lower fitting error with more than 200 wrenches as a quartic has 126 variables and an ellipsoid has 21. An appropriate LS model can be selected based on the trade-off between the fitting error and the runtime required by the application. Figure 3.10 shows a representative 3D cross-section of the quartic and the ellipsoidal 6DLS model, where the remaining three components are zero. Each LS model is fit to 600 frictional wrenches (orange dots) computed with $\mathcal{S}_4$ (ellipsoid). One observes that the wrenches are closer to the quartic surface compared to the ellipsoidal one. Large differences are visualized with dashed rectangles.

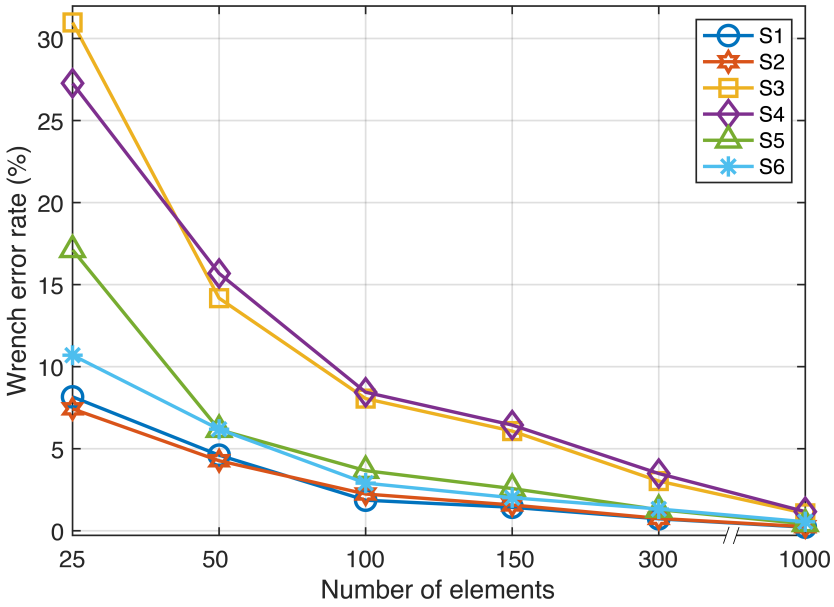

Figure 3.8: Wrench error rate of the six meshed surfaces with an increased number of triangular elements (adapted from [1] ©2021 IEEE).

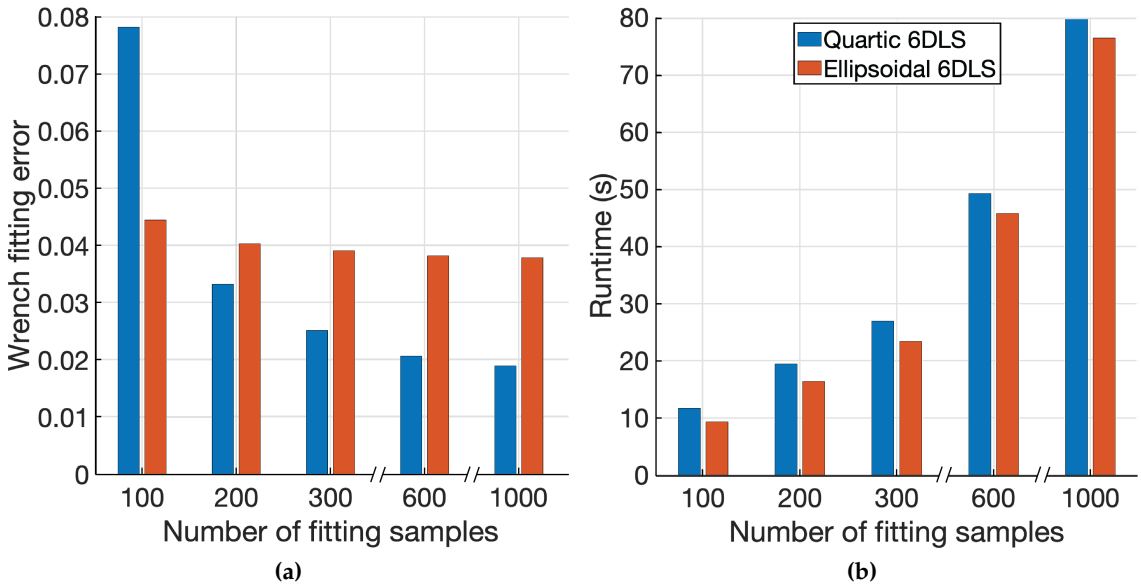

Figure 3.9: Wrench error (a) and runtime (b) of the quartic and the ellipsoidal 6DLS model fit to 100–1,000 frictional wrenches (adapted from [1] ©2021 IEEE).

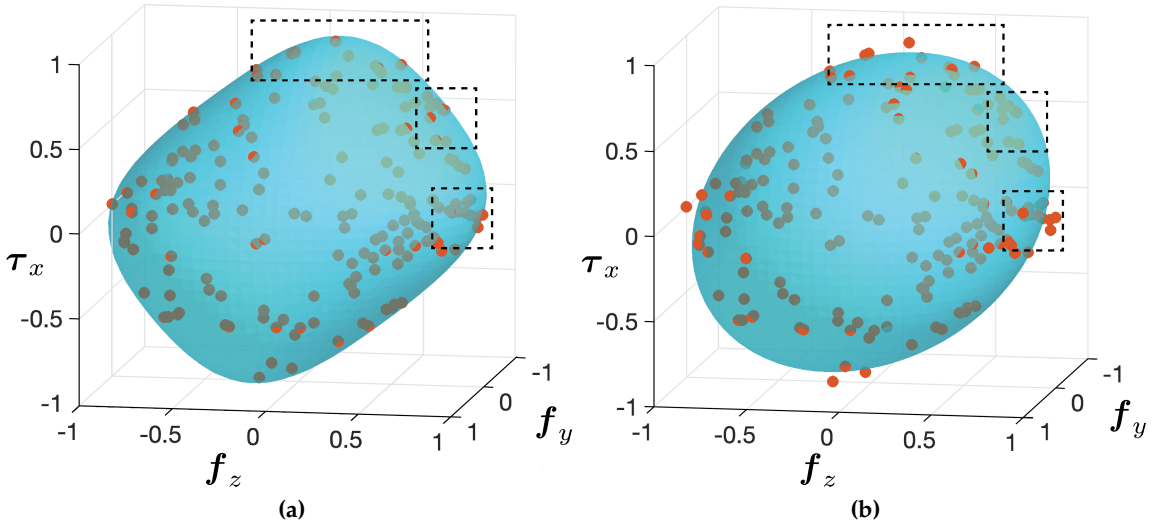

Figure 3.10: A representative 3D cross-section of (a) the quartic and (b) the ellipsoidal 6DLS fit to the normalized frictional wrenches shown as orange dots. The figure is adapted from [1] ©2021 IEEE.

3.5.2 Evaluation with Discrete Contact Surfaces

So far, the 6DLS models are computed with six parametric surfaces. While such surfaces allow an evaluation of the frictional wrench computation for continuous nonplanar surfaces, the number of contact profiles is limited. This section presents experiments with a large variety of contact profiles obtained from FEM simulations. Specifically, the contacts between a parallel-jaw gripper and thin-walled objects are simulated using the commercial software ANSYS [178] based on the work presented in [9]. The objects for the simulations are rigid, similar to closed plastic bottles.

The object geometry is described with nonuniform rational B-Splines (NURBS), which is later meshed according to quality preferences. The top of Figure 3.11(a) depicts the object geometry generation. An ellipse defines the base and a spline curve shapes the wall, which is controlled by the variables $p_1, \ldots, p_{12}$. As illustrated in Figure 3.11(a) bottom, the spline curve are vertically sampled to create an ellipse at each sample. The object surface is created by ruling the adjacent ellipses; the hatched surface at the bottom of Figure 3.11(a) shows a representative ruled surface. The squares and circles mark the locations of the antipodal grasps with two approach directions, which are spread vertically. By varying the 12 variables, 24 objects with different geometries are efficiently generated, as shown in Figure 3.11(b).

Rectangular gripper jaws are selected for the simulations. Each jaw is covered with a soft silicon pad with 5mm thickness, as gripper jaws with compliant materials are widely used in robot grasping [30], [5] to increase grasp robustness. Figure 3.11(c) shows the meshed bodies (left) and the nodal solution (right) of a representative FEM simulation. A displacement (orange arrow) parallel to the grasp axis is applied as the load to each jaw. For each grasp location, three displacements in the range of 1–3 mm are applied, resulting in a total of

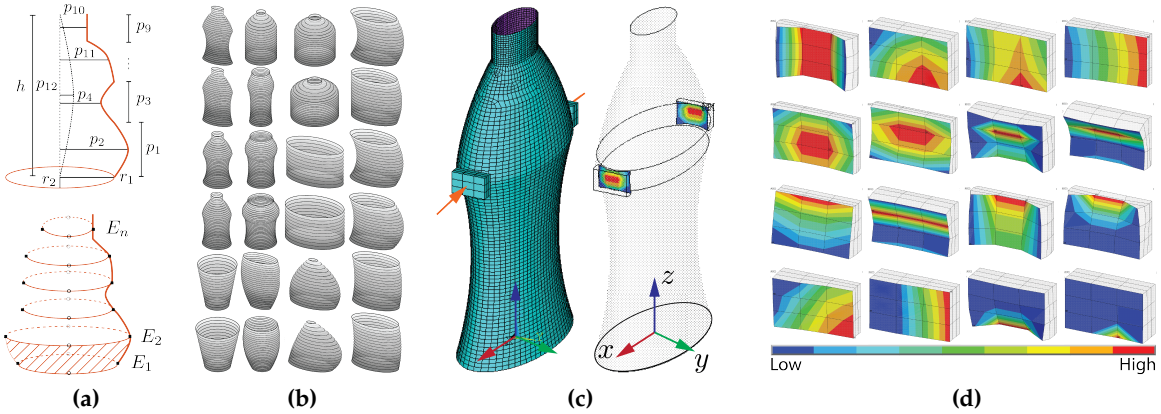

Figure 3.11: FEM simulations to create a large variety of contact profiles to evaluate the 6DLS models (adapted from [1] ©2021 IEEE). (a) Object model generator. (b) 24 rigid objects used for the simulations, where eight objects are asymmetric. (c) Meshed object and the nodal solution of a representative FEM simulation. (d) Representative contact profiles obtained from the simulations, where red means high pressure.

Table 3.3: Fitting error of the 6DLS models fit to frictional wrenches computed with contact profiles from 2,932 FEM simulations.

Quartic model	Ellipsoidal model
0.011 ± 0.006	0.019 ± 0.005

2,932 grasps. Figure 3.11(d) shows representative contact profiles with interpolated pressure values. Each contact surface consists of 3×3 rectangular elements and each element has a single pressure value. For each contact profile, 600 frictional wrenches are sampled and the two 6DLS models are fit to the normalized wrenches. Table 3.3 summarizes the means and standard deviations of the fitting errors. Similar to the results for the parametric surfaces in Section 3.5.1.3, the quartic model yields a lower fitting error. The low standard deviations of both models suggest that the proposed 6DLS models achieve consistent performance and are suitable for a large variety of contact profiles.

3.6 Chapter summary

This chapter presented two 6D limit surface models and two 6D contact wrench models for nonplanar frictional surface contacts. First, the 6D contact wrench is computed for a given contact profile and object motion. Next, the concept of a 6D limit surface is introduced to describe the 6D frictional wrench limit at a nonplanar surface contact. Due to the high computational effort of a 6DLS, ellipsoidal and quartic 6D limit surface models are presented to approximate the 6DLS. This chapter further introduced the ellipsoidal 6D contact wrench model, based on the ellipsoidal 6DLS and the normal wrench, to approximate the contact wrench limit. For scenarios with unknown grasp forces, this chapter presented the 6D friction cone, extended from the traditional friction cone of a point contact and the ellipsoidal 6D

contact wrench model. The 6DFC approximates the contact wrench constraints by considering any normal force magnitudes between 0N and the maximal grasp force of the physical robot. Finally, simulation results are presented to evaluate the proposed 6DLS models. Fitting results with six parametric surfaces and 2,932 FEM simulations showed that the quartic and ellipsoidal 6DLS models reached as low as 0.02 and 0.04 mean wrench error, respectively, which suggested that both models well describe frictional wrenches for a large variety of nonplanar surface contacts.

Chapter 4

Applications and Experiments

This chapter shows three applications of the proposed nonplanar frictional surface contact models with physical experiments:

1. Grasp success prediction for rigid known objects (Section 4.1). Two types of gripper jaws are used in the experiments: deformable plastic fin ray jaws and rigid jaws covered with deformable rubbers. The former creates elliptic cylindrical contact surfaces, while the latter creates arbitrary contact surfaces. The proposed models are further evaluated with a grasp dataset collected on the ABB YuMi robot with silicon gripper jaws.

2. Grasp planning for previously unseen rigid objects (Section 4.2). The proposed models are used to create a grasp dataset to train a hybrid grasp planner. Given a depth image, the planner outputs the optimal grasp for compliant gripper jaws to pick and place a novel rigid object.

3. Grasp planning for known deformable hollow objects, such as plastic cups and bottles (Section 4.3). A novel grasp quality metric, which is computed with the proposed models, is proposed to plan physical grasps.

Parts of the work presented in this chapter have been published in [1], [3], [6].

4.1 Grasp Success Prediction for Known Rigid Objects

This section presents the grasp analysis algorithms using the proposed nonplanar frictional surface contact models and physical experiments on grasp success prediction to evaluate the models.

4.1.1 Problem statement

The 6D limit surface models and the 6D friction cone are applied to predict grasp success for a vertical lifting task with a parallel-jaw gripper. One 6DLS or 6DFC model is computed for each gripper jaw and the grasp success is predicted with these two models by either building a GWS or solving an optimization problem.

4.1.1.1 Assumptions

In addition to the assumptions for the nonplanar frictional surface contact models described in Section 3.1, the following assumptions are required for the prediction:

1. Both jaws are in contact with the grasped object simultaneously. Specifically, the object is assumed to remaining static while grasping. This assumption is required to estimate the contact profiles for the experiments later introduced in Section 4.1.4.

2. The change of the contact profile is minor during the manipulation. Therefore, the frictional contact models are not recomputed during the manipulation.

3. Inertial terms (quasi-static physics) are neglected. Specifically, it is assumed that the robot arm lifts the object in a slow manner, so that the acceleration is negligible. The prediction can be too optimistic as the acceleration is not considered. For the scenarios with fast robot arm movement, the acceleration can be modeled as an additional external disturbance.

4.1.1.2 Metrics

The precision and recall of binary predictions on physical experiments are used as metrics. Denoting n_{tp} as the number of true positive predictions, n_{fp} as false positives, n_{fn} as false negatives, precision and recall are $n_{\text{tp}}/(n_{\text{tp}} + n_{\text{fp}})$ and $n_{\text{tp}}/(n_{\text{tp}} + n_{\text{fn}})$, respectively. A combination of high precision and recall indicates that the algorithm predicts few false positives and false negatives. Both metrics are commonly used for datasets with unequal class distributions in robot grasping applications [5], [36] and describe if the algorithm is overconfident or too conservative [179].

4.1.2 Grasp Analysis using Frictional Nonplanar Surface Contact Models

To analyze the total wrench that a grasp can exert on an object, one needs to combine the frictional contact model for each contact of the grasp. This thesis proposes two ways to combine them: building a grasp wrench space or solving a quadratic program (QP). While a GWS provides more conservative grasp wrench estimation due to the linearization techniques of the frictional constraints, it is less computationally efficient compared to solving a QP.

4.1.2.1 Grasp Wrench Space-based Grasp Analysis

Given a 6DLS or 6DFC for each contact of a grasp, this part introduces the process of building the GWS. Once the GWS is computed, one can use Equation (2.99) to predict grasp success and use GWS-based metrics in Section 2.5.5 to estimate the grasp quality for grasp planning.

Building a GWS with the nonplanar frictional surface contact models is similar to constructing it for planar area contacts (Section 2.4.3). However, the wrench basis introduced in Section 2.4.1 can be omitted for the nonplanar cases since the frictional constraints are in 6D.

Recall that the frictional constraints described in Section 3.3 are for one contact with respect to a local contact frame. The next step is to compute the contact wrench constraints

$\{\boldsymbol{c}_1, \ldots, \boldsymbol{c}_M\}$ by combining the constraints for the frictional and the normal wrench, where the latter is the wrench impressed by the pressure. Then, one computes the contact wrench constraints with respect to the object frame O, whose origin is at the center of mass $\boldsymbol{o}_{\text{COM}}$ of the grasped object.

Consider the nth contact with $n \in \{1, \ldots, N\}$. For instance, $N = 2$ for a parallel-jaw gripper if both jaws are in contact with the object. Given the contact surface $\mathcal{S}_n$ and the pressure distribution p_n, one can compute the linear frictional constraints $\mathcal{X}_n$ and the normal wrench $\boldsymbol{w}_{\perp_n}$ using Algorithm 1 as well as Equation (3.2), (3.19), and (3.20). Let $\boldsymbol{t}_n \in \mathbb{R}^3$ and $\boldsymbol{R}_n \in \mathbb{R}^{3\times3}$ be the translation and rotation of the nth local contact frame relative to the object frame, respectively. Denoting $\boldsymbol{s}^{\text{LS}}_{n,m} \in \mathcal{X}_n$ as the mth frictional constraint of the nth contact, the mth contact wrench constraint $\boldsymbol{c}_{n,m} \in \mathbb{R}^6$ with respect to $\boldsymbol{o}_{\text{COM}}$ is computed with

$$\boldsymbol{c}_{n,m} = \begin{bmatrix} \boldsymbol{R}_n & \boldsymbol{0} \\ \hat{\boldsymbol{t}}_n \boldsymbol{R}_n & \boldsymbol{R}_n \end{bmatrix} \left(\boldsymbol{s}^{\text{LS}}_{n,m} + \boldsymbol{w}_{\perp_n} \right) \tag{4.1}$$

where $\hat{\boldsymbol{t}}_n \in \mathbb{R}^{3\times3}$ is the cross product matrix of $\boldsymbol{t}_n$ and introduces an additional torque due to the change of frame.

Recall that Ferrari *et al.* [14] proposed two ways to build a GWS: by upper bounding the magnitude of each contact force individually for $\mathcal{W}_{L_\infty}$ or by bounding the sum magnitude of the contact normal forces for $\mathcal{W}_{L_1}$ (Section 2.4.3). The former is selected for the experiments described later in Section 4.1.3 since Krug *et al.* [62] suggested that the latter is overly conservative. The grasp wrench space $\mathcal{W}_{L_\infty}$ is

$$\mathcal{W}_{L_\infty} = \text{Conv}(\oplus_{n=1}^{N} \{\boldsymbol{c}_{n,1}, \ldots, \boldsymbol{c}_{n,m}, \ldots, \boldsymbol{c}_{n,M}\}) \tag{4.2}$$

where $\text{Conv}(\cdot)$ denotes the convex hull and $\oplus$ is the Minkowski sum operation. Algorithm 2 summarizes the process to build a grasp wrench space using the nonplanar surface contact models.

4.1.2.2 Solving a Quadratic Program

The grasp quality can also be accessed by solving a QP using Equation (2.100) with the outer linearized contact wrench constraints of a 6DLS with Equation (3.28) or a 6DFC with Equation (3.30).

4.1.3 Physical Experiments for Elliptic Cylindrical Contact Surfaces

The proposed nonplanar frictional contact models are applied to predict physical grasp success for a vertical lifting task in these experiments. Given the external wrench disturbance $\boldsymbol{w}_{\text{ext}}$, the friction coefficient μ, the gripper pose, and an estimated contact profile for each gripper jaw, the algorithm predicts if the grasp can counterbalance $\boldsymbol{w}_{\text{ext}}$ by checking if the opposite of $\boldsymbol{w}_{\text{ext}}$ is in the grasp wrench space, as summarized in Algorithm 2. The physical experiments are designed so that the uncertainties during the experiments are minimized.

Algorithm 2 Building a Grasp Wrench Space using 6DLS models.

Require:
- Friction coefficient μ
- External disturbance $\boldsymbol{w}_{\text{ext}}$
- Details of each contact
  - Contact surface $\mathcal{S}$
  - Pressure distribution p
  - Rotation $\boldsymbol{R}$ and translation $\boldsymbol{t}$ between the local contact and the object frame

Output: The grasp wrench space $\mathcal{W}$

for $n \leftarrow 1$ to N **do**
  // Find the 6DLS model $\boldsymbol{A}$ with Algorithm 1
  $\boldsymbol{A}, \boldsymbol{w}_{\text{max}} \leftarrow \mu, \mathcal{S}_n, p_n$
  // Linearizing the frictional constraints
  $\{\boldsymbol{s}_1^{\text{cube}}, \ldots, \boldsymbol{s}_M^{\text{cube}}\} \leftarrow$ Sampling a 6D hypercube
  $\{\hat{\boldsymbol{s}}_{n,1}^{\text{LS}}, \ldots, \hat{\boldsymbol{s}}_{n,M}^{\text{LS}}\} \leftarrow \boldsymbol{A}, \{\boldsymbol{s}_1^{\text{cube}}, \ldots, \boldsymbol{s}_M^{\text{cube}}\}$ // Equation (3.19)
  // Denormalizing the linear frictional constraints
  $\mathcal{X}_n \leftarrow \{\hat{\boldsymbol{s}}_{n,1}^{\text{LS}}, \ldots, \hat{\boldsymbol{s}}_{n,M}^{\text{LS}}\}, \boldsymbol{w}_{\text{max}}$ // Equation (3.20)
  $\boldsymbol{w}_{\perp_n} \leftarrow \mathcal{S}_n, p_n$ // Normal wrench with Equation (3.2)
  // Contact wrench constraints
  $\{\boldsymbol{c}_{n,1}, \ldots, \boldsymbol{c}_{n,M}\} \leftarrow \mathcal{X}_n, \boldsymbol{w}_{\perp_n}, \boldsymbol{R}_n, \boldsymbol{t}_n$ // Equation (4.1)
end for
$\mathcal{W} \leftarrow \{\boldsymbol{c}_{1,1}, \ldots, \boldsymbol{c}_{1,M}\}, \ldots, \{\boldsymbol{c}_{N,1}, \ldots, \boldsymbol{c}_{N,M}\}$ // Equation (4.2)
return $\mathcal{W}$

4.1.3.1 Experiment Setup

Figure 4.1 (left) depicts the setup of a KUKA robot arm and a SCHUNK parallel-jaw gripper mounted with customized deformable fin ray jaws [180] (blue). The rigid grasped objects are 3D-printed to control the contact surface.

A 3D-printed mechanical assembly (pink) is further attached to the grasped object to create different wrench disturbances $\boldsymbol{w}_{\text{ext}}$ by mounting weight plates at various locations. Such design allows large torques due to the long torque arms and efficient computation for $\boldsymbol{w}_{\text{ext}}$, and therefore, reduces uncertainties compared to grasping real life objects.

The next step is to define an object frame, as the GWS and $\boldsymbol{w}_{\text{ext}}$ are computed with respect to the origin of the object frame. The COM of the grasped object is selected as the origin in the experiments, instead of the COM of both the grasped object and the wrench disturbance assembly. This frame selection enables easier comparison between the grasp wrench spaces constructed with different contact models and does not affect the predictions as one can select an arbitrary reference point to compute torques, and therefore, the GWS.

Two approach directions are used to create $\boldsymbol{w}_{\text{ext}}$. Figure 4.1 (left) illustrates the x, y, z-axes of the object frame for a representative vertical and horizontal grasp with the x-axis parallel to the grasp axis. The wrench disturbance assembly generates $\boldsymbol{w}_{\text{ext}}$ in the (f_y, τ_x, τ_z)- and

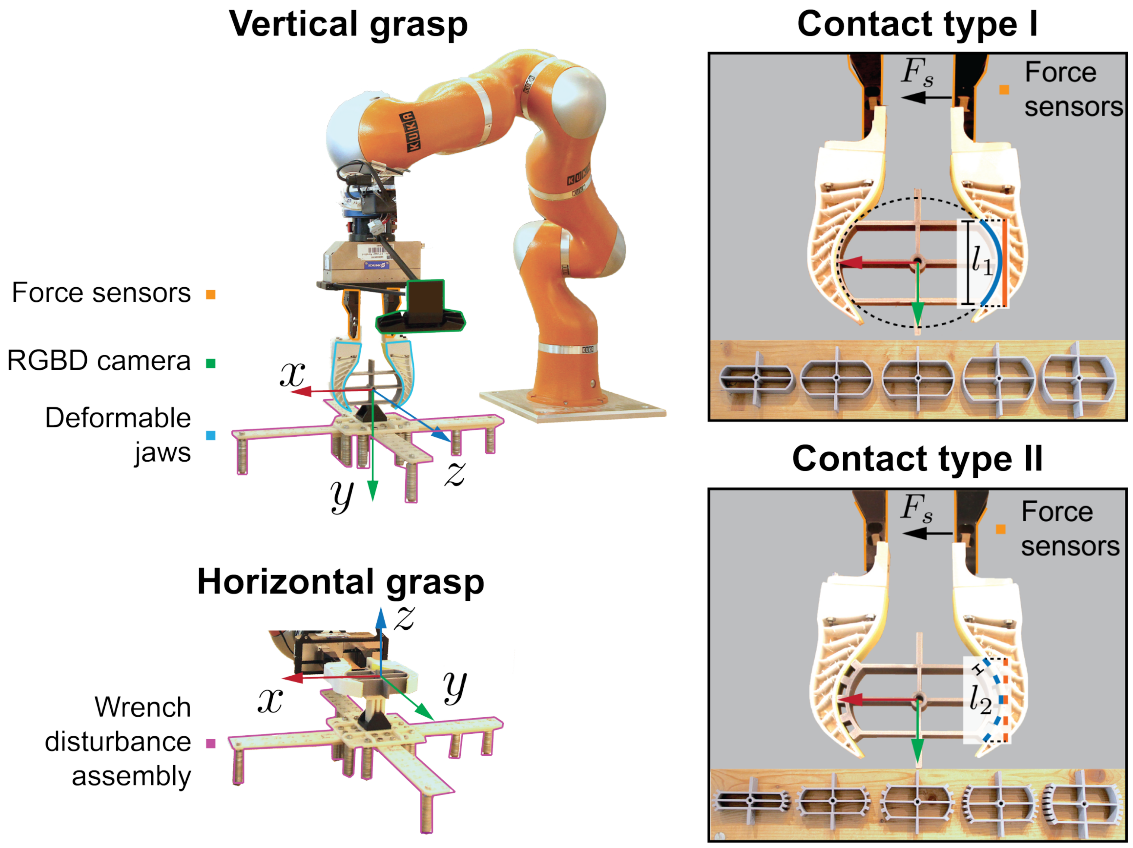

Figure 4.1: Experiment setup for grasp success prediction. Left: deformable gripper jaws (blue) grasp a 3D-printed object with nonplanar surfaces. The 3D printed assembly (pink) attached to the grasped object generates external disturbances. Right: Ten 3D-printed rigid objects that create two types of contact surfaces (adapted from [1] ©2021 IEEE).

(f_z, τ_x, τ_y)-space with the vertical and horizontal grasp direction, respectively. The locations of weight plates are selected so that the disturbances are well-scattered in each space.

A force sensor is mounted on each gripper jaw to measure the grasp force along the x-axis. An Intel RealSense SR300 RGBD camera (green) is mounted on the gripper to label the grasp success by tracking the object pose with the pcl library [181]. Specifically, the object point clouds captured at two poses, when the object was grasped and when it reached the highest point of the vertical lifting task, are compared using the Super4PCS algorithm [182] to detect the object pose change. If the object rotation angle and translation are below a threshold pair, the grasp is labeled as a success. However, the jaws' deformation during the manipulation also leads to a changed object pose, even though there is nearly no relative motion between the object and the gripper jaws. The threshold pair 5° and 9mm is selected so that about half of the physical grasps are successful. If the thresholds are high, the grasps will be labeled as a success even if there is a relative motion; whereas with low thresholds, the grasps will be labeled as a failure even if there is no relative motion but the gripper jaws deformed during the manipulation. The prediction results with different threshold pairs are discussed in Section 4.1.3.5, as robot applications have different tolerance of object motion during the manipulation. While assembly tasks require minimal object motion, bin-picking

allows larger object pose change. In future work, one can use a tactile sensor to label grasp success by detecting slips.

4.1.3.2 Contact Profile Estimation

The contact profile, including the contact surface $\mathcal{S}$ and the pressure distribution p, is estimated for each gripper jaw.

Figure 4.1 (right) shows two types of contact surfaces created by ten 3D-printed rigid objects. As illustrated on the top, the five object models of type I are cut from elliptic cylinders, whose horizontal radii are identical, whereas the vertical radii vary to change the surface curvature. The cylinders are cut so that the contact surface is the same when the grasp force of each jaw is higher than a threshold (20N). The contact surface is completely defined by the radii and the contact length l_1, which is depicted in Figure 4.1 (right). If the elliptic cylinders are directly used as the grasped objects, one needs to measure the contact surface for each trial as the surface increases with the grasp force. As shown on the bottom, each of the type II objects creates five or eight narrow planar contact surfaces with 3–5 mm width. The contact length l_2 of type II is defined as the length of each narrow surface. The direction of frictional forces are constrained to lie in each planar surface, as described in Section 3.2.4. Type II objects show that the contact surface can be nonplanar, even if the local contact surfaces are planar. Such discrete nonplanar surfaces also occur, for instance, when a silicon jaw pad deforms to the corner of a rigid cube. Both types of objects create ten different contact surfaces in total as the grasp forces used in the experiments are larger than the threshold and each object creates one contact surface. The effect of contact lengths on grasp prediction results is discussed in Section 4.1.3.5.

To estimate the pressure distribution, the contacts between the fin ray jaw and the rigid elliptic cylinders of type I are first simulated by using the FEM. Figure 4.2(a) shows the simulation results by applying a displacement on the jaw, as well as the interpolated pressure values of the contact. Although one can simulate each physical grasp for the contact profile, the system will be potentially computationally infeasible. Furthermore, one can observe that a change of the pressure distribution with a small translation of the object pose along the y-axis; therefore, it is difficult to align the exact same object pose in the simulation and the experiment. Hence, the pressure distribution is approximated with the power-law model proposed by Xydas *et al.* [80] based on the FEM simulation results. As the power-law model is originally evaluated with planar circular contacts, the model is modified in the thesis so that it applies to the contacts used in the experiments. For other types of contact surfaces, one can use the REACH model proposed by Danielczuk *et al.* [5] in Section 2.3.1.3, which approximates the contact profile between a rigid object and a gripper jaw mounted with a deformable pad. Section 4.1.4 presents physical experiments for arbitrary contact surfaces using the REACH model.

Figure 4.2(a) shows that the pressure along the z-axis is nearly constant but varies along the y-axis. Figure 4.2(b) shows the top view of the contact and the computation of the power-law model. The pressure distribution is assumed to be symmetric about the center $\boldsymbol{o}_g$ of the grasped object. Limitations of the assumption are discussed in Section 4.1.3.6. The modified

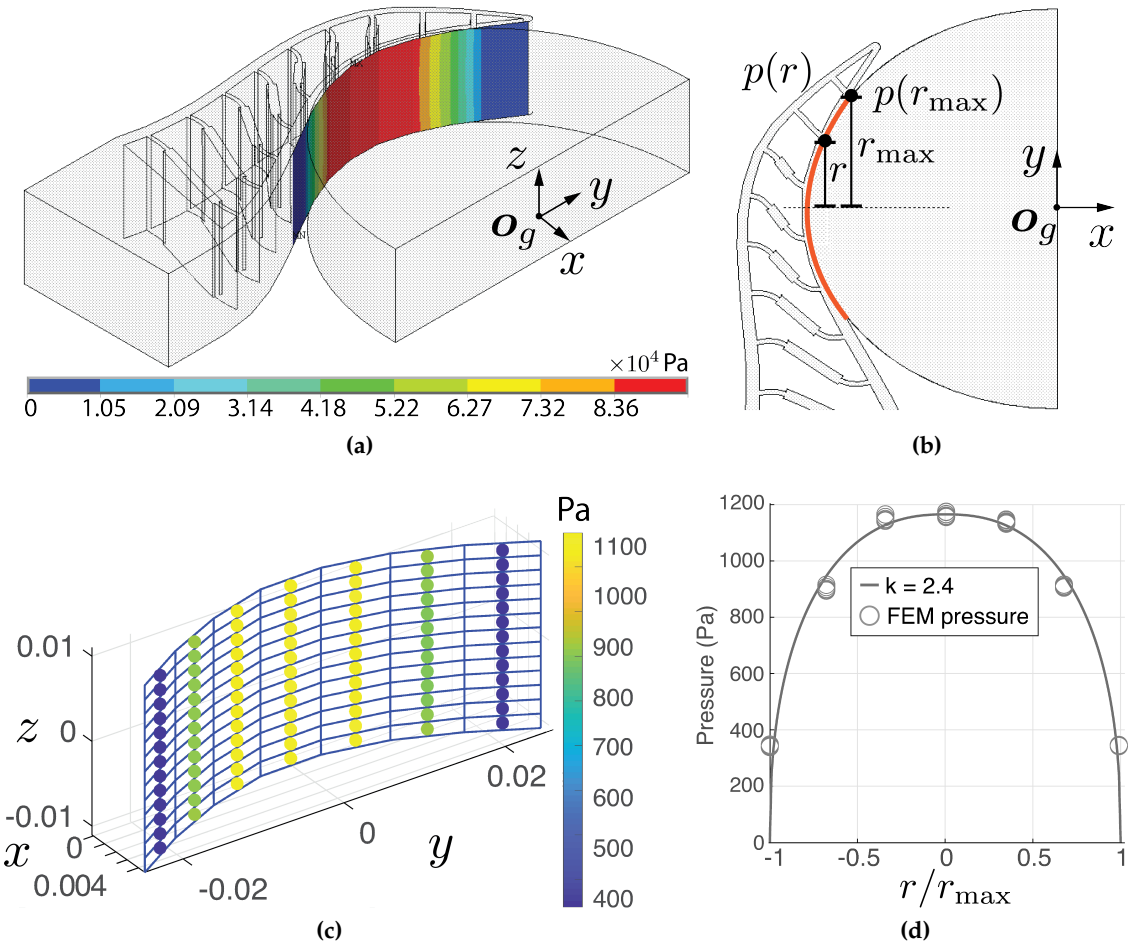

Figure 4.2: FEM simulation and the power-law pressure distribution of a nonplanar surface contact between a deformable fin-ray jaw and a rigid elliptic cylinder (adapted from [1] ©2021 IEEE). Pa in (a) and (c) is short for pascal, which is the unit of pressure.

power-law model expresses the pressure at a point as a function of the y component of the distance between the point to $\boldsymbol{o}_g$, denoted as $r \geq 0$. Let $r_{\max}$ be the y component of the maximal distance between any point on the contact surface to $\boldsymbol{o}_g$ and $\hat{p}(r_{\max}) = 0$, the normalized power-law pressure distribution is

$$\hat{p}(r) = p_0 \left[1 - \left(\frac{r}{r_{\max}} \right)^k \right]^{1/k}. \tag{4.3}$$

The exponent $k \in \mathbb{R}^+$ controls the shape of the pressure distribution and $\hat{p}(r)$ is a uniform pressure distribution with $k = \infty$. p_0 is a normalization constant such that $\int_{\mathcal{S}} \hat{p}(r)\, \mathrm{d}\mathcal{S} = 1$. Figure 4.2(c) illustrates the extracted contact surface with a normalized pressure distribution $\hat{p}$ from the FEM simulation, where each element has a single pressure value. Figure 4.2(d) depicts the pressure values from Figure 4.2(c) as a function of $r/r_{\max}$ and a power-law model with $k = 2.4$ fit to the pressure values. The pressure values, depicted as circles in Figure 4.2(d), are close to the curve, which suggests that the power-law model is an applicable approximation for the nonplanar contact surfaces used in these experiments. However,

there is an interesting observation that the exact k value varies from 2.4 to 5.5 for the elliptic cylinders under different loads during the FEM simulations. Therefore, the grasp success prediction results with different k values are discussed in Section 4.1.3.5.

Next, $\hat{p}$ is scaled so that the normal force of each contact matches the force sensor reading F_s. As shown in Figure 4.1 (right), F_s measures $\|f_{\perp_x}\|$, the magnitude of the x component of the normal force; therefore, $\hat{p}$ is scaled so that $\|f_{\perp_x}\| = F_s$. Thus, $\|\hat{f}_{\perp_x}\|$ is computed with $\hat{p}$ using Equation (3.2) and obtained the pressure distribution $p(r) = \lambda_p \cdot \hat{p}(r)$ with $\lambda_p = F_s / \|\hat{f}_{\perp_x}\|$.

4.1.3.3 Evaluated Contact Models

The following contact models are evaluated for physical grasp success prediction

- *3DLS-planar*: the traditional planar area contact models. As shown in Figure 4.1 (right), a planar contact surface (orange line) is created by projecting the nonplanar surface (blue line) along the x-axis onto the yz-plane. The frictional wrenches are computed in the (f_y, f_z, τ_x)-space and the 3DLS models are fit to the wrenches.
- *6DFW*: 6D frictional wrenches (6DFWs) are computed for a nonplanar surface contact. The 6DFWs of each jaw are directly used to construct the GWS without a LS model. The GWS is built by first computing the minkowski sum of the 6DFWs from the left and right contacts, then compute the convex hull of the minkowski sum results.
- *3DLS-nonplanar*: the 3DLS models are fit to the three major components, f_y, f_z, τ_x, of the 6DFWs, while the remaining three components are set to zero [4].
- *6DLS*: the proposed 6DLS models are fit to all components of the 6DFWs.

There are in a total of seven baseline contact models, as each LS model has the quartic and ellipsoid variants. Note that the 6DFC model is not evaluated in these experiments since one expects that the 6DFC will likely have similar results as 6DLS for such grasps, where the contacts of the left and right jaws are symmetric and the grasp force is known.

4.1.3.4 Grasp Success Prediction Results

For the experiments, 115 well-distributed wrench disturbances for the ten grasped objects. For each disturbance, three grasp forces in the range of 20–35 N are randomly chosen. By repeating each grasp three times, 1,035 physical grasps are collected. Each grasp is followed by a slow vertical lifting so that the acceleration affects the disturbances minimally. For the scenarios with a medium to high moving speed of the robot arm, one can model the acceleration of the grasped object as an additional external disturbance as the current algorithm neglects the inertial terms. The friction coefficient $\mu = 0.3$ is experimentally determined and the power-law pressure distribution with $k = 2.4$ is used for each contact. The predictions with each model are ran five times and precision and recall are used to evaluate the results. Note that precision is inversely related to the number of false positive predictions, whereas high recall indicates low false negatives. The F_1 score and the accuracy of each model are also computed. Specifically, the F_1 score is a harmonic mean of the precision and recall and

Table 4.1: Prediction results of 1,035 physical grasps for the ten objects of type I and II.

Contact model	LS model	Precision (%)	Recall (%)	F_1 score (%)	Accuracy (%)
3DLS-planar	Quartic	68.2±0.1	46.8±0.1	55.5±0.1	59.9±0.0
	Ellipsoid	**71.0±0.2**	50.8±0.2	59.2±0.2	62.6±0.2
6DFW	None	63.2±0.5	64.5±1.2	63.9±0.8	61.0±0.7
3DLS-nonplanar [4]	Quartic	66.0±0.1	64.4±0.2	65.2±0.1	63.3±0.1
	Ellipsoid	67.6±0.3	68.4±0.3	68.0±0.2	65.6±0.2
Proposed 6DLS	Quartic	65.7±0.1	73.5±0.4	69.4±0.2	65.3±0.1
	Ellipsoid	66.8±0.0	**76.9±0.2**	**71.5±0.1**	**67.3±0.1**

is computed with 2·precision·recall/(precision + recall). The accuracy is computed with the number of correct predictions divided by the number of all samples. Table 4.1 shows the means and the standard deviations of the seven baseline models for grasps with both object types, as similar results for object type I and II are observed during the experiments.

Table 4.1 shows that the proposed 6DLS models outperform the 3DLS-planar, the 6DFW, and the 3DLS-nonplanar by up to 26%, 12%, and 9% in recall, respectively, while maintaining a comparable precision. High recall indicates that the 6DLS models reduce false negatives, and therefore, avoids unnecessary grasp force and grasp pose adaptations in robot manipulation. In addition, the 6DLS models also increase the F_1 score and accuracy by up to 16% and 7% compared to the remaining models. Furthermore, the standard deviation of 6DFW is higher as the frictional wrenches are randomly sampled. Hence, in addition to a higher accuracy, a limit surface model also increases repeatability in predictions.

One can further observe that the ellipsoidal LS models slightly outperform the quartic ones even though the quartic achieves a lower wrench fitting error, as shown in Section 3.5.1.3. Figure 4.3(a) shows the convex hulls in the first quadrant of a 2D projection of the GWSs constructed with an ellipsoidal and a quartic 6DLS linearized with 728 points. The difference between the two GWSs is small, as the LS models are not densely sampled for linearization due to the high computational complexity of the Minkowski sum operation. Fewer samples on the LS model lead to an overly conservative LS approximation due to the convex hull operation.

The following shows the comparison between GWSs constructed with the 6DFW and the three ellipsoidal LS models. Figure 4.3(b) shows the 2D projections of the GWSs. The GWS constructed with the proposed 6DLS is larger than with the 3DLS models, as it considers the full 6D frictional wrenches, and therefore, reduces false negatives. Note that the τ_y^{GWS} and τ_z^{GWS} components of the GWS constructed with the 3DLS-planar and the 3DLS-nonplanar models are not zero, because although the 3DLS models did not consider the frictional torques τ_y and τ_z with respect to the pressure center when computing the LS, the frictional forces introduced an additional torque when constructing the GWS due to the change

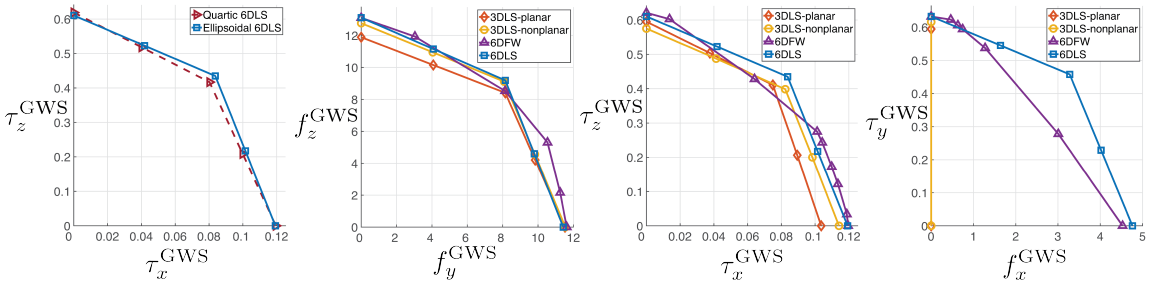

Figure 4.3: 2D projections of a representative 6D grasp wrench space constructed (a) with a quartic and an ellipsoidal 6DLS model, (b) with the 6DFW and the ellipsoidal limit surface models (adapted from [1] ©2021 IEEE).

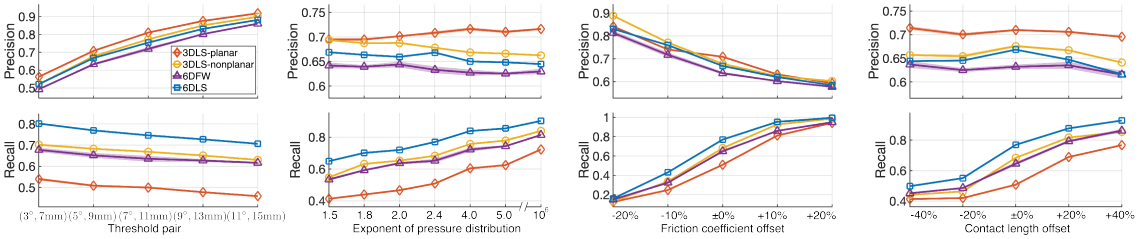

Figure 4.4: Precision and recall for each contact model as a function of (a) the threshold pairs in increasing order, (b) the exponent k of the power-law pressure model [80] with $k = 10^6$ being close to a uniform distribution, (c) friction coefficient offset with $\pm 0\%$ meaning the experimentally determined value $\mu = 0.3$, (d) contact length offset with $\pm 0\%$ meaning the measured contact length l_1 or l_2 for the two contact types, respectively. The contact area increases with the contact length (adapted from [1] ©2021 IEEE).

of frame using Equation (2.78). Although the 6DFW also considers 6D frictional wrenches, the constructed GWS is not symmetric, as the initial frictional wrenches are randomly sampled, resulting in worse and less repeatable prediction results. The largest difference between the GWSs constructed with the 6DLS and the 3DLS is the f_x^{GWS} component, as shown in the right of Figure 4.3(b). The f_x^{GWS} component of the GWSs constructed with both 3DLS models is zero as they do not consider the frictional force component f_x and the normal forces of the left and the right jaws cancel out. However, force disturbances along the x-axis are not evaluated in the experiments as the x-axis is the grasp axis.

4.1.3.5 Sensitivity Analysis

As each of the contact models contains several parameters, such as friction coefficient, pressure distribution, this thesis includes an analysis of each model's sensitivity to a subset of these parameters. Figure 4.4 shows the precision and recall of the 6DFW and the ellipsoidal LS models with shaded error bars showing the standard deviations of five runs of each model.

Effect of Threshold Pairs As described in Section 4.1.3.1, the grasp is labeled as a success if the object rotation and translation are below a threshold pair. The prediction results are compared with five threshold pairs in increasing order, where the second pair is used to evaluate the models in Section 4.1.3.4. With an increasing threshold, the precision of each model increases, as more grasps are labeled as success and the number of true positive predictions increases, whereas recall decreases because the models predict more false negatives. Figure 4.4(a) further shows that the proposed ellipsoidal 6DLS has the highest recall with similar precision for all thresholds. A large threshold pair is suitable to robot applications such as bin-picking, as the exact object pose is not critical to the manipulation success. With precision (88%) higher than recall (71%), the 6DLS model becomes conservative for such applications, but still increases recall by up to 24% over the remaining three baseline models.

Effect of Pressure Distributions As the exponent k of the power-law pressure distribution [80] changes with contact surfaces and grasp forces, the effect of k is also analyzed. Note that the pressure distribution is close to uniformity with $k = 10^6$. Figure 4.4(b) shows that the recall of each contact model increases with k as the frictional torque of each contact increases and the models predict more positives.

Effect of Friction Coefficients Figure 4.4(c) illustrates the prediction results with different friction coefficient offsets. The symbol $\pm 0\%$ indicates that the models used the experimentally determined value $\mu = 0.3$ and $+10\%$ offset represents $\mu = 0.33$. The predictions of all baseline models are relatively sensitive to μ as a LS linearly scales with μ. For scenarios with an unknown friction coefficient, one can select a lower μ value for conservative predictions as each model predicts fewer positives.

Effect of Contact Lengths Figure 4.4(d) illustrates the results with different contact length offsets. The symbol $\pm 0\%$ indicates that the models used the measured contact length l_1 and l_2 for the two contact types illustrated in Figure 4.1 (right). The recall of each baseline model increases with the contact length as the surface area and the frictional torque of each contact also increases.

4.1.3.6 Discussion

The power-law pressure distribution described in Section 4.1.3.2 is based on the assumption that the pressure is symmetric about the object center. However, the results shown in [20] suggest that the pressure distribution can be asymmetric depending on the object pose relative to the fin ray jaw. With the vertical grasp direction shown in Figure 4.1 (left), an asymmetric pressure distribution leads to a component of the normal force that is parallel to the gravity direction, and therefore, affects the prediction results. Furthermore, contact profiles can change during the manipulation due to the jaws' deformation. One way to address the two limitations is to relax the assumption of a constant symmetric contact profile and to constantly predict grasp success with updated profiles captured with deformable tactile sensors such as GelSlim [24] or the tactile fingertip sensors by Romero *et al.* [26]. A tactile sensor

can further better detect relative motions between the grasped object and the jaws compared to tracking object poses using point clouds.

The contact surfaces evaluated in the physical experiments in this section are restricted in (discrete) elliptic cylinders due to the design of the fin ray jaws. Therefore, the next experiments are designed to evaluate the proposed models for various contact profiles created by gripper jaws covered with compliant materials.

4.1.4 Physical Experiments for Arbitrary Contact Surfaces

The proposed 6DLS and 6DFC models are evaluated with various contacts caused by compliant gripper jaws contacting adversarial objects, which are objects without parallel surfaces, hence especially difficult to grasp. The grasps are sampled in simulation. To compute the corresponding physical grasp pose, the transformation of the object pose from simulation to real world is estimated by using the Super4PC algorithm [182]. Specifically, the object pose transformation is estimated by matching the synthetic and real point cloud of the grasp object. The grasp success prediction results are evaluated based on the physical grasp success and the predicted grasp quality using the robust wrench resistance metric (Section 2.5.3.2) by solving a quadratic program (Section 4.1.2.2).

4.1.4.1 Contact Profile Estimation using the REACH Model

The contact profiles, which is the input of a frictional contact model, are computed using the REACH model [5] (Section 2.3.1.3). Figure 4.5 shows the contact profiles between a representative adversarial object and the SCHUNK gripper with two compliant jaws. The redder colors indicate higher pressure values. Note that the deformed shape of the jaws are not visualized in this figure.

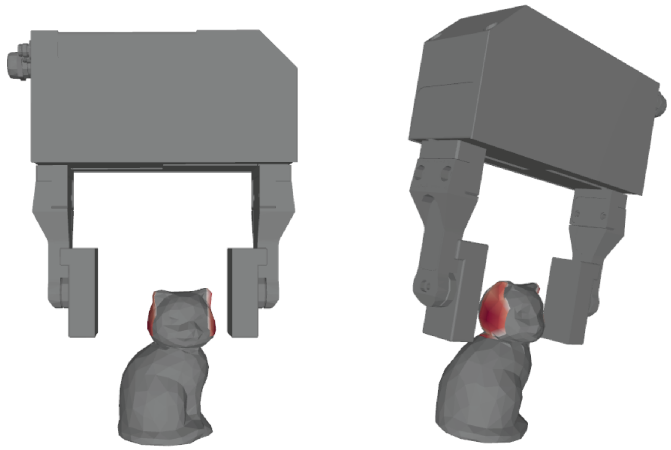

(a) (b)

Figure 4.5: Contact profiles of nonplanar surface contacts estimated by the REACH model [5].

4.1.4.2 Experiment Setup

A KUKA robot with a SCHUNK parallel-jaw gripper is used to collect physical grasps, as depicted in Figure 4.6. Each gripper jaw is mounted with a deformable rubber layer of 5 mm thickness. As illustrated in Figure 4.6(b), nonplanar surface contacts are created when the jaws contact an object with nonplanar local geometry. An overhead Intel RealSense D455 RGBD camera is mounted to capture object pose for the sim2real object pose transfer.

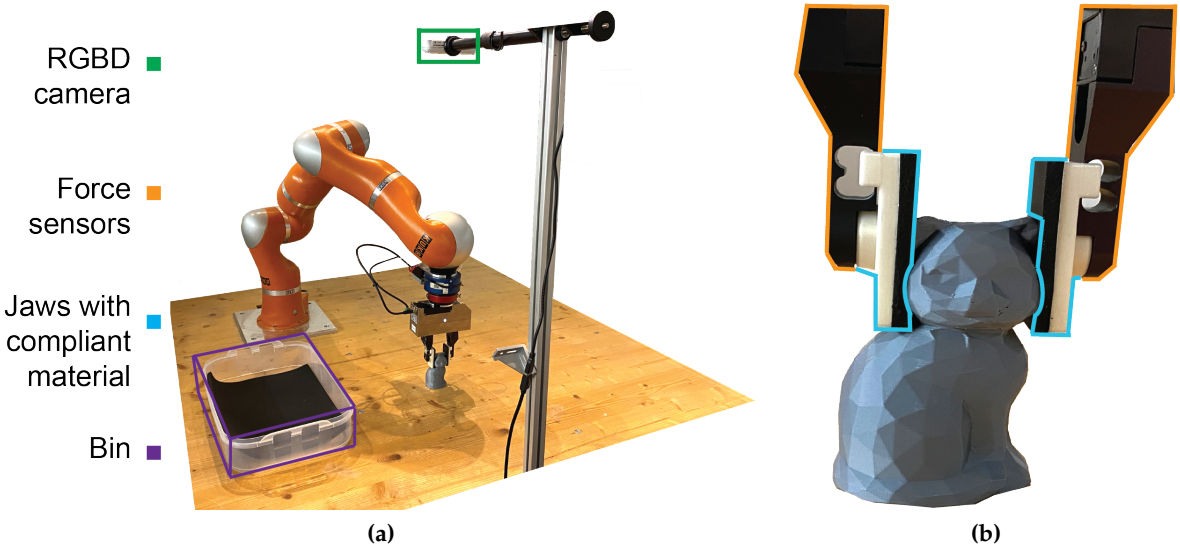

Figure 4.6: (a) Robot setup for grasp success prediction and grasp planning. (b) An enlarged view of representative nonplanar surface contacts caused by compliant gripper jaws deformed to the grasp object.

A total of 920 physical grasps are collected for the experiments. Specifically, eight adversarial objects are selected for the experiments, as shown in Figure 4.7. For each object, 24 different grasps are planned in the simulation with each grasp being executed with a physical robot for five trials. For each physical grasp, the gripper slowly closes until the 20N normal force of each jaw is reached. A grasp is considered as a success if it lifts the object and places it in the bin, which is illustrated in Figure 4.6(a) as a purple box.

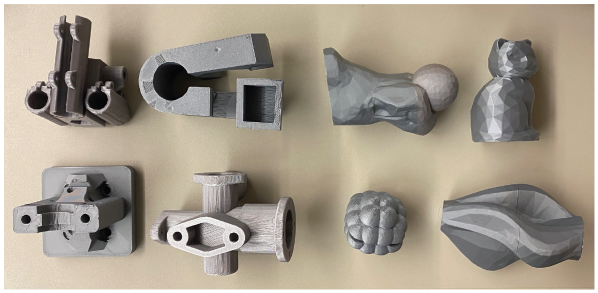

Figure 4.7: Physical objects for the grasp success prediction experiments using KUKA Robot with SCHUNK parallel-jaw gripper and RealSense D455 RGBD camera.

4.1.4.3 Evaluated Contact Models

Four contact models are used to predict the grasp success. Specifically, each contact model provides different contact wrench constraints for the quadratic program in Equation (2.100).

- *Soft Point Contact (Point)*: As described in Section 2.3.5.2, this algorithm constrains the wrench applied at the contact through a set of linearized 4D contact wrench constraints in Equation (2.50) with an additional constraint $f_\perp \leq 20$, where 20N is the maximum normal force that can be applied at the contact.

- *Planar Area Contact (Planar)*: As described in Section 2.3.3.3, this algorithm assumes a planar area contact and uses the ellipsoidal limit surface model as the frictional constraints. To find the plane that fits best to the nonplanar contact surface, the principal component analysis (PCA) is performed on the vertices of the contact surface obtained by the REACH model. The two most significant components define the plane.

- *Ellipsoidal 6D limit surface model (6DLS)*: This algorithm constructs the ellipsoidal 6DLS model by the $f_\perp = 20N$ using the least square method (Section 3.3.4.2). Then the contact wrench constraints in Equation (3.28) are obtained by linearizing the 6D ellipsoid and combines them with the normal wrench.

- *6D friction cone (6DFC)*: This algorithm constructs a 6D friction cone and uses the linearized outer frictional constraints in Equation (3.30) as the contact wrench constraints.

4.1.4.4 Metrics

Both average precision (AP) and average recall (AR) are used as metrics for each object using the dataset's ground-truth physical grasp labels and each algorithm's predictions. The performance is measured with mean average precision (mAP) and mean average recall (mAR), which are the AP and AR of the algorithm averaged over all objects to account for discrepancies in the number of successful grasps for each object. Runtime per grasp computation is also measured for each model on the an Ubuntu 16.04 machine with a 12-core 3.7 GHz i7-8700k processor.

4.1.4.5 Results

Table 4.2 shows the prediction results for the four frictional contact models. The 6DLS and 6DFC algorithms can increase mAP by 4% and mAR by 21% and 25%, respectively, over the traditional soft point contact model. The 6DFC has higher recall than 6DLS as it is less conservative. One can expect a higher increase in mAR with the 6DFC for grasps with unknown normal forces, since the 6DFC considers all normal forces between 0–20 N of each jaw, whereas the normal force is controlled to be 20N in these experiments. Furthermore, the prediction performance with all models can be enhanced with a RGBD camera that provides high-quality depth images, so that the sim2real object pose transformation can be estimated

Frictional Contact Model	mAP	mAR	Runtime (ms/grasp)
Point	0.67 ± 0.01	0.40 ± 0.01	$\mathbf{14.2 \pm 0.8}$
Planar	0.68 ± 0.01	0.48 ± 0.01	41.3 ± 0.4
6DLS (proposed)	$\mathbf{0.71 \pm 0.00}$	0.61 ± 0.01	235.9 ± 2.0
6DFC (proposed)	$\mathbf{0.71 \pm 0.01}$	$\mathbf{0.65 \pm 0.01}$	245.4 ± 2.3

Table 4.2: Results of physical grasp success using KUKA robot arm, SCHUNK gripper, and Intel RealSense SR300 RGBD camera.

more accurately. Therefore, this thesis further evaluates the proposed frictional contact models with physical experiments using high-quality RGBD camera and a gripper without force sensors.

4.1.4.6 Experiments using High Resolution RGBD Camera

The proposed 6DLS and 6DFC are further evaluated on physical grasps collected with grippers without force sensors and a high-resolution RGBD camera. Specifically, the proposed models are evaluated on 1,500 grasps on 12 3D-printed adversarial objects from the Soft Area-Contact Physical Robot Grasp Dataset [5], collected on a physical ABB YuMi robot with a compliant parallel-jaw gripper and the PhotoNeo Phoxi RGBD camera. Although exerted forces are not actively controlled, as the gripper does not have force sensors, the upper limit of the closing force is known.

Results in Table 4.3 show that the 6DFC can increase the recall by as much as 17% over existing models while maintaining a similar mAP. Furthermore, the precision and recall shown in Table 4.3 are up to 13% and 10% than results in Table 4.2 largely due to the higher quality of the depth images.

Frictional Contact Model	mAP	mAR	Runtime (ms/grasp)
Point	0.80 ± 0.01	0.50 ± 0.01	$\mathbf{13.0 \pm 2.7}$
Planar	0.75 ± 0.01	0.55 ± 0.01	43.9 ± 0.6
6DLS (proposed)	$\mathbf{0.83 \pm 0.02}$	0.60 ± 0.01	247.9 ± 9.6
6DFC (proposed)	0.82 ± 0.01	$\mathbf{0.67 \pm 0.01}$	251.6 ± 14.2

Table 4.3: Prediction results of physical grasp success using ABB YuMi robot and PhotoNeo Phoxi RGBD camera.

4.1.4.7 Discussion

Experiments with two physical setups show that the proposed nonplanar frictional surface contact models increase mAP and mAR by up to 4% and 25% compared to the traditional soft point contact model, respectively. One observation is that the 6DFC accurately predicts

success of dynamic grasps, where the object moved when the gripper jaws close. However, the 6DFC algorithm also predicts false positives. One hypothesis is that the 6DFC allows different contact forces of each jaw, which is not feasible with the current physical setup. In future work, one can evaluate 6DFC with a three-jaw gripper that allows fully controllable forces to further investigate this effect.

4.2 Grasp Planning for Previously Unseen Rigid Objects

The second application of the proposed nonplanar frictional surface contact models is grasp planning, which addresses the problem of detecting the optimal grasp to manipulate an object for the desired task. A frictional contact model is commonly applied in analytical or hybrid grasp planning algorithms. One limitation of the former is that it requires prior knowledge such as the geometry and the mass of the object to plan grasps, which is less realistic in an unstructured environment. Therefore, building on Dex-Net and GQ-CNN (Section 2.6.1), this thesis proposes a hybrid grasp planner, which detects grasps with compliant gripper jaws for previously unseen, or novel, rigid objects. While the pipeline of the proposed hybrid planner is similar to Dex-Net 4.0 [36], the grasp dataset, which is required to train the planner, is generated based on the nonplanar frictional surface contact models, instead of the soft point contact model. The next part introduces details about the grasp dataset and the synthetic depth images, as well as the physical experiments to evaluate the grasp planners based on different frictional contact models.

4.2.1 Problem Statement

Given a depth image, the proposed grasp planner outputs the optimal grasp pose to lift and place a novel object. Note that the planned grasp is restricted to top grasps, which means that the gripper approaches the object from the top. To create a grasp dataset, the assumptions for the nonplanar frictional surface contacts and grasp analysis listed in Section 3.1 and Section 4.1.1, respectively, are required. The quality of a grasp in the dataset is computed with the robust wrench resistance metric (Section 2.5.3.2) by solving the quadratic program in Equation (2.100).

4.2.2 Dataset Generation

The pipeline to generate the grasp dataset in simulation is similar to finding the grasp quality map for an analytical grasp planner, as illustrated in Figure 1.2(b). Given the mesh of an object, the first step is to sample the grasp candidates. Then, the quality of each candidate is computed based on the selected frictional contact model.

This thesis uses the grasp sampling algorithm proposed by Mahler *et al.* [89], which is a variation of [183], and is suitable for objects with an arbitrary geometry. The idea is to first generate a contact point by sampling the object surface. For each contact point, the direction of the grasp axis is further sampled within the friction cone at the point by assuming a point contact. Sampling within the friction cone eliminates potential nonrobust grasps, hence re-

duces the search space of the grasp candidates. One can use a larger friction coefficient for the cone to preserve more grasps. Finally, the second contact point on the object can be computed from the first point, the grasp axis direction, and the gripper width. These two contact points define a grasp. The grasp is considered as a candidate if it is not in collision with the grasp object or the objects in the work space, such as the table.

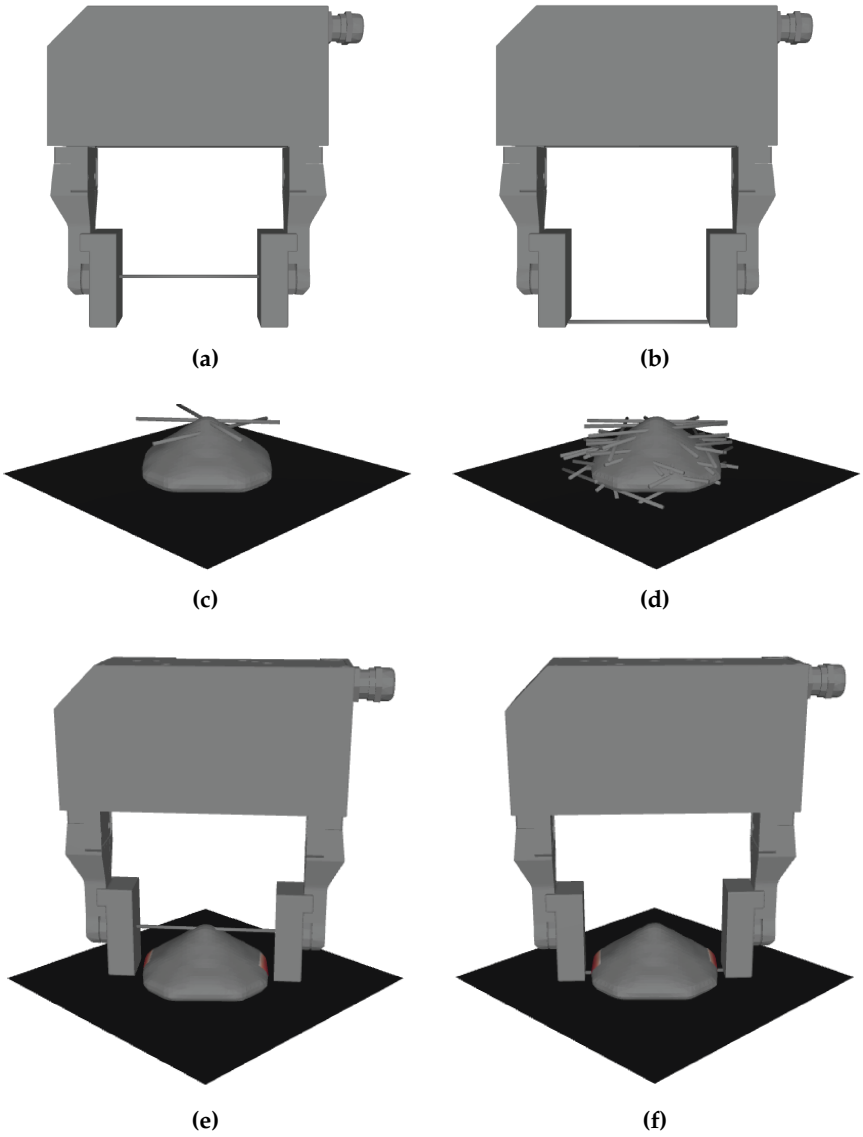

Figure 4.8: Comparison of two grasp axis definitions. (a)(c)(e): grasp candidates, where the grasp axis is between the center of two jaws; (b)(d)(f): grasp candidates, where the grasp axis is between the bottom of the jaws.

Next, the grasp axis needs to be defined. Intuitively, the grasp axis can be the axis between the center of two gripper jaws, as illustrated in Figure 4.8(a). However, with this grasp axis definition, there are only a limited number of sampled grasps for flat objects, as the remaining grasps may collide with the table underneath the object. Figure 4.8(c) shows the sampled grasps for a representative flat object from the EGAD dataset [184]. Figure 4.8(e)

illustrates one of the grasp candidates with the contact profiles estimated by the REACH model. To address this issue, this thesis defines the grasp axis as the axis between the bottom of the two jaws, as shown in Figure 4.8(b). Figure 4.8(d) shows that more grasps can be sampled for the same object with the new grasp axis definition. A representative grasp candidate with the new axis is presented in Figure 4.8(f).

As the second step to generate a grasp dataset, the quality of each grasp candidate is computed based on the selected frictional contact model using the robust wrench resistance metric (Section 2.5.3.2). Figure 4.9(a)–(d) show the grasp quality maps for the EGAD flat object computed with the soft point contact, planar area contact, the ellipsoidal 6DLS model, and the 6DFC, respectively. Figure 4.9(e)–(h) present the highest-quality grasp among these candidates with the respective frictional contact model. Figure 4.9(a) shows that the soft point contact model is overly conservative as the grasp qualities are less than or equal to 0.2, while the highest-quality grasp depicted in Figure 4.9(e) will likely fail during the physical robot execution. While the planar area contact model finds the same highest-quality grasp in (f) as the 6DLS in (g) and the 6DFC in (h), it is also too conservative. A grasp planner with such conservative frictional contact models will likely fail to find any grasps to lift up the object. Figure 4.9(c) and (d) show that the grasp qualities computed with the 6DLS and 6DFC are similar for this object.

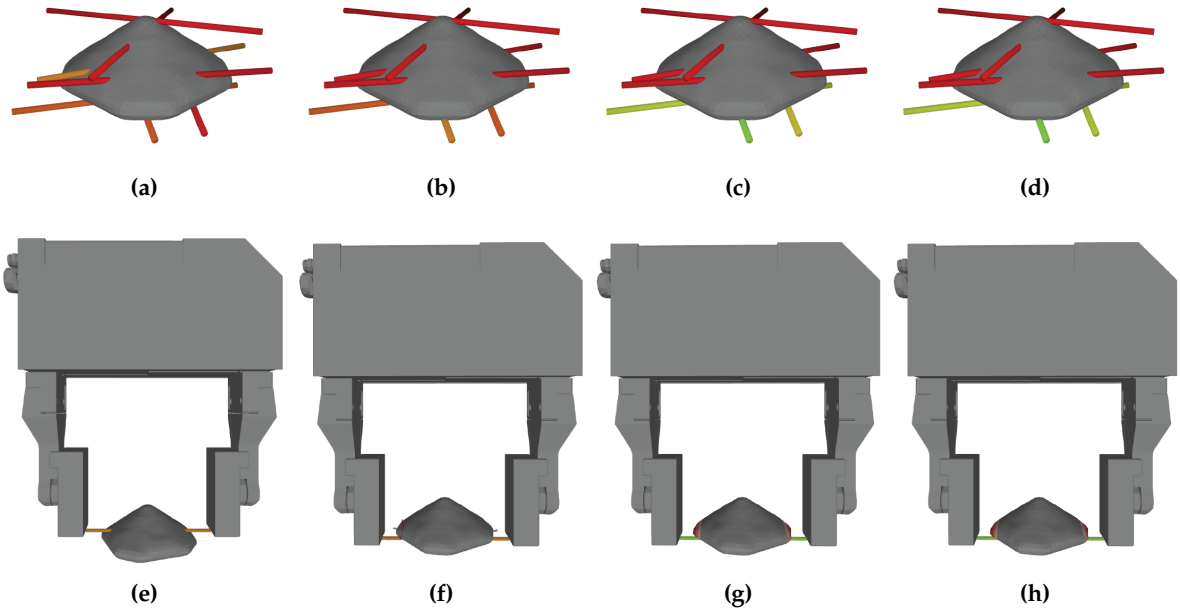

Figure 4.9: Quality of grasp candidates computed with four frictional contact models. (a)–(d): Grasp maps computed with the four models. (e)–(h) the highest-quality grasp among the corresponding candidates. (a)(e) grasps with the point contact model; (b)(f) grasps with the planar area contact model; (c)(g) grasps with the ellipsoidal 6DLS model; (d)(h) grasps with the 6DFC.

For each frictional contact model, a grasp dataset containing over 500K grasp candidates for 1,080 meshes from Dex-Net 1.0 [89] is created. For a grasp dataset, N_s synthetic depth images are rendered for each grasp by randomly sampling N_s camera poses within a range.

Specifically, the height of the overhead camera is fixed, same as in the physical experiments. The x- and y- coordinates of the camera are sampled with the object being fixed on the table, which is equivalent to sampling the object poses relative to a fixed overhead camera. Each depth image is cropped to 96×96 around the grasp center and rotated so that the grasp axis is horizontal. In this thesis, $N_s = 5$ depth images are rendered for each grasp. Therefore, there are over 2,500,000 synthetic depth images to train the GQ-CNN for each model.

4.2.3 Physical Experiments

The grasp planners based on three frictional contact models are evaluated for a pick-and-place task. Note that the planar area contact model is not evaluated as [5] suggested that it is worse than soft point contact in grasp success prediction with compliant gripper jaws. The robot setup is illustrated in Figure 4.6, which is identical to the setup for grasp success prediction. A singulated object is placed on the table and a depth image is taken and fed into GQ-CNN. The highest-quality collision-free grasp is executed. If no grasps are found, a new depth image will be taken and passed to GQ-CNN. This process is repeated up to ten iterations. Note that the grasps from GQ-CNN may differ at each iteration as the grasp sampling process has randomly sampled parameters and the depth images can be slightly different, for instance, at the edges on the object. A grasp is considered as a success if it lifts the object and places it into the bin on the table. A grasp is labeled as a failure if it fails to place the object or no grasps can be found by GQ-CNN after ten iterations.

The physical grasps are collected on 32 objects, including eight adversarial training objects [90] and 24 novel objects from the YCB dataset [185], the EGAD dataset [184], and novel household objects, as shown in Figure 4.10, where the eight training objects are above the dashed line in the figure.

Figure 4.10: 32 physical objects for the grasp planning experiments. The objects with a green underline are flat objects, which are potentially difficult to grasp.

Each object is grasped ten times with different stable poses. The stable poses are the same for each frictional contact model to enable a fair comparison. There are in a total of 80 grasps for the training objects and 240 grasps for the novel objects for each model.

4.2.3.1 Metrics

Two metrics are used to evaluate the performance of GQ-CNN

1. *Grasp Success Rate*, which is the rate of successful grasps among all executed grasps. A higher grasp success rate means that the grasp planner can find more robust grasps.

2. *Precision and Recall*, which are computed with the estimated grasp quality from GQ-CNN and the physical grasp success. A combination of high precision and high recall indicates that GQ-CNN accurately predicts the quality of the planned grasp.

4.2.3.2 Results

The results for training and novel objects are compared with the three frictional contact models. Results for training objects are used to tune the parameters and provide a benchmark for different physical settings. Table 4.4 shows the results for the eight training objects. The 6DLS reaches the highest grasp success rate, as well as the highest precision and recall. The results indicate that the grasp planner based on the 6DLS model detects the best grasps for the training objects and predicts the grasp quality more accurately compared to the remaining models.

Frictional Contact Model	Grasp Success Rate	Precision	Recall
Point	0.88	0.87	0.56
6DLS (proposed)	**0.91**	**0.96**	**0.80**
6DFC (proposed)	0.90	0.88	0.57

Table 4.4: Results of planned grasps with three frictional contact models for eight training objects.

Table 4.5 shows the results for the 24 novel objects. The 6DLS achieves 92% grasp success, 10% higher over the traditional soft point contact model. Furthermore, the recall of the 6DLS is up to 14% higher than the remaining models. The main difference comes from the five flat objects, which are depicted in Figure 4.10 with a green line underneath the object. The 6DLS is able to find robust grasps for these flat objects, whereas the traditional model can not. Results for the flat objects in Table 4.5 shows that the ellipsoid model increases grasp success, precision, and recall by 30%, 1%, and 22% compared to the remaining models, respectively. This observation is consistent with the planned grasps in simulation, illustrated in Figure 4.9. Furthermore, by comparing Table 4.4 and 4.5, one observes that the 6DLS model achieves a similar grasp success rate for the training and novel objects, whereas there is a 6% drop for the point and 6DFC frictional contact models. This suggests that the 6DLS-based grasp planner generalizes well to previously unseen objects. However, it is surprising that the results of 6DFC are worse than 6DLS. One reason can be the physical setup used in the experiments, as the closing force is actively controlled by using the force sensors and the 6DFC is more suitable for cases with unknown grasp forces. In future work, the 6DFC model can be further evaluated with a three-jaw gripper.

	All Objects			Flat Objects		
Frictional Contact Model	Grasp Success Rate	Precision	Recall	Grasp Success Rate	Precision	Recall
Point	0.82	0.95	0.69	0.50	0.84	0.55
6DLS (proposed)	**0.92**	0.95	**0.83**	**0.80**	**0.85**	**0.77**
6DFC (proposed)	0.84	**0.96**	0.71	0.52	0.84	0.60

Table 4.5: Results of planned grasps with three frictional contact models for 24 novel objects and five flat objects.

4.2.3.3 Discussion

One typical failure case for all frictional contact models are dynamic grasps, which occur when one jaw contacts the object first, resulting in an object motion and a failed grasp. In future work, one can also consider such dynamics using simulation, such as the method proposed by Kim *et al.* [186], to further update the grasp quality.

4.3 Grasp Planning for Known Deformable Hollow Objects

The third application of the proposed nonplanar frictional surface contact models is grasp planning for deformable hollow objects, such as plastic bottles and cups, with compliant gripper jaws. Grasping such deformable objects is challenging, as the grasp should resist disturbances while minimally deforming the object so as not to damage it or dislodge liquids. This thesis proposes minimal work as a novel grasp quality metric that combines object deformation and wrench resistance by using the ellipsoidal 6DLS model. An efficient algorithm is further proposed to compute the work required to resist an external wrench for a manipulation task by solving a linear program. The algorithm first computes the minimum required grasp force and an estimation of the gripper jaw displacements based on the object's empirical stiffness at different locations. The work done by the jaws is the product of the grasp force and the displacements. Grasps requiring minimal work are considered to be of high quality.

Consider a representative grasp in Figure 4.11. The left part shows the stiffness of the cup, where blue indicates high stiffness and red indicates low stiffness. Intuitively, the cup is stiffer near the rim and bottom, where the shape provides reinforcement. The middle part illustrates three planned grasps, shown as cylinders representing the grasp axis for a parallel-jaw gripper, where green indicates high quality and red indicates low quality according to the minimal work metric. The right figure shows the execution of the highest quality grasp according to the minimal work grasp metric.

4.3.1 Problem Statement

The proposed metric addresses the problem of grasp planning and grasp success prediction for 3D deformable hollow objects with compliant jaw pads based on the ability of a grasp to

Figure 4.11: Plastic cup example for the proposed minimal work quality metric (adapted from [6] ©2020 IEEE).

resist external wrenches and the deformability of the object at the grasp location.

4.3.1.1 Assumptions

In addition to the assumptions for the nonplanar surface contacts and grasp analysis listed in Section 3.1 and Section 4.1.1, respectively, the proposed algorithm requires the following assumptions:

1. The stiffness is known for the objects to be grasped. This is required to compute the object deformation for a given grasp force.

2. A linear elastic model (linear stiffness) of soft jaw pads and objects. The assumption allows the computation of object deformation for an arbitrary grasp force.

4.3.1.2 Metrics

A grasp is considered to be successful if it completes the manipulation task without damaging the object or dislodging contents and to be failed otherwise. The predicted grasp success is binary and evaluates to 1 if the metric is higher than a threshold. Balanced accuracy is used in these experiments to evaluate the predictions made by a given metric by comparing them with real-world grasp success labels. Balanced accuracy is suitable for imbalanced datasets and is computed by weighting each sample with the inverse prevalence of its true class when finding the accuracy.

4.3.2 Algorithm

To evaluate a grasp candidate, the algorithm computes the minimal work of the gripper jaws required to complete a manipulation task. Applying the ellipsoidal 6DLS model as the frictional constraints, the minimal grasp force is computed by solving a linear program (LP). Then, the object deformation is estimated based on the grasp force and the object's empirical stiffness at the contact locations. The work of each gripper jaw is the product of the grasp force and the jaw displacement. The sum of the work of each jaw forms the work of the

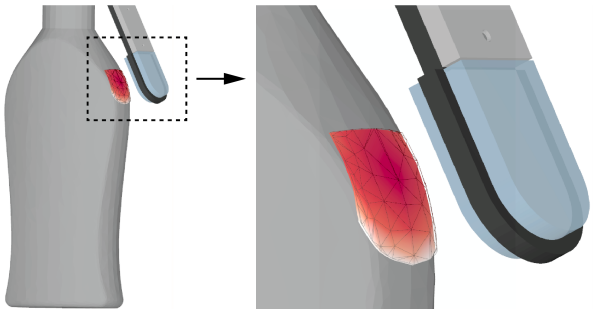

Figure 4.12: Contact profile with an enlarged view obtained by the REACH model [5]. The contact area consists of triangles and the redder colors represent higher pressure due to larger deformation of the soft jaw pad at that point (adapted from [6] ©2020 IEEE).

grasp. The pipeline, including contact profile estimation, frictional constraints computation, and the minimal work quality computation, is introduced in the following.

4.3.2.1 Contact Profile Estimation

The REACH model [5] (Section 2.3.1.3) is used to estimate the profile for contacts between compliant jaw pads and deformable hollow objects due to its computational efficiency compared to the Finite Element Method. Figure 4.12 shows a representative contact profile consisting of a triangular mesh and the pressure distribution. However, the obtained contact profiles may be less accurate for objects with low stiffness since the model assumes that the grasped object is rigid.

4.3.2.2 Contact Wrench Constraints

Contact wrench constraints, which are constraints of frictional and normal wrenches, are essential to determine the minimal required grasp force to counter an expected external disturbance. Given the contact profile, an ellipsoidal 6DLS model $\boldsymbol{A}_e$ is computed with Algorithm 1. Next, the outer linearized contact wrench constraints $\mathcal{C}^{\text{outer}}$ in Equation (3.28) are obtained by linearizing the 6D ellipsoid and combining the frictional wrench constraints with the normal wrench.

4.3.2.3 Minimal Work Quality Metric

For a grasp with N contacts, let $\boldsymbol{G} \in \mathbb{R}^{6\times 6N}$ be the grasp map (Section 2.4.2). Let $\boldsymbol{c}_i \in \mathbb{R}^6$ be the contact wrench applied at the ith contact and let $\boldsymbol{f}_\perp = [f_{\perp_1}, \ldots, f_{\perp_N}]^T$ be a vector of magnitudes of the normal forces, where $f_{\perp_i}$ is the magnitude of the normal force at the ith

contact. The minimal required grasp force to resist an external wrench $\boldsymbol{w}_{\text{ext}} \in \mathbb{R}^6$ is

$$\begin{aligned} \min_{\boldsymbol{f}_\perp, \boldsymbol{c}_1, \ldots, \boldsymbol{c}_N} \quad & {\boldsymbol{f}_\perp}^T \mathbf{1}_N \\ \text{subject to} \quad & \boldsymbol{G} \begin{bmatrix} \boldsymbol{c}_1 \\ \vdots \\ \boldsymbol{c}_N \end{bmatrix} + \boldsymbol{w}_{\text{ext}} = 0, \\ & \boldsymbol{c}_i \in \mathcal{C}_i^{\text{outer}}, \forall i \in \{1, \ldots, N\}. \end{aligned} \tag{4.4}$$

Denoting d_i as the displacement of the ith jaw and s_i as the object stiffness at the ith contact, the work W is computed based on Hooke's law:

$$W = \sum_{i=1}^{N} \left(f_{\perp_i} \cdot d_i \right) \text{ with } d_i = \frac{f_{\perp_i}}{s_i} + \epsilon, \tag{4.5}$$

where ϵ is a small positive number, which allows the minimal work quality metric to also apply to rigid objects or objects containing a rigid part. In this case, the displacement d_i is equal to ϵ and the minimal work grasp quality metric reduces to the minimal force metric.

Denoting $W_{\max}$ as the maximal work for normalization, the minimal work grasp quality q_{work} is computed with

$$q_{\text{work}} = 1 - \frac{W}{W_{\max}}. \tag{4.6}$$

$W_{\max}$ is selected based on the collected physical data.

4.3.3 Grasp Planning in Simulation

The following part presents the object's stiffness acquisition required to compute work and the planned grasps in simulation with the proposed minimal work quality metric compared to two baseline metrics.

4.3.3.1 Acquisition of Object Stiffness

The object's stiffness is estimated with physical experiments. One can use the Finite Element Method to compute the object's deformation with a closing force of the gripper. However, the stiffness of hollow objects, such as plastic bottles and cups, highly depends on the wall thickness, the geometry, and material of the object, which are non-trivial to simulate. Therefore, a physical robot is used to collect object's stiffness at different locations in this work. Specifically, the KUKA robot and the SCHUNK parallel-jaw gripper with a force sensor on each jaw are used to collect the stiffness. The object's stiffness is estimated based on

1. The target normal force $f_\perp$;
2. The gripper opening l_s when it first makes contact with the object;
3. The gripper opening l_e when $f_\perp$ is reached;

First, antipodal grasps are planned in simulation for each object. At each planned grasp location, the SCHUNK gripper closes with a target force $f_\perp = 10N$ of each jaw. The object's stiffness s_i at the location i, which is the intersection point of the grasp axis and the object surface, is computed with $s_i = f_{\perp_i}/(l_{s,i} - l_{e,i})$. Each grasp is repeated five times and the median of the stiffness is chosen.

4.3.3.2 Evaluated Metrics

The proposed minimal work grasp quality metric is compared with two baseline metrics.

- *Grasp reliability metric* q_{robust}: as introduced in Section 2.5.3.2, q_{robust} addresses uncertainties in actuation by using Monte-Carlo sampling over the grasp pose and is the average grasp success over the K samples

$$q_{\text{robust}} = \frac{1}{K}\sum_{i=1}^{K} R_i.$$

- *Minimal force metric* q_{force}: The grasp quality is the minimal required grasp force $f_\perp$ to resist $\boldsymbol{w}_{\text{ext}}$ given the maximal force limit $f_{\perp_{\max}}$

$$q_f = 1 - \frac{f_\perp}{f_{\perp_{\max}}},$$

  where $f_{\perp_{\max}}$ is determined experimentally.

- *Minimal work metric*: the proposed metric computed with

$$q_{\text{work}} = 1 - \frac{W}{W_{\max}}.$$

4.3.3.3 Grasp Planning in Simulation

Planned grasps in simulation with the three quality metrics are compared. Figures 4.13(a) and (b) show the planned grasps for three objects based on their 3D meshes and the interpolated stiffness maps.

Antipodal grasp candidates are sampled and the quality of each grasp is computed for 1) vertical lifting and 2) lifting and 90° rotation tasks. Grasps planned with three quality metrics are compared, as shown in Figures 4.13(c) and (d). The two tasks are modeled with a 6D gravity wrench to be resisted under one and three object poses obtained by discretizing the manipulation trajectory, respectively, since the gravity wrench remains the same for the vertical lifting task. The lowest quality value of a grasp among all object poses is selected as the value for each metric. The colored lines represent the grasp axes; green indicates high quality under the given metric, while red indicates low quality. Figure 4.13 shows that the planned grasps using the proposed minimal work quality metric avoid causing large deformations of the object while resisting the gravitational disturbances of the manipulation tasks.

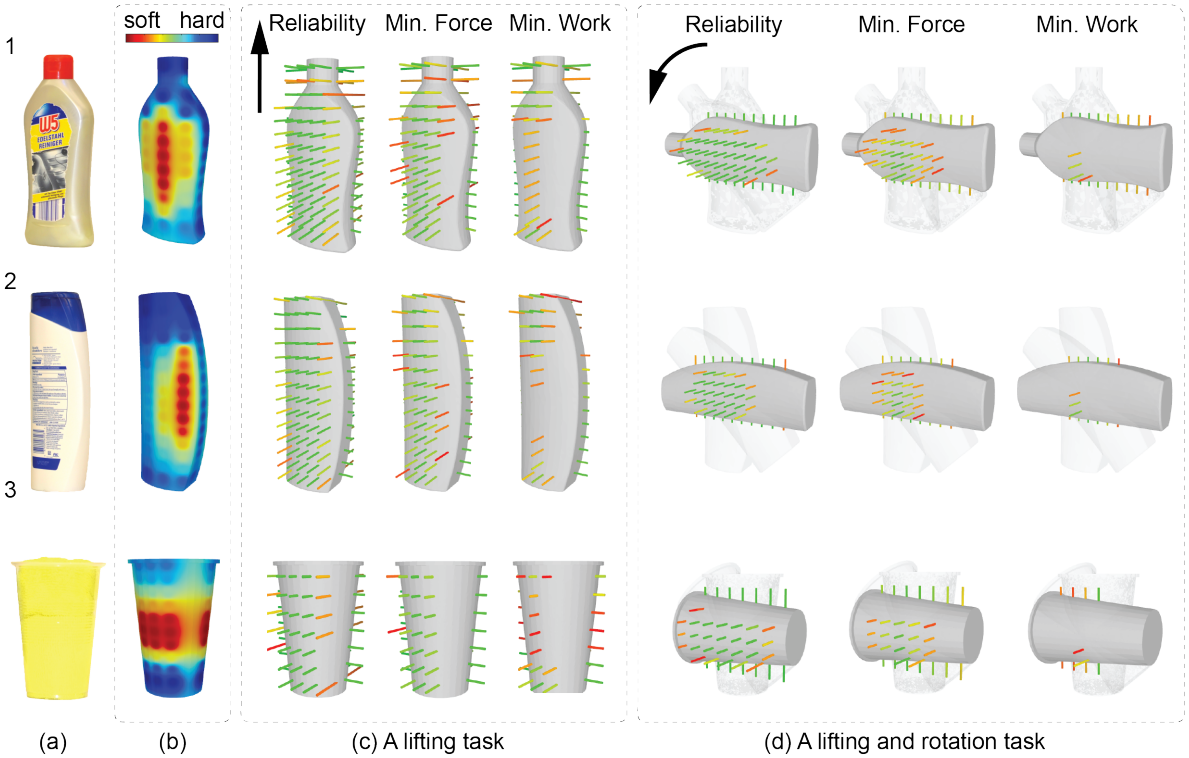

Figure 4.13: Planned grasps for three physical objects with three quality metrics.

4.3.4 Physical Experiments

The planned grasps are evaluated with physical experiments for the two manipulation tasks. A total of 46 grasp poses are selected for the three objects that cover different regions of each object. Each grasp is repeated five times, resulting in 230 grasps for each task. A grasp is considered to be successful if 1) the task is completed, 2) the object returns to its original shape when the grasp force is released, and 3) the content is not dislodged during the grasp.

The objects are filled with wet towels to simulate the mass of the object filled with liquid without changing the object's stiffness or damaging the electrical devices. Object 1 and 2 are sealed with a balloon to infer the content spillage. By measuring the balloon's inflation before and after the grasp, the content is considered spilled if the inflation difference is larger than a threshold.

The balanced accuracy, or the accuracy weighted by the number of successful and failed grasps in the collected data, is selected as the metric to evaluate the prediction accuracy. Each metric's grasp quality prediction is binarized by thresholding the quality at a threshold $\sigma = 0.5$. Table 4.6 shows the balanced accuracy of the three grasp quality metrics for the two manipulation tasks. The proposed metric reaches 77.5% and 78.9% balanced accuracy for the two tasks, up to 28.8% and 22.7% higher than the other metrics, respectively.

4.3.5 Discussion

The section proposes a minimal work quality metric to plan grasps for 3D deformable hollow objects. During the experiments, one can observe that the proposed method may not

Table 4.6: Balanced accuracy of three quality metrics.

Object	Vertical lifting			Lifting and 90° rotation		
	q_{robust}	q_{force}	q_{work}	q_{robust}	q_{force}	q_{work}
1	0.500	0.711	**0.833**	0.575	0.600	**0.875**
2	0.391	0.539	**0.831**	0.516	0.714	**0.759**
3	0.500	0.535	**0.610**	0.630	0.570	**0.760**
All	0.487	0.606	**0.775**	0.562	0.641	**0.789**

perform well for objects having large deformations due to the linear stiffness assumption and the simplified model to acquire contact profiles. To address this, one can simulate the contacts with the FEM and fit a strain-stress curve for each grasp location by applying different loads. The algorithms then use the obtained pressure distribution and the deformed object shape to compute the grasp quality.

Note that the minimal work grasp quality metric is also applicable to grasps on rigid objects with compliant gripper jaws. As future work, this duality can be further investigated and applied in grasp planning for both rigid and deformable objects.

4.4 Chapter summary

This chapter evaluated the proposed nonplanar frictional surface contact models, including the two 6DLS models and the 6DFC, for three applications. The first application was grasp success prediction for rigid known objects. The frictional contact models were evaluated with over 3,000 grasps on 3D-printed objects with three physical setups equipped with different deformable gripper jaws. The results showed that the proposed model increases the precision and recall in all experiments by up to 4% and 25% over the traditional frictional contact models, respectively. This chapter further presented a hybrid grasp planner that finds robust grasps for previously unseen rigid objects given a depth image. The proposed ellipsoidal 6DLS model and the 6DFC were used to create a grasp dataset and a synthetic depth image dataset in simulation to train the grasp planners. Physical experiments showed that the grasp planner based on the proposed 6DLS model was able to find robust grasps for 24 novel objects and achieved 92% grasp success rate, 10% higher compared to the traditional frictional contact models. The third application was grasp planning and grasp success prediction for known deformable hollow objects. The novel minimal work quality metric applies the ellipsoidal 6DLS model and increased balanced accuracy for physical grasp success prediction by up to 28.8%.

Chapter 5

Conclusion

Robust robot grasping enables object manipulation with promising applications in industry, households, and health care, such as intra-logistics, cooking, and elderly care. One key challenge of grasping is grasp planning, which requires a frictional contact model to estimate the grasp quality so that the planner can find the most robust grasp among the grasp candidates. While deformable gripper jaws are widely applied in many of the aforementioned applications to increase grasp robustness, they create nonplanar surface contacts when they deform to the object's nonplanar local geometry. As the frictional contact models for nonplanar surfaces are not well studied, this thesis focuses on modeling the frictional nonplanar surface contacts and their applications in grasp success prediction and grasp planning with deformable gripper jaws. This chapter discusses the results and the limitations of the proposed models and further presents potential future research directions for a grasp planner toward human level performance.

5.1 Summary of the Results

The thesis derived the 6DFW given a contact profile and object motion. Results with six nonplanar parametric surfaces in simulation showed that the traditional planar area contact model results in a frictional wrench that is over-conservative in four dimensions and overconfident in one dimension, which suggests the importance of considering the nonplanar surface geometry. This thesis further evaluated the two 6DLS models that approximate a 6DLS, which describes the frictional wrench limit at a nonplanar surface contact. Fitting results with six parametric surfaces and 2,932 contacts from FEM simulations showed that the quartic and ellipsoidal 6DLS models reached as low as 0.02 and 0.04 mean wrench error, respectively, which suggests that both models well approximate the frictional wrench limit for a large variety of nonplanar surface contacts.

For the first application in grasping, the 6DLS and 6DFC models are used to predict physical grasp success. The first experiment setup evaluated the 6DLS models for elliptic cylindrical contact surfaces caused by the deformable 3D-printed plastic jaws with the fin ray structure. Prediction results for 1,035 physical grasps showed that the ellipsoidal 6DLS model improves the F_1 score by up to 16% compared to the traditional frictional contact models. As the ellipsoid has lower computational effort and slightly outperforms the quartic

in this experiment setup, the ellipsoid is used as a representative 6DLS model for the next experiments. The second experiment setup evaluated the 6DLS and the 6DFC models for arbitrary nonplanar surface contacts caused by rigid jaws covered with compliant materials. Two physical grasp datasets, 920 grasps collected with the SCHUNK gripper on the KUKA robot and 1,500 grasps collected with the ABB YuMi robot, showed that the ellipsoidal 6DLS model outperforms the traditional frictional contact models by up to 4% mAP and 21% mAR. Compared to the 6DLS model, the 6DFC further improves mAR by 4%, while keeping the same mAP.

This dissertation further evaluated the proposed hybrid grasp planners for novel rigid objects based on the 6DLS and the 6DFC models. Physical experiments with 22 novel objects showed that the grasp planner trained with the proposed ellipsoidal 6DLS model achieved 92% grasp success, which is 10% higher than the traditional soft point contact model used in the state-of-the-art hybrid grasp planner Dex-Net [36], [90]. One key observation is that the 6DLS-based grasp planner is also able to find robust grasps for flat objects, while the soft point contact model can not in this case.

As the third application of the 6DLS model, this dissertation presented a novel minimal work quality metric for deformable hollow objects. Grasps planned with the minimal work metric in simulation can resist gravitational disturbances without causing large deformations. Furthermore, the proposed metric was evaluated with a total of 460 physical grasps for grasp success prediction for two manipulation tasks. The minimal work metric reached 77.5% and 78.9% balanced accuracy for the two tasks, up to 28.8% and 22.7% higher than the traditional metrics, respectively.

5.2 Limitations

While the proposed 6DLS and 6DFC models increase the accuracy for grasp success prediction and grasp success for planning, this section discusses three limitations of the proposed methods.

To predict grasp success, the change of the contact profile is assumed to be minor during the manipulation; therefore, the 6DLS model is not recomputed during the manipulation. However, one can observe that the contact profile can change during the manipulation due to the jaws' deformation. One way to address this limitation is to constantly predict grasp success with updated profiles captured with deformable tactile sensors.

Furthermore, 6DLS-based grasp analysis requires the assumption that both gripper jaws are in contact with the object simultaneously; therefore, the object remains static while the gripper closes. However, one can observe that the object moves if one jaw touches the object first. This object motion results in a less accurate contact profile estimation or even a grasp failure. This issue can be addressed by simulating or predicting the object dynamics during grasping.

Finally, the minimal work metric is less suitable for objects with large deformations due to the linear stiffness assumption and the simplified model to acquire the contact profiles. To address this, one can simulate the contacts with the FEM and use the obtained pressure

distribution to compute the minimal grasp force. With the simulated deformed shape of the object, one can further fit a strain-stress curve for each grasp location by applying different loads to accurately estimate the object deformation.

5.3 Future Work

In addition to addressing the limitations above as future work, this section also points out promising future research directions so that a robot can robustly manipulate arbitrary novel objects for wide-range applications.

1. **Accurate and efficient contact profile estimation:** While the REACH model [5] efficiently estimates contact profiles, the estimations are less accurate compared to the FEM simulations. Furthermore, the model should also consider the object dynamics during the grasp due to one jaw contacting the object first. Such an accurate and efficient model allows largescale dataset generation for an optimal grasp planner.

2. **Planning six DoF grasps for novel objects:** The proposed planner is limited to top grasps, which is not sufficient for manipulation tasks such as pouring liquids. The challenges of training a six DoF grasp planner include efficient grasp representation to reduce the number of grasp candidates, six DoF grasp sampling for the given depth image, and preventing grasps colliding with the environments.

3. **Grasp planner for different manipulation tasks:** While the majority of grasp planners focuses on the pick-and-place task, a planner should be able to generalize to different tasks. Rather than training a grasp planner for a specific task, one can consider modular tasks and combine them to find the best grasp for the main task [7]. The key challenges include the definition of modular tasks and how to guarantee the success of the main task if modular tasks are predicted to be successful.

4. **Quality metric for both rigid and deformable objects:** The proposed minimal work metric is also applicable to grasps on rigid objects with compliant gripper jaws, as it reduces to the minimal force metric. This duality can be further studied for a universal metric for both rigid and deformable objects.

5. **Object pose control with compliant gripper jaws:** During a successful grasp with deformable gripper jaws, the object pose can change even if there is no relative motion between the object and the jaws due to the jaws's deformation. Such pose change may cause manipulation failure in applications such as assembly, as the object pose has to be precisely controlled. Therefore, an ideal manipulator should also consider the deformation of the jaws to control the object pose.

6. **Grasp planning for novel rigid and deformable objects:** An ideal grasp planner should be able to find robust grasps for arbitrary objects. The challenges include a unified grasp quality metric for arbitrary objects, identification of the object stiffness prior to the manipulation, as well as updating the grasp pose for unexpected object

stiffness. For such scenarios, a recurrent neural network (RNN) can be used to train a grasp planner. Specifically, the planner first finds a grasp by assuming the object is rigid at the grasp location. If the object deforms during the grasp, the object stiffness is feed into the RNN so that the planner updates the optimal grasp pose.

Bibliography

Publications by the author

Journal publications

[1] J. Xu, T. Aykut, D. Ma, and E. Steinbach, "6DLS: Modeling nonplanar frictional surface contacts for grasping using 6-D limit surfaces," *IEEE Transactions on Robotics (T-RO)*, vol. 37, no. 6, pp. 2099–2116, 2021. DOI: 10.1109/TRO.2021.3070102.

[2] T. Aykut, J. Xu, and E. Steinbach, "Realtime 3D 360-degree telepresence with deep-learning-based head-motion prediction," *IEEE Journal on Emerging and Selected Topics in Circuits and Systems*, vol. 9, no. 1, pp. 231–244, 2019. DOI: 10.1109/JETCAS.2019.2897220.

Conference publications

[3] J. Xu, M. Danielczuk, E. Steinbach, and K. Goldberg, "6DFC: Efficiently planning soft non-planar area contact grasps using 6D friction cones," in *IEEE International Conference on Robotics and Automation (ICRA)*, 2020, pp. 7891–7897. DOI: 10.1109/ICRA40945.2020.9197293.

[4] J. Xu, N. Alt, Z. Zhang, and E. Steinbach, "Grasping posture estimation for a two-finger parallel gripper with soft material jaws using a curved contact area friction model," in *IEEE International Conference on Robotics and Automation (ICRA)*, 2017. DOI: 10.1109/ICRA.2017.7989258.

[5] M. Danielczuk, J. Xu, J. Mahler, M. Matl, N. Chentanez, and K. Goldberg, "REACH: reducing false negatives in robot grasp planning with a robust efficient area contact hypothesis model," in *International Symposium on Robotics Research (ISRR)*, 2019.

[6] J. Xu, M. Danielczuk, J. Ichnowski, J. Mahler, E. Steinbach, and K. Goldberg, "Minimal Work: A grasp quality metric for deformable hollow objects," in *IEEE International Conference on Robotics and Automation (ICRA)*, 2020, pp. 1546–1552. DOI: 10.1109/ICRA40945.2020.9197062.

[7] J. Xu, A. Bhardwaj, G. Sun, T. Aykut, N. Alt, M. Karimi, and E. Steinbach, "Learning-based modular task-oriented grasp stability assessment," in *IEEE/RSJ International Conference on Intelligent Robots and Systems (IROS)*, 2018, pp. 3468–3475. DOI: 10.1109/IROS.2018.8594412.

[8] N. Alt, J. Xu, and E. Steinbach, "Grasp planning for thin-walled deformable objects," in *Workshop on Robotic Hands, Grasping, and Manipulation, in conjunction with IEEE International Conference on Robotics and Automation (ICRA)*, 2015.

[9] ——, "A dataset of thin-walled deformable objects for manipulation planning," in *Int. Workshop on Grasping and Manipulation Datasets, in conjunction with IEEE International Conference on Robotics and Automation (ICRA)*, Stockholm, Sweden, 2016.

[10] J. Ichnowski, M. Danielczuk, J. Xu, V. Satish, and K. Goldberg, "GOMP: Grasp-optimized motion planning for bin picking," in *IEEE International Conference on Robotics and Automation (ICRA)*, 2020, pp. 5270–5277. DOI: 10.1109/ICRA40945.2020.9197548.

[11] T. Aykut, C. Zou, J. Xu, D. Van Opdenbosch, and E. Steinbach, "A delay compensation approach for pan-tilt-unit-based stereoscopic 360 degree telepresence systems using head motion prediction," in *IEEE International Conference on Robotics and Automation (ICRA)*, 2018, pp. 3323–3330. DOI: 10.1109/ICRA.2018.8460750.

[12] T. Aykut, C. Burgmair, M. Karimi, J. Xu, and E. Steinbach, "Delay compensation for actuated stereoscopic 360 degree telepresence systems with probabilistic head motion prediction," in *IEEE Winter Conference on Applications of Computer Vision (WACV)*, 2018, pp. 2010–2018. DOI: 10.1109/WACV.2018.00222.

General publications

[13] S. Goyal, A. Ruina, and J. Papadopoulos, "Planar sliding with dry friction part 1. limit surface and moment function," *Wear*, vol. 143, no. 2, pp. 307–330, 1991. DOI: 10.1016/0043-1648(91)90104-3.

[14] C. Ferrari and J. Canny, "Planning optimal grasps," in *IEEE International Conference on Robotics and Automation (ICRA)*, 1992, pp. 2290–2295. DOI: 10.1109/ROBOT.1992.219918.

[15] R. M. Murray, Z. Li, S. S. Sastry, and S. S. Sastry, *A mathematical introduction to robotic manipulation*. CRC press, 1994.

[16] R. D. Howe and M. R. Cutkosky, "Practical force-motion models for sliding manipulation," *International Journal of Robotics Research (IJRR)*, vol. 15, no. 6, pp. 557–572, 1996. DOI: 10.1177/027836499601500603.

[17] A. Bicchi and V. Kumar, "Robotic grasping and contact: A review," in *IEEE International Conference on Robotics and Automation (ICRA)*, vol. 1, 2000, pp. 348–353. DOI: 10.1109/ROBOT.2000.844081.

[18] J. Zhou, M. T. Mason, R. Paolini, and D. Bagnell, "A convex polynomial model for planar sliding mechanics: Theory, application, and experimental validation," *International Journal of Robotics Research (IJRR)*, vol. 37, no. 2-3, pp. 249–265, 2018. DOI: 10.1177/0278364918755536.

[19] N. Kuppuswamy, A. Alspach, A. Uttamchandani, S. Creasey, T. Ikeda, and R. Tedrake, "Soft-bubble grippers for robust and perceptive manipulation," in *IEEE/RSJ International Conference on Intelligent Robots and Systems (IROS)*, 2020, pp. 9917–9924. DOI: 10.1109/IROS45743.2020.9341534.

[20] X. Shan and L. Birglen, "Modeling and analysis of soft robotic fingers using the fin ray effect," *International Journal of Robotics Research (IJRR)*, vol. 39, no. 14, pp. 1686–1705, 2020. DOI: 10.1177/0278364920913926.

[21] V. Wall, G. Zöller, and O. Brock, "A method for sensorizing soft actuators and its application to the RBO hand 2," in *IEEE International Conference on Robotics and Automation (ICRA)*, 2017, pp. 4965–4970. DOI: 10.1109/ICRA.2017.7989577.

[22] A. M. Dollar and R. D. Howe, "The highly adaptive SDM hand: Design and performance evaluation," *The International Journal of Robotics Research*, vol. 29, no. 5, pp. 585–597, 2010. DOI: 10.1177/0278364909360852.

[23] M. Guo, D. V. Gealy, J. Liang, J. Mahler, A. Goncalves, S. McKinley, J. A. Ojea, and K. Goldberg, "Design of parallel-jaw gripper tip surfaces for robust grasping," in *IEEE International Conference on Robotics and Automation (ICRA)*, 2017, pp. 2831–2838. DOI: 10.1109/ICRA.2017.7989330.

[24] D. Ma, E. Donlon, S. Dong, and A. Rodriguez, "Dense tactile force distribution estimation using GelSlim and inverse FEM," in *IEEE International Conference on Robotics and Automation (ICRA)*, 2019, pp. 5418–5424. DOI: 10.1109/ICRA.2019.8794113.

[25] N. Alt and E. Steinbach, "Navigation and manipulation planning using a visuo-haptic sensor on a mobile platform," *IEEE Transactions on Instrumentation and Measurement*, vol. 63, no. 11, pp. 2570–2582, 2014. DOI: 10.1109/TIM.2014.2315734.

[26] B. Romero, F. Veiga, and E. Adelson, "Soft, round, high resolution tactile fingertip sensors for dexterous robotic manipulation," in *IEEE International Conference on Robotics and Automation (ICRA)*, 2020, pp. 4796–4802. DOI: 10.1109/ICRA40945.2020.9196909.

[27] M. Ciocarlie, A. Miller, and P. Allen, "Grasp analysis using deformable fingers," in *IEEE/RSJ International Conference on Intelligent Robots and Systems (IROS)*, 2005, pp. 4122–4128. DOI: 10.1109/IROS.2005.1545525.

[28] M. Ciocarlie, C. Lackner, and P. Allen, "Soft finger model with adaptive contact geometry for grasping and manipulation tasks," in *IEEE Second Joint EuroHaptics Conference and Symposium on Haptic Interfaces for Virtual Environment and Teleoperator Systems*, 2007, pp. 219–224. DOI: 10.1109/WHC.2007.103.

[29] T. Tsuji, S. Uto, K. Harada, R. Kurazume, T. Hasegawa, and K. Morooka, "Grasp planning for constricted parts of objects approximated with quadric surfaces," in *IEEE/RSJ International Conference on Intelligent Robots and Systems (IROS)*, 2014, pp. 2447–2453. DOI: 10.1109/IROS.2014.6942895.

[30] K. Harada, T. Tsuji, S. Uto, N. Yamanobe, K. Nagata, and K. Kitagaki, "Stability of soft-finger grasp under gravity," in *IEEE International Conference on Robotics and Automation (ICRA)*, 2014, pp. 883–888. DOI: 10.1109/ICRA.2014.6906958.

[31] J. B. Mahler, "Efficient policy learning for robust robot grasping," PhD thesis, Department of Electrical Engineering and Computer Science, University of California at Berkeley, 2018.

[32] "intelrealsense.com", *Intel RealSense D455® RGBD camera*, Accessed on: Jan. 20, 2022. [Online]. Available: https://www.intelrealsense.com/depth-camera-d455/.

[33] N. Sünderhauf, O. Brock, W. Scheirer, R. Hadsell, D. Fox, J. Leitner, B. Upcroft, P. Abbeel, W. Burgard, M. Milford, *et al.*, "The limits and potentials of deep learning for robotics," *International Journal of Robotics Research (IJRR)*, vol. 37, no. 4-5, pp. 405–420, 2018. DOI: 10.1177/0278364918770733.

[34] J. Bohg, A. Morales, T. Asfour, and D. Kragic, "Data-driven grasp synthesis—a survey," *IEEE Transactions on Robotics (T-RO)*, vol. 30, no. 2, pp. 289–309, 2014. DOI: 10.1109/TRO.2013.2289018.

[35] D. Morrison, P. Corke, and J. Leitner, "Learning robust, real-time, reactive robotic grasping," *International Journal of Robotics Research (IJRR)*, vol. 39, no. 2-3, pp. 183–201, 2020. DOI: 10.1177/0278364919859066.

[36] J. Mahler, M. Matl, V. Satish, M. Danielczuk, B. DeRose, S. McKinley, and K. Goldberg, "Learning ambidextrous robot grasping policies," *Science Robotics*, vol. 4, no. 26, 2019. DOI: 10.1126/scirobotics.aau4984.

[37] E. Johns, S. Leutenegger, and A. J. Davison, "Deep learning a grasp function for grasping under gripper pose uncertainty," in *IEEE/RSJ International Conference on Intelligent Robots and Systems (IROS)*, 2016, pp. 4461–4468. DOI: 10.1109/IROS.2016.7759657.

[38] M. Danielczuk, M. Matl, S. Gupta, A. Li, A. Lee, J. Mahler, and K. Goldberg, "Segmenting unknown 3D objects from real depth images using mask R-CNN trained on synthetic data," in *IEEE International Conference on Robotics and Automation (ICRA)*, 2019, pp. 7283–7290. DOI: 10.1109/ICRA.2019.8793744.

[39] K. He, G. Gkioxari, P. Dollár, and R. Girshick, "Mask R-CNN," in *IEEE International Conference on Computer Vision (ICCV)*, 2017, pp. 2980–2988. DOI: 10.1109/ICCV.2017.322.

[40] A. Saxena, J. Driemeyer, and A. Y. Ng, "Robotic grasping of novel objects using vision," *International Journal of Robotics Research (IJRR)*, vol. 27, no. 2, pp. 157–173, 2008. DOI: 10.1177/0278364907087172.

[41] J. Redmon and A. Angelova, "Real-time grasp detection using convolutional neural networks," in *IEEE International Conference on Robotics and Automation (ICRA)*, 2015, pp. 1316–1322. DOI: 10.1109/ICRA.2015.7139361.

[42] L. Pinto and A. Gupta, "Supersizing self-supervision: Learning to grasp from 50k tries and 700 robot hours," in *IEEE International Conference on Robotics and Automation (ICRA)*, 2016, pp. 3406–3413. DOI: 10.1109/ICRA.2016.7487517.

[43] S. Levine, P. Pastor, A. Krizhevsky, J. Ibarz, and D. Quillen, "Learning hand-eye coordination for robotic grasping with deep learning and large-scale data collection," *International Journal of Robotics Research (IJRR)*, vol. 37, no. 4-5, pp. 421–436, 2018. DOI: 10.1177/0278364917710318.

[44] D. Rao, Q. V. Le, T. Phoka, M. Quigley, A. Sudsang, and A. Y. Ng, "Grasping novel objects with depth segmentation," in *IEEE/RSJ International Conference on Intelligent Robots and Systems (IROS)*, 2010, pp. 2578–2585. DOI: 10.1109/IROS.2010.5650493.

[45] I. Lenz, H. Lee, and A. Saxena, "Deep learning for detecting robotic grasps," *International Journal of Robotics Research (IJRR)*, vol. 34, no. 4-5, pp. 705–724, 2015. DOI: 10.1177/0278364914549607.

[46] M. Danielczuk, A. Angelova, V. Vanhoucke, and K. Goldberg, "X-Ray: Mechanical search for an occluded object by minimizing support of learned occupancy distributions," in *IEEE/RSJ International Conference on Intelligent Robots and Systems (IROS)*, 2020, pp. 9577–9584. DOI: 10.1109/IROS45743.2020.9340984.

[47] S. Luo, J. Bimbo, R. Dahiya, and H. Liu, "Robotic tactile perception of object properties: A review," *Mechatronics*, vol. 48, pp. 54–67, 2017. DOI: 10.1016/j.mechatronics.2017.11.002.

[48] Q. Li, O. Kroemer, Z. Su, F. F. Veiga, M. Kaboli, and H. J. Ritter, "A review of tactile information: Perception and action through touch," *IEEE Transactions on Robotics (T-RO)*, vol. 36, no. 6, pp. 1619–1634, 2020. DOI: 10.1109/TRO.2020.3003230.

[49] P. Piacenza, K. Behrman, B. Schifferer, I. Kymissis, and M. Ciocarlie, "A sensorized multicurved robot finger with data-driven touch sensing via overlapping light signals," *IEEE Transactions on Mechatronics*, vol. 25, no. 5, pp. 2416–2427, 2020. DOI: 10.1109/TMECH.2020.2975578.

[50] G. Cheng, E. Dean-Leon, F. Bergner, J. R. G. Olvera, Q. Leboutet, and P. Mittendorfer, "A comprehensive realization of robot skin: Sensors, sensing, control, and applications," *Proceedings of the IEEE*, vol. 107, no. 10, pp. 2034–2051, 2019. DOI: 10.1109/JPROC.2019.2933348.

[51] T. P. Tomo, A. Schmitz, W. K. Wong, H. Kristanto, S. Somlor, J. Hwang, L. Jamone, and S. Sugano, "Covering a robot fingertip with uskin: A soft electronic skin with distributed 3-axis force sensitive elements for robot hands," *IEEE Robotics and Automation Letters (RA-L)*, vol. 3, no. 1, pp. 124–131, 2017. DOI: 10.1109/LRA.2017.2734965.

[52] W. Yuan, S. Dong, and E. H. Adelson, "Gelsight: High-resolution robot tactile sensors for estimating geometry and force," *Sensors*, vol. 17, no. 12, p. 2762, 2017. DOI: 10.3390/s17122762.

[53] E. Donlon, S. Dong, M. Liu, J. Li, E. Adelson, and A. Rodriguez, "Gelslim: A high-resolution, compact, robust, and calibrated tactile-sensing finger," in *IEEE/RSJ International Conference on Intelligent Robots and Systems (IROS)*, 2018, pp. 1927–1934. DOI: 10.1109/IROS.2018.8593661.

[54] J. Konstantinova, A. Stilli, and K. Althoefer, "Fingertip fiber optical tactile array with two-level spring structure," *Sensors*, vol. 17, no. 10, p. 2337, 2017. DOI: 10.3390/s17102337.

[55] G. H. Büscher, R. Kõiva, C. Schürmann, R. Haschke, and H. J. Ritter, "Flexible and stretchable fabric-based tactile sensor," *Robotics and Autonomous Systems*, vol. 63, pp. 244–252, 2015. DOI: 10.1016/j.robot.2014.09.007.

[56] B. Ward-Cherrier, N. Pestell, and N. F. Lepora, "Neurotac: A neuromorphic optical tactile sensor applied to texture recognition," in *IEEE International Conference on Robotics and Automation (ICRA)*, 2020, pp. 2654–2660. DOI: 10.1109/ICRA40945.2020.9197046.

[57] F. R. Hogan, M. Bauza, O. Canal, E. Donlon, and A. Rodriguez, "Tactile regrasp: Grasp adjustments via simulated tactile transformations," in *IEEE/RSJ International Conference on Intelligent Robots and Systems (IROS)*, 2018, pp. 2963–2970. DOI: 10.1109/IROS.2018.8593528.

[58] R. Calandra, A. Owens, D. Jayaraman, J. Lin, W. Yuan, J. Malik, E. H. Adelson, and S. Levine, "More than a feeling: Learning to grasp and regrasp using vision and touch," *IEEE Robotics and Automation Letters (RA-L)*, vol. 3, no. 4, pp. 3300–3307, 2018. DOI: 10.1109/LRA.2018.2852779.

[59] M. A. Lee, Y. Zhu, P. Zachares, M. Tan, K. Srinivasan, S. Savarese, L. Fei-Fei, A. Garg, and J. Bohg, "Making sense of vision and touch: Learning multimodal representations for contact-rich tasks," *IEEE Transactions on Robotics (T-RO)*, vol. 36, no. 3, pp. 582–596, 2020. DOI: 10.1109/TRO.2019.2959445.

[60] B. Heyneman and M. R. Cutkosky, "Slip classification for dynamic tactile array sensors," *International Journal of Robotics Research (IJRR)*, vol. 35, no. 4, pp. 404–421, 2016. DOI: 10.1177/0278364914564703.

[61] W. Yuan, M. A. Srinivasan, and E. H. Adelson, "Estimating object hardness with a gelsight touch sensor," in *IEEE/RSJ International Conference on Intelligent Robots and Systems (IROS)*, 2016, pp. 208–215. DOI: 10.1109/IROS.2016.7759057.

[62] R. Krug, Y. Bekiroglu, and M. A. Roa, "Grasp quality evaluation done right: How assumed contact force bounds affect wrench-based quality metrics," in *IEEE International Conference on Robotics and Automation (ICRA)*, 2017, pp. 1595–1600. DOI: 10.1109/ICRA.2017.7989189.

[63] Y. Narang, B. Sundaralingam, M. Macklin, A. Mousavian, and D. Fox, *Sim-to-real for robotic tactile sensing via physics-based simulation and learned latent projections*, 2021. arXiv: 2103.16747 [cs.RO].

[64] G. Sutanto, K. Rombach, Y. Chebotar, Z. Su, S. Schaal, G. S. Sukhatme, and F. Meier, *Supervised learning and reinforcement learning of feedback models for reactive behaviors: Tactile feedback testbed*, 2020. arXiv: 2007.00450 [cs.RO].

[65] E. W. Hawkes, H. Jiang, and M. R. Cutkosky, "Three-dimensional dynamic surface grasping with dry adhesion," *International Journal of Robotics Research (IJRR)*, vol. 35, no. 8, pp. 943–958, 2016. DOI: 10.1177/0278364915584645.

[66] E. W. Hawkes, H. Jiang, D. L. Christensen, A. K. Han, and M. R. Cutkosky, "Grasping without squeezing: Design and modeling of shear-activated grippers," *IEEE Transactions on Robotics (T-RO)*, vol. 34, no. 2, pp. 303–316, 2017. DOI: 10.1109/TRO.2017.2776312.

[67] M. R. Cutkosky and P. K. Wright, "Friction, stability and the design of robotic fingers," *International Journal of Robotics Research (IJRR)*, vol. 5, no. 4, pp. 20–37, 1986. DOI: 10.1177/027836498600500402.

[68] L. U. Odhner, L. P. Jentoft, M. R. Claffee, N. Corson, Y. Tenzer, R. R. Ma, M. Buehler, R. Kohout, R. D. Howe, and A. M. Dollar, "A compliant, underactuated hand for robust manipulation," *International Journal of Robotics Research (IJRR)*, vol. 33, no. 5, pp. 736–752, 2014. DOI: 10.1177/0278364913514466.

[69] M. Ciocarlie, F. M. Hicks, R. Holmberg, J. Hawke, M. Schlicht, J. Gee, S. Stanford, and R. Bahadur, "The velo gripper: A versatile single-actuator design for enveloping, parallel and fingertip grasps," *International Journal of Robotics Research (IJRR)*, vol. 33, no. 5, pp. 753–767, 2014. DOI: 10.1177/0278364913519148.

[70] D. M. Aukes, B. Heyneman, J. Ulmen, H. Stuart, M. R. Cutkosky, S. Kim, P. Garcia, and A. Edsinger, "Design and testing of a selectively compliant underactuated hand," *International Journal of Robotics Research (IJRR)*, vol. 33, no. 5, pp. 721–735, 2014. DOI: 10.1177/0278364913518997.

[71] W. Crooks, S. Rozen-Levy, B. Trimmer, C. Rogers, and W. Messner, "Passive gripper inspired by manduca sexta and the fin ray® effect," *International Journal of Advanced Robotic Systems*, vol. 14, no. 4, pp. 1–7, 2017. DOI: 10.1177/1729881417721155.

[72] M. Li and Z. Deng, "Learning optimal fin-ray finger design for soft grasping," *Frontiers in Robotics and AI*, vol. 7, pp. 1–8, 2020. DOI: 10.3389/frobt.2020.590076.

[73] R. Deimel and O. Brock, "A novel type of compliant and underactuated robotic hand for dexterous grasping," *International Journal of Robotics Research (IJRR)*, vol. 35, no. 1-3, pp. 161–185, 2016. DOI: 10.1177/0278364915592961.

[74] D. Rus and M. T. Tolley, "Design, fabrication and control of soft robots," *Nature*, vol. 521, no. 7553, pp. 467–475, 2015. DOI: 10.1038/nature14543.

[75] M. G. Catalano, G. Grioli, E. Farnioli, A. Serio, C. Piazza, and A. Bicchi, "Adaptive synergies for the design and control of the Pisa/IIT softhand," *International Journal of Robotics Research (IJRR)*, vol. 33, no. 5, pp. 768–782, 2014. DOI: 10.1177/0278364913518998.

[76] H. Lin, F. Guo, F. Wang, and Y.-B. Jia, "Picking up a soft 3d object by "feeling" the grip," *International Journal of Robotics Research (IJRR)*, vol. 34, no. 11, pp. 1361–1384, 2015. DOI: 10.1177/0278364914564232.

[77] S. Arimoto, P. T. A. Nguyen, H.-Y. Han, and Z. Doulgeri, "Dynamics and control of a set of dual fingers with soft tips," *Robotica*, vol. 18, no. 1, pp. 71–80, 2000. DOI: 10.1017/S0263574799002441.

[78] S. Arimoto, Z. Doulgeri, P. T. A. Nguyen, and J. Fasoulas, "Stable pinching by a pair of robot fingers with soft tips under the effect of gravity," *Robotica*, vol. 20, no. 3, pp. 241–249, 2002. DOI: 10.1017/S0263574701003976.

[79] T. Inoue and S. Hirai, *Mechanics and control of soft-fingered manipulation*. Springer, 2008.

[80] N. Xydas and I. Kao, "Modeling of contact mechanics and friction limit surfaces for soft fingers in robotics, with experimental results," *International Journal of Robotics Research (IJRR)*, vol. 18, no. 9, pp. 941–950, 1999. DOI: 10.1177/02783649922066673.

[81] H. Hertz, "Über die Berührung fester elastischer Körper," *Journal für die reine und angewandte Mathematik*, vol. 1882, no. 92, pp. 156–171, 1882.

[82] H. R. Hertz, "Über die Berührung fester elastischer Körper und über die Härte," *Verhandlung des Vereins zur Beförderung des Gewerbefleißes, Berlin*, 1882.

[83] K. L. Johnson, "Contact mechanics," in. Cambridge university press, 1987, ch. 4, pp. 84–106. DOI: 10.1017/CBO9781139171731.

[84] Q. Wang and D Zhu, "Hertz theory: Contact of ellipsoidal surface," in *Encyclopedia of tribology*, Q. J. Wang and Y.-W. Chung, Eds., Springer, 2013, pp. 1647–1654. DOI: 10.1007/978-0-387-92897-5_493.

[85] A. Fakhari, M. Keshmiri, and I. Kao, "Development of realistic pressure distribution and friction limit surface for soft-finger contact interface of robotic hands," *Journal of Intelligent Robotic Systems*, vol. 82, no. 1, pp. 39–50, 2016.

[86] K. M. Lynch and F. C. Park, *Modern robotics*. Cambridge University Press, 2017. [Online]. Available: https://modernrobotics.northwestern.edu/nu-gm-book-resource/12-2-1-friction/#department.

[87] Y.-B. Jia, "Plücker coordinates for lines in the space," *Problem Solver Techniques for Applied Computer Science, Com-S-477/577 Course Handout. Iowa State University. http://web.cs.iastate.edu/~cs577/handouts/plucker-coordinates.pdf*, 2018.

[88] M. T. Mason, *Mechanics of robotic manipulation*. MIT press, 2001. DOI: 10.7551/mitpress/4527.001.0001.

[89] J. Mahler, F. T. Pokorny, B. Hou, M. Roderick, M. Laskey, M. Aubry, K. Kohlhoff, T. Kröger, J. Kuffner, and K. Goldberg, "Dex-Net 1.0: A cloud-based network of 3d objects for robust grasp planning using a multi-armed bandit model with correlated rewards," in *IEEE International Conference on Robotics and Automation (ICRA)*, 2016, pp. 1957–1964. DOI: 10.1109/ICRA.2016.7487342.

[90] J. Mahler, J. Liang, S. Niyaz, M. Laskey, R. Doan, X. Liu, J. A. Ojea, and K. Goldberg, "Dex-Net 2.0: Deep learning to plan robust grasps with synthetic point clouds and analytic grasp metrics," in *Robotics: Science and Systems (RSS)*, 2017. DOI: 10.15607/RSS.2017.XIII.058.

[91] I. Kao and M. R. Cutkosky, "Quasistatic manipulation with compliance and sliding," *International Journal of Robotics Research (IJRR)*, vol. 11, no. 1, pp. 20–40, 1992. DOI: 10.1177/027836499201100102.

[92] J. Zhou, R. Paolini, J. A. Bagnell, and M. T. Mason, "A convex polynomial force-motion model for planar sliding: Identification and application," in *IEEE International Conference on Robotics and Automation (ICRA)*, 2016, pp. 372–377. DOI: 10.1109/ICRA.2016.7487155.

[93] K. M. Lynch, H. Maekawa, and K. Tanie, "Manipulation and active sensing by pushing using tactile feedback," in *IEEE/RSJ International Conference on Intelligent Robots and Systems (IROS)*, vol. 1, 1992, pp. 416–421. DOI: 10.1109/IROS.1992.587370.

[94] F. R. Hogan and A. Rodriguez, "Feedback control of the pusher-slider system: A story of hybrid and underactuated contact dynamics," pp. 800–815, 2020. DOI: 10.1007/978-3-030-43089-4_51.

[95] K.-T. Yu, M. Bauza, N. Fazeli, and A. Rodriguez, "More than a million ways to be pushed. a high-fidelity experimental dataset of planar pushing," in *IEEE/RSJ International Conference on Intelligent Robots and Systems (IROS)*, 2016, pp. 30–37. DOI: 10.1109/IROS.2016.7758091.

[96] J. J. Moreau, "On unilateral constraints, friction and plasticity," *New variational techniques in mathematical physics*, vol. 63, G. Capriz and G. Stampacchia, Eds., pp. 175–322, 1973.

[97] M. Buss, H. Hashimoto, and J. Moore, "Dextrous hand grasping force optimization," *IEEE Transactions on Robotics and Automation*, vol. 12, no. 3, pp. 406–418, 1996. DOI: 10.1109/70.499823.

[98] L. Han, J. C. Trinkle, and Z. X. Li, "Grasp analysis as linear matrix inequality problems," *IEEE Transactions on Robotics and Automation*, vol. 16, no. 6, pp. 663–674, 2000. DOI: 10.1109/70.897778.

[99] T. Tsuji, K. Harada, and K. Kaneko, "Easy and fast evaluation of grasp stability by using ellipsoidal approximation of friction cone," in *IEEE/RSJ International Conference on Intelligent Robots and Systems (IROS)*, 2009, pp. 1830–1837. DOI: 10.1109/IROS.2009.5354501.

[100] T. Tsuji, K. Harada, K. Kaneko, F. Kanehiro, and K. Maruyama, "Grasp planning for a multifingered hand with a humanoid robot," *Journal of Robotics and Mechatronics*, vol. 22, no. 2, pp. 230–318, 2010. DOI: 10.20965/jrm.2010.p0230.

[101] S. H. Lee and M. Cutkosky, "Fixture planning with friction," *Journal of Manufacturing Science and Engineering*, vol. 113, no. 3, 1991. DOI: 10.1115/1.2899703.

[102] R. D. Howe, I. Kao, and M. R. Cutkosky, "The sliding of robot fingers under combined torsion and shear loading," in *IEEE International Conference on Robotics and Automation (ICRA)*, 1988, pp. 103–105. DOI: 10.1109/ROBOT.1988.12032.

[103] A. Magnani, S. Lall, and S. Boyd, "Tractable fitting with convex polynomials via sum-of-squares," in *IEEE Conference on Decision and Control*, 2005, pp. 1672–1677. DOI: 10.1109/CDC.2005.1582399.

[104] J. Zhou, Y. Hou, and M. T. Mason, "Pushing revisited: Differential flatness, trajectory planning, and stabilization," *International Journal of Robotics Research (IJRR)*, vol. 38, no. 12-13, pp. 1477–1489, 2019. DOI: 10.1177/0278364919872532.

[105] Z. Li and S. S. Sastry, "Task-oriented optimal grasping by multifingered robot hands," *IEEE Journal on Robotics and Automation*, vol. 4, no. 1, pp. 32–44, 1988. DOI: 10.1109/56.769.

[106] D. Kirkpatrick, B. Mishra, and C.-K. Yap, "Quantitative steinitz's theorems with applications to multifingered grasping," *Discrete & Computational Geometry*, vol. 7, no. 1, pp. 295–318, 1992. DOI: 10.1007/BF02187843.

[107] R. Krug, A. J. Lilienthal, D. Kragic, and Y. Bekiroglu, "Analytic grasp success prediction with tactile feedback," in *IEEE International Conference on Robotics and Automation (ICRA)*, 2016, pp. 165–171. DOI: 10.1109/ICRA.2016.7487130.

[108] C. Borst, M. Fischer, and G. Hirzinger, "A fast and robust grasp planner for arbitrary 3D objects," in *IEEE International Conference on Robotics and Automation (ICRA)*, vol. 3, 1999, pp. 1890–1896. DOI: 10.1109/ROBOT.1999.770384.

[109] E. Rimon and J. Burdick, *The Mechanics of Robot Grasping*. Cambridge University Press, 2019. DOI: 10.1017/9781108552011.

[110] M. A. Roa and R. Suárez, "Grasp quality measures: Review and performance," *Autonomous robots*, vol. 38, no. 1, pp. 65–88, 2015. DOI: 10.1007/s10514-014-9402-3.

[111] B. Mishra, "Grasp metrics: Optimality and complexity," in *Algorithmic Foundations of Robotics*, K. Goldberg, D. Halperin, J. Latombe, and R. Wilson, Eds., AK Peters, 1995, pp. 137–166.

[112] C. Rubert, B. León, A. Morales, and J. Sancho-Bru, "Characterisation of grasp quality metrics," *Journal of Intelligent & Robotic Systems*, vol. 89, no. 3-4, pp. 319–342, 2018. DOI: 10.1007/s10846-017-0562-1.

[113] K. B. Shimoga, "Robot grasp synthesis algorithms: A survey," *International Journal of Robotics Research (IJRR)*, vol. 15, no. 3, pp. 230–266, 1996. DOI: 10.1177/027836499601500302.

[114] J. C. Trinkle, "On the stability and instantaneous velocity of grasped frictionless objects," *IEEE Transactions on Robotics and Automation*, vol. 8, no. 5, pp. 560–572, 1992. DOI: 10.1109/70.163781.

[115] W. S. Howard and V. Kumar, "On the stability of grasped objects," *IEEE Transactions on Robotics and Automation*, vol. 12, no. 6, pp. 904–917, 1996. DOI: 10.1109/70.544773.

[116] A. T. Miller and P. K. Allen, "Graspit! a versatile simulator for robotic grasping," *IEEE Robotics & Automation Magazine*, vol. 11, no. 4, pp. 110–122, 2004. DOI: 10.1109/MRA.2004.1371616.

[117] D. Prattichizzo and J. C. Trinkle, "Grasping," in *Handbook of Robotics*, B. Siciliano and O. Khatib, Eds., Springer, 2008, ch. 28, pp. 671–700.

[118] F. Reuleaux, *The kinematics of machinery*. Macmillan, republished by Dover in 1963, 1876.

[119] P Somoff, "Über Gebiete von Schraubengeschwindigkeiten eines starren Körpers bieverschiedener Zahl von Stützflächen," *Zeitschrift fur Mathematic and Physik*, vol. 45, pp. 245–306, 1900.

[120] K Lakshminarayana, "Mechanics of form closure. ASME," 78-DET-32, Tech. Rep., 1978.

[121] J. C. Trinkle, "A quantitative test for form closure grasps," in *IEEE/RSJ International Conference on Intelligent Robots and Systems (IROS)*, vol. 3, 1992, pp. 1670–1677. DOI: 10.1109/IROS.1992.594246.

[122] A. Rodriguez, M. T. Mason, and S. Ferry, "From caging to grasping," *International Journal of Robotics Research (IJRR)*, vol. 31, no. 7, pp. 886–900, 2012. DOI: 10.1177/0278364912442972.

[123] S. Makita and W. Wan, "A survey of robotic caging and its applications," *Advanced Robotics*, vol. 31, no. 19-20, pp. 1071–1085, 2017. DOI: 10.1080/01691864.2017.1371075.

[124] T. F. Allen, J. W. Burdick, and E. Rimon, "Two-finger caging of polygonal objects using contact space search," *IEEE Transactions on Robotics (T-RO)*, vol. 31, no. 5, pp. 1164–1179, 2015. DOI: 10.1109/TRO.2015.2463651.

[125] W. Kuperberg, "Problems on polytopes and convex sets," in *DIMACS Workshop on polytopes*, 1990, pp. 584–589.

[126] M. Vahedi and A. F. van der Stappen, "Caging polygons with two and three fingers," *International Journal of Robotics Research (IJRR)*, vol. 27, no. 11-12, pp. 1308–1324, 2008. DOI: 10.1177/0278364908098485.

[127] W. Wan and R. Fukui, "Efficient planar caging test using space mapping," *IEEE Transactions on Automation Science and Engineering (T-ASE)*, vol. 15, no. 1, pp. 278–289, 2016. DOI: 10.1109/TASE.2016.2620175.

[128] A. Varava, D. Kragic, and F. T. Pokorny, "Caging grasps of rigid and partially deformable 3-d objects with double fork and neck features," *IEEE Transactions on Robotics (T-RO)*, vol. 32, no. 6, pp. 1479–1497, 2016. DOI: 10.1109/TRO.2016.2602374.

[129] J. Mahler, F. T. Pokorny, S. Niyaz, and K. Goldberg, "Synthesis of energy-bounded planar caging grasps using persistent homology," *IEEE Transactions on Automation Science and Engineering (T-ASE)*, vol. 15, no. 3, pp. 908–918, 2018. DOI: 10.1109/TASE.2018.2831724.

[130] K. Hauser, S. Wang, and M. R. Cutkosky, "Efficient equilibrium testing under adhesion and anisotropy using empirical contact force models," *IEEE Transactions on Robotics (T-RO)*, vol. 34, no. 5, pp. 1157–1169, 2018. DOI: 10.1109/TRO.2018.2831722.

[131] J. Mahler, M. Matl, X. Liu, A. Li, D. Gealy, and K. Goldberg, "Dex-Net 3.0: computing robust vacuum suction grasp targets in point clouds using a new analytic model and deep learning," in *IEEE International Conference on Robotics and Automation (ICRA)*, 2018, pp. 5620–5627. DOI: 10.1109/ICRA.2018.8460887.

[132] V.-D. Nguyen, "Constructing force-closure grasps," *International Journal of Robotics Research (IJRR)*, vol. 7, no. 3, pp. 3–16, 1988. DOI: 10.1177/027836498800700301.

[133] Y. Zheng, "An efficient algorithm for a grasp quality measure," *IEEE Transactions on Robotics (T-RO)*, vol. 29, no. 2, pp. 579–585, 2012. DOI: 10.1109/TRO.2012.2222274.

[134] M. Teichmann, "A grasp metric invariant under rigid motions," in *IEEE International Conference on Robotics and Automation (ICRA)*, vol. 3, 1996, pp. 2143–2148. DOI: 10.1109/ROBOT.1996.506187.

[135] A. T. Miller and P. K. Allen, "Examples of 3d grasp quality computations," in *IEEE International Conference on Robotics and Automation (ICRA)*, vol. 2, 1999, pp. 1240–1246. DOI: 10.1109/ROBOT.1999.772531.

[136] B. Mirtich and J. Canny, "Easily computable optimum grasps in 2-D and 3-D," in *IEEE International Conference on Robotics and Automation (ICRA)*, 1994, pp. 739–747. DOI: 10.1109/ROBOT.1994.351399.

[137] C. Borst, M. Fischer, and G. Hirzinger, "Grasp planning: How to choose a suitable task wrench space," in *IEEE International Conference on Robotics and Automation (ICRA)*, vol. 1, 2004, pp. 319–325. DOI: 10.1109/ROBOT.2004.1307170.

[138] N. S. Pollard, "Parallel methods for synthesizing whole-hand grasps from generalized prototypes," PhD thesis, Department of Electrical Engineering and Computer Science, Massachusetts Institute of Technology, 1994.

[139] X. Markenscoff and C. H. Papadimitriou, "Optimum grip of a polygon," *International Journal of Robotics Research (IJRR)*, vol. 8, no. 2, pp. 17–29, 1989. DOI: 10.1177/027836498900800202.

[140] A. M. Howard and G. A. Bekey, "Intelligent learning for deformable object manipulation," *Autonomous Robots*, vol. 9, no. 1, pp. 51–58, 2000. DOI: 10.1023/A:1008924218273.

[141] G. Mantriota, "Communication on optimal grip points for contact stability," *International Journal of Robotics Research (IJRR)*, vol. 18, no. 5, pp. 502–513, 1999. DOI: 10.1177/027836499901800506.

[142] S. P. Boyd and B. Wegbreit, "Fast computation of optimal contact forces," *IEEE Transactions on Robotics (T-RO)*, vol. 23, no. 6, pp. 1117–1132, 2007. DOI: 10.1109/TRO.2007.910774.

[143] H. Kruger and A. F. van der Stappen, "Partial closure grasps: Metrics and computation," in *IEEE International Conference on Robotics and Automation (ICRA)*, 2011, pp. 5024–5030. DOI: 10.1109/ICRA.2011.5980171.

[144] R. Haschke, J. J. Steil, I. Steuwer, and H. Ritter, "Task-oriented quality measures for dextrous grasping," in *IEEE International Symposium on Computational Intelligence in Robotics and Automation*, 2005, pp. 689–694. DOI: 10.1109/CIRA.2005.1554357.

[145] Y. Lin and Y. Sun, "Grasp planning to maximize task coverage," *International Journal of Robotics Research (IJRR)*, vol. 34, no. 9, pp. 1195–1210, 2015. DOI: 10.1177/0278364915583880.

[146] R. Holladay, T. Lozano-Pérez, and A. Rodriguez, "Force-and-motion constrained planning for tool use," in *IEEE/RSJ International Conference on Intelligent Robots and Systems (IROS)*, 2019, pp. 7409–7416. DOI: 10.1109/IROS40897.2019.8967889.

[147] Y. Lin and Y. Sun, "Task-based grasp quality measures for grasp synthesis," in *IEEE/RSJ International Conference on Intelligent Robots and Systems (IROS)*, 2015, pp. 485–490. DOI: 10.1109/IROS.2015.7353416.

[148] M. Strandberg and B. Wahlberg, "A method for grasp evaluation based on disturbance force rejection," *IEEE Transactions on Robotics (T-RO)*, vol. 22, no. 3, pp. 461–469, 2006. DOI: 10.1109/TRO.2006.870665.

[149] H. Jeong and J. Cheong, "Evaluation of 3d grasps with physical interpretations using object wrench space," *Robotica*, vol. 30, no. 3, pp. 405–417, 2012. DOI: 10.1017/S0263574711000713.

[150] H. Dang and P. K. Allen, "Semantic grasping: Planning task-specific stable robotic grasps," *Autonomous Robots*, vol. 37, no. 3, pp. 301–316, 2014. DOI: 10.1007/s10514-014-9391-2.

[151] J. Song, A. Tanwani, J. Ichnowski, M. Danielczuk, K. Sanders, J. Chui, J. A. Ojea, and K. Goldberg, "Robust task-based grasping as a service," in *IEEE Conference on Automation Science and Engineering (CASE)*, 2020, pp. 22–28. DOI: 10.1109/CASE48305.2020.9216952.

[152] P. Li, B. DeRose, J. Mahler, J. A. Ojea, A. K. Tanwani, and K. Goldberg, "Dex-Net as a service (dnaas): A cloud-based robust robot grasp planning system," in *IEEE Conference on Automation Science and Engineering (CASE)*, 2018, pp. 1420–1427. DOI: 10.1109/COASE.2018.8560447.

[153] N. S. Pollard, "Synthesizing grasps from generalized prototypes," in *IEEE International Conference on Robotics and Automation (ICRA)*, vol. 3, 1996, pp. 2124–2130. DOI: 10.1109/ROBOT.1996.506184.

[154] J. Aleotti and S. Caselli, "Interactive teaching of task-oriented robot grasps," *Robotics and Autonomous Systems*, vol. 58, no. 5, pp. 539–550, 2010. DOI: 10.1016/j.robot.2010.01.004.

[155] P. Long, W. Khalil, and P. Martinet, "Force/vision control for robotic cutting of soft materials," in *IEEE/RSJ International Conference on Intelligent Robots and Systems (IROS)*, 2014, pp. 4716–4721. DOI: 10.1109/IROS.2014.6943233.

[156] Y. Li, Y. Yue, D. Xu, E. Grinspun, and P. K. Allen, "Folding deformable objects using predictive simulation and trajectory optimization," in *IEEE/RSJ International Conference on Intelligent Robots and Systems (IROS)*, 2015, pp. 6000–6006. DOI: 10.1109/IROS.2015.7354231.

[157] D. Seita, N. Jamali, M. Laskey, R. Berenstein, A. K. Tanwani, P. Baskaran, S. Iba, J. Canny, and K. Goldberg, "Deep Transfer Learning of Pick Points on Fabric for Robot Bed-Making," in *International Symposium on Robotics Research (ISRR)*, 2019.

[158] T. Bretl and Z. McCarthy, "Quasi-static manipulation of a kirchhoff elastic rod based on a geometric analysis of equilibrium configurations," *International Journal of Robotics Research (IJRR)*, vol. 33, no. 1, pp. 48–68, 2014. DOI: 10.1177/0278364912473169.

[159] J. Sanchez, J.-A. Corrales, B.-C. Bouzgarrou, and Y. Mezouar, "Robotic manipulation and sensing of deformable objects in domestic and industrial applications: A survey," *International Journal of Robotics Research (IJRR)*, vol. 37, no. 7, pp. 688–716, 2018. DOI: 10.1177/0278364918779698.

[160] K. Gopalakrishnan and K. Goldberg, "D-space and deform closure grasps of deformable parts," *International Journal of Robotics Research (IJRR)*, vol. 24, no. 11, pp. 899–910, 2005. DOI: 10.1177/0278364905059055.

[161] H. Wakamatsu, S. Hirai, and K. Iwata, "Static analysis of deformable object grasping based on bounded force closure," in *IEEE International Conference on Robotics and Automation (ICRA)*, vol. 4, 1996, pp. 3324–3329. DOI: 10.1109/ROBOT.1996.509219.

[162] A Delgado, C. A. Jara, D. Mira, and F Torres, "A tactile-based grasping strategy for deformable objects' manipulation and deformability estimation," in *IEEE International Conference on Informatics in Control, Automation and Robotics (ICINCO)*, vol. 2, 2015, pp. 369–374.

[163] Y.-B. Jia, F. Guo, and H. Lin, "Grasping deformable planar objects: Squeeze, stick/slip analysis, and energy-based optimalities," *International Journal of Robotics Research (IJRR)*, vol. 33, no. 6, pp. 866–897, 2014. DOI: 10.1177/0278364913512170.

[164] L. Zaidi, J. A. Corrales, B. C. Bouzgarrou, Y. Mezouar, and L. Sabourin, "Model-based strategy for grasping 3d deformable objects using a multi-fingered robotic hand," *Robotics and Autonomous Systems*, vol. 95, pp. 196–206, 2017. DOI: 10.1016/j.robot.2017.06.011.

[165] Y. Zheng, M. C. Lin, and D. Manocha, "On computing reliable optimal grasping forces," *IEEE Transactions on Robotics (T-RO)*, vol. 28, no. 3, pp. 619–633, 2012. DOI: 10.1109/TRO.2012.2183057.

[166] J. Kerr and B. Roth, "Analysis of multifingered hands," *International Journal of Robotics Research (IJRR)*, vol. 4, no. 4, pp. 3–17, 1986. DOI: 10.1177/027836498600400401.

[167] Y.-H. Liu, "Qualitative test and force optimization of 3-d frictional form-closure grasps using linear programming," *IEEE Transactions on Robotics and Automation*, vol. 15, no. 1, pp. 163–173, 1999. DOI: 10.1109/70.744611.

[168] F.-T. Cheng and D. E. Orin, "Efficient algorithm for optimal force distribution - the compact-dual LP method," *IEEE Transactions on Robotics and Automation*, vol. 6, no. 2, pp. 178–187, 1990. DOI: 10.1109/70.54733.

[169] M. Buss, L. Faybusovich, and J. B. Moore, "Dikin-type algorithms for dextrous grasping force optimization," *International Journal of Robotics Research (IJRR)*, vol. 17, no. 8, pp. 831–839, 1998. DOI: 10.1177/027836499801700802.

[170] V. Lippiello, B. Siciliano, and L. Villani, "A grasping force optimization algorithm for multiarm robots with multifingered hands," *IEEE Transactions on Robotics (T-RO)*, vol. 29, no. 1, pp. 55–67, 2012. DOI: 10.1109/TRO.2012.2212633.

[171] M. S. Lobo, L. Vandenberghe, S. Boyd, and H. Lebret, "Applications of second-order cone programming," *Linear algebra and its applications*, vol. 284, no. 1-3, pp. 193–228, 1998. DOI: 10.1016/S0024-3795(98)10032-0.

[172] U. Helmke, K. Huper, and J. B. Moore, "Quadratically convergent algorithms for optimal dextrous hand grasping," *IEEE Transactions on Robotics and Automation*, vol. 18, no. 2, pp. 138–146, 2002. DOI: 10.1109/TRA.2002.999643.

[173] L. Shao, F. Ferreira, M. Jorda, V. Nambiar, J. Luo, E. Solowjow, J. A. Ojea, O. Khatib, and J. Bohg, "Unigrasp: Learning a unified model to grasp with multifingered robotic hands," *IEEE Robotics and Automation Letters (RA-L)*, vol. 5, no. 2, pp. 2286–2293, 2020. DOI: 10.1109/LRA.2020.2969946.

[174] P. Ni, W. Zhang, X. Zhu, and Q. Cao, "Pointnet++ grasping: Learning an end-to-end spatial grasp generation algorithm from sparse point clouds," in *IEEE International Conference on Robotics and Automation (ICRA)*, 2020, pp. 3619–3625. DOI: 10.1109/ICRA40945.2020.9196740.

[175] H.-S. Fang, C. Wang, M. Gou, and C. Lu, "Graspnet-1billion: A large-scale benchmark for general object grasping," in *IEEE Conference on Computer Vision and Pattern Recognition (CVPR)*, 2020, pp. 11 441–11 450. DOI: 10.1109/CVPR42600.2020.01146.

[176] A. Mousavian, C. Eppner, and D. Fox, "6-DOF GraspNet: Variational grasp generation for object manipulation," in *IEEE International Conference on Computer Vision (ICCV)*, 2019, pp. 2901–2910. DOI: 10.1109/ICCV.2019.00299.

[177] M. Sundermeyer, A. Mousavian, R. Triebel, and D. Fox, "Contact-GraspNet: Efficient 6-DoF grasp generation in cluttered scenes," in *IEEE International Conference on Robotics and Automation (ICRA)*, 2021, pp. 13 438–13 444. DOI: 10.1109/ICRA48506.2021.9561877.

[178] ANSYS® Academic Research, Release 17.2.

[179] M. Everingham, L. Van Gool, C. K. Williams, J. Winn, and A. Zisserman, "The pascal visual object classes (voc) challenge," *International journal of computer vision*, vol. 88, no. 2, pp. 303–338, 2010. DOI: 10.1007/s11263-009-0275-4.

[180] "festo.com", *Festo fin ray® finger*, Accessed on: Mar. 01, 2019. [Online]. Available: https://www.festo.com/group/de/cms/10221.htm.

[181] R. B. Rusu and S. Cousins, "3D is here: Point cloud library (PCL)," in *IEEE International Conference on Robotics and Automation (ICRA)*, 2011, pp. 1–4. DOI: 10.1109/ICRA.2011.5980567.

[182] N. Mellado, D. Aiger, and N. J. Mitra, "Super4PCS: fast global pointcloud registration via smart indexing," *Computer Graphics Forum*, vol. 33, no. 5, pp. 205–215, 2014. DOI: 10.1111/cgf.12446.

[183] G. Smith, E. Lee, K. Goldberg, K. Bohringer, and J. Craig, "Computing parallel-jaw grips," in *IEEE International Conference on Robotics and Automation (ICRA)*, vol. 3, 1999, pp. 1897–1903. DOI: 10.1109/ROBOT.1999.770385.

[184] D. Morrison, P. Corke, and J. Leitner, "EGAD! an evolved grasping analysis dataset for diversity and reproducibility in robotic manipulation," *IEEE Robotics and Automation Letters (RA-L)*, vol. 5, no. 3, pp. 4368–4375, 2020. DOI: 10.1109/LRA.2020.2992195.

[185] B. Calli, A. Walsman, A. Singh, S. Srinivasa, P. Abbeel, and A. M. Dollar, "Benchmarking in manipulation research: Using the Yale-CMU-Berkeley object and model set," *IEEE Robotics & Automation Magazine*, vol. 22, no. 3, pp. 36–52, 2015. DOI: 10.1109/MRA.2015.2448951.

[186] C. M. Kim, M. Danielczuk, I. Huang, and K. Goldberg, *Simulation of parallel-jaw grasping using incremental potential contact models*, 2021. arXiv: 2111.01391 [cs.RO].

List of Figures

List of Tables